NAVAL POSTGRADUATE SCHOOL

MONTEREY, CALIFORNIA

DISSERTATION

**THE RE-INTENSIFICATION OF
TYPHOON SINLAKU (2008)**

by

Elizabeth R. Sanabia

June 2010

Dissertation Supervisor: Patrick A. Harr

Approved for public release; distribution is unlimited

THIS PAGE INTENTIONALLY LEFT BLANK

REPORT DOCUMENTATION PAGE		*Form Approved OMB No. 0704-0188*

Public reporting burden for this collection of information is estimated to average 1 hour per response, including the time for reviewing instruction, searching existing data sources, gathering and maintaining the data needed, and completing and reviewing the collection of information. Send comments regarding this burden estimate or any other aspect of this collection of information, including suggestions for reducing this burden, to Washington headquarters Services, Directorate for Information Operations and Reports, 1215 Jefferson Davis Highway, Suite 1204, Arlington, VA 22202-4302, and to the Office of Management and Budget, Paperwork Reduction Project (0704-0188) Washington DC 20503.

1. AGENCY USE ONLY *(Leave blank)*	**2. REPORT DATE** June 2010	**3. REPORT TYPE AND DATES COVERED** Dissertation

4. TITLE AND SUBTITLE: The Re-Intensification of Typhoon Sinlaku (2008)	**5. FUNDING NUMBERS**
6. AUTHOR(S) Sanabia, Elizabeth R.	

7. PERFORMING ORGANIZATION NAME(S) AND ADDRESS(ES) Naval Postgraduate School Monterey, CA 93943-5000	**8. PERFORMING ORGANIZATION REPORT NUMBER**

9. SPONSORING / MONITORING AGENCY NAME(S) AND ADDRESS(ES) N/A	**10. SPONSORING / MONITORING AGENCY REPORT NUMBER**

11. SUPPLEMENTARY NOTES The views expressed in this thesis are those of the author and do not reflect the official policy or position of the Department of Defense or the U.S. Government. IRB Protocol Number:_____.

12a. DISTRIBUTION / AVAILABILITY STATEMENT Approved for public release; distribution is unlimited	**12b. DISTRIBUTION CODE** A

13. ABSTRACT (maximum 200 words)

In September 2008, Typhoon Sinlaku re-intensified from a sheared, asymmetric, weak tropical storm to a typhoon southwest of Japan. The evolution of the tropical cyclone (TC) structure was observed by multiple aircraft as part of the TCS-08 and T-PARC field programs. Airborne dual-Doppler radar, dropwindsondes, and flight-level observations reveal critical interactions among the decaying TC and three mesoscale vortices that initiated the re-intensification of Sinlaku. The structural characteristics of the three vortices, which include a vigorously growing convective tower, a mesoscale convective vortex, and a low-level hybrid vortex, are defined with respect to representative precipitation processes.

Following interaction with the mesoscale vortices, re-intensification proceeded via processes consistent with axisymmetrization as multiple convective bursts rotated cyclonically and inward while a region of older convection propagated outward to become a principal band. Subsequent aircraft observations revealed a warm-core, near-symmetric typhoon.

The overall re-intensification scenario is examined with respect to interactions among a variety of processes that vary from synoptic scale to convective scale. Synoptic-scale southwest monsoon flow over elevated sea-surface temperatures and high ocean heat content preconditioned the region where the critical convective episodes began. Mesoscale processes then acted to produce and re-distribute positive vorticity that defined the re-intensification of TY Sinlaku.

14. SUBJECT TERMS Tropical Cyclones, TCS-08, T-PARC, Extratropical Transition, Airborne Dual Doppler Radar, ELDORA, Axisymmetrization, Mesoscale Vortices, Mesoscale Convective System	**15. NUMBER OF PAGES** 233
	16. PRICE CODE

17. SECURITY CLASSIFICATION OF REPORT Unclassified	**18. SECURITY CLASSIFICATION OF THIS PAGE** Unclassified	**19. SECURITY CLASSIFICATION OF ABSTRACT** Unclassified	**20. LIMITATION OF ABSTRACT** UU

THIS PAGE INTENTIONALLY LEFT BLANK

THE RE-INTENSIFICATION OF TYPHOON SINLAKU (2008)

Elizabeth R. Sanabia
Commander, United States Navy
B.S., United States Naval Academy, 1993
M.S., Naval Postgraduate School, 2006

Submitted in partial fulfillment of the
requirements for the degree of

DOCTOR OF PHILOSOPHY IN METEOROLOGY

from the

**NAVAL POSTGRADUATE SCHOOL
June 2010**

Author: _____
Elizabeth R. Sanabia

Approved by:

_____
Patrick A. Harr
Professor of Meteorology
Dissertation Supervisor

_____	_____
Russell L. Elsberry	Michael T. Montgomery
Distinguished Professor of	Professor of Meteorology
Meteorology	
_____	_____
Philip A. Durkee	Francis X. Giraldo
Professor of Meteorology	Professor of Mathematics

Approved by: _____
Philip A. Durkee, Chair, Department of Meteorology

Approved by: _____
Douglas Moses, Vice Provost for Academic Affairs

THIS PAGE INTENTIONALLY LEFT BLANK

ABSTRACT

In September 2008, Typhoon Sinlaku re-intensified from a sheared, asymmetric, weak tropical storm to a typhoon southwest of Japan. The evolution of the tropical cyclone (TC) structure was observed by multiple aircraft as part of the TCS-08 and T-PARC field programs. Airborne dual-Doppler radar, dropwindsondes, and flight-level observations reveal critical interactions among the decaying TC and three mesoscale vortices that initiated the re-intensification of Sinlaku. The structural characteristics of the three vortices, which include a vigorously growing convective tower, a mesoscale convective vortex, and a low-level hybrid vortex, are defined with respect to representative precipitation processes.

Following interaction with the mesoscale vortices, re-intensification proceeded via processes consistent with axisymmetrization as multiple convective bursts rotated cyclonically and inward while a region of older convection propagated outward to become a principal band. Subsequent aircraft observations revealed a warm-core, near-symmetric typhoon.

The overall re-intensification scenario is examined with respect to interactions among a variety of processes that vary from synoptic scale to convective scale. Synoptic-scale southwest monsoon flow over elevated sea-surface temperatures and high ocean heat content preconditioned the region where the critical convective episodes began. Mesoscale processes then acted to produce and re-distribute positive vorticity that defined the re-intensification of TY Sinlaku.

THIS PAGE INTENTIONALLY LEFT BLANK

TABLE OF CONTENTS

viii

LIST OF FIGURES

ACKNOWLEDGMENTS

THIS PAGE INTENTIONALLY LEFT BLANK

I.   INTRODUCTION

A.   MOTIVATION

Over the past two decades, tropical cyclone (TC) motion forecast accuracy has improved dramatically. This progress is a direct result of concentrated research that increased understanding of the interaction between the TC and its environment and defined important TC structural characteristics that impact TC motion. The concurrent increase in numerical weather prediction capability enabled the simulation of these important TC and environmental characteristics, which led to further improvement in forecast accuracy of TC motion.

While the forecast accuracy of TC intensity has also improved (JTWC 2008 ATCR), such a significant increase in the accuracy of forecasts related to TC structure, structure changes, and intensity has yet to be achieved. The TC structure defines the outer wind distribution that impacts the forcing on ocean wave field and interaction with the environment. Two current research programs designed to study TC structure and structure change provide the basis for this research.

Tropical Cyclone Structure 2008 (TCS-08) is a program sponsored by the Office of Naval Research that is focused on increasing the understanding and predictability of TC characteristics during formation, intensification, and recurvature. The primary objectives of TCS-08 are to examine the TC structure and structure change in the context of the large-scale environment, mesoscale organization, and the relative roles of vortex structures. In this study of the re-intensification of Sinlaku, the role of the large-scale environment is examined with respect to preconditioning and enhancement of deep convection. Mesoscale organization pathways are examined with respect to low-level convergence and updrafts in deep convective cells and stratiform regions of tropical mesoscale convective systems (MCSs). The TCS-08 field program was conducted in the late summer and early fall of 2008, and has been followed by an extensive research period.

1

The Observing-System Research and Predictability Experiment (THORPEX) – Pacific Asian Regional Campaign (T-PARC) is endorsed by the World Meteorological Organization and is funded in the United States by the National Science Foundation and the Office of Naval Research. In partnership with TCS-08, the T-PARC focus is on predictability of the entire TC life cycle. The primary objectives of T-PARC include improving understanding of the impacts of a TC on downstream development and predictability of high-impact weather events, identifying the relative roles of the TC vortex structure characteristics and the midlatitude circulation into which the TC is moving, and systematically evaluating the impacts of observations in regions of forecast sensitivity. The T-PARC field program was conducted in conjunction with TCS-08 and also has been followed by an extensive research period.

A unique aspect of the TCS-08 / T-PARC field program was that the entire TC lifecycle was investigated. In late September 2008, Typhoon (TY) Sinlaku offered the first opportunity during TCS-08 / T-PARC to observe the extratropical transition (ET) portion of the TC lifecycle. The WC-130J and P-3 each flew four ET missions through Sinlaku, and between the first two missions, the TC underwent a period of re-intensification that was not accurately forecast by global numerical models. These errors in forecast intensity have subsequently been linked to forecast errors in extratropical transition and downstream development, and have provided the motivation for this research, which is focused on identifying the physical mechanisms responsible for the re-intensification of Sinlaku from a minimal tropical storm ($\geq$34 kt, $\geq$17 m s^{-1}) to near typhoon intensity ($\geq$64 kt, $\geq$32 m s^{-1}) over a 24-h period prior to extratropical transition.

B.   BACKGROUND

The lifecycle of Sinlaku spanned multiple ocean regions over a period of nearly three weeks in September 2008. During this time, the TC interacted with features and processes on multiple scales of space and time, and these interactions will be carefully examined throughout this work. Definitions of the scales utilized in this research are adapted from Orlanski (1975). The synoptic scale is defined as features and processes that occur over several thousand kilometers and many days. The vortex scale is defined

to fit the meso-alpha scale, and occurs over distances between 200–2000 km and over a few days. The mesoscale in this research is defined to fit the meso-beta scale and describes features that occur over distances of 20–200 km and over a period of hours. The convective scale is considered as the meso-gamma scale and entails features that occur between 2–20 km and on the order of hours.

Prior to analyzing the re-intensification of TY Sinlaku, the stages in a TC lifecycle are reviewed. While the re-intensification took place late in the TC lifecycle, an understanding of the typical pathways to formation will establish a framework in which the observed synoptic and mesoscale features and processes are examined during the re-intensification of Sinlaku. An understanding of the mechanisms that can impact TC intensification are also important, since the re-intensification of Sinlaku will be examined over the span of 24 hours. As the redevelopment of Sinlaku took place prior to the onset of ET, the extratropical transition process is also reviewed.

1. Tropical Cyclone Formation

a. The Role of the Synoptic Scale

Several synoptic-scale conditions are known to be favorable to TC formation. These include minimum vertical wind shear, a moist mid-troposphere, low-level positive relative vorticity, and sea-surface temperatures greater than or equal to 26°C (Gray 1968). Over the western North Pacific, several synoptic-scale features exhibit many of the above factors. The monsoon trough, monsoon depressions, and monsoon gyres are all synoptic-scale components of the western North Pacific environment that often contain conditions favorable to TC formation. The large-scale features necessary for TC formation may be present for a sustained period or in more temporary conditions where large-scale processes precondition a region to make it suitable for TC formation. Simpson et al. (1997) state that establishment of these conditions by the large scale is the first step toward tropical cyclone development.

b. *The Role of the Mesoscale*

While there is general agreement on the large-scale conditions that are necessary but not sufficient for tropical cyclone formation, there are multiple views regarding the mesoscale features and processes that are principally responsible for TC spin-up. Prominent theories of tropical cyclone formation differ in the feature responsible for the generation of positive relative vorticity, the level at which that vorticity is initially generated, and the means by which that vorticity is redistributed through the column. In the context of the objectives of TCS-08, mesoscale pathways are defined as being either top-down or bottom-up.

Top-Down: The top-down theory of TC formation is based on the presence of mid-level vortex from which positive vorticity is transported downward to the surface. Mesoscale convective vortices (MCVs) are commonly found within the stratiform region of a mesoscale convective system (MCS) in the region between the ascending updraft and descending rear inflow (Houze et al. 1989). The column is stretched and a vortex develops in this mid-level region (Bartels and Maddox 1991; Houze 2004). One of the challenges in the top-down pathway to development is that beneath the mid-level vortex there is a pool of relatively warm and dry air below the stratus cloud region of the MCS, and a cool, moist layer just above the surface. For the TC to develop, a coherent vortex must form in the vertical, and for the already-present mid-level vortex to extend to the surface, the region beneath the mid-level vortex must be made more suitable for development.

One method to extend mid-level vorticity to the surface was advanced by Bister and Emanuel (1997), who hypothesized that a mid-level vortex could be transported to low-levels through moistening of the cold pool region. In their theory, the dry air beneath the stratiform region becomes more moist by sustained precipitation, and the near-surface cool layer is warmed from below through surface heat fluxes from the warm ocean surface. Generation of convection would then result in the production of low-level positive vorticity through stretching in the convective updraft with a minimum of evaporative-driven downdrafts. Latent heat release would then contribute to lowering

the surface pressure. In their modeling study, Rogers and Fritsch (2001) found that repeated deep convection would bring the MCV to the surface. Sustained latent heat release resulted in the increased cyclonic flow at successively lower levels, and reduction of the Rossby radius of deformation kept the heating within the scale of the MCV to ensure that heat generated in the convection remained contained within the system, and thereby warming the core, instead of propagating away in the form of gravity waves.

In an analysis of TY Irving, Ritchie and Holland (1997) attributed the formation of the typhoon to the development of multiple MCSs and the interaction between their associated MCVs. The merger of the MCVs increased the depth of the mid-level vorticity maximum toward the surface. The subsequent merger with the low-level tropical depression vortex extended the positive vorticity to the surface. A similar case was observed by Simpson et al. (1997). They found evidence of interactions between multiple MCVs in satellite imagery during a Southern Hemisphere TC (Oliver 1993). The rotation and subsequent merger of three MCVs was followed shortly thereafter by the merger of two MCVs that resulted in the development of TC Oliver and a primary spiral band.

Bottom-up: Hendricks et al. (2004) and Montgomery et al. (2006) proposed an alternate method for TC development. They have shown that it is possible for positive relative vorticity to be generated at lower levels in deep convective towers and redistributed throughout the troposphere. "Central cores" embedded in deep convection that rose undisturbed from the surface were defined as the mechanism by which heat was transported to upper levels in the tropics and by which the heat balance was maintained (Riehl and Malkus 1958). A subsection of these hot towers that exhibited substantial positive vorticity was the focus of Hendricks et al. (2004), who defined "vortical hot towers" (VHTs) as cores of deep cumulus convection that contain a significant amount of vertical vorticity. In numerical simulations, multiple regions of low-level potential vorticity were produced by the release of latent heat within these VHTs, and the aggregation of the towers increased the low-level PV centers and resulted in the formation of Hurricane Diana in the simulation. The results of this single case were extended to a general paradigm for TC development by Montgomery et al. (2006).

From their simulation, they defined a two-step process by which multiple VHTs within a MCV with a convectively unstable layer below the MCV rather than an inversion could develop into a tropical cyclone. In the first step, VHTs are generated by convective updrafts that tilt tubes of horizontal vorticity filaments into the vertical, which results in alternating columns of positive and negative relative vorticity. In the second step, the VHTs undergo vortex mergers that increase the magnitude of positive vorticity and near-surface mean tangential winds, and were shown to establish a tropical depression vortex within 1-2 days.

The process of axisymmetrization attributes significant weight to convective-scale disturbances, as one or more regions of deep convection in close proximity to the TC center enhance the relative vorticity of the parent (mean) vortex. Studies of TC intensification through axisymmetrization (Montgomery and Kallenbach 1997, Montgomery and Enagonio 1998, Enagonio and Montgomery 2001) focused on the importance of deep convection, but place the development within background flow of environmental positive vorticity, in cases of both a barotropic vortex and an MCV with maximum winds at midlevels. The "convection" (PV anomaly) interacted favorably with both the barotropic vortex and MCV and were shown in multiple experiments to result in the spinup of a symmetric vortex.

The process of axisymmetrization relies on the radial gradient of relative vorticity and the shear in the tangential winds. Montgomery and Kallenbach (1997) derived a formulation of the radial group speed of wave packets generated within PV asymmetries at various distances from the mean vortex. For vortices that are tilted downshear, the direction of the wave propagation is dependent upon the radial gradient of relative vorticity. If the gradient is positive, the radial group speed will be negative and the flow will be toward the vortex center. If the gradient is negative, the radial group speed will be positive and the flow will be away from the vortex center. Inward flow of positive relative vorticity is balanced by the expulsion of negative vorticity from the vortex. Outward flow of positive vorticity is constrained to a stagnation radius and may result in the development of spiral bands on the periphery of the vortex. Guinn and Schubert (1993) had previously shown that the development of inner spiral bands resulted

from the outward propagation of potential vorticity, rather than gravity waves. Bands of potential vorticity were shown to be strongly coupled with convection in a simulation by Chen and Yau (2001). Satellite data are a significant component of this analysis, and this link between convection and potential vorticity will be an important one.

2. Tropical Cyclone Intensification

a. The Role of Vertical Wind Shear

Although it is one of the necessary-but-not-sufficient conditions for tropical cyclone formation, varying views exist on the impact of vertical wind shear on TC intensity. Although agreement exists that wind shear above a certain threshold is detrimental to the integrity of the TC core, a few studies have shown that a minimal amount of vertical wind shear may favor re-intensification (Molinari et al. 2004, 2006). In their examination of Hurricane Guillermo (1997), Reasor et al. (2009) found that rapid intensification of the system occurred in 7-8 m s^{-1} of deep vertical wind shear as a result of deep convective bursts on the downshear left side of the system.

The impact of vertical wind shear on tropical cyclone structure has been studied in the framework of potential vorticity (Jones 1995), as well as that of wave dynamics (Reasor and Montgomery 2001). Jones explained that the tilted TC core will result in an offset of the PV maxima associated with the upper and lower level circulations. This offset will result in the rotation of one maximum about the other and the precession of the vortex. She also found that beneath the upper-level center, upward tilt in the isentropes would provide a lifting mechanism and increase convection. Reasor and Montgomery (2001) also described the offset of the upper- and lower-level circulations, but did so by adding a baroclinic perturbation to an otherwise symmetric vortex and determining the effect in terms of linear dynamics. For a large Rossby radius of deformation, they found results similar to the precession that Jones (1995) detected. With a smaller Rossby radius of deformation, they found that the vortex responds to the shear with a smaller degree of tilt.

It is commonly accepted that vertical wind shear will tilt the TC in the direction of the shear. Davis et al. (2008) investigated the response of the TC to vertical wind shear and found that a vortex may precess, form a new center, or evolve into a baroclinic cyclone. As it is being sheared, the TC continues to move. Corbosiero and Molinari (2003) studied the relationship between vertical wind shear and TC motion and found that TC tracks are most commonly left of the shear vector.

b.   The Role of Convection

The role of convection in TC intensification has been further investigated in recent research. Theoretical and observational studies have shown that convection close to the TC center enhances development. Vigh and Schubert (2009) showed that rapid intensification was favored when deep convection was located inside the radius of maximum winds. In their observational study, Shelton and Molinari (2009) showed that Hurricane Claudette rapidly developed when deep convection shifted into the vortex center. Rogers (2010) simulated the rapid intensification of Hurricane Dennis (2005) and found a link between the onset of rapid intensification and the increase in convection near the inner core of the TC.

Three observational studies of TCs using dual Doppler radar data have shed further light on the structures of both the deep convection and TC vortex. Reasor et al. (2000) used seven consecutive passes of airborne dual-Doppler radar data to analyze the evolution of the vortex structure of Hurricane Olivia (1994) over a 3.5-h period as the system weakened. Although a variety of asymmetries were observed in the vorticity fields, the weakening of the system was not attributed to these asymmetries, but to increased vertical wind shear and decreasing SSTs. Houze et al. (2009) examined the role of convection in the formation of Hurricane Ophelia. In a detailed examination of the structural characteristics of a deep, wide, and intense convective cell, they found that the primary generation of positive vorticity occurred within convective cells at low levels and was then stored within the stratiform region at midlevels. Bell and Montgomery (2010) examined multiple deep convective towers with coincident regions of buoyancy and vorticity in the pre-formation stage of TY Hagupit during TCS-08. They concluded

that vorticity and convergence within these features indicated that these convective bursts were the primary features responsible for the formation of TY Hagupit. This analysis of TY Sinlaku will also utilize airborne dual-Doppler radar data and will focus on the characteristics of the Sinlaku vortex and convective regions in the immediate vicinity of the TC.

3. Extratropical Transition

Extratropical transition is the process during which a TC shifts in structure from a tropical to an extratropical cyclone (Jones et al. 2003). During ET, both the TC structure and the midlatitude environment can change dramatically. As the cyclone evolves from a symmetric, warm-core, nearly equivalent barotropic, tropical system to an asymmetric, cold-core, baroclinic, extratropical system notable changes occur in frontal development, precipitation distribution, and outer wind structure in the surrounding midlatitude environment. These changes include warm frontogenesis to the north and east of the weakening TC core (Harr and Elsberry 2000). Frontolytic conditions often occur to the west of the TC core (Harr and Elsberry 2000), and a "delta rain region" (Shimazu 1998) is often found to the north of the storm with potentially extensive areas of precipitation. Previous studies have focused on the changes in thermal structure that occur within the ex-TC core (Evans and Hart 2003) as well as on those that occur in the surrounding midlatitude environment (Harr and Elsberry 2000).

Klein et al. (2000) divided the extratropical transition process into two stages. The transformation stage starts when the TC begins to interact with a pre-existing midlatitude baroclinic zone. On satellite imagery, the transformation stage is marked by the appearance of a dry slot south of the TC core. The decaying TC begins to couple with an upper-level open wave to the northwest of the ex-TC core. The transformation stage is complete when the ex-TC has transformed completely into a baroclinic system. The re-intensification stage involves the deepening of the transformed ex-TC as an extratropical cyclone.

Jones et al. (2003) defined a framework for the ET process composed of three stages – tropical, transformation, and extratropical. Each stage is based on the evolution

of the cyclone's structural characteristics. In the tropical cyclone stage, the storm is symmetric, warm-core and nearly equivalent barotropic. The transformation stage connects the tropical and extratropical phases and the evolution of its structure is as defined by Klein et al. (2000) described above. The extratropical stage begins when the ex-TC has become an asymmetric, cold-core, midlatitude system. The re-intensification of TCs in this third (extratropical) stage remains the subject of much research, as these systems may deepen rapidly and are often accompanied by potentially severe weather. The re-intensification of Sinlaku occurred between the tropical and transition stages of the TC lifecycle, which may have delayed the onset of ET.

C.   OBJECTIVE AND HYPOTHESES

The objective of this research is to identify and understand the physical mechanisms that were responsible for the re-intensification of Typhoon Sinlaku prior to extratropical transition. Unique, high-density observational data will be used to reveal the identity, characteristics, and relationship between multiple vortices at multiple levels in the vicinity of a tilted TC vortex under moderate shear immediately prior to the re-intensification of the system as a warm-core typhoon. Satellite data will be used to analyze the environment preceding and following the interaction between TY Sinlaku and these multiple vortices to detail scales and processes principally responsible for the re-intensification of the TC.

This objective will be met by addressing the following hypotheses:

1.   Synoptic-scale processes facilitated the re-intensification of Sinlaku by preconditioning the region west of Okinawa, which resulted in multiple episodes of deep convection in the path of TY Sinlaku.

2. Mesoscale and convective-scale processes contributed to an increase in the vorticity of the TC, which resulted in the re-intensification of Sinlaku.

10

a. The interaction between the tilted TC vortex and multiple mesoscale circulations within varying stages of convective development arrested the decay of Sinlaku following recurvature and initiated re-intensification of the system.

b. The re-intensification of Sinlaku continued through processes consistent with axisymmetrization, as multiple episodes of deep convection rotated cyclonically around and inward toward the TC center, which increased the positive vorticity associated with the system.

The outline of this paper is as follows. In Chapter II, the data and methods used to address these hypotheses will be discussed. The synoptic conditions leading up to the re-intensification of Sinlaku will be addressed in Chapter III. In Chapter IV, the structure of the TC and surrounding mesoscale vorticies will be defined, and the interaction between the Sinlaku vortex and these mesoscale vortices will be examined. In Chapter V, the evolution of the deep convection following the TC-multivortex interaction will be analyzed, the structure of the re-intensified TY Sinlaku will be defined, and a method for re-intensification will be proposed. Chapter VI will entail a discussion on the contribution of the interactions among features and processes of varying scales to the re-intensification of TY Sinlaku.

THIS PAGE INTENTIONALLY LEFT BLANK

II.   DATA AND METHODS

A.   FRAMEWORK

In the diagnostic study that follows, satellite data, model analyses, and aircraft observations from two TCS-08/T-PARC flights through the environment of TY Sinlaku during the re-intensification period are analyzed. Aircraft observations were collected during the first two of four "ET flights" from 16-18 September 2008 by the USAF WC-130J and NRL P-3, and during the first of six ET flights by the DLR Falcon. The Joint Typhoon Warning Center (JTWC) best track and intensity values (JTWC 2008 ATCR) were used in this research to define the locations and intensities of TY Sinlaku.

B.   NUMERICAL MODEL DATA

The period between the recurvature (1800 UTC 14 September 2008) and redevelopment (0000 UTC 18 September 2008) of TY Sinlaku is examined using the ECMWF Year of Tropical Convection (YOTC) data set. The equivalent horizontal resolution of the T799 spectral model data is 0.25^o and data on the 91 σ levels in the vertical are interpolated to pressure levels. The ECMWF analyses are not expected to accurately depict meso- and convective-scale features.   However, the special YOTC diabatic fields provide a framework to interpret the convection detected in the reflectivity measurements of the ELDORA.

Ocean characteristics (sea-surface current, sea-surface temperature, and ocean heat content) are evaluated using the Naval Research Laboratory (NRL) Experimental Real-Time East Asian Seas Ocean Nowcast/Forecast System (EAS16NFS).   The EAS16NFS is a regional adaptation of the Navy Coastal Ocean Model (Martin et al. 2008), with a resolution of $1/16^{th}$-degree in the horizontal, and 41 sigma-z levels (19 levels in σ, 21 in z) in the vertical (Riedlinger et al. 2006). The EAS16NAS uses the Global Navy Ocean Model for boundary conditions and continuously assimilates real-time satellite observations of sea-surface temperature and sea-surface height from

Advanced Very High Resolution Radar (AVHRR) satellite data through the Modular Ocean Data Assimilation System (MODAS) (Fox et al. 2002).

C. DATA SETS

1. Satellite Data

Satellite data are used to assess the evolution of TY Sinlaku following recurvature and three episodes of deep convection east of Sinlaku on 16 September 2008. Standard and enhanced IR (4-km resolution), water vapor (4-km resolution) and visible (1-km resolution) MTSAT-1R satellite imagery are provided by the Naval Research Laboratory (NRL) and the Cooperative Institute for Meteorological Satellite Studies (CIMSS). Digital MTSAT-1R data are provided by the Japan Meteorological Agency. The 85 GHz microwave imagery (5.1-km resolution) from the Tropical Rainfall Measuring Mission (TRMM) satellite, also provided by NRL, is used to define regions of deep convection. Corrected brightness temperatures and corresponding position data for the Advanced Microwave Sounding Unit-A (AMSU-A) (48-km resolution at nadir) are provided by the Cooperative Institute for Meteorological Satellite Studies (CIMSS) and are used to examine the thermal structure of the re-intensified TC.

To track deep convection between TCS-08/T-PARC flights, a WV/IR brightness temperature (Tb) differencing technique (Fritz and Laszlo 1993; Ackerman 1996; Olander and Velden 2009; Bedka et al. 2010) is used. This technique is based on the usual location of cloud tops beneath the tropopause. In these cases, the water vapor brightness temperature just above the cloud top will be lower than the cloud top brightness temperature, and the brightness temperature difference between the water vapor (7.6μm) and IR (11μm) channels is negative. However, this is no longer true once deep convection penetrates the tropopause. The temperature inversion at the tropopause leads to an increase in water vapor brightness temperature as air parcels are advected into the lower stratosphere by deep convective updrafts. Photons from these water vapor particles are emitted at temperatures higher than those from the surrounding cloud tops, which creates a positive difference between water vapor and IR brightness temperatures.

Consequently, a positive difference in WV-IR brightness temperatures ($Tb_{6.7}$-Tb_{11}) may be used as an indicator of very deep convection. Here, greatest weight is given to differences greater than 2 K, to take into account possible instrument calibration errors (Ackerman 1996).

The AMSU-A is a cross-track scanning microwave radiometer that resides on multiple polar-orbiting satellites (NOAA-15--19). The instrument rotates through a circular pattern, alternately scanning the earth and cold space, depending on the direction the instrument is facing. When scanning the earth, radiances are measured through 30 view angles, which are continuous, but irregular in size due to the geometry of the scan. Radiances measured for each field of view are averaged to a single value for each of 15 channels. In the vertical, each of these 15 channels represents a range of altitudes from the earth's surface and varies depending on the channel frequency and the corresponding transmissivity through the atmosphere. To achieve consistent geographic representation of brightness temperatures from the irregularly spaced fields of view, AMSU-A brightness temperatures for each channel were interpolated to a grid through a Cressman objective analysis scheme (Cressman 1959). Brightness temperature anomalies were then determined for each channel for the 2104 UTC 17 September 2008 pass. Anomalies are defined by calculating the mean brightness temperature over each grid for each level and then subtracting the mean from the value at each gridpoint at each level.

2.   Dropwindsonde Data

Dropwindsondes from the USAF WC-130J, NRL P-3, and DLR Falcon were quality controlled by the National Center for Atmospheric Research (NCAR) Earth Observing Laboratory (EOL) (Young et al. 2009a-c). Measurements of pressure, temperature, and relative humidity were made by each dropwindsonde at 0.5-s intervals during descent. The geopotential altitude was calculated from the hydrostatic equation by integrating upward from the sea surface. Wind and position data were computed from GPS navigation signals received by the dropwindsonde. The vertical wind was calculated from the pressure-calculated and theoretical dropwindsonde fall rates in the manner of Wang et al. (2009).

Several quality control measures affected the dropwindsondes released during the 16-17 September 2008 flights of the WC-130J, P-3, and DLR Falcon. Winds from "fast fall" cases in which the parachute on the dropwindsonde failed to deploy, which doubled the fall rate of the dropwindsonde and resulted in degraded wind data, were eliminated. No WC-130J dropwindsondes were affected by this error. Dropwindsondes from the P-3 affected by this error include those released at 0141 UTC and 0152 UTC 17 September 2008. The affected Falcon dropwindsondes include those released at 0437 UTC, 0535 UTC, 0541 UTC, and 0608 UTC 17 September 2008. During the descent of the 0141 UTC 17 September 2008 Falcon dropwindsonde, interference from another dropwindsonde signal affected some of these observations and they were removed.

Several dropwindsondes also did not transmit data to the surface. In these cases, the geopotential altitudes were calculated downward from the flight level. These dropwindsondes included the WC-130J dropwindsonde released at 0137 UTC 17 September 2008, the P-3 dropwindsonde released at 0141 UTC 17 September 2008, and the Falcon dropwindsonde released at 0437 UTC 17 September 2008.

Processing of the quality-controlled 0.5-s data included linear interpolation to pressure levels at 25-hPa increments using the values closest to each pressure level. If values were unavailable within 15 hPa of the desired level, that level was flagged as missing in the interpolated data set.

3.   **Flight-Level Data**

Flight-level winds collected by the NRL P-3 were also quality controlled by EOL (Jensen 2009). Specifically, the GPS-corrected longitudinal (UXC) and longitudinal (VXC) components, and the GPS-corrected wind speed (WSC) and wind direction (WDC) were used. Several cases of icing impacted temperature measurements, and the flight-level data for the 16-17 September 2008 P-3 flight were divided into two files. The first of these data sets (305rf13a.nc) between take-off (2053 UTC 16 September 2008) and 0244 UTC 17 September 2008 includes the subset of the flight track adjacent to the Sinlaku circulation center and deep convection, and is the data set used in this analysis. These 1-s data were binned in 25-hPa altitude increments, that is, within +/- 12.5 hPa

from the named level (i.e., the 550 hPa value includes observations from flight levels between 562.5-537.5 hPa) and were thinned as required to facilitate plot clarity.

Flight-level observations from the WC-130J were quality controlled by the Air Force Reconnaissance Weather Officer (ARWO). Error codes from the 16-17 September 2008 flight frequently reflected the unreliability of the SFMR data since the WC-130J was operating at a flight level near 10 km. These SFMR data during the affected time periods were not used.

The WC-130J flight-level dew-point temperatures were intermittently coded as missing in the vicinity of deep convection near 0100 UTC 17 September 2008. This missing code may reflect an automated correction for super-saturation when dew-point temperatures exceed air temperature measurements, which may result from inaccurate temperature measurements due to wetting of the temperature sensor (Zipser et al. 1981, Eastin et al. 2002a,b). Since the flight-level temperature is the variable of interest, those temperatures are flagged as suspect when the dew-point temperatures are coded as missing. These temperatures each ½ s are binned in 25-hPa increments and thinned as required.

4.   ELDORA Data

The Electra Doppler Radar (ELDORA), which is operated onboard the NRL P-3, is a significant focus of this research. Unique to this airborne, dual-beam, complex waveform mesoscale meteorological measuring system is the capability to provide 2-D and inferred 3-D velocity fields from a single platform at more than four times the horizontal resolution of the NOAA P-3D (Jorgensen 2002).

The ELDORA consists of two radars aligned back-to-back along the longitudinal axis of the aircraft and mounted in a rotodome on the tail of the P-3. The two antennae are positioned to scan forward and aft of the perpendicular to the aircraft flight path (Fig. 1, left) to achieve a separation angle of approximately 30° (Hildebrand et al. 1996). In flight, the rotodome spins about the longitudinal axis of the aircraft and the radar traces conical helixes as the aircraft moves forward. Each parcel of air is sampled multiple times by both the forward- and aft-pointing radars (Fig. 1, right), with the exact number

of samples determined by the forward speed of the aircraft. With the typical flight velocity of 120-125 m s^{-1} (240-250 kt), a beam separation of 37°, and a scan rate of 144° s^{-1}, the time lag between sampling by the forward and aft radars is approximately 1 minute for each 11-km range from the aircraft (Hildebrand et al. 1996).
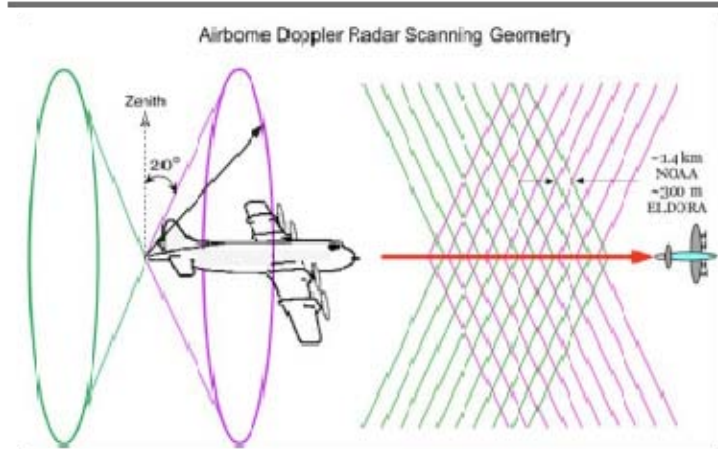
Figure 1.   Schematic of the ELDORA scan geometry. At left, the path of the forward-scanning radar is outlined in purple, and the path of the aft-scanning radar is outlined in green. At right, the intersection of sampled points is indicated where the purple and green lines cross as the P-3 moves along its flight path (modified from Houze et al. 2005).

The radar operates in the X-band with a 3.2-cm wavelength, and during TCS-08/T-PARC the transmission frequencies were 9.7 GHz (fore) and 9.6 GHz (aft) (Lee et al. 2009). The 3.2-cm wavelength gives the maximum possible resolution without risking the attenuation caused by heavy rain at shorter wavelengths (Hildebrand et al. 1996). A complex waveform transmits four sub-pulses at stepped and discrete frequencies within a single radar pulse, and each sub-pulse is then received and processed separately upon return of the signal. The signals are then averaged, which enhances the independence of the sample by a factor of 2-3 (Hildebrand et al. 1996, Wakimoto et al. 1996,). This is important because the time to independence for convective storms is 2-5 ms for a 3.2-cm wavelength radar with measured Doppler spectral widths of 1-3 m s^{-1}. With a forward airspeed near 130 m s^{-1} for the P-3 and a desired sampling every 300-500m, the radar rotation rate must be near 24 RPM (Lee et al. 2009). At this rate, the dwell time at each degree of rotation is on the order of 8 ms, which allows only 2-3

independent samples during each angle of rotation. To achieve the 1 m s^{-1} velocity accuracy requirement for airborne Doppler radar, 10 independent samples must be measured (Hildebrand et al. 1996). The additional independence factor that results from the complex waveform enables this requirement to be met (Hildebrand et al. 1996).

During TCS-08/T-PARC, only three of four frequencies were utilized due to a problem with the fourth receiver prior to the field program, which required a slowing of the radar rotation to 78° s^{-1} (near 13 RPM). This adjustment enabled a dwell time of 18 ms for additional independent samples to be measured (Lee et al. 2009). As a result, features of 2 km and greater were well resolved (M. Bell, 2010, personal communication).

The raw ELDORA data collected include the Doppler velocity, reflectivity, spectral width, and normalized coherent power. The Doppler velocity and reflectivity observations are the focus in this study. Spectral width (a measure of the amount of variation in the Doppler velocity within a radar cell) and normalized coherent power (a method to decrease noise and threshold velocity) are used during the quality control and post-processing phases.

The EOL provided quality-controlled ELDORA data sets corrected for navigation for each TCS-08/T-PARC P-3 flight. The ELDORA observations used in this study are during the time periods between 0135-0205 UTC 17 September 2008 and 0137-0207 UTC 18 September 2008. During these times, no additional errors were identified in the EOL quality control process (Lee et al. 2009).

The reflectivity and Doppler velocities were edited to remove noise, ground clutter, and radar artifacts. The corrected fields were then interpolated to a 500-m Cartesian grid. Interpolated velocities were synthesized using a variational approach as described in Reasor et al. (2009) to arrive at 3-dimensional wind and precipitation fields.

Pressure and temperature perturbation gradients were processed as in Houze et. al (2009), who used the methods of Roux and Ju (1990) and Roux et al. (1993). The 3-D wind field and a composite environmental sounding derived from a downstream upper-air

sounding and two in-situ aircraft dropwindsondes enabled characterization of the relative temperatures of the Sinlaku LLCC, deep convective towers, and the surrounding environment.

III. TROPICAL CYCLONE DECAY AND THE DEVELOPMENT OF DEEP CONVECTION

In this chapter, the general structural characteristics of TY Sinlaku and the evolution of convection are examined. Although convection associated with Sinlaku dissipated rapidly following recurvature of the TC, satellite imagery reveals that a separate area of moisture and convection extended northeastward from the South China Sea toward Japan. As the weakened TC approached the southwest-northeast oriented region of convection, three distinct episodes of enhanced convection occurred between the TC and the northeastward-extending region over a 24-h period. As the TC approached from the west, each successive convective episode occurred in increasingly close proximity to the TC center, and contributed to the re-establishment and organization of convection in the TC.

The third convective episode occurred during TCS-08/T-PARC aircraft operations. In Chapter IV, the aircraft data are analyzed to provide a detailed examination of the impact of the convective episodes on the structure of Sinlaku. In this chapter, the lifecycle and TC structure of Sinlaku following recurvature and the development of the deep convective episodes are examined in satellite and model analyses. The ECMWF Year of Tropical Convection (YOTC) data set provides a unique opportunity to analyze the broad impact of these convective episodes. While the resolution of the ECMWF analysis is not adequate to identify the mesoscale environment of the TC, it does provide a context in which the analysis of the high-resolution aircraft data may be placed. As defined in Chapter II, the YOTC data set compiled at the ECMWF contains a unique set of parameters that allow detailed examination of precipitation processes, and the impacts of those processes on the environment into which Sinlaku was moving.

A. TYPHOON SINLAKU

Typhoon Sinlaku developed east of the Philippines in the western North Pacific Ocean and reached tropical storm strength at 1200 UTC 8 September 2008 (Fig. 2). The

TC intensified rapidly as it tracked north-northwestward and reached typhoon intensity in less than 24 hours at 0900 UTC 9 September 2008. Sinlaku moved northward along 125°E and continued to deepen to a maximum intensity of 125 kts at 0000 UTC 11 September 2008. The typhoon turned northwestward at 0000 UTC 12 September 2008 and began to make landfall over Taiwan on 13 September 2008 while continuing to slowly weaken. Sinlaku reached its western-most position shortly thereafter, as it recurved at 1800 UTC 14 September 2008 and then began to move slowly east-northeastward over the East China Sea. The system continued to weaken for another two days until 0000 UTC 17 September 2008 when it began to gradually intensify northwest of Okinawa. Sinlaku then turned northeastward toward mainland Japan. After 48 hours of re-intensification, Sinlaku re-gained typhoon intensity between 0000-1200 UTC 19 September 2008 as it moved parallel to the east coast of southern Japan. Once south of Tokyo at 1800 UTC 19 September 2008, Sinlaku moved eastward along 35°N and began to undergo extratropical transition (ET). The TC weakened over the next 36 hours due to strong westerly vertical wind shear and failed to complete ET based on the definition of Klein et al. (2000).

The movement of TY Sinlaku toward the midlatitudes following recurvature is compared with the characteristic transformation stage of extratropical transition as defined by Klein et al. (2000), Jones et al. (2003), and Evans and Hart (2003) and previously discussed in the background section of Chapter I. The cyclone phase space of Hart (2003) is used to define synoptic-scale structural characteristics during the life cycle of Sinlaku (Fig. 3). The cyclone phase space is defined by a parameter B that represents the amount of symmetry contained in the circulation. A second parameter is defined as the low-level thermal wind that represents the amount of baroclinity in the environment of the circulation. Hart (2003) defined a typical pathway through the phase space during the lifecycle of a TC and then ET. As the TC intensifies, the path through the phase space proceeds to the right side of the symmetric warm core quadrant. As the transformation state of ET begins, the path turns back toward the origin and begins to turn into the asymmetric warm core quadrant. As ET proceeds, the path moves into the asymmetric cold-core quadrant.

In general, the path of Sinlaku through the cyclone phase as defined by ECMWF analyses (Fig. 3) is similar to the characteristic path defined by Hart (2003). However, just as the path extends into the asymmetric warm-core quadrant at 0000 UTC 18 September 2008, a sharp turn occurs back into the symmetric warm core quadrant (1200 UTC 18 September 2008). This path is maintained for a short period before it proceeds into the quadrant that defines an asymmetric cold-core structure, which suggests that in the ECMWF analysis a short-lived change in the TC structure occurred that temporarily favored redevelopment to a warm-core typhoon. The question addressed here is what caused the change in the TC structure and therefore enabled the redevelopment.

B.   INTERACTION BETWEEN TY SINLAKU AND THE LARGE-SCALE ENVIRONMENT

1.   Evolution of TY Sinlaku Following Maximum Intensity

Although Sinlaku began a period of steady weakening after reaching peak intensity on 11 September 2008 (Fig. 2b), the structure of the typhoon remained predominantly intact as the western eyewall made landfall over Taiwan in the early hours of 13 September 2008 (Fig. 4a). Although clouded over in IR imagery, an eye of nearly 100 km in diameter was evident in the 85 GHz microwave imagery (Fig. 4b). By the point of recurvature (Figs. 4c-d), nearly two days of land interaction had resulted in the loss of symmetry. The storm weakened significantly and very little deep convection remained associated with the decaying tropical circulation (Figs. 4e-f) as Sinlaku began to move eastward over the western North Pacific.

Although Sinlaku remained well south of the nearly zonal-oriented mid-latitude jet near 40°N (Fig. 5a), the TC was still in an environment of substantial westerly vertical wind shear with values near 15 kt based on satellite-derived values of deep vertical wind shear (Fig. 5b) provided by the Cooperative Institute for Meteorological Satellite Studies (CIMSS). The satellite-based vertical shear is in good agreement with 200 hPa – 850 hPa shear calculated over a storm-centered annulus between 4-6° latitude using ECMWF analyses (Fig. 6). As the TC turned eastward between 0000 UTC 15 September 2008 – 1200 UTC 16 September 2008, the 200 hPa – 850 hPa vertical wind shear rotated from

the west-northwest to west (Fig. 6) and steadily decreased in magnitude. Throughout this period, convection was concentrated downshear (Fig. 4f) and the storm motion was generally headed to the left of the shear vector. At 0000 UTC 17 September 2008, the 200 hPa – 850 hPa shear reached a minimum (Fig. 6), and was oriented from the west. At this time, the storm direction changed to be toward the northeast, or near 45° counter-clockwise from the shear vector. This storm heading relative to the shear vector is consistent with those found in many cases of sheared TCs with an asymmetric distribution of convection studied by Corbosiero and Molinari (2003).

The deep convection that began to be concentrated east of the exposed center of Sinlaku was also over the main path of the Kuroshio Current between the northeast coast of Taiwan and the southeast coast of mainland Japan (Fig. 7a). At 0000 UTC 16 September 2008, winds in the southeast quadrant of Sinlaku had fairly long trajectories over sea-surface temperatures greater than 27^oC (Fig. 7b) and regions with ocean heat content exceeding 100 kJ/cm^2 (Fig. 7c), which provided a nearly continuous source of high-Θ_e air along the eastern side of the TC.

2.   Evolution of Deep Convection

A band of moisture extended over the path of the Kuroshio Current from the South China Sea to the southern coast of mainland Japan at 0430 UTC 16 September 2008 (Fig. 8). Within that band, a sequence of three periods of deep convective activity began east of TY Sinlaku on 16 September 2008. The first convective period began at 0657 UTC 16 September 2008 (Fig. 9a) near 26.7^{o}N, 125.5^{o}E, east-southeast of the Sinlaku low-level circulation center (LLCC). Two hours later (Fig. 9b), the intensifying convective burst was clearly evident in the enhanced IR imagery. Circular spreading of cold cloud tops indicated vigorous convective development. The cold cloud tops continued to expand rapidly (Fig. 9c), and reached the largest areal coverage near 1300 UTC 16 September 2008 (Fig. 9 d). Notice that in each of these images (Figs. 9a-c), the lower-level cyclonic circulation on the southern side of the Sinlaku vortex converges with

24

the south-southwest-to-north-northeast band of moisture (which was noted in the water vapor image in Fig. 8 to originate in the deep tropics) in the region of the deepening convection.

Following the 6-hour expansion of this initial convective burst, the convection began to weaken as the areal coverage of the lowest cloud top temperatures became smaller at 1557 UTC 16 September 2008 (Fig. 9e). As the region of low cloud top temperatures decreased, it became split in two with one region of relatively cold cloud tops west of Okinawa and a second smaller region to the north of Okinawa (Fig. 9f). The region northwest of Okinawa rotated cyclonically and became elongated in a band oriented northwest-to-southeast. While both regions continued to have intermittent deep convection that resulted in isolated regions of very cold cloud tops, these convective regions were not sustained, and the two remnant convective regions began to dissipate by 1930 UTC 16 September 2008 (Fig. 10a).

While the convection associated with the first convective episode was weakening, two nearly simultaneous bursts along the western edge of the first convective episode marked the beginning of the second convective episode. The northern burst first appeared near 27.2^{o}N, 126.8^{o}E at 1857 UTC 16 September 2008 (Fig. 9f). Less than an hour later (Fig. 10 a), the northern burst began to expand as a second burst appeared to the south near 26.0^{o}N, 126.4^{o}E. This second burst was near the northwestern edge of the broad region of cloudiness associated with the weakening first convective episode. Notice that here again the convection was located at the intersection between the Sinlaku circulation and the band of moist tropical air.

By 2030 UTC 16 September 2008 (Fig. 10b), the northern and southern bursts that defined the second convective episode intensified rapidly. Meanwhile, the remnants of the first convective episode continued to weaken with embedded convective bands oriented from the northwest to southeast to the north of Okinawa.

An hour later (Fig. 10c), the uniform spreading of the cold cloud tops of the near-simultaneous bursts of the second convective episode merged into a common region of cold cloud tops. On the southeast side of this cold cloud top, a new burst erupted over

25

southwestern Okinawa near 26.0°N, 127.5°E. On the northeast side of Okinawa, the two linear bands of convection remaining from the first episode propagated northeastward. The leading band to the northeast continued to diminish in intensity, while the band just northeast of Okinawa intensified and maintained a northwest-to-southeast orientation (Fig. 10c).

By 2230 UTC 16 September 2008 (Fig. 10d), the cold cloud tops associated with the second convective episode had moved east-northeastward and expanded over Okinawa.   To the northeast, the leading linear band from the first convective episode continued to weaken, while the trailing band spread horizontally and weakened in intensity.

Just as the second convective episode began with convection growing on the western periphery of the previous episode, the third episode began with convection growing on the western edge of the second episode near 27.5°N, 126.5°E (Fig. 11a). This burst erupted due east of the approaching Sinlaku and in much closer proximity to the LLCC than the previous epsisodes and may have been due in part to convergence between the inner TC circulation and the monsoon flow. Within an hour (Fig. 11b), the burst initiating the third episode of deep convection intensified rapidly to form a near-circular region of cold, high clouds. As this convective burst developed, older convection associated with the two previous episodes continued to move east and northeastward. Remnants of the first convective episode were oriented in a line along 130°E.   The decaying convection of the second burst rotated to form a curved band of cold clouds that encircled the new convection from the east-southeast to the north-northeast. As the third convective burst continued to deepen over the next hour and a half (Figs. 11c-d), the TC continued to approach from the west, such that the Sinlaku LLCC came much closer to the deepening convection than had been the case in the preceding two episodes. At this time, the period of re-intensification (Fig. 2b) was initiated and the vertical wind shear was reduced (Fig. 6). Unlike the previous two episodes (Figs. 11c-d), this burst of deep convection initiating the third convective episode was observed by the USAF WC-130J and NRL P-3 during the first ET flight of the TCS-08/T-PARC field program.

3. Transition Between the Second and Third Convective Episodes

The development of the convective burst that initiated the third convective episode (Fig. 11) resulted in the rapid expansion of cold cloud tops in the enhanced IR imagery prior to observation by the TCS-08/T-PARC aircraft. To gain a better understanding of the environment through which the TCS-08/T-PARC observation aircraft flew, the transition between the second and third convective episodes is examined using water vapor imagery to reveal in greater detail the horizontal distribution of the moisture and convection in the third episode.

In water vapor imagery (Fig. 12a), the principle features from the first and second convective episodes at 2230 UTC 16 September 2008 coincided closely with the low cloud-top temperatures previously noted in the enhanced IR imagery from the same time (Fig. 10d). The two banded features from the first episode were oriented south-southeast-to-north-northwest in an arch around the northern Ryuku Islands. The leading band (to the northeast) was drier compared to the higher moisture content in the trailing band (to the southwest), which was centered over the island of Tokunoshima near 27.8^{o}N, 129.0^{o}E. The distribution of water vapor in the region of the near-simultaneous bursts that defined the second convective episode dominated the region, with brightness temperatures less than -60°C over the 40,000 km^{2} region located between 25.8^{o}-27.8^{o}N, and 126.2^{o}-128.2^{o}E. At this time, a smaller and much more subtle convective region (denoted as "2b" hereafter) developed on the northern side of this older expansive region of low brightness temperatures that correspond to a region of high atmospheric moisture content near 27.8^{o}N, 127.2^{o}E (Fig. 12a).

Just over 15 minutes later at 2313 UTC 16 September 2008 (Fig. 12b), a new mini-burst (considered the "newer 2b") developed southwest of the "older 2b" convection near 27.8^{o}N, 127.0^{o}E. The distribution of water vapor from the region of weaker convective bursts from 2b merged and defined a larger distribution of enhanced water vapor near 28.0^{o}N, 127.0^{o}E. Southwest of both of these circular features in the water

vapor imagery, a new burst began near 27.5^{o}N, 126.8^{o}E (Fig. 12b) on the northwest edge of the water vapor signal from the second convective episode, which defined the start of the third convective episode.

After another 15 minutes (Fig. 12c), the growing convective tower of the third episode is clearly evident in the water vapor imagery. Although the burst that initiated the third convective episode was intensifying rapidly, the distributions of water vapor associated with the 2b convection were still distinguishable as independent features. The older 2b signal to the northeast began to fade while the newer 2b region continued to exhibit a circular pattern in the water vapor imagery.

Over the next hour and a half (Fig. 12d), the third convective burst increased in intensity, and the rapid growth defined by the uniform circular spreading of cold cloud tops in the enhanced IR imagery was also evident in the water vapor imagery. The distribution of water vapor from the second episode became re-oriented in a crescent shape on the east side of the third burst. The distribution of water vapor associated with 2b near 28.0^{o}N, 127.0^{o}E (Fig. 12c) weakened and expanded to the northeast (Fig. 12d) as a curved region oriented from the north of the third episode to the northeast.

Review of the enhanced IR and water vapor imagery indicates good agreement between the low brightness temperatures that represent cold cloud tops and the low brightness temperatures that represent high atmospheric moisture content in defining the major features associated with the three convective episodes that occurred on 16 September 2008. Closer review of the transition period between the second and third convective bursts in the water vapor imagery (Fig. 12) reveals a small convective burst (2b) that occurred north of the second episode cloud shield and began an hour before the deep convective burst and initiated the third episode. The low brightness temperatures in the water vapor imagery associated with this small feature faded rapidly and contributed to the definition of the cyclonically curved distribution of water vapor to the north-northeast of the expanding third convection episode. At the time when episode three was being observed by the TCS-08/T-PARC aircraft, a complex distribution of precipitation structures existed in the environment to the east of Sinlaku. The decaying second episode

was defined by a combination of broad remnant cloud and smaller convective cells while a vigorously growing region of deep convection defined the third episode.

C. MODEL ANALYSIS FOLLOWING THE RECURVATURE OF TY SINLAKU

Satellite imagery clearly documented the eastward progression of Sinlaku following recurvature and the development of three convective episodes beginning 16 September 2008. The character of the synoptic-scale flow patterns is examined using ECMWF analyses to define the variation of the vortex with height and the relationship between the TC outflow and the midlatitude jet. The model fields are intended to complement the observation analysus in Chapter IV and provide a three-dimensional perspective of the evolution of TY Sinlaku following recurvature that led to the deployment of TCS-08/T-PARC aircraft.

1. 0000 UTC 15 September 2008

At 0000 UTC 15 September 2008, TY Sinlaku was centered in the ECMWF operational analyses (Figs. 13, 5a) over the northern Taiwan Strait between the northwest coast of Taiwan and mainland China with a minimum sea-level pressure of 993 hPa. The inner circulation at 850 hPa (Fig. 13a) was symmetric over the Taiwan Strait but extended southwestward in an elliptical shape at outer radii. Immediately east of the TC strong southerly flow between 123-127°E extended more than 20° lat. meridionally between 10-30°N.

At 500 hPa (Fig. 13b), the circulation center was analyzed to be north of Taiwan, which indicated a slight eastward tilt with height that was left of the shear vector (Fig. 6). Flow to the east was dominated by the southwest extension of the subtropical ridge. North of the TC, the flow was predominantly zonal, although a weak trough was northwest of the TC along the east Asian seaboard between 30-35°N and a short wave ridge was immediately east of the trough and north-northeast of the TC. At 200 hPa (Fig. 5a), outflow from the TC extended northeastward from the TC position into the region of the 55 m s^{-1} zonal jet maximum near 38°N over mainland Japan.

2. 1200 UTC 15 September 2008

Over the next 12 hours (Fig. 14), TY Sinlaku moved slowly northeastward on a track left of the shear vector that was associated with the 0000 UTC 15 September 2008 analysis (Fig. 6). By 1200 UTC 15 September 2008, the LLCC was near 27°N, directly north of Taiwan (Fig. 14a). The TC had weakened slightly with a minimum sea-level pressure of 995 hPa. The 850-hPa circulation had become somewhat more circular, possibly as a result of the reduced influence of the Taiwan Central Mountain Range and the coastal topography on the west side of the Taiwan Strait. Strong southerlies remained east of the TC. At 500 hPa (Fig. 14b), the TC center was still displaced slightly east of the 850 hPa center. Circulation about the TC center at 500 hPa remained closed and became oriented northeast-to-southwest.

At upper levels (Fig. 14c), the TC outflow continued to extend into the jet maximum that had increased to 60 m s^{-1} and moved offshore east of Japan. Flow along the jet remained zonal and predominantly along 40°N. A second weaker jet maximum of 45 m s^{-1} was located west of Korea.

3. 0000 UTC 16 September 2008

The TC continued to move on a track that was oriented slightly left of the shear vector (Fig. 6) over the next 12 hours through 0000 UTC 16 September 2008. Sinlaku also continued to weaken slightly with an increase in central pressure to 996 hPa. At 850 hPa (Fig. 15a), the circulation became more symmetric as the TC moved farther eastward over the East China Sea. At 500 hPa (Fig. 15b), the circulation remained closed, but was much weaker and continued to be elliptical with an orientation from north-northeast to south-southwest. At 200 hPa (Fig. 15c), outflow from the TC continued to arc anticyclonically toward the jet maximum that had moved farther east off the coast of Japan. The outflow appears to contribute to the ridging to the northeast of Sinlaku before returning southward toward the equator. Flow throughout the jet remained zonal, and the western jet maximum of 45 m s^{-1} northwest of Korea extended westward.

30

An analysis of the convective available potential energy (CAPE) (Fig. 16) over the western North Pacific at 0000 UTC 16 September 2008 illustrates the extension of a region of high CAPE northward from the deep tropics between 126-130°E. This region coincided with the high ocean heat content (Fig. 7c) northeast of Taiwan and the region of high atmospheric water vapor content (Fig. 8) from the Philippine Strait northeastward to the southern coast of mainland Japan. The region of elevated CAPE near 26°N, 127°E was in a region of upper-level diffluence (Fig. 15c) and was in close proximity to where the first convective burst (Fig. 9) would begin nearly seven hours later at 0657 UTC 16 September 2008.

4.   1200 UTC 16 September 2008

Over the next 12 hours (Fig. 6), TY Sinlaku again weakened slightly in the model analysis as it moved due eastward. At 1200 UTC 16 September 2008, the eastern side of the extensive 850-hPa circulation (Fig. 17a) moved into the region of southerly flow that had been prevalent for the preceding 36 hours between 125-130°E. This corresponds well with the convergence between the outer TC circulation and northerly flow observed in the satellite analysis. Although the typhoon became elongated in the north-south direction at both 850 hPa and 500 hPa (Figs. 17a-b), the mid-level circulation center was located at 126°E, while the 850-hPa circulation center was located a full degree west, at 125°E. While the 200-850 hPa vertical wind shear in the ECMWF analyses had decreased by nearly 30% over the previous 12 hours (Fig. 6), the TC was still tilted a full degree eastward between 850 hPa and 500 hPa.

At 1200 UTC 16 September 2008, the jet structure at 200 hPa (Fig. 17c) differed substantially from the preceding 36 hours. While there was still zonal flow along 40°N and a 55 m s^{-1} jet maximum northwest of Korea, a new 45 m s^{-1} maximum appeared over southern Japan and appeared to be related to the TC outflow. The outflow continues to arc anticyclonically into a ridge northeast of Sinlaku. The new jet maximum is just west of the ridge axis.

These 1200 UTC 16 September 2008 analyses were the first following the initiation of the first episode of deep convection. The northward extension of elevated

31

CAPE values (Fig. 18) was less robust than it had been 12 hours prior. A region of elevated CAPE still extended northward to nearly the latitude of the TC, but the magnitude was reduced.

To investigate the impact of the first six hours of deep convection to the east of the low-level TC, a closer view of the TC is examined. At 850 hPa (Fig. 19a), a vorticity maximum defines the TC center. The region of positive vorticity is circular, but not fully symmetric, and is centered at 27.0^oN, 125.2^oE. The eastward tilt of the vortex with height is clear in a vertical cross-section through the vorticity maximum along 27.0^oN (Fig. 19b). Two vorticity maxima are identified in the sloping vortex. The low-level center at 950 hPa is near 125.2^oE, and the mid-level center at 400 hPa is near 126.5^oE. While the vortex tilts with height, below 600 hPa, the low-level maximum is near vertical.

A vertical cross-section through the mid-level maximum along 126.5^oE (Fig. 19c) reveals the upper-level vorticity maximum associated with the TC at 400 hPa near 27.0^oN. There is an elongated region of lower positive vorticity between 900 hPa – 700 hPa that extends northward to 30.0^oN, which is consistent with the 850-hPa plan view in Fig. 19.

A southwest-to-northeast vertical cross-section of relative vorticity (Fig.19d) at 1200 UTC 16 September 2008 reveals the vorticity maximum associated with the TC is vertical beneath 600 hPa, then tilts northeastward toward a mid-level maximum at 400 hPa near 127.5^oE. This maximum near 127.5^oE is the upper-level maximum associated with the TC in the zonal cross-section (Fig. 19b). Examination of a vertical cross-section along 127.5^oE (Fig. 19e) through that maximum reveals that it is a mid-level feature only and is also centered at 400 hPa.

In a plan view of relative vorticity at 400 hPa (Fig. 19f), there is a single maximum that is associated with the TC at 27.0^oN, 126.5^oE. The region of positive vorticity extends northeastward along the trough axis toward the maximum observed in Fig. 19e at 28.5^oN, 128.0^oE.

In contrast with the pattern of 850-hPa relative vorticity (Fig. 19a), there were two maxima in the 850-hPa PV pattern (Fig. 20a). One maximum was near the TC center at 26.9^{o}N, 124.7^{o}E, and there was a smaller maximum to the northeast at 27.5^{o}N, 125.5^{o}E. The vertical cross-section through 27.0^{o}N (Fig. 20b) reveals several maxima within a PV structure tilted eastward with height. The low-level maximum is at 950 hPa near 125.4^{o}E, which is in the same location as the relative vorticity low-level maximum (Fig. 19b). The upper-level PV maximum is at 400 hPa near 126.7^{o}E, which is very close to the upper-level relative vorticity maximum. Although the positive relative vorticity structure was upright vertically through 600 hPa, the PV structure tilts eastward with height, even below 600 hPa and has two distinct regions of elevated PV instead of a single low-level maximum.

In the vertical cross-section along 126.5^{o}E (Fig. 20c), the upper-level PV maximum associated with the TC at 400 hPa near 27.0^{o}N has the greatest magnitude. Just to the north, though, that maximum appears to connect with another mid-level feature over 28.0^{o}N, and that feature extends to lower levels.

The southwest-to-northeast vertical cross-section of PV at 1200 UTC 16 September 2008 (Fig. 20d) reveals three features at increasing heights. A two-lobe maximum is present between 800-1000 hPa, which extends toward the northeast through 500 hPa where it joins a second feature that extends toward the surface. Farther to the northeast, there is another maximum at 400 hPa, which corresponds with the upper-level relative vorticity maximum (Fig. 19d) between 127.5^o-128.0^{o}E. As with the relative vorticity, a vertical cross-section of PV along 127.5^{o}E (Fig. 20e) reveals an upper-level PV maximum that extends toward the surface, but does not pass below 750 hPa.

The 400-hPa PV pattern (Fig. 20e) also corresponds to the 400-hPa relative vorticity pattern (Fig. 19f) in that they both follow the trough axis. Unlike the relative vorticity, there are several PV maxima at 400 hPa. The largest maximum is associated with the upper level maximum associated with the TC at 27.0^{o}N, 126.5^{o}E. To the northeast, there are several smaller regions of positive PV near 28.5^{o}N 127.5^{o}E, which corresponds with the location of the upper-level PV maximum in Fig. 20e.

5.   0000 UTC 17 September 2008

Between 1200 UTC 16 September 2008 (Fig. 17) and 0000 UTC 17 September 2008 (Fig. 21), TY Sinlaku moved east-northeastward as it continued to weaken slightly to a mean sea-level pressure of 999 hPa. This movement was again left of the deep shear vector (Fig. 6), which had further decreased in magnitude by 25% over the previous 12-h period. Even with the reduction in shear, the representation of the TC vortex in the 0000 UTC 17 September 2008 ECMWF analysis indicates a tilt northeastward with height. The center of the 850-hPa streamline circulation (Fig. 21a) is clearly northeast of the TC LLCC at 27.1^{o}N, 125.8^{o}E. At mid-levels (Fig. 21b), the 500-hPa circulation center near 28.0^{o}N, 127.0^{o}E was shifted even farther northeast relative to the 850-hPa center in the ECMWF analyses. (These locations were determined by detailed examination of the streamlines at each level in the ECMWF analysis.)

The southwestward extension of the eastern jet maximum at 200 hPa (Fig. 21c) over southern Japan was no longer present by 0000 UTC 17 September 2008. The 50 m s^{-1} western jet maximum moved nearly 10° long. eastward and was now centered over the Sea of Japan just south of 40°N. Outflow from the TC still arched northward before turning eastward along 35°N, but this trajectory was now well south of the jet axis.

By 0000 UTC 17 September 2008, the three episodes of deep convection had occurred to the east of the Sinlaku LLCC (Figs. 9-11). The eastward movement of the TC directly toward the burst presumably contributed to the initiation of the third episode of deep convection (Fig. 11) near 27.5^{o}N, 126.8^{o}E, which corresponds closely to the region of CAPE (Fig. 22) exceeding 1200 J kg^{-1} that is oriented meridionally along 127.5^{o}E between 26-28°N in the ECMWF analysis at 0000 UTC 17 September 2008.

The impact of the convection on the TC structure in the ECMWF analysis was clearly evident at 850 hPa (Fig. 23a). A large region of positive 850-hPa vorticity defined the TC center near 27.0^{o}N, 126.0^{o}E, and a second vorticity maximum was located northeast of the primary TC circulation center near 28.2^{o}N, 127.5^{o}E. The eastward tilt with height is defined in a vertical cross-section of relative vorticity (Fig. 23b) through the TC center along 27.0^{o}N. Similar to the 1200 UTC 16 September 2008 analysis, there

34

is a low-level maximum at 900 hPa at 125.9°E near the TC center, and a second maximum at 400 hPa near 127.0°E. This 1.1° eastward tilt with height over 500 hPa is comparable to the 1.3° eastward tilt with height over 550 hPa from the previous 12 h.

A meridional vertical cross-section along 127.5°E (Fig. 23c) passes just east of the upper-level vorticity maximum of the tilted TC and extends northward through the second vorticity maximum identified at 850 hPa. The tilted outline of the upper-level TC maximum is defined by the broad region of relative vorticity that exceeds $1.5*10^4$ s^{-1} at 400 hPa near 27.0°N. To the north, the 850-hPa vorticity maximum at 28.0°N is oriented vertically through 450 hPa before arching slightly northward through 400 hPa.

Finally, a vertical cross-section (Fig. 23d) from the southwest through the vorticity maximum that defines the TC center to the vorticity center to the northeast indicates the tilted vorticity maximum of the primary TC structure extends northeastward to connect with the upper portion of the vertically upright vorticity maximum near 127.25°E. Although the resolution of the ECMWF is coarse, it appears that the precipitation processes associated with the convection to the east of Sinlaku may have contributed to a second vorticity maximum downshear and left of the TC center. It is also at this time that the track of Sinlaku turns to the northeast (Figs. 2a,6) in the direction of the second vorticity maximum (Fig. 23a).

To gain a better understanding of the relationship between these two relative vorticity maxima and their evolution with height, contours of relative vorticity values in excess of $2*10^4$ s^{-1} are plotted at 850 hPa, 600 hPa, 500 hPa, and 400 hPa (Fig. 24). At 850 hPa (white contours, Fig. 24), the two maxima analyzed previously (Fig. 23a) are clearly distinct. At 600 hPa (red contours, Fig. 24), the outer vorticity contours connect around the features, but the maxima remain separate. The eastward tilt of the TC along 27.0°N is evident, and the vertical orientation of the feature to the northeast is clear as the vorticity maximum remains centered close to 28.1°N, 127.2°E. At 500 hPa (green contours, Fig. 24), the vorticity maximum associated with the TC weakens, and the only center greater than $2.5*10^4$ s^{-1} is over the feature to the northeast. At 400 hPa (blue contours, Fig. 24), the two vorticity maxima are replaced by a single maximum between the two features.

Potential vorticity at 850 hPa (Fig. 25) reveals a structure very similar to the relative vorticity in Fig. 23, except that the center to the northeast near 28.25^{o}N 127.5^{o}E has a larger magnitude than the TC center. In a vertical cross-section through the TC center PV maximum at 27.0^{o}N (Fig. 25b), the two maxima again reveal an eastward tilt with height. The first is at 700 hPa near 126.0^{o}E, and the second is farther east at 400 hPa near 127.0^{o}E. In contrast to the relative vorticity distribution, a small lobe of positive PV at 500 hPa extends beyond the apparent TC vortex eastward through 128.5^{o}E. A vertical cross-section along 127.5^{o}E (Fig. 25c) through the PV maximum northeast of the Sinlaku LLCC has a PV tower to the northeast that is vertically upright. In contrast to the relative vorticity, the lower-level maximum is between 900-700 hPa, while the larger, upper-level maximum is at 500 hPa near 27.5-28.75^{o}N.

In a southwest-to-northeast vertical cross-section through both the TC and convective 850-hPa maxima (Fig. 25d), the connection between the two features appears somewhat similar to the relative vorticity (Fig. 23d). The TC and convection low-level maxima are distinct, while the upper-level maxima appear to be connected. The PV associated with the TC appears more upright below 600 hPa than in the zonal cross-section (Fig. 25d), while the PV to the northeast is upright. It appears that the upper PV structure associated with the TC connects with the upper PV structure of the convection.

D.   SYNTHESIS

Following recurvature, satellite data indicate that the low-level center of TY Sinlaku was exposed and that convection was present only on the east side of the circulation. While the east side of the TC was also the downshear side, the deep convective bursts on 16 September 2008 appeared to be principally the result of the interaction between the synoptic-scale environmental flow and the outer TY Sinlaku circulation. Southerly flow from the deep tropics moved northward over an area of high sea-surface temperatures, ocean heat content, and atmospheric moisture in a region with elevated CAPE. Through 17 hours of convective activity on 16 September 2008, the deep convective bursts initiating each episode developed along a line of convergence between the outer TC circulation and the southwest monsoon flow that was generally

36

near 27°N 126°E (Figs. 9-11). As the dissipating convection moved to the northeast, new convective burst(s) of the subsequent episode developed on the northwest side of the remnant convection. Throughout these convective episodes, the deep convection remained in a similar region west of Okinawa, while TY Sinlaku moved eastward 2° long. (Figs. 9-11), left of the shear vector (Fig. 6), and in closer proximity to each successive burst over the high-CAPE region. It is possible that the downshear side of Sinlaku, while not directly responsible for the convection, provided a favorable environment for the development of the deep convection in a similar manner as the high sea-surface temperatures, ocean heat content and atmospheric moisture.

To test whether the deep convection is the source of the nearly vertical vorticity maximum northeast of the TC, the diabatic fields available in the YOTC data set are analyzed. The convective and stratiform precipitation accumulations through the initial 3 h of the model integration that was initialized at 0000 UTC 17 September 2008 (Fig. 26) define a region of both convective and stratiform precipitation associated with the vorticity maximum northeast of the TC. The maximum accumulation from convective precipitation is directly east of the TC center and the stratiform precipitation maximum is north of the convective maximum and northeast of the TC center. The overall pattern of precipitation accumulation is somewhat similar to that of the first and second convective episodes in satellite imagery. However, it is clear that the ECMWF analyses are not resolving the distinction between the second and third convective episodes. Rather, it may be that the convective accumulation maximum east of the TC center that extends northward with a stratiform precipitation maximum is a representation of a combined second and third episode. Nevertheless, the convection east of Sinlaku altered the structure of Sinlaku in the model analysis. In the model representation immediately prior to observation by the TCS-08/T-PARC aircraft, the TC center was tilted eastward with height through 500 hPa. The vorticity to the northeast was vertically upright. Between 500 hPa and 400 hPa the vorticity associated with each center became connected to define a single maximum.

Although the resolution of the ECMWF model is rather coarse relative to mesoscale features associated with convection in a typical cyclone, the impact of the

vertical wind shear and the convective episodes on the structure of TY Sinlaku is clearly identified in the analyzed ECMWF fields. A tilt of the primary circulation of Sinlaku to the east-northeast is defined. A second vorticity and PV center is located to the northeast of the LLCC and is a mid-level feature at 1200 UTC 16 September 2008 before becoming an upright feature from the surface to 400 hPa at 0000 UTC 17 September 2008. At this time, the center to the northeast has its maximum near the level of the upper-most extension of the tilted primary vortex. However, the vorticity and PV distribution of the center for the northeast is vertically upright. Comparing the distribution of convection during the three episodes with the distribution of PV suggests that precipitation processes east of the LLCC such that each successive episode may have contributed to the increase in PV east of Sinlaku. Furthermore, the presence of the primary vortex may have shielded the region of deep convection downshear from the vertical wind shear to provide an environment in which the PV structure could develop upright.
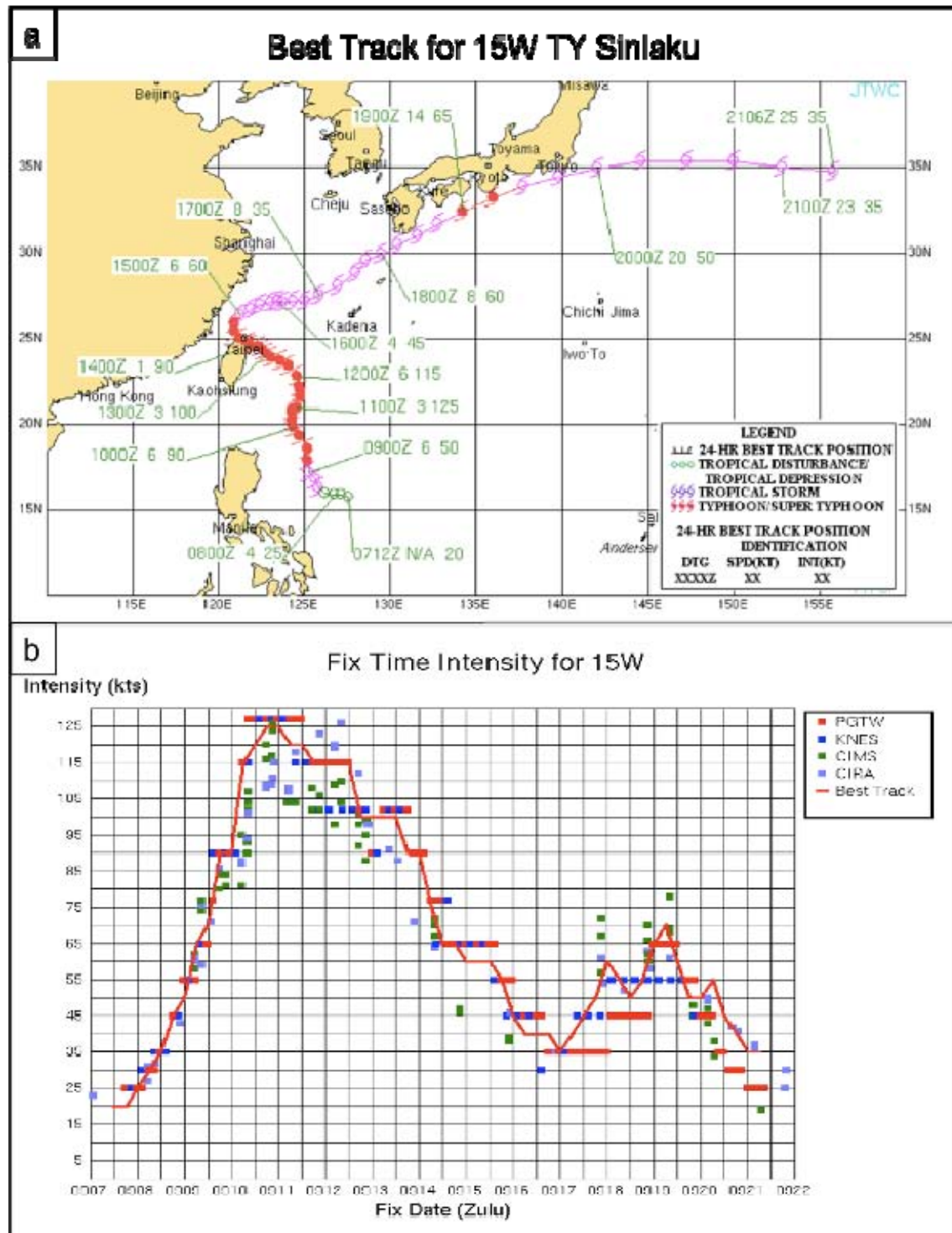
Figure 2.   Typhoon Sinlaku (a) best track and (b) fix time intensity (from Joint Typhoon Warning Center 2008 Annual Tropical Cyclone Report, p. 30).
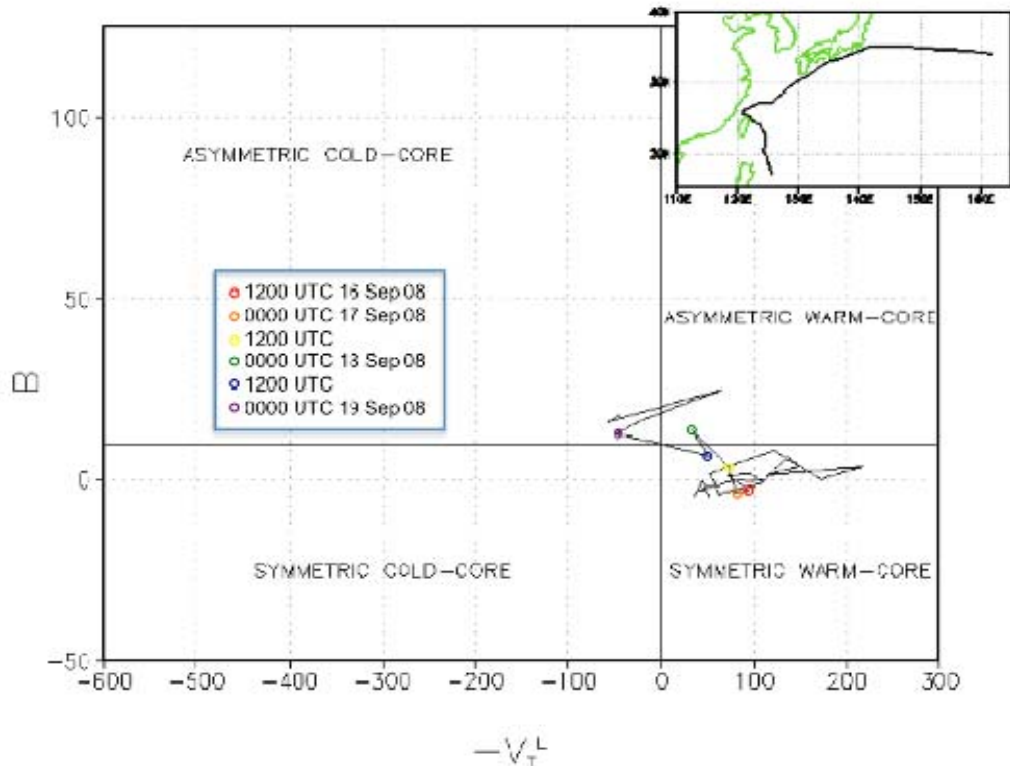
Figure 3.   Cyclone Phase Space diagram for TY Sinlaku utilizing ECMWF analysis fields. The thermal symmetry parameter "B" defines the difference in 900-600 hPa thickness calculated as areal mean over two semicircles – left and right of the storm track – out to a radius of 500 km (the left-of-track value is subtracted from the right-of track value).   The thermal wind values in the same layer (900-600 hPa) are plotted along the abscissa. (Figure courtesy Professor Jenni Evans, Pennsylvania State University.)
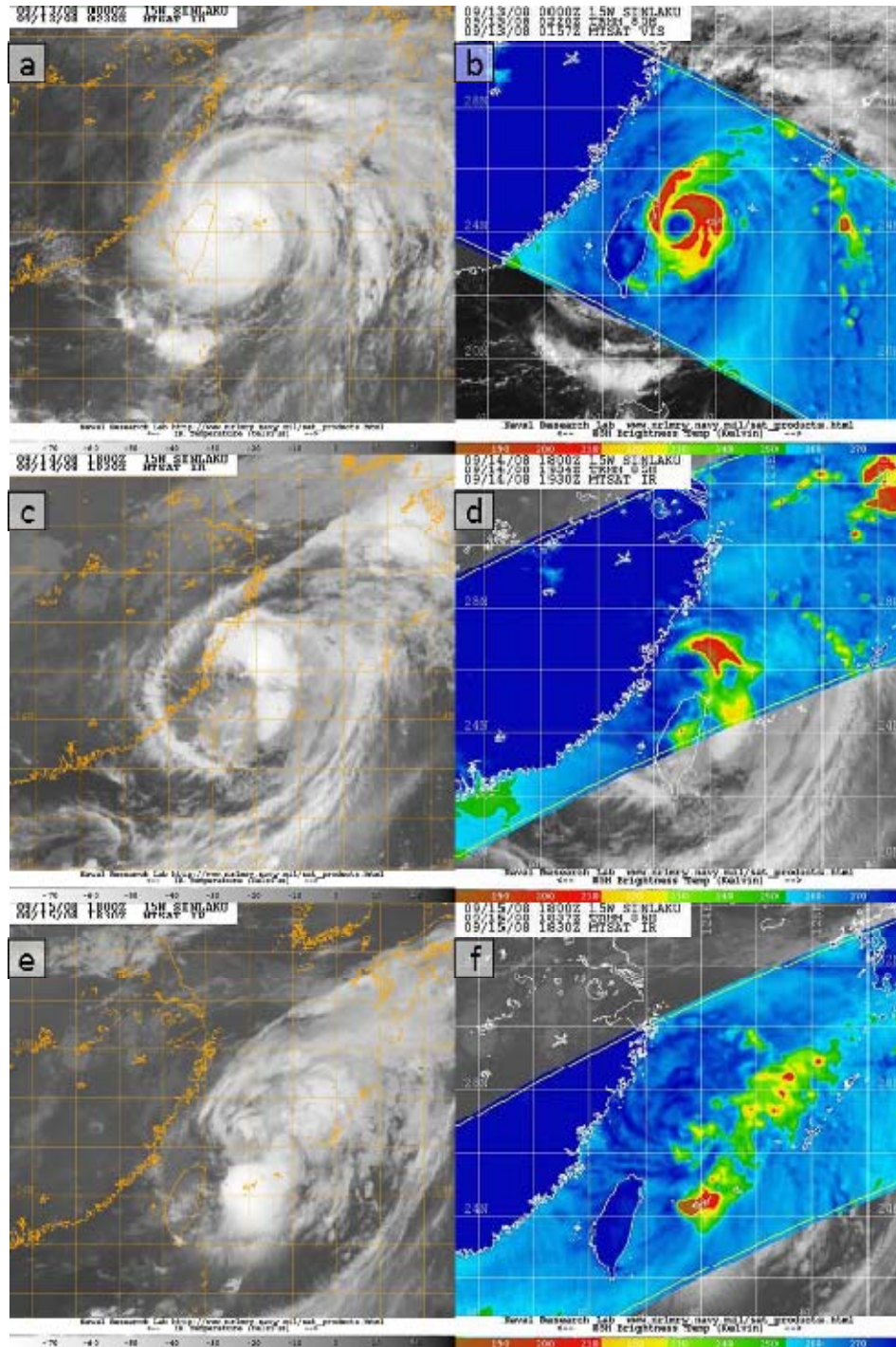
Figure 4.   Geostationary infrared imagery (left column) and 85 GHz TRMM imagery (right column) of Typhoon Sinlaku during the (a-b) landfall, (c-d) recurvature, and (e-f) post-recurvature aspects of the TC lifecycle. Infrared MTSAT imagery for (a) 0230 UTC 13 September 2008, (c) 1930 UTC 14 September 2008, and (e) 1830 UTC 15 September 2008. The 85 GHz TRMM imagery for (b) UTC 13 September 2008, (d) UTC 14 September 2008, and (f) 1837 UTC 15 September 2008.
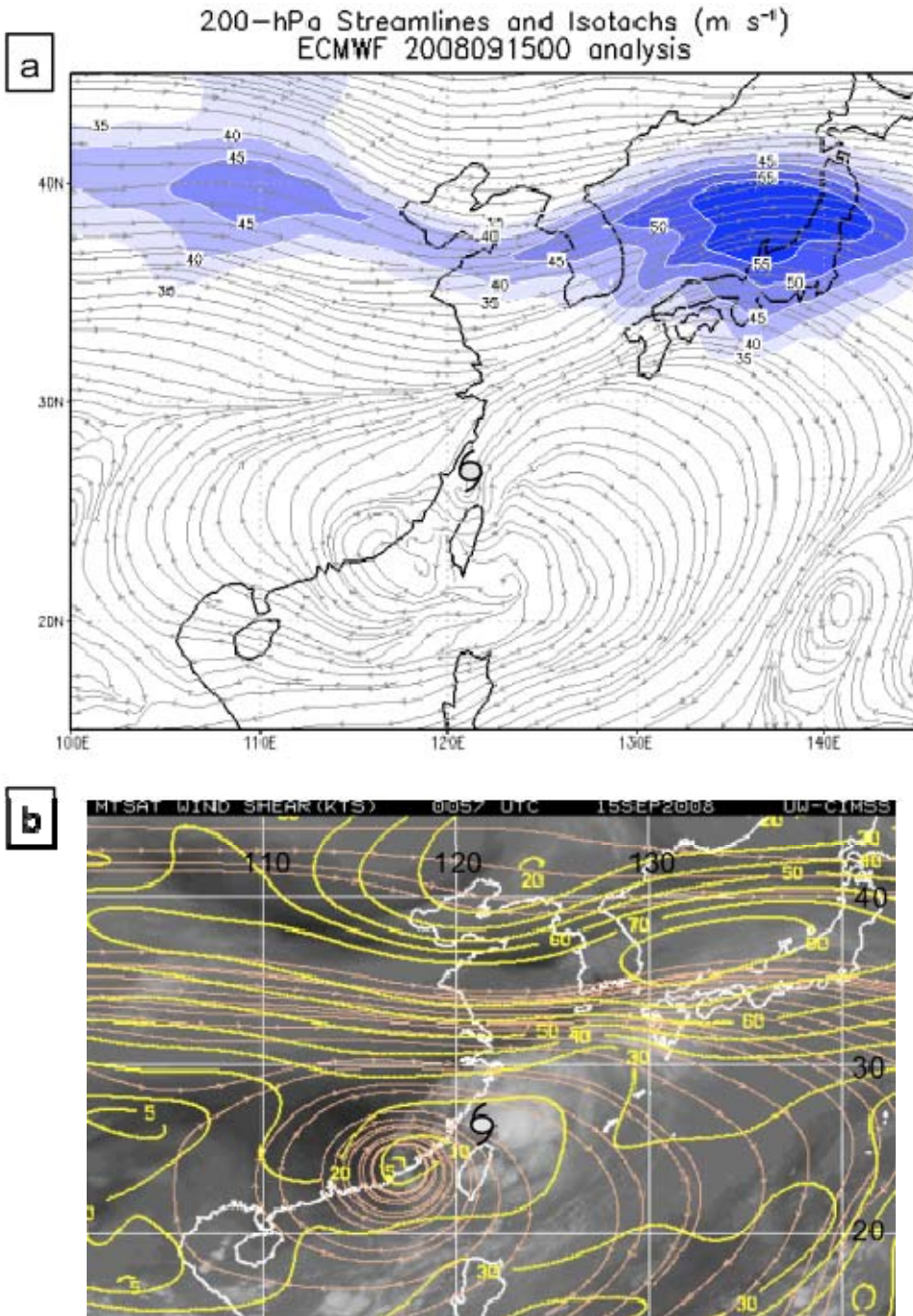
Figure 5.   (a) Streamlines and isotachs exceeding 35 m s^{-1} (shaded) at 200 hPa from the ECMWF operational analysis at 0000 UTC 15 September 2008. (b) Infrared satellite imagery of TY Sinlaku at 0057 UTC 15 September 2008.   The streamlines indicate the direction and yellow isolines indicate the magnitude of deep vertical wind shear (kt) between an upper-atmosphere layer average (150-300 hPa) and a lower-atmosphere layer average (925-700 hPa) (after http://catalog.eol.ucar.edu/tparc_2008/). The typhoon symbol represents the location of TY Sinlaku at 0000 UTC 15 September 2008.

ECMWF TC−centered Vertical Wind Shear (m s⁻¹)

Deep (200-850hPa) Shear (m s⁻¹)				Mid (500-850hPa) Shear (m s⁻¹)			
time	u shear	v shear	shear	time	u shear	v shear	shear
1500	8.15	-4.13	9.14	1500	5.2	-4.86	7.11
1512	10.69	-2.48	10.97	1512	5.17	-4.09	6.59
1600	7.62	-3.98	8.6	1600	5.25	-4.7	7.05
1612	5.77	-0.94	5.85	1612	1.78	-3.6	4.02
1700	4.24	-0.68	4.29	1700	4.2	-4.31	6.02
1712	8.38	5.78	10.18	1712	4.54	-1.45	4.77
1800	5.12	7.91	9.42	1800	4.28	-0.96	4.39

Date	BT Lat	BT Lon
2008091500	26.4N	121.3E
2008091506	26.7N	121.9E
2008091512	27.0N	122.5E
2008091518	27.1N	123.1E
2008091600	27.2N	123.5E
2008091606	27.1N	123.8E
2008091612	27.2N	124.4E
2008091618	27.2N	125.1E
2008091700	27.5N	125.9E
2008091706	28.1N	127.0E
2008091712	28.8N	128.0E
2008091718	29.6N	128.6E
2008091800	29.9N	129.5E
2008091806	30.5N	130.5E

5 m s⁻¹

Figure 6.   Storm-centered vertical wind shear (m s⁻¹) at 12-h increments between 0000 UTC 15 September 2008 – 0000 UTC 18 September 2008 based on ECMWF analyses for deep (200-850 hPa) (blue arrow) and mid-level (500-850 hPa) (green arrow) vertical wind shear. The TC symbols are plotted at JTWC Best Track locations at 6-h intervals between 0000 UTC 15 September 2008 – 0600 UTC 18 September 2008.

43
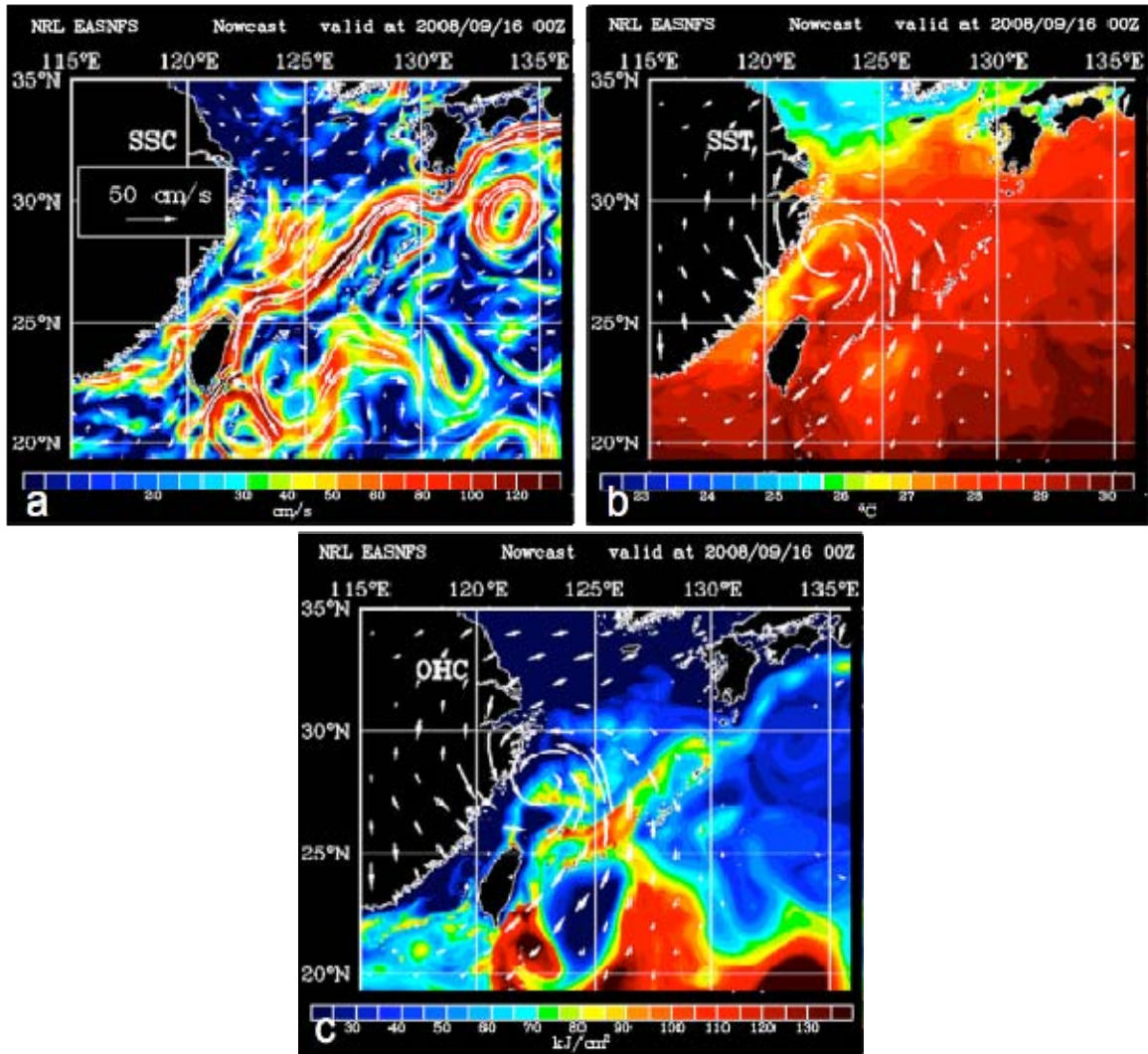
Figure 7.   Ocean characteristics from the Naval Research Laboratory (NRL)
Experimental Real-Time East Asian Seas Ocean Nowcast/Forecast System
(EASNFS) at 0000 UTC 16 September 2008 as TY Sinlaku moved eastward over
the western North Pacific and approached the Kuroshio Current. (a) Sea-surface
current (shaded in cm s^{-1}; magnitude and direction annotated with vectors), (b)
Sea-surface temperature (shaded in ^{o}C), and (c) Ocean heat content (shaded in kJ
cm^{-2}). Vectors in (b) and (c) represent relative strength and direction of the
surface winds.
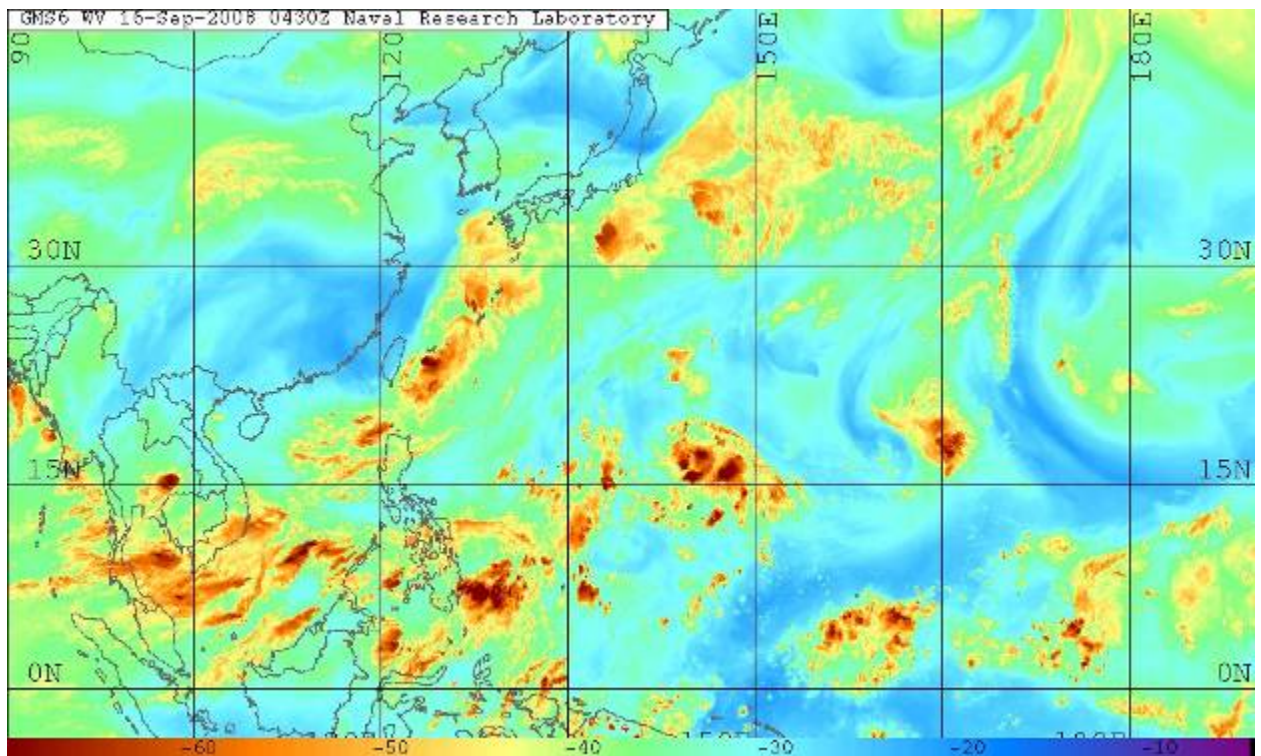
Figure 8.   Water vapor imagery from MTSAT over the western North Pacific at 0430 UTC 16 September 2008. Warm colors define regions of low brightness temperatures (^{o}C) that indicate higher atmospheric moisture content. Cool colors define regions of high brightness temperatures that indicate lower atmospheric moisture content.
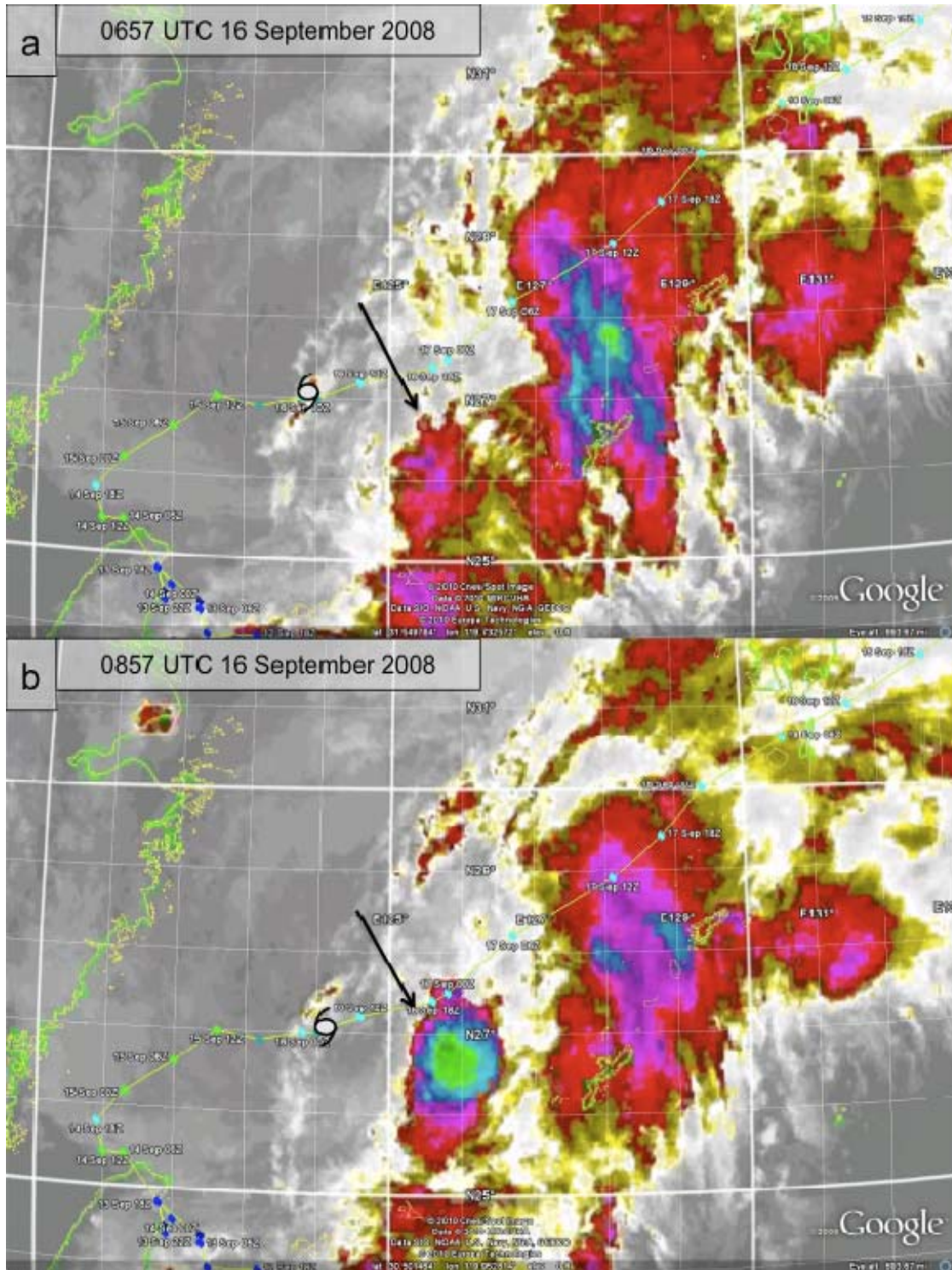
Figure 9.   Enhanced MTSAT IR imagery of TY Sinlaku at (a) 0657, (b) 0857, (c) 1057, (d) 1257, (e) 1557, and (f) 1857 UTC 16 September 2008. The typhoon symbol is located at the center of the TY Sinlaku circulation at the time of each image based on the JTWC best track positions in (Fig. 2b). Arrows define the location of significant aspects of the first (a-b) and second (f) convective episodes.
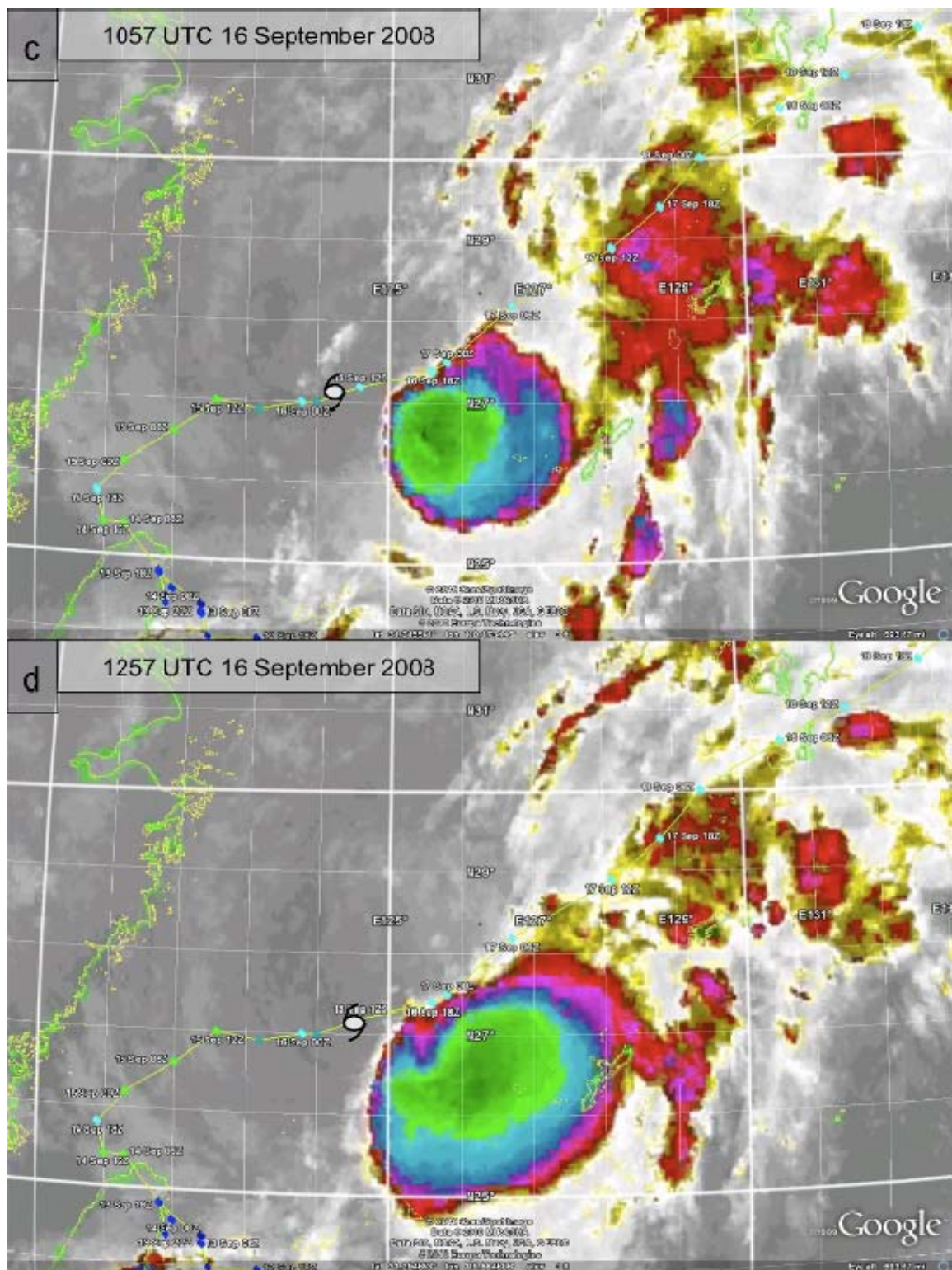
Fig. 9, continued.
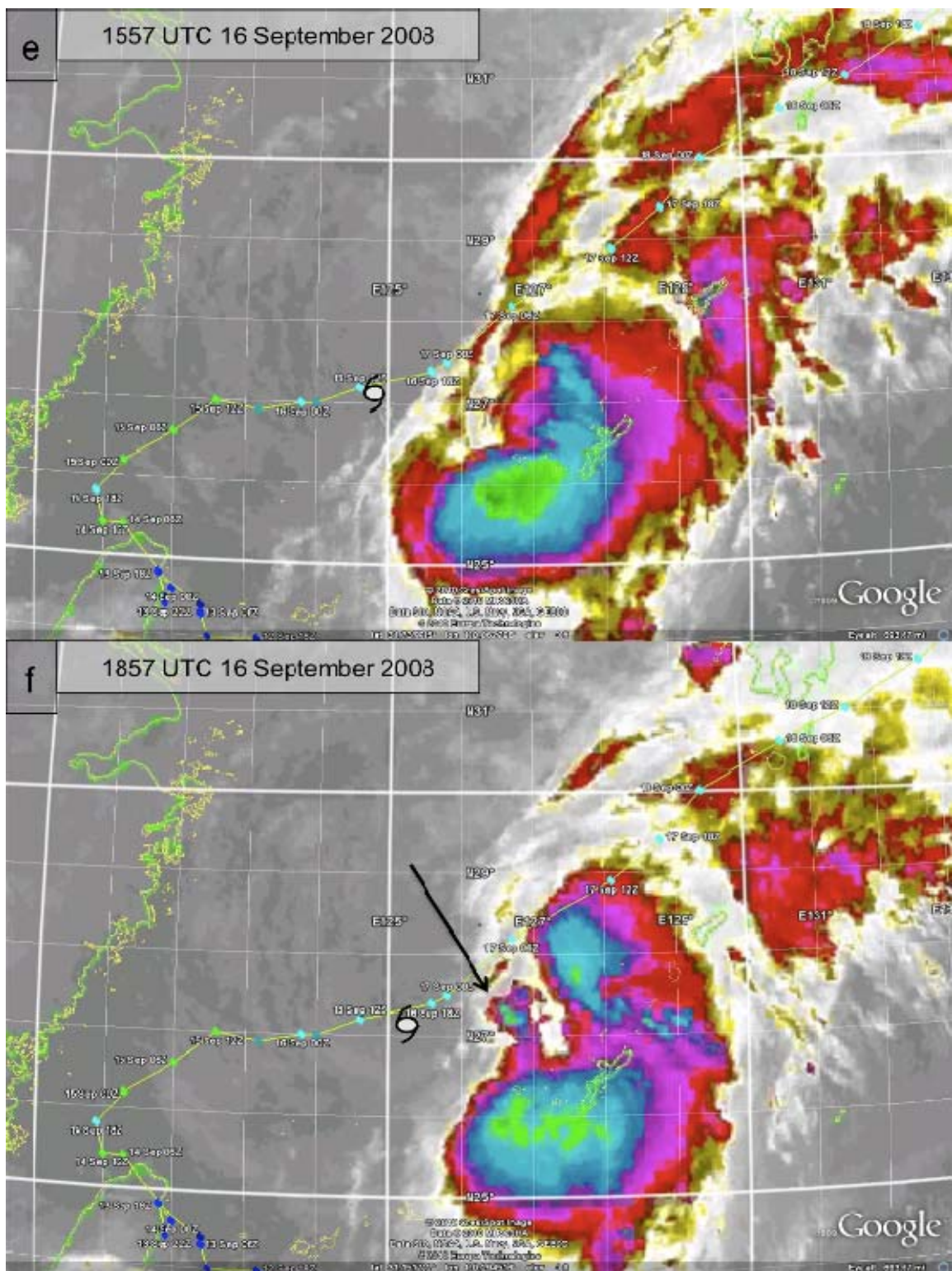
Fig. 9, continued.
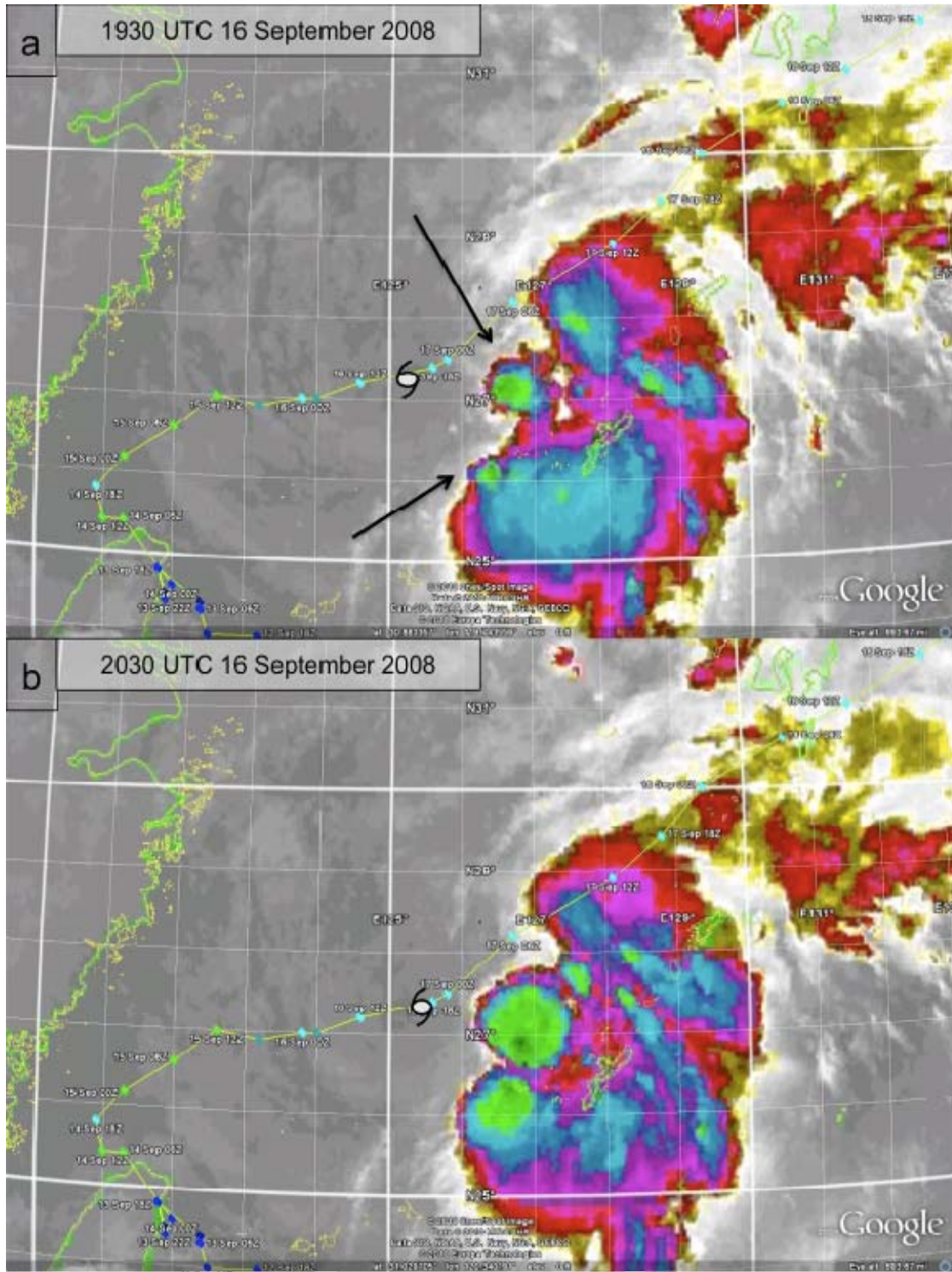
Figure 10.   Enhanced MTSAT IR imagery of TY Sinlaku at (a) 1930, (b) 2030, (c) 2130, and (d) 2230 UTC 16 September 2008. The typhoon symbol is located at the center of the TY Sinlaku circulation at the time of each image based on the JTWC best track positions in (Fig. 2b). Arrows define the location of significant aspects of the second convective episode.
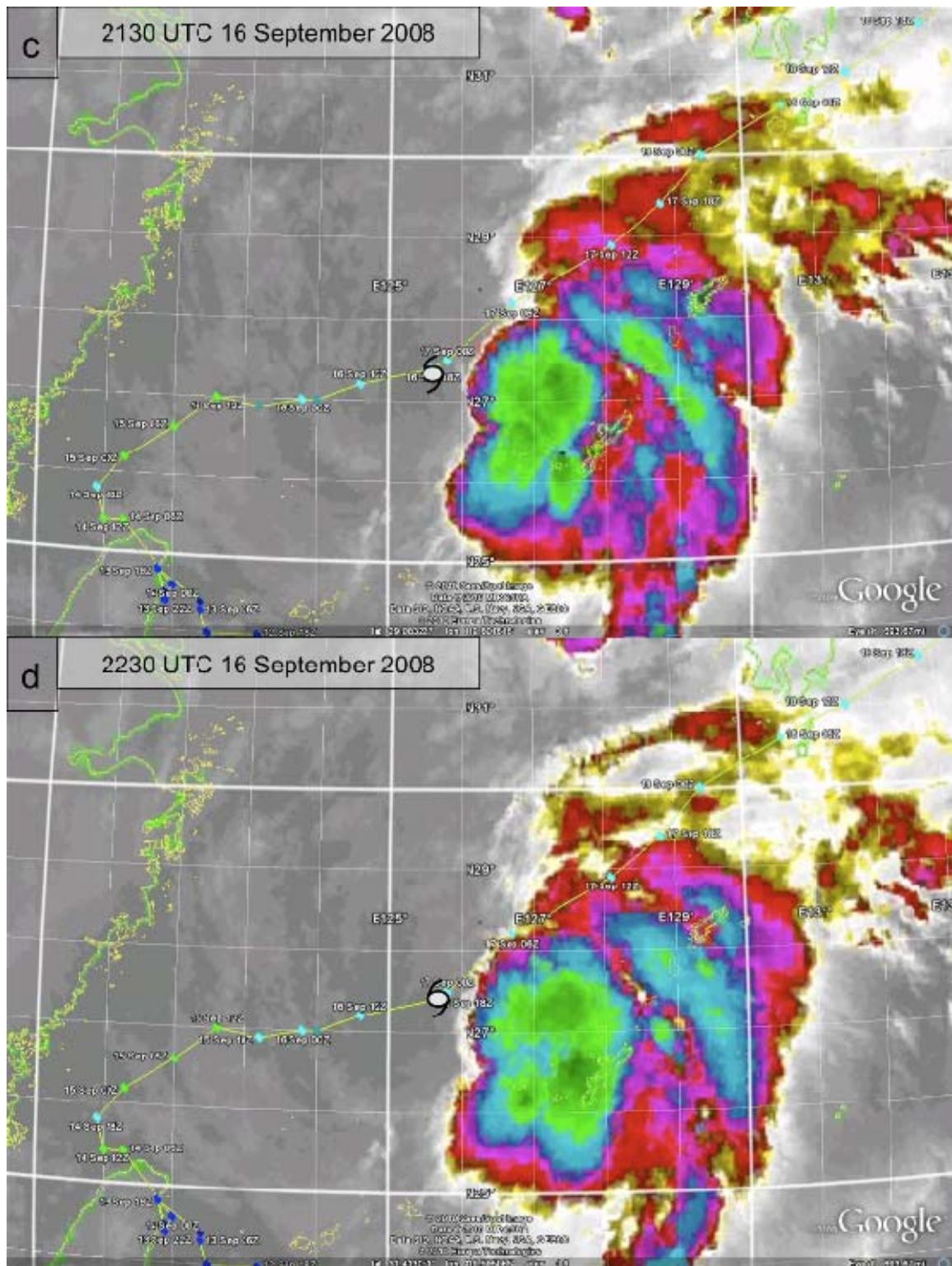
Fig. 10, continued.
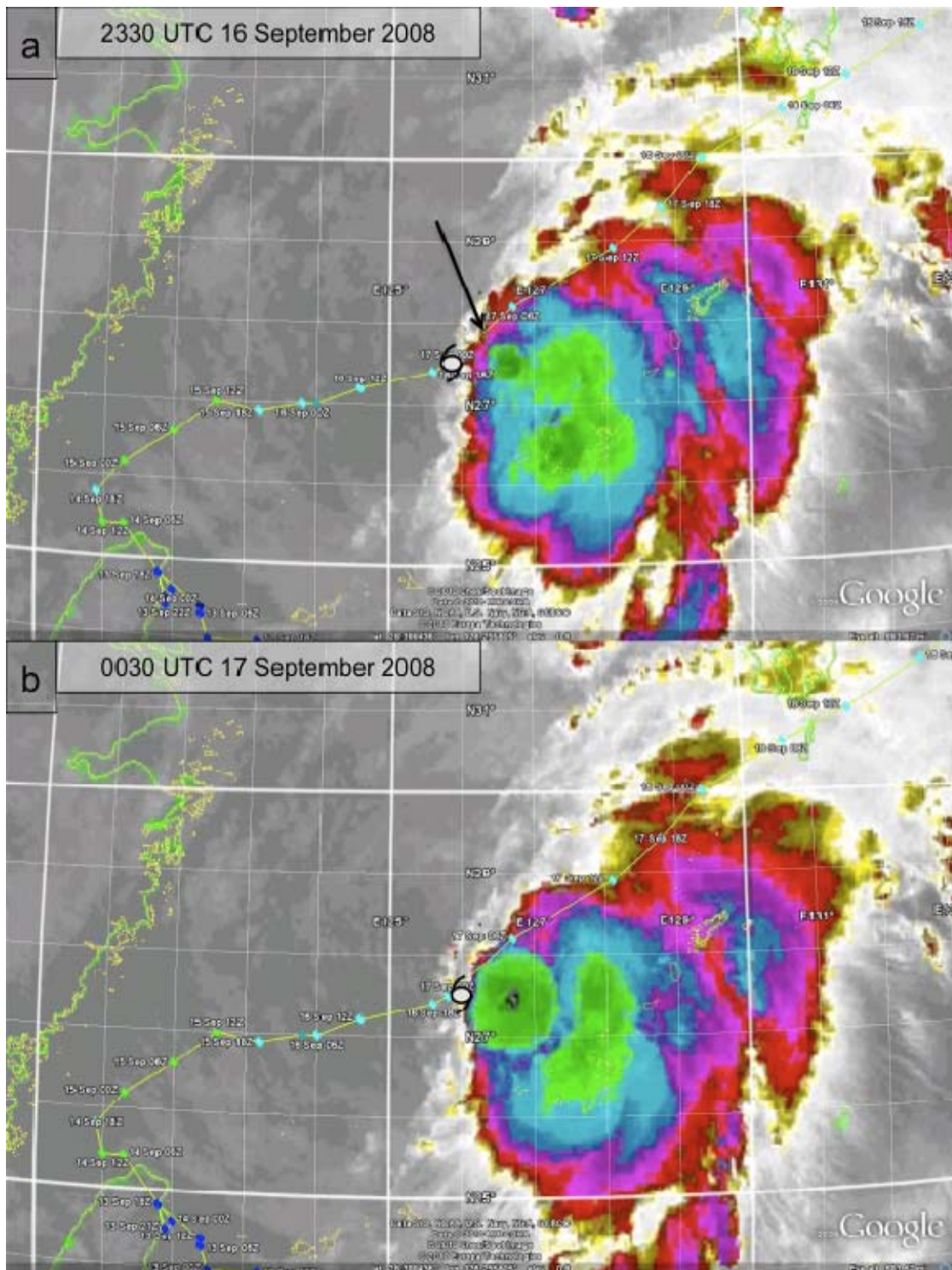
Figure 11. Enhanced MTSAT IR imagery of TY Sinlaku at (a) 2330 16 September 2008; (b) 0030, (c) 0130, and (d) 0157 UTC 17 September 2008. The typhoon symbol is located at the center of the TY Sinlaku circulation at the time of each image based on the JTWC best track positions in (Fig. 2b). Arrows define the location of significant aspects of the third convective episode.

51
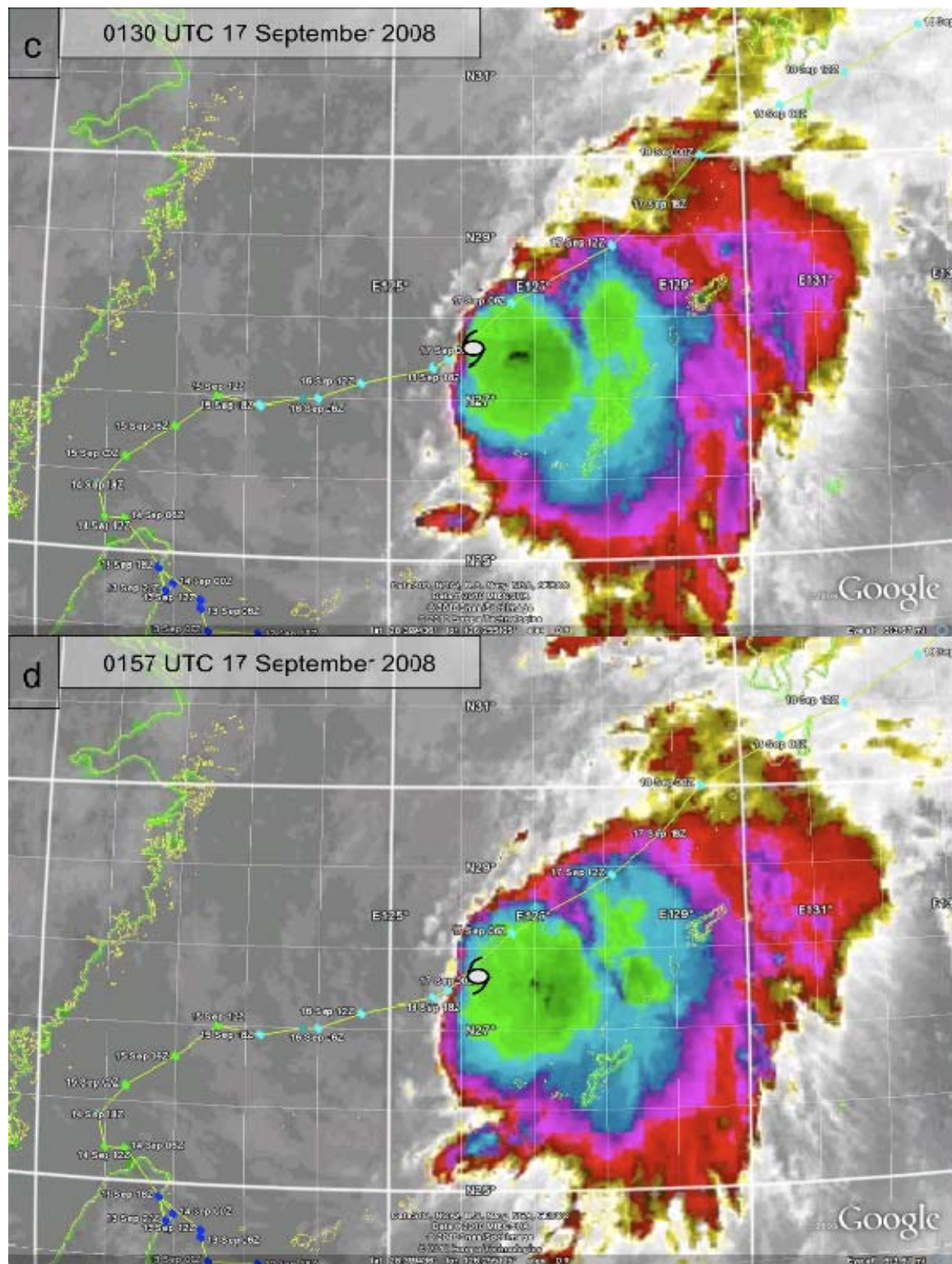
Fig. 11, continued.
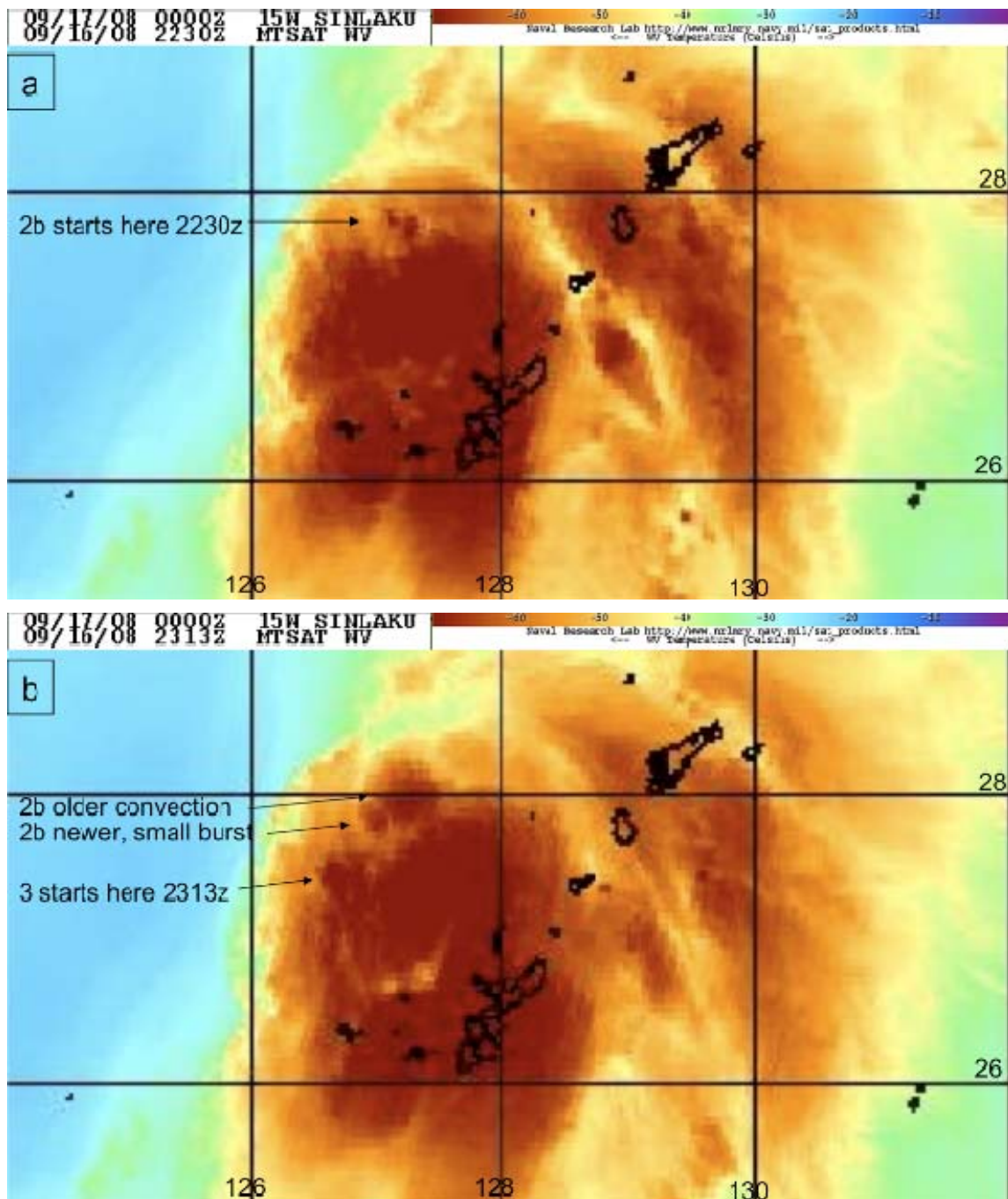
Figure 12.   Water vapor imagery from MTSAT at (a) 2230 UTC, (b) 2313 UTC, and (c) 2330 UTC 16 September 2008, and (d) 0057 UTC 17 September 2008. Warm colors define regions of low brightness temperatures (^{o}C) that indicate higher atmospheric moisture content. Cool colors define regions of high brightness temperatures that indicate lower atmospheric moisture content.
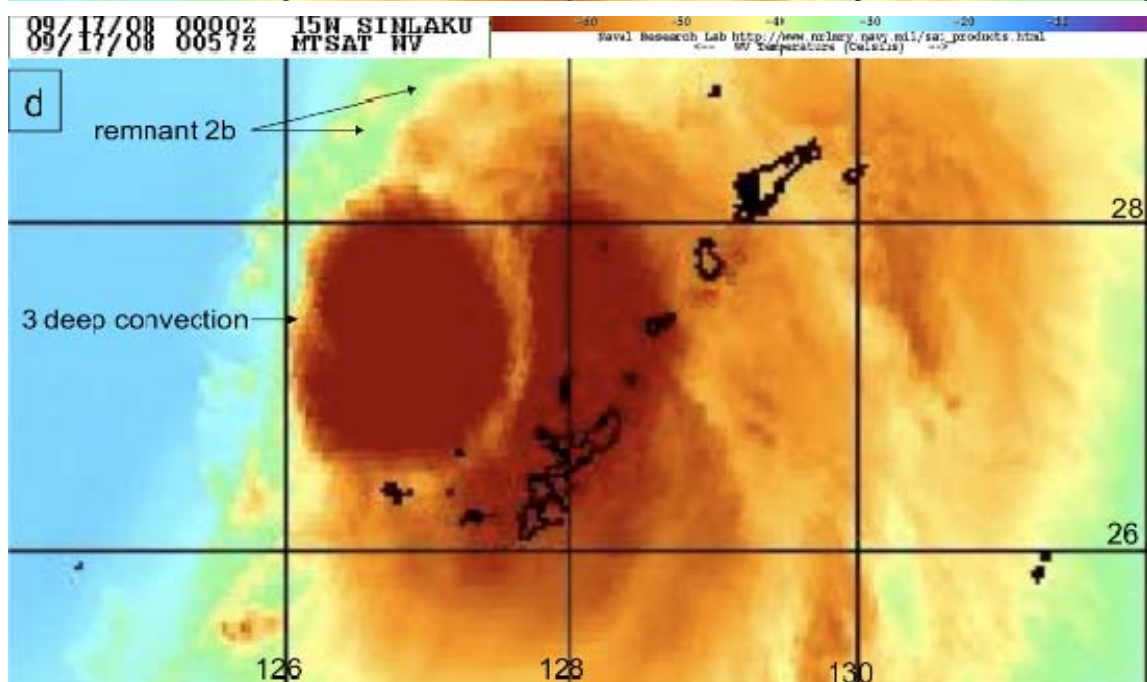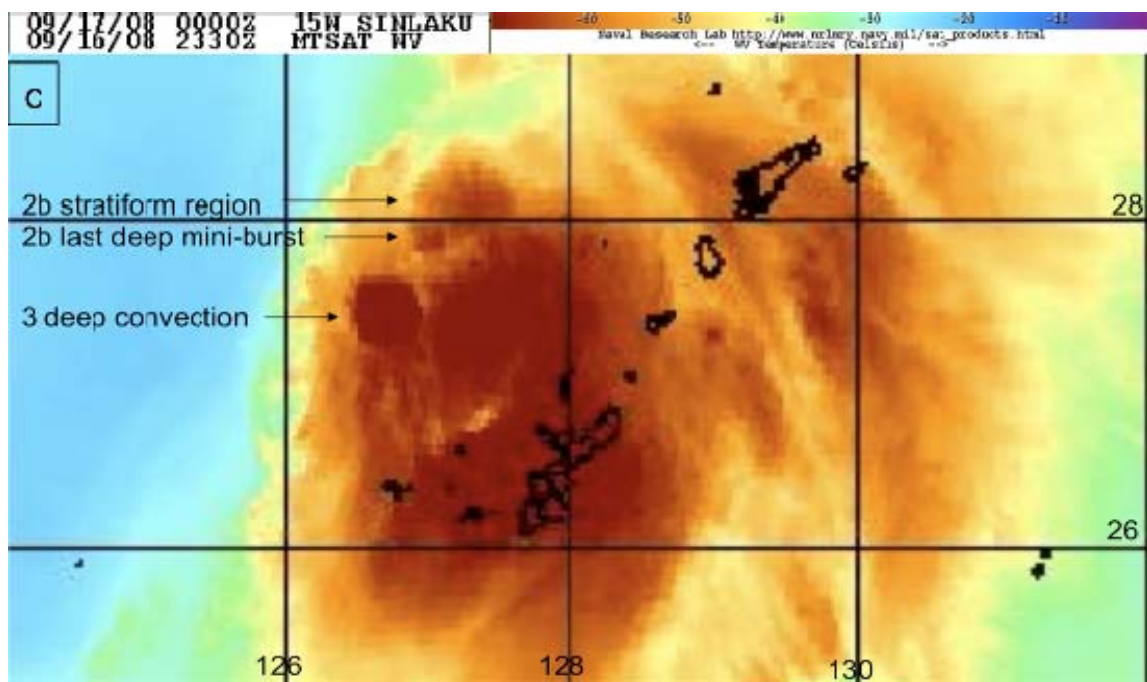
Fig. 12, continued.
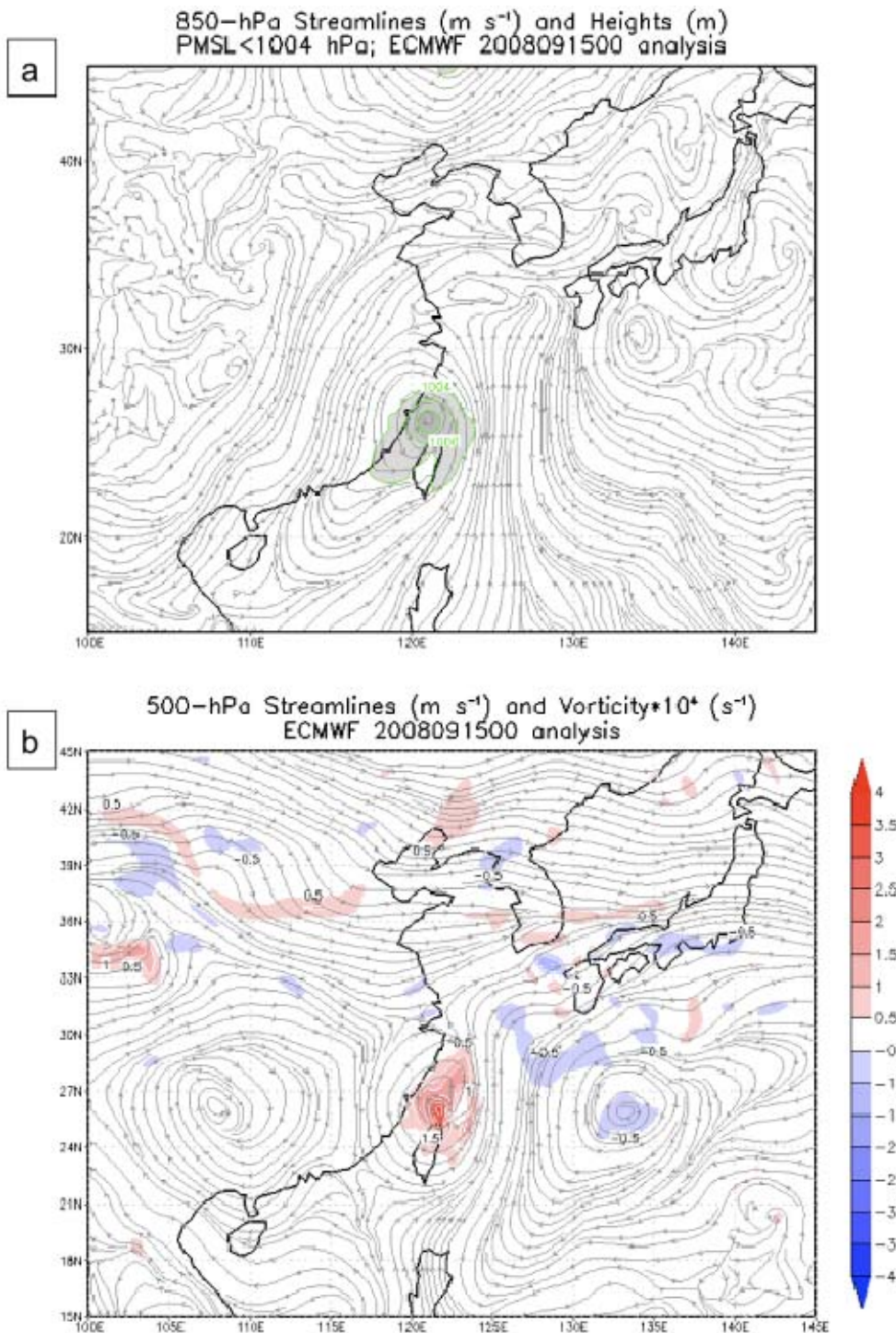
Figure 13. Streamlines from the ECMWF operational analysis for 0000 UTC 15 September 2008 at (a) 850 hPa and (b) 500 hPa. In panel (a), sea-level pressures (hPa) less than 1004 hPa are shaded in gray and outlined in black contours. In panel (b), relative vorticity (10^{-4} s^{-1}) regions at 500 hPa are shaded with positive values in red and negative values in blue.

850-hPa Streamlines (m s⁻¹) and Heights (m)
PMSL<1004 hPa; ECMWF 2008091512 analysis

500-hPa Streamlines (m s⁻¹) and Vorticity*10⁻ (s⁻¹)
ECMWF 2008091512 analysis
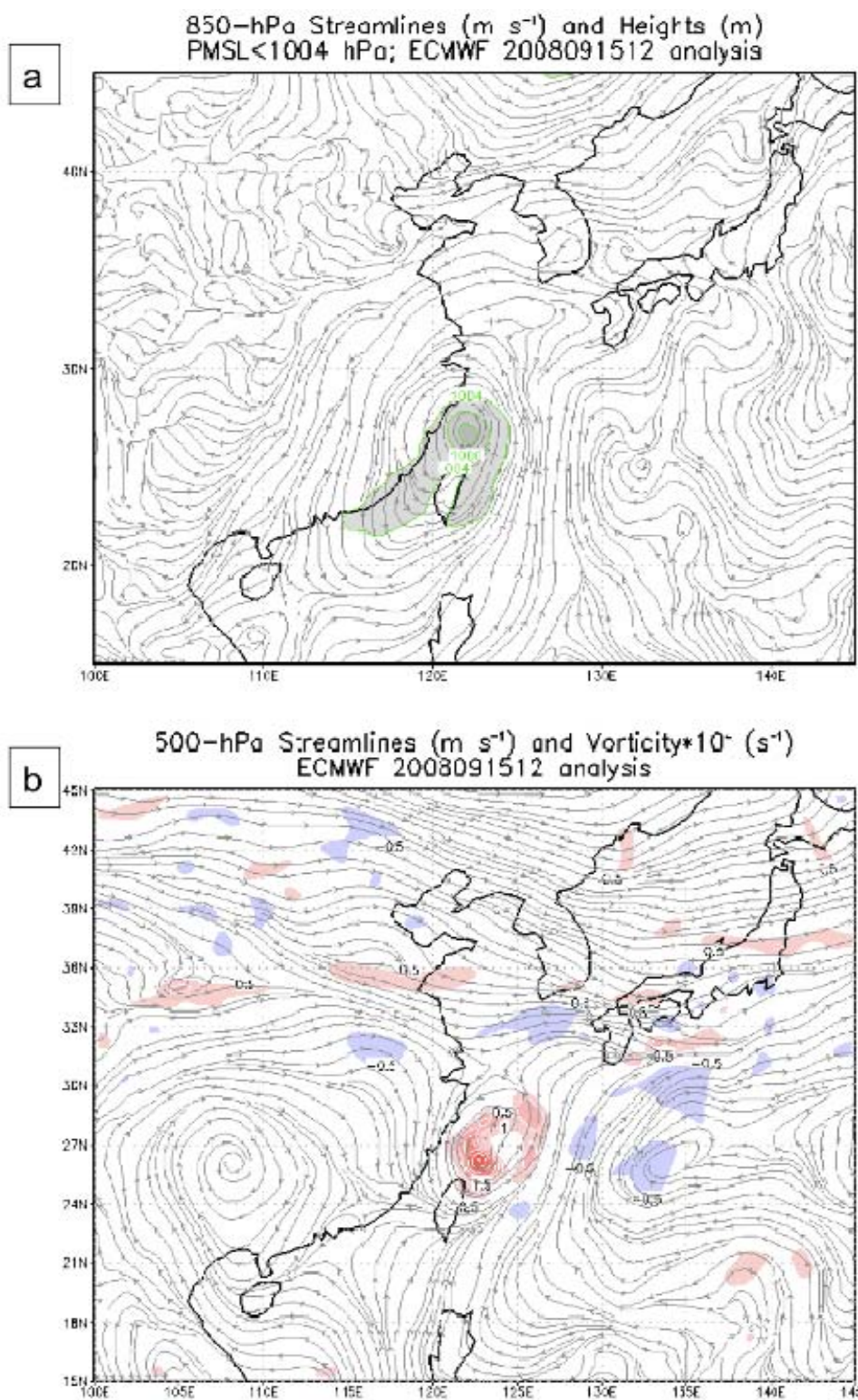
Figure 14.   (a-b) As in Fig. 13, and (c) as in Fig. 5a, except for 1200 UTC 15 September 2008.

56

200-hPa Streamlines and Isotachs (m s⁻¹)
ECMWF 2008091512 analysis

Fig. 14, continued.

850-hPa Streamlines (m s⁻¹) and Heights (m)
PMSL<1004 hPa; ECMWF 2008091600 analysis

500-hPa Streamlines (m s⁻¹) and Vorticity*10⁵ (s⁻¹)
ECMWF 2008091600 analysis
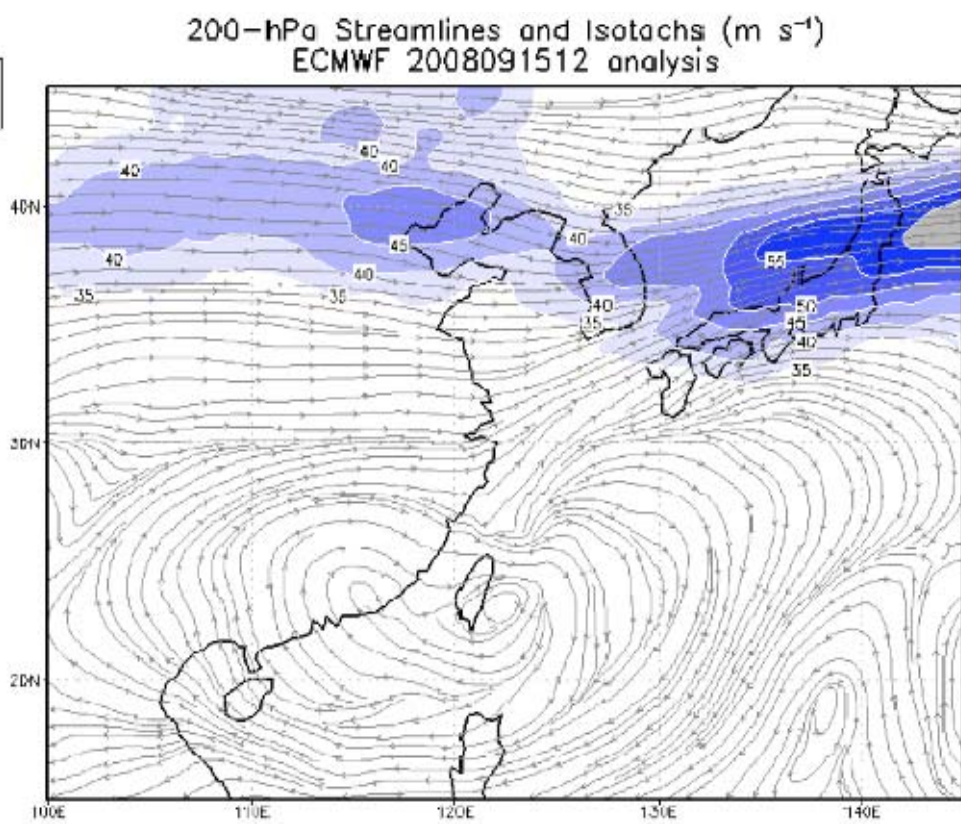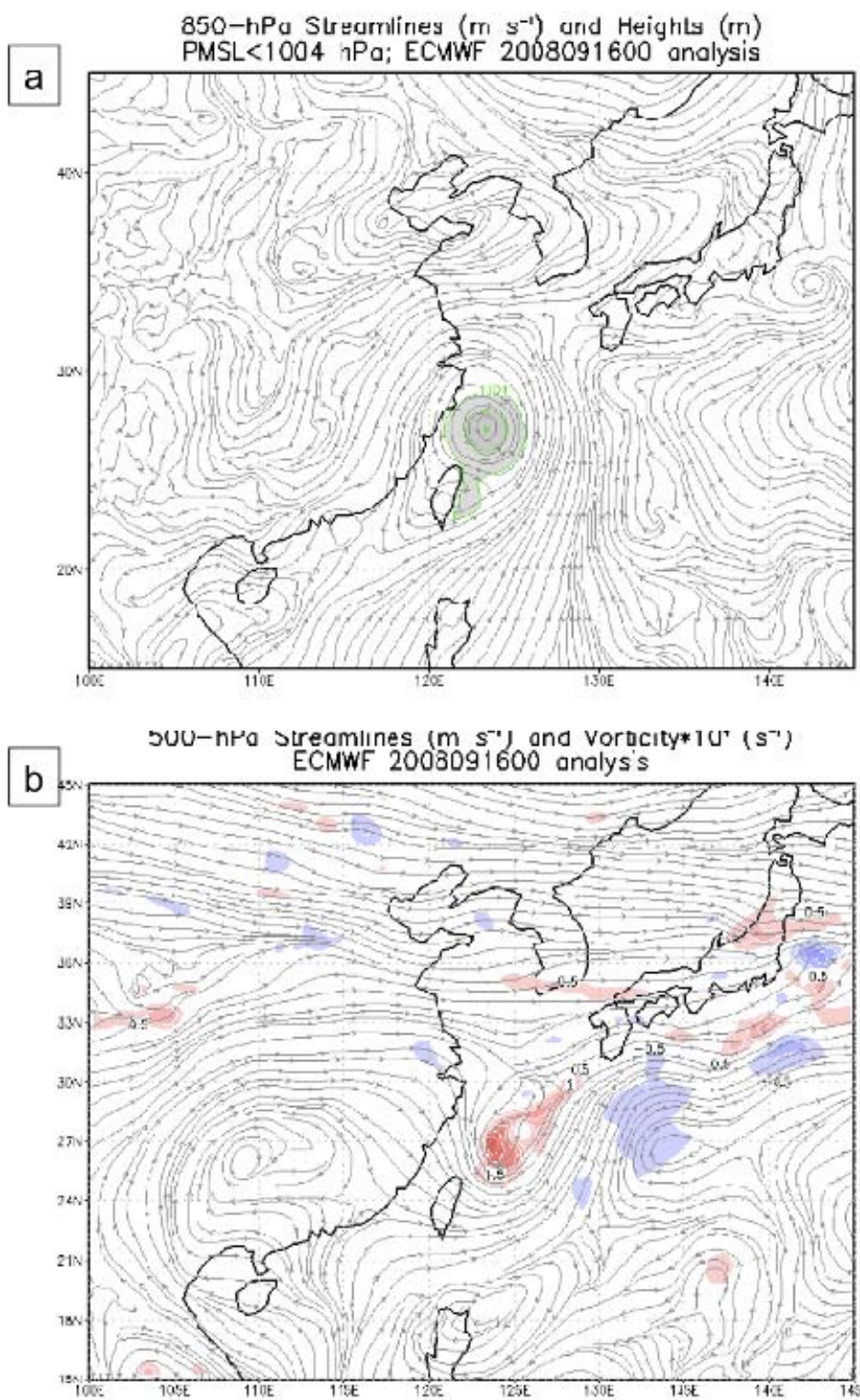
Figure 15.   As in Fig. 14, except for 0000 UTC 16 September 2008.

200-hPa Streamlines and Isotachs (m s⁻¹)
ECMWF 2008091600 analysis
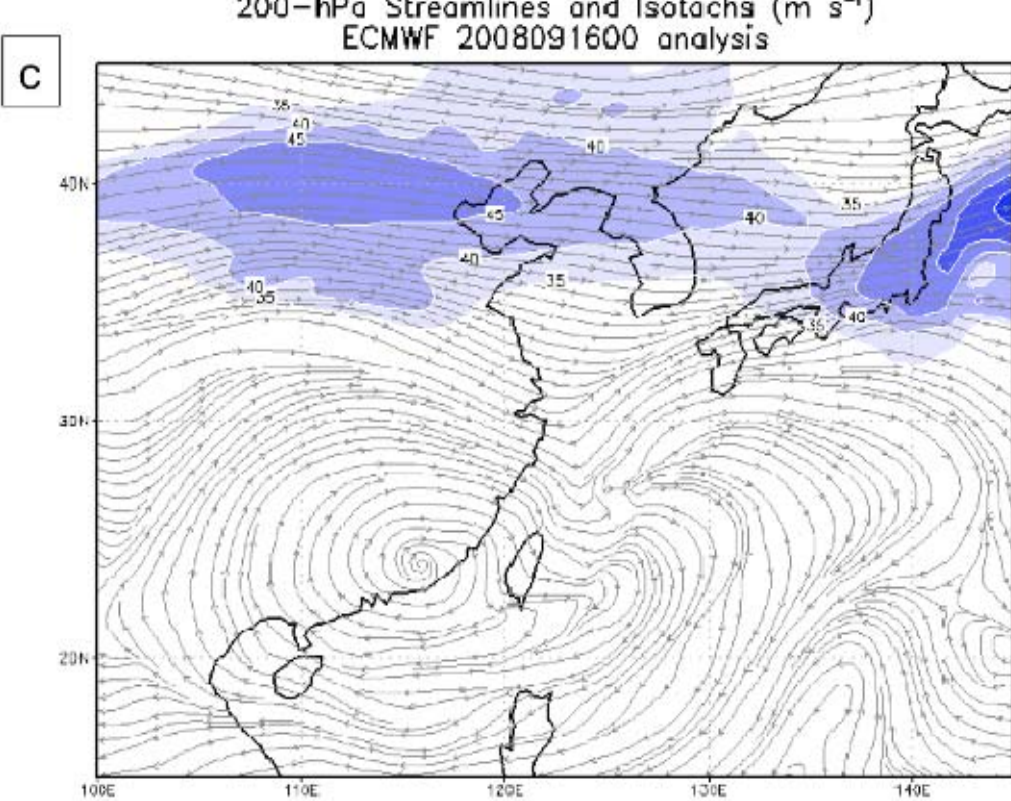
Fig. 15, continued.
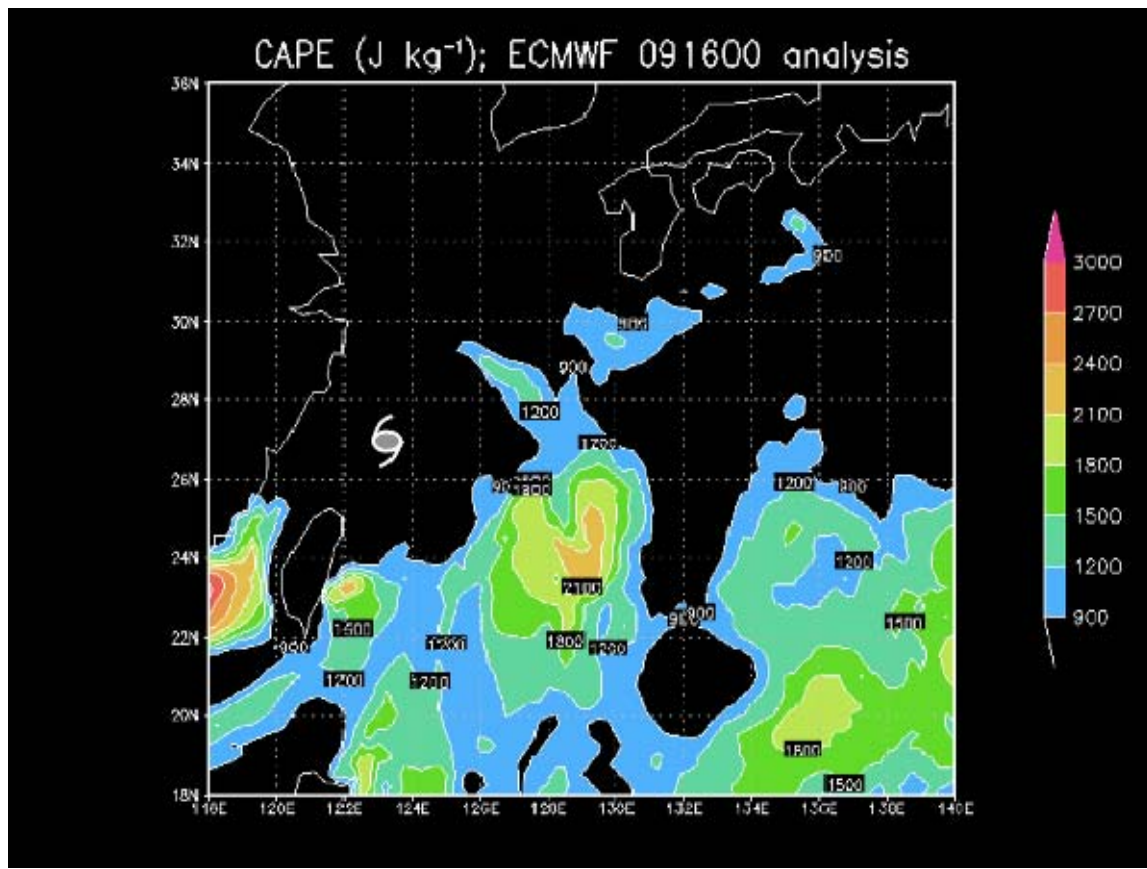
Figure 16.   Convective Available Potential Energy (CAPE) (J kg^{-1}) from the 0000 UTC 16 September 2008 ECMWF operational analysis. The TC symbol is plotted at the location of the Sinlaku LLCC in the EC model at the time of the plot.
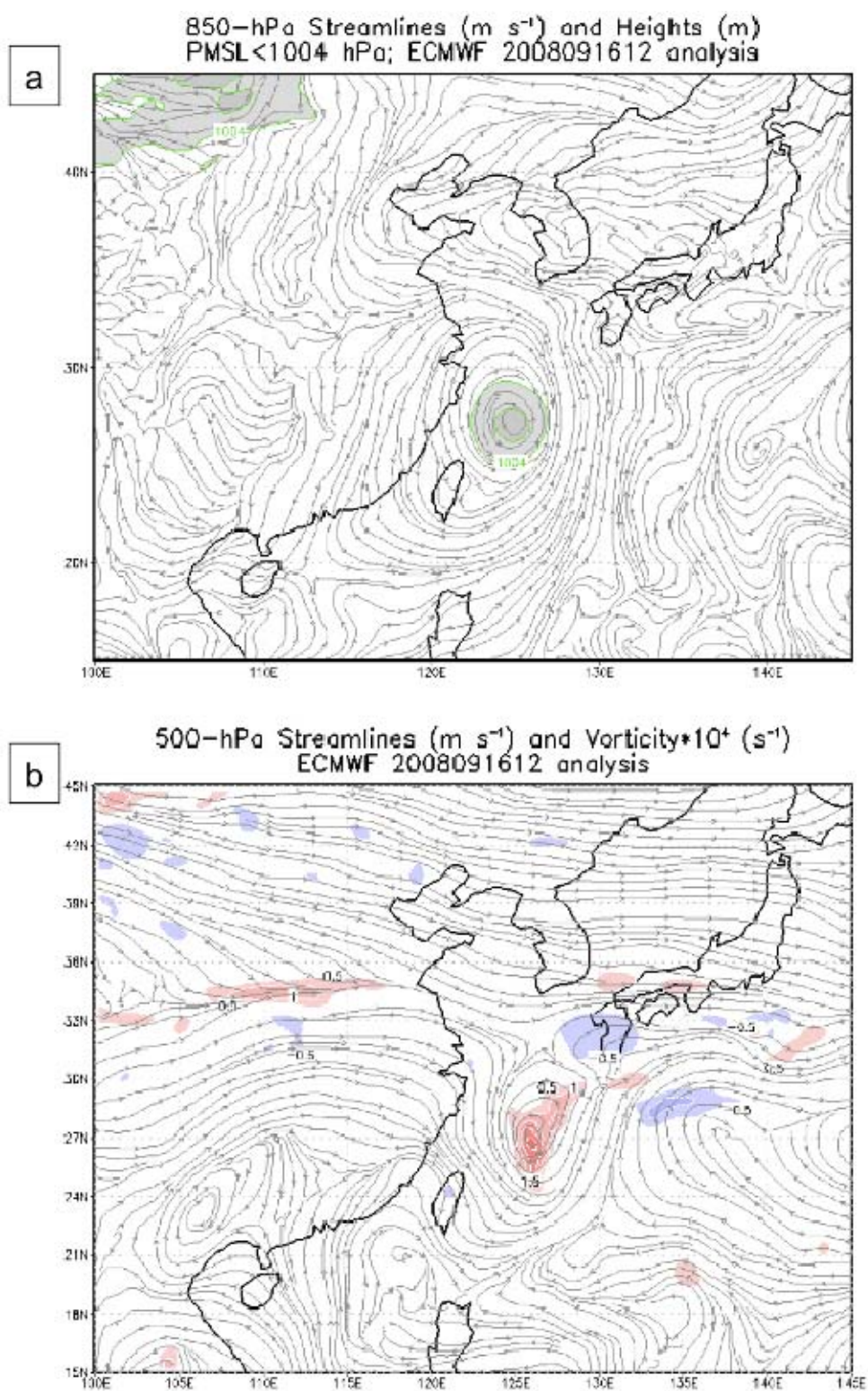
Figure 17.   As in Fig. 14, except for 1200 UTC 16 September 2008.

200-hPa Streamlines and Isotachs (m s⁻¹)
ECMWF 2008091612 analysis
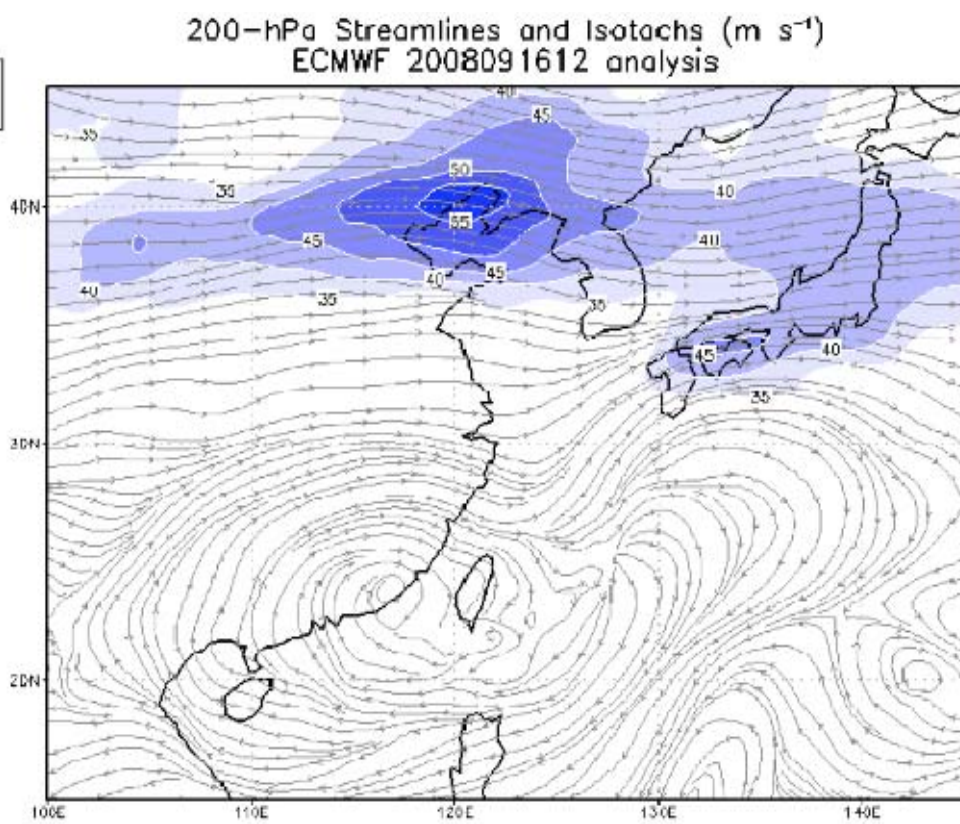
Fig. 17, continued.
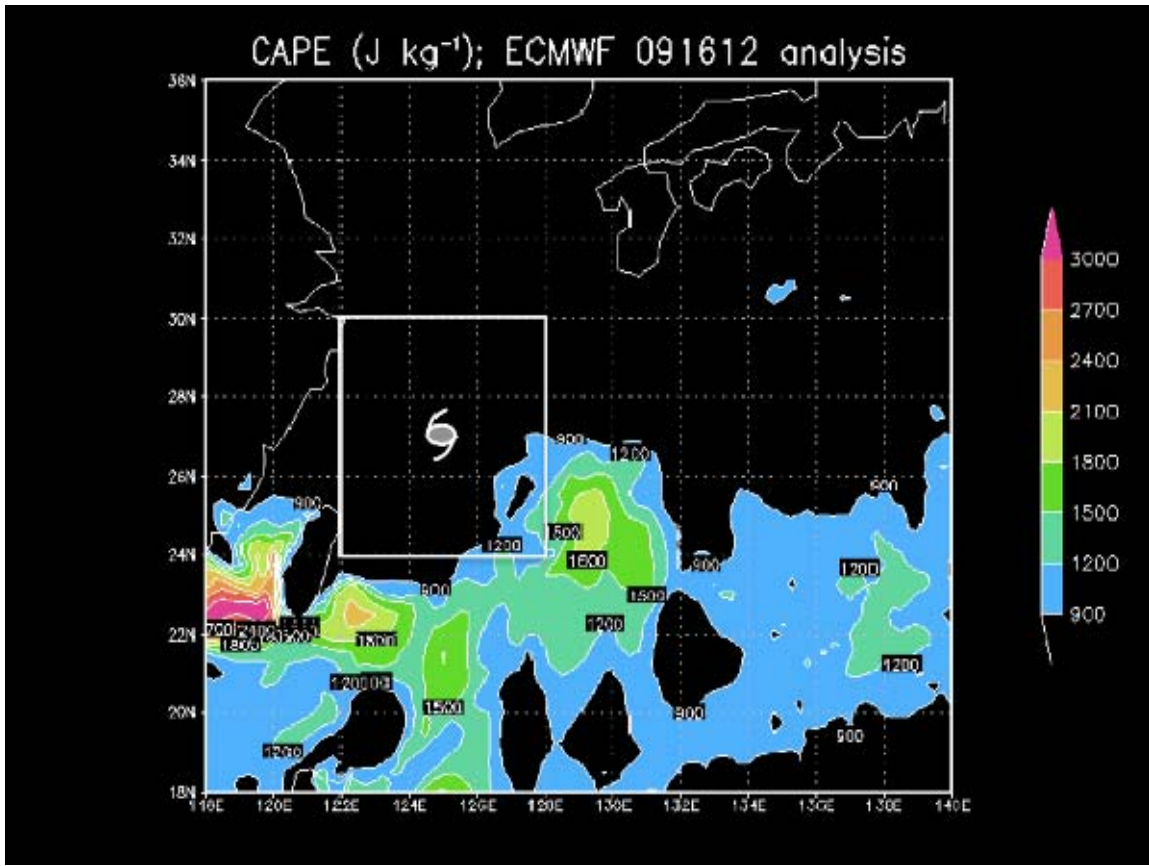
Figure 18.   Convective Available Potential Energy (CAPE) (J kg^{-1}) from the 1200 UTC 16 September 2008 ECMWF operational analysis. The TC symbol is plotted at the location of the Sinlaku LLCC in the EC model at the time of the plot. The boxed region defines the area in Fig. 19.
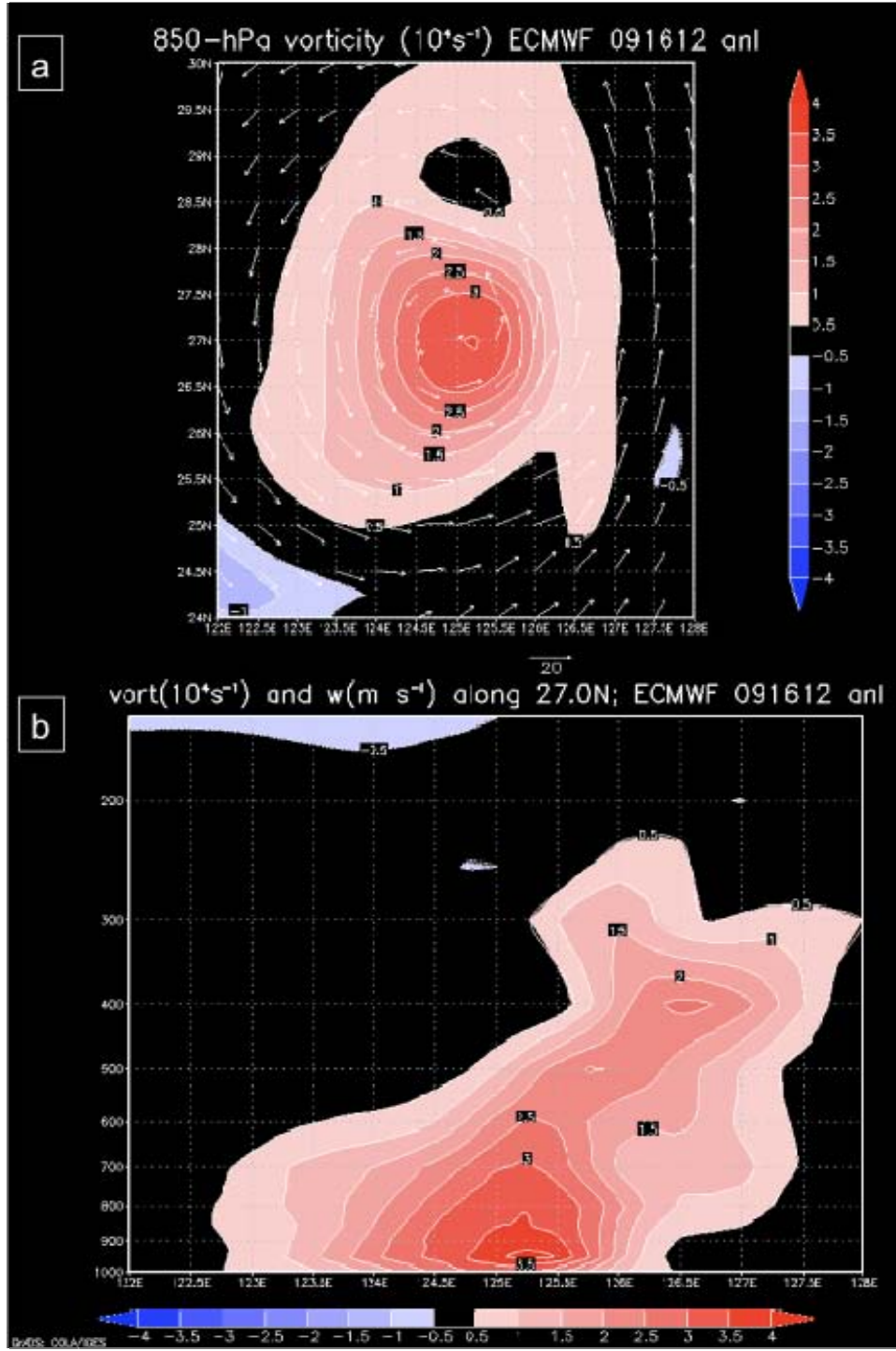
Figure 19.   Relative vorticity (10^{-4} s^{-1}) from the 1200 UTC 16 September 2008 ECMWF model analysis in a (a) plan view across 850 hPa, vertical cross-sections (b) along 27.0^{o}N, (c) along 126.5^{o}E, (d) between 25°N, 122°E and 29°N, 128°E, and (e) along 127.5^{o}N, and (f) a plan view across 400 hPa. White arrows in (a) and (f) indicate wind speed (m s^{-1}, reference vector below each panel) and direction at 850 hPa and 400 hPa, respectively.
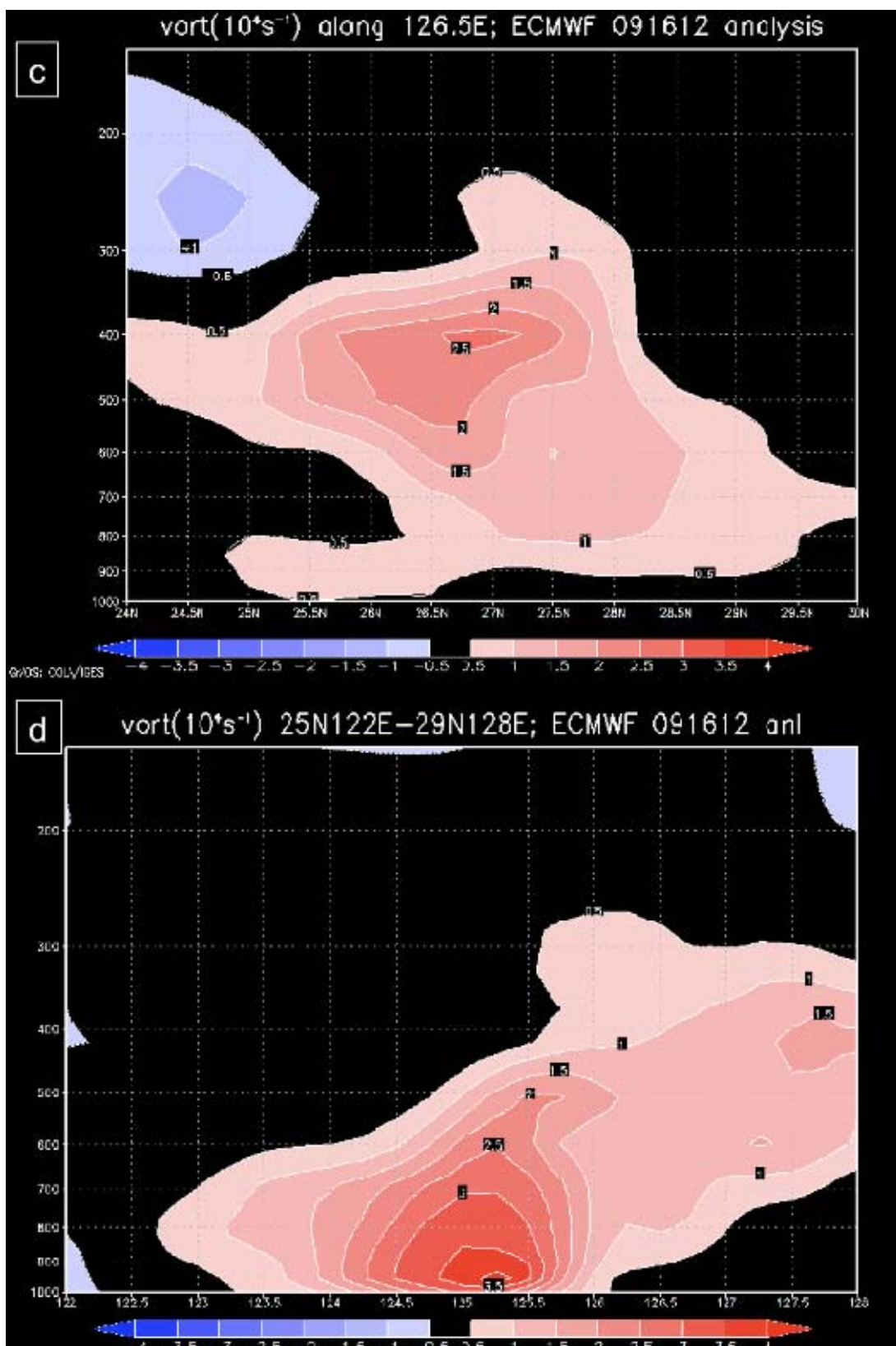
Fig. 19, continued.
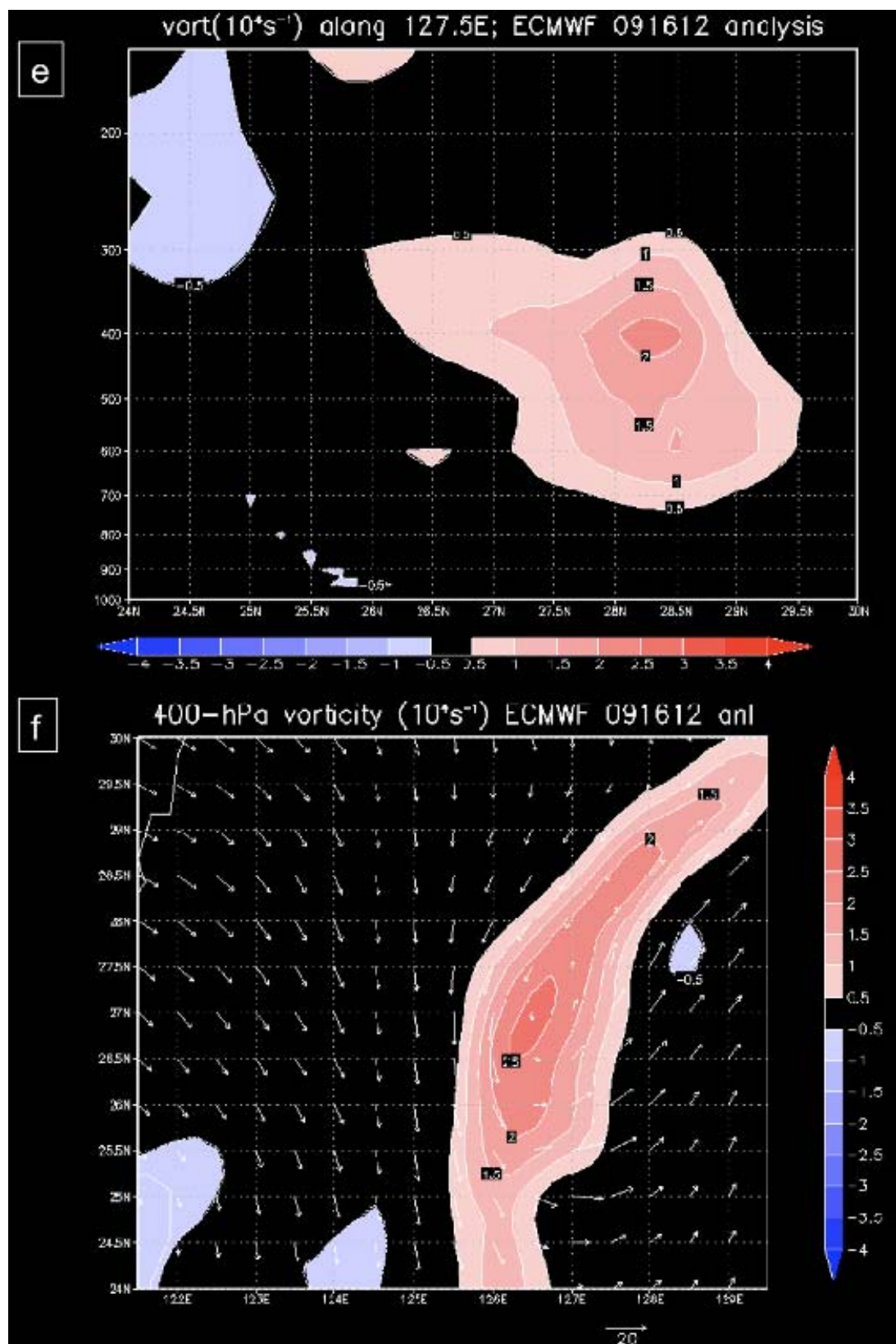
Fig. 19, continued.
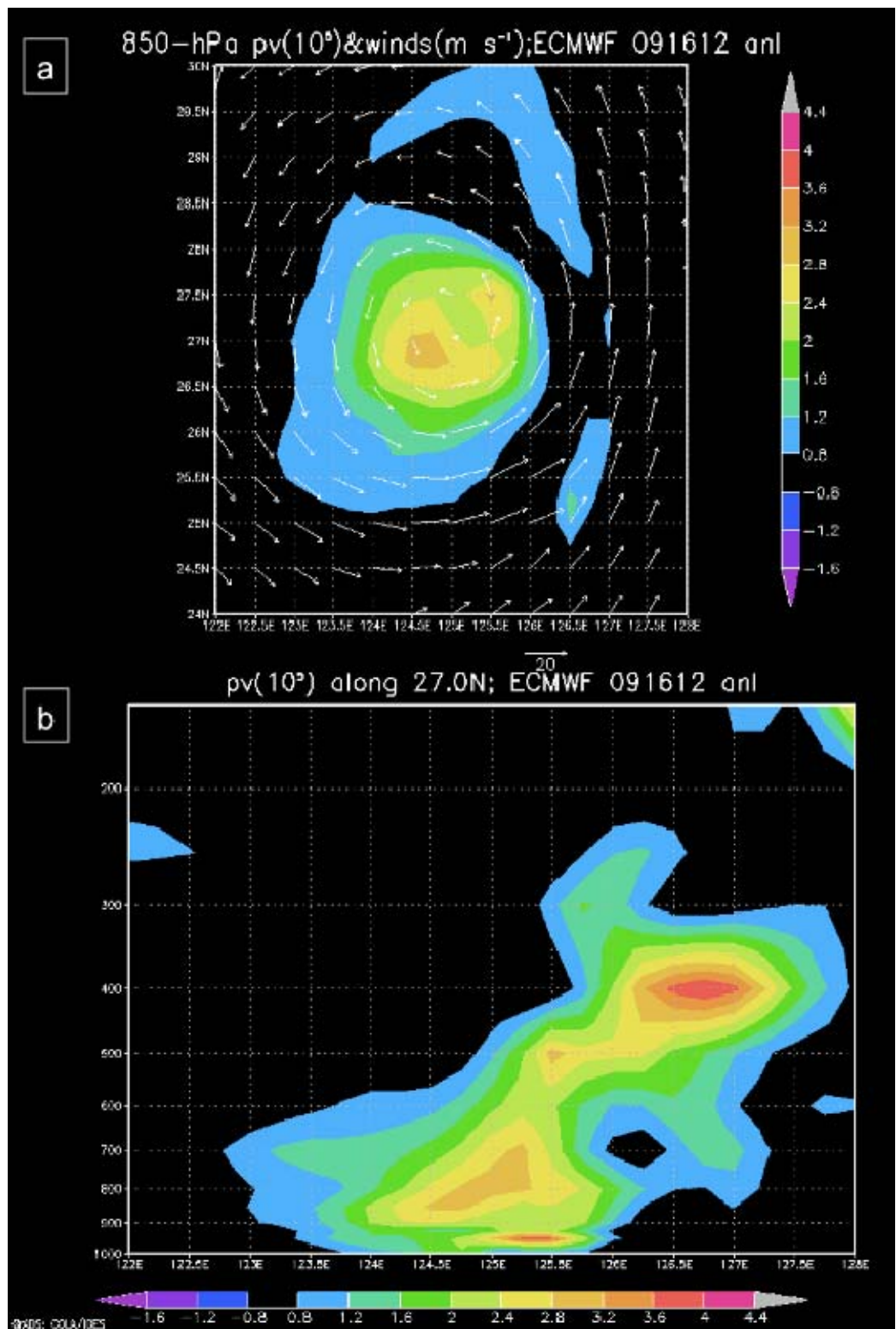
Figure 20.   Potential vorticity (10^{-5}) from the ECMWF model analyses for 1200 UTC 16
September 2008 analogous to the relative vorticity analysis in Fig. 19.
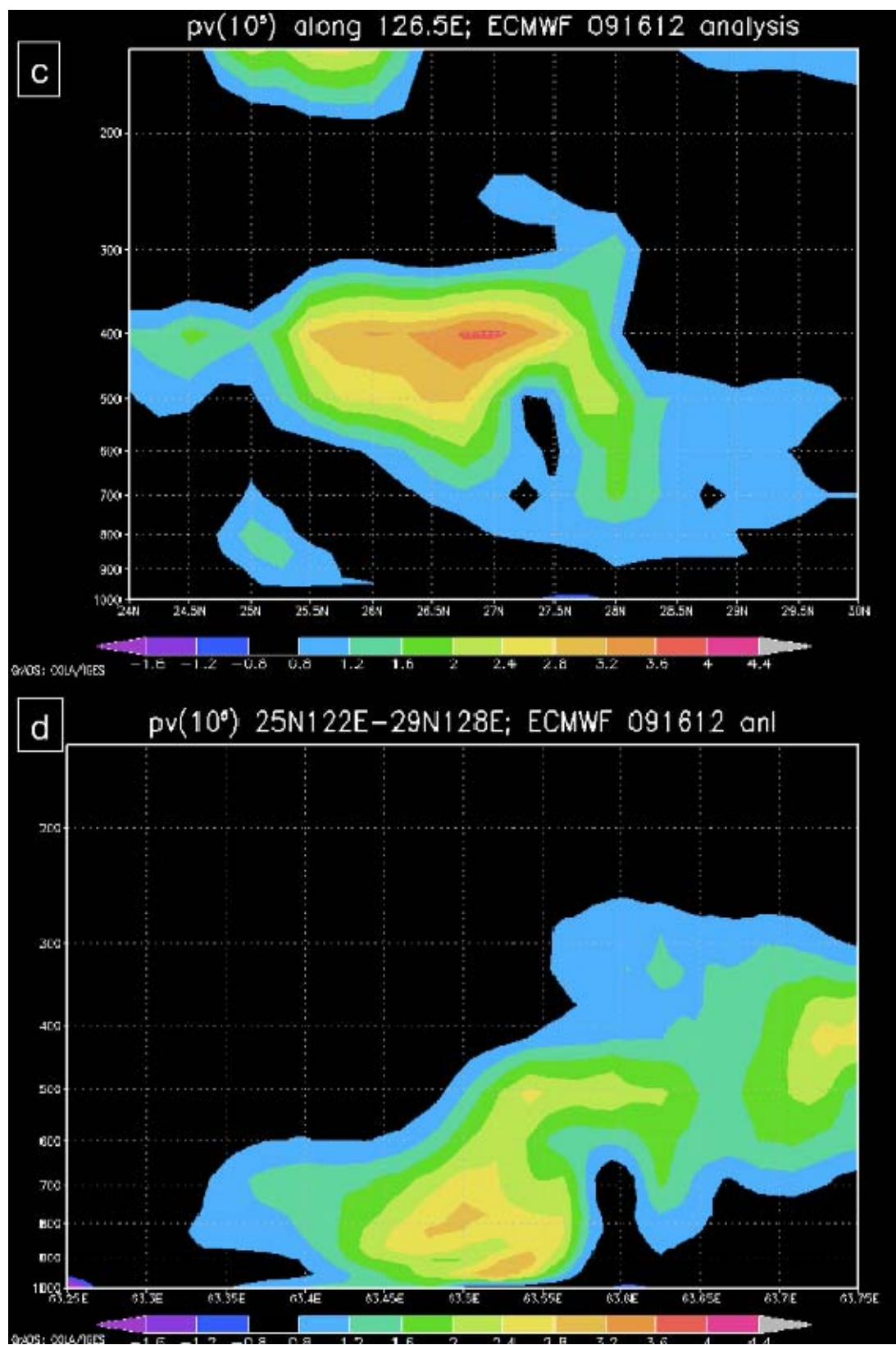
Fig. 20, continued.

Fig. 20, continued.

650-hPa Streamlines (m s⁻¹) and Heights (m)
PMSL<1004 hPa; ECMWF 2008091700 analysis
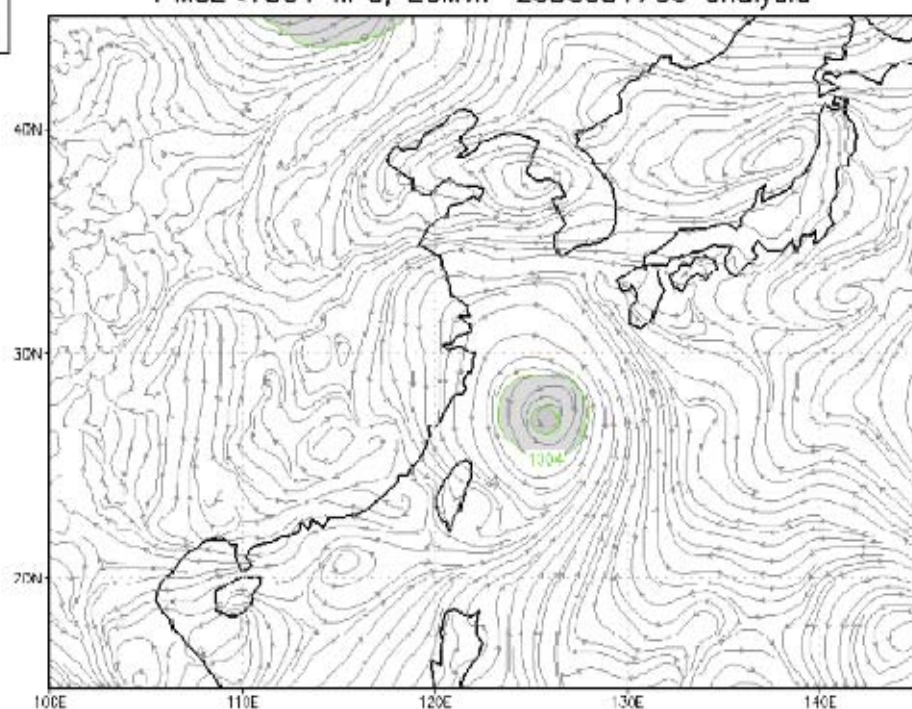
GrADS: COLA/IGES

500-hPa Streamlines (m s⁻¹) and Vorticity*10⁴ (s⁻¹)
ECMWF 2008091700 analysis
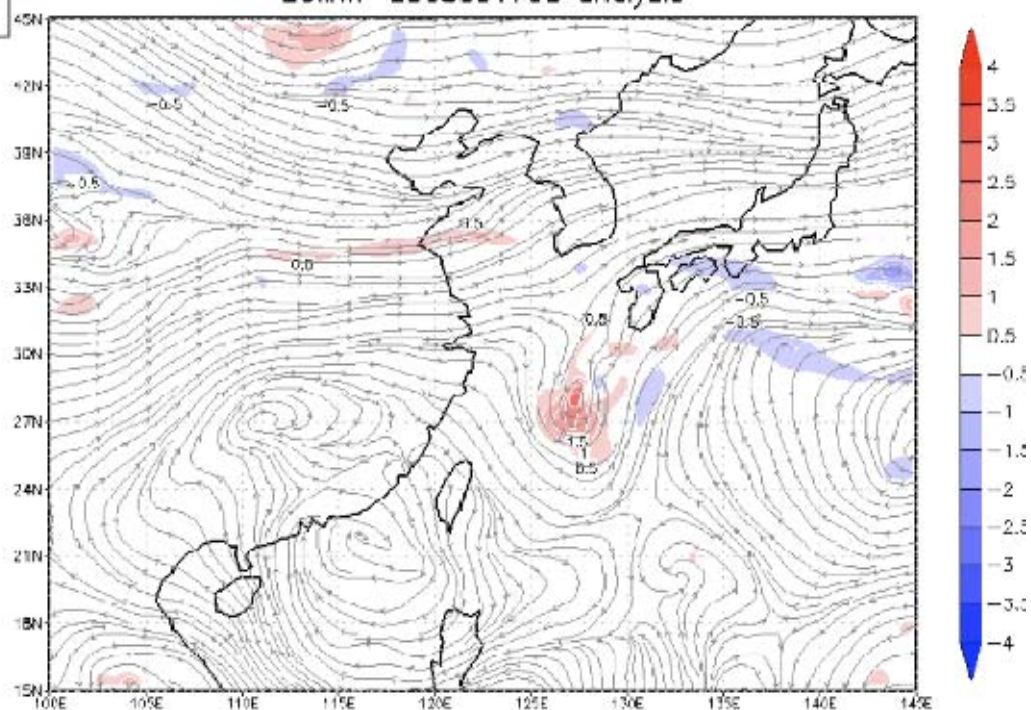
Figure 21.   As in Fig. 14, except for 0000 UTC 17 September 2008.

70

200-hPa Streamlines and Isotachs (m s⁻¹)
ECMWF 2008091700 analysis
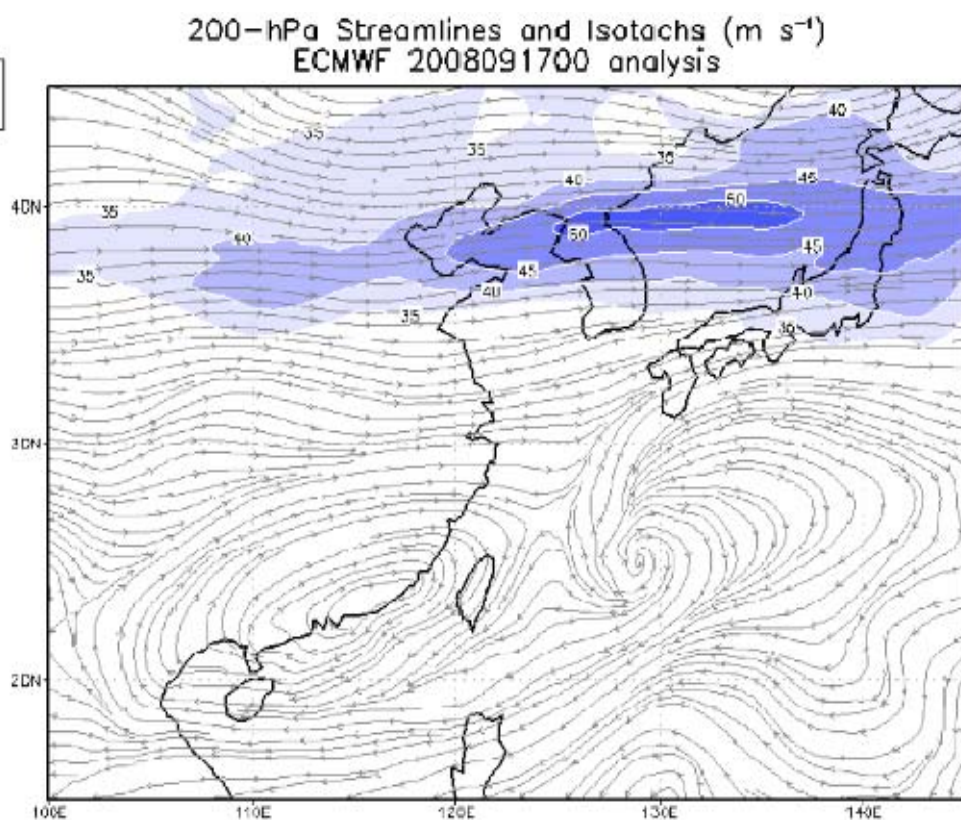
Fig. 21, continued.
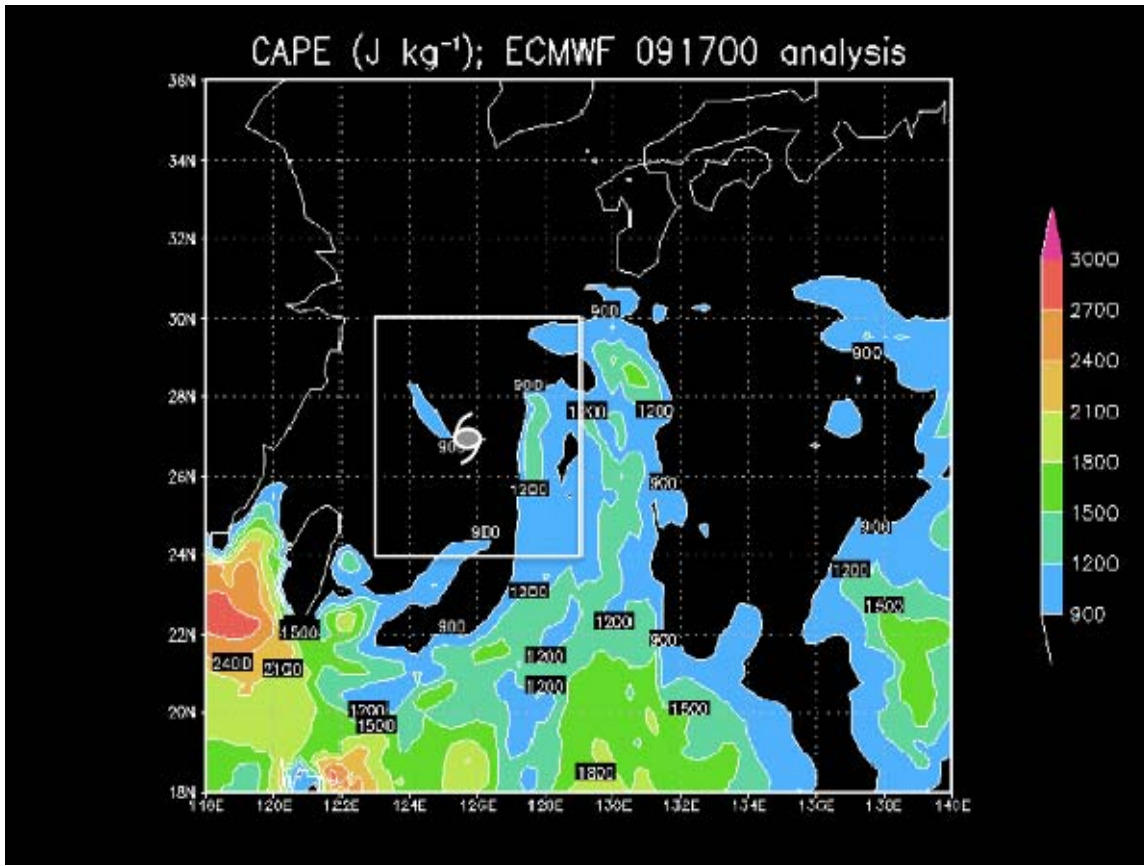
Figure 22.   Convective Available Potential Energy (CAPE) (J kg^{-1}) for 0000 UTC 17 September 2008 from the ECMWF. The TC symbol is plotted at the location of the Sinlaku LLCC in the EC model at the time of the plot. The boxed region defines the area in Fig. 23.
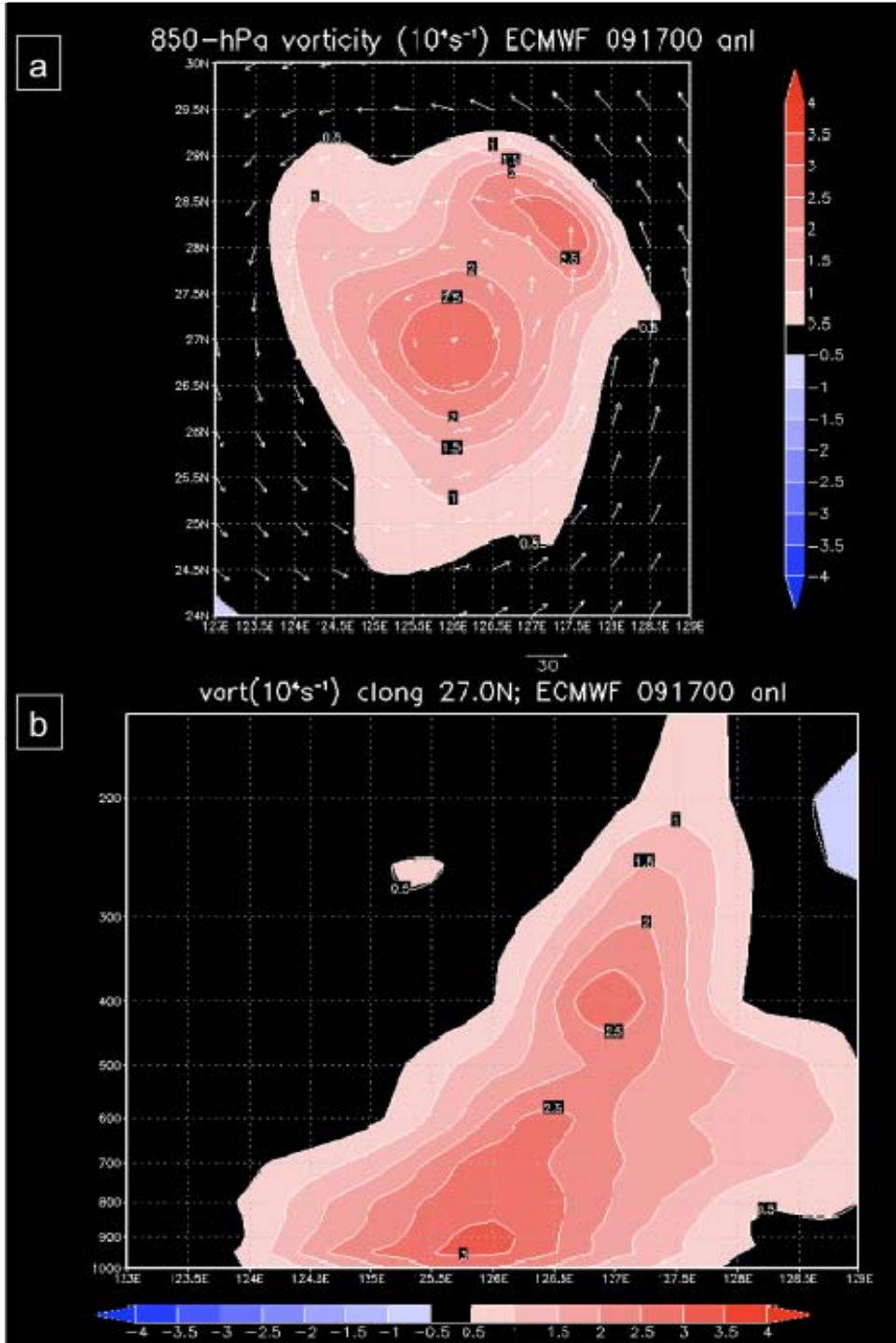
Figure 23.   Relative vorticity (10^{-4} s^{-1}) from the 0000 UTC 17 September 2008 ECMWF
model analysis in a (a) plan view across 850 hPa, vertical cross-sections (b) along
27.0°N, (c) along 127.5°E, and (d) between 24.0°N, 123.0°E and 30.0°N, 129.0°E,
and (f) plan view across 400 hPa. White arrows in (a) and (e) indicate wind speed
(m s^{-1}, reference vector below each panel) and direction at 850 hPa and 400 hPa,
respectively.
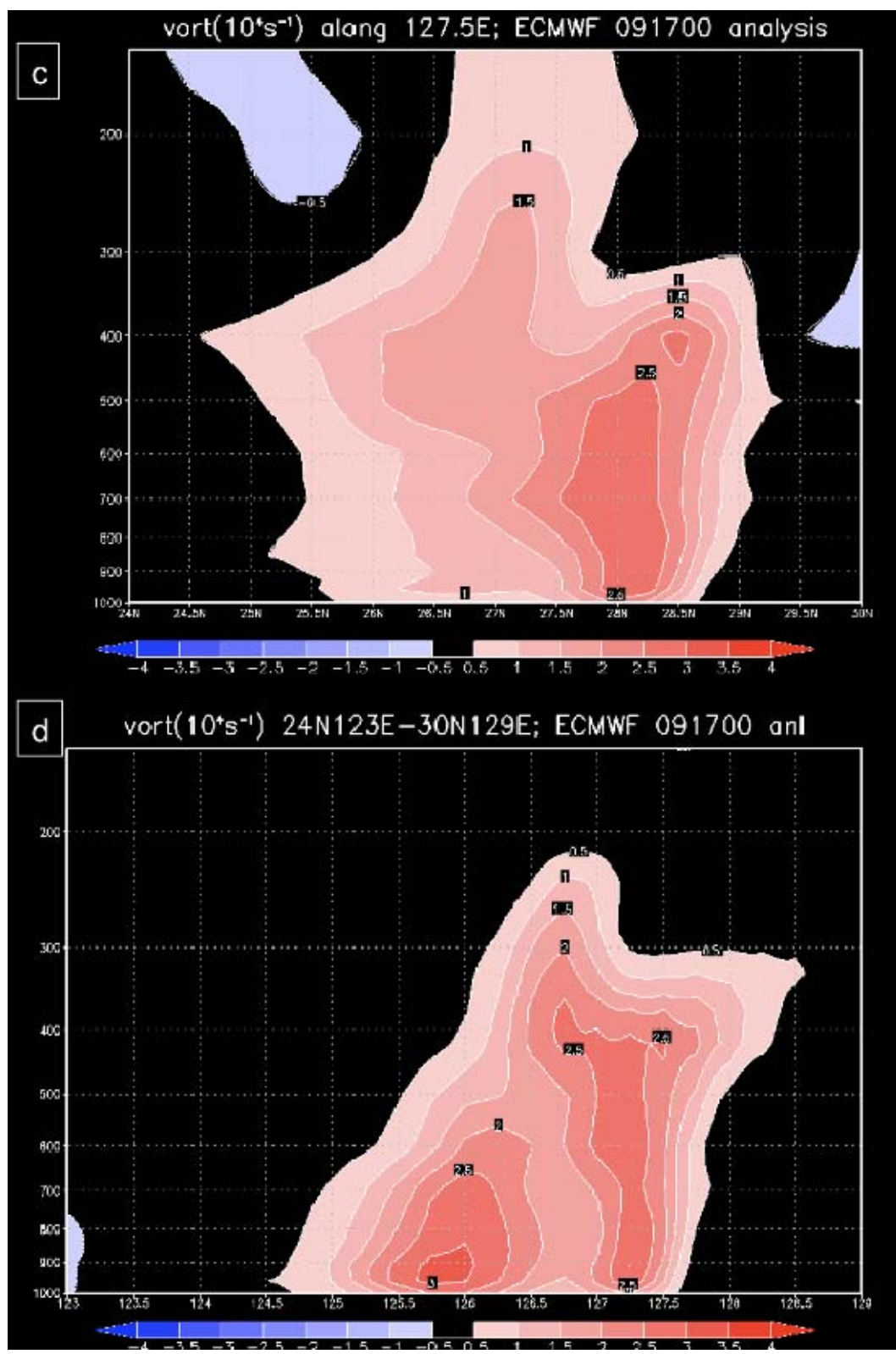
Fig. 23, continued.
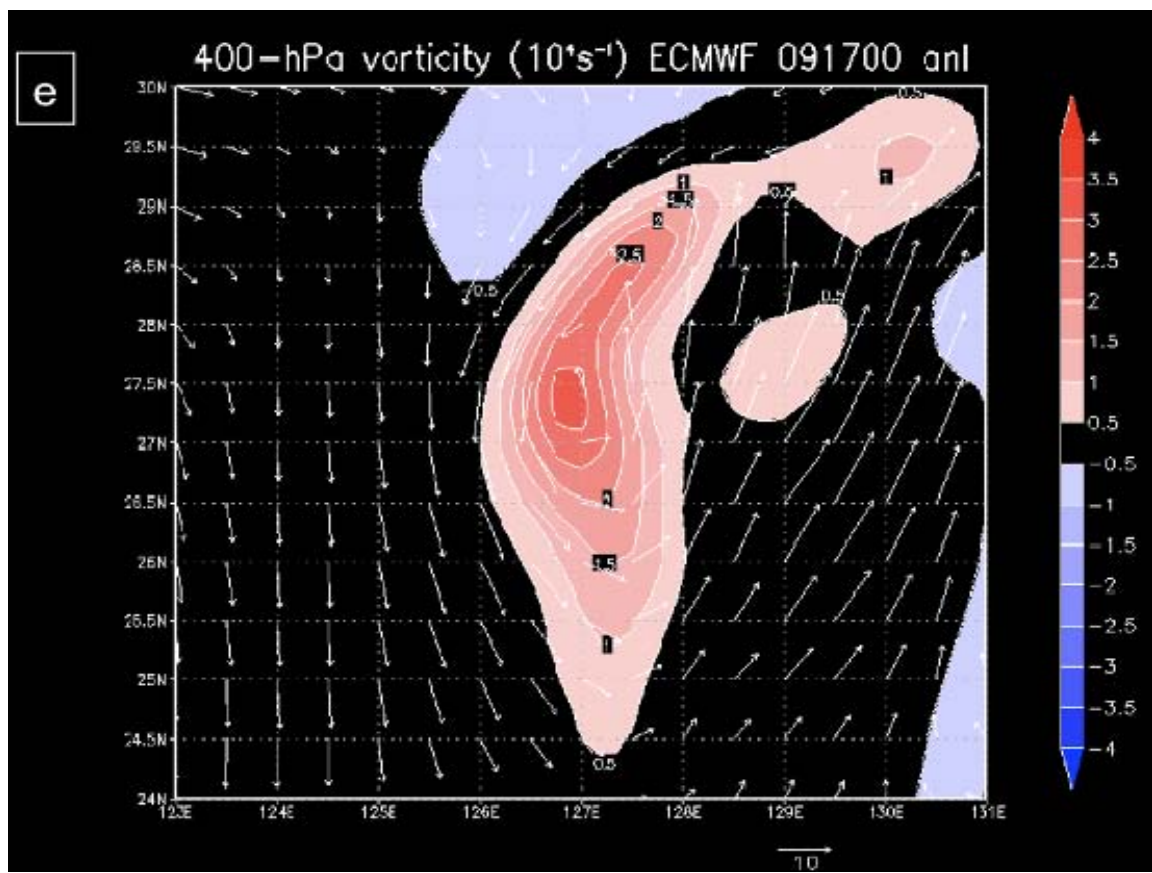
Fig. 23, continued.
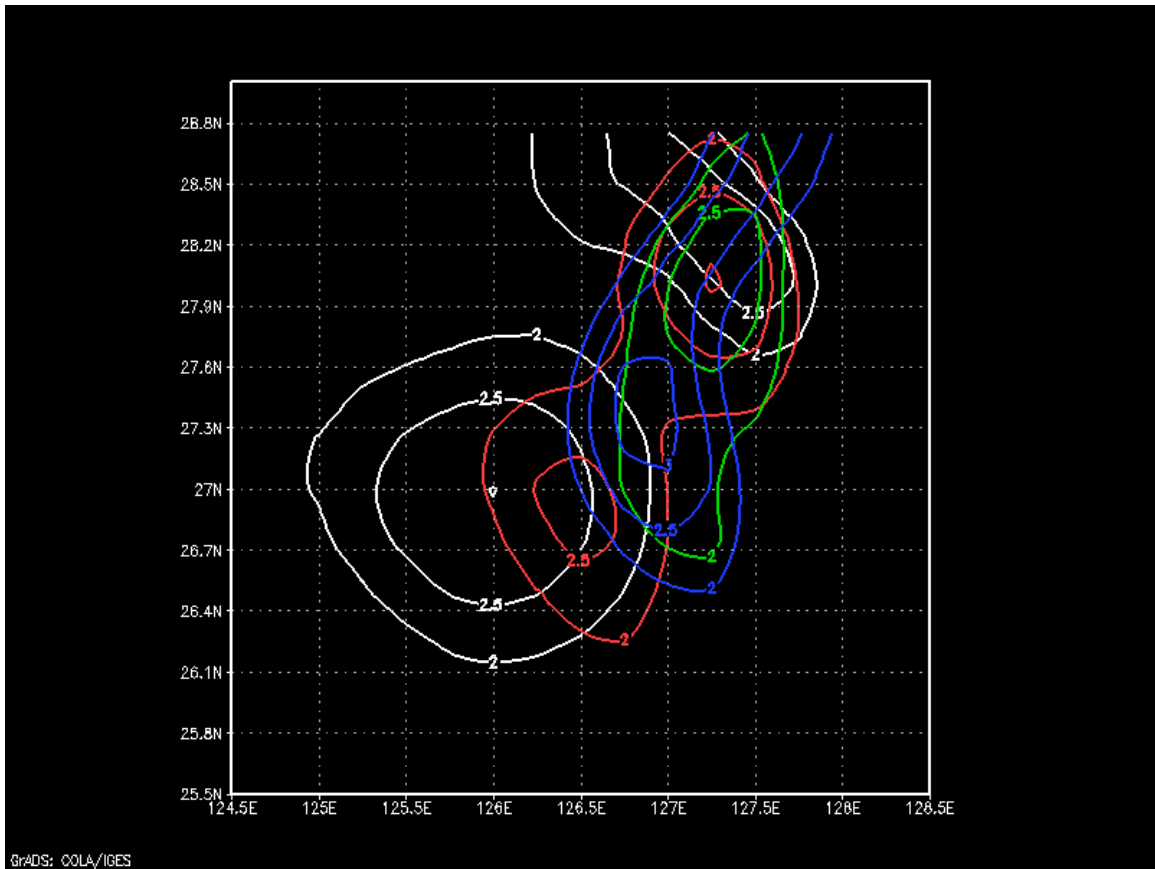
Figure 24.   Relative vorticity (10^{-4} s^{-1}) values in excess of $2*10^{-4}$ s^{-1} at 850 hPa (white contours), 600 hPa (red contours), 500 hPa (green contours), and 400 hPa (blue contours) from the 0000 UTC 17 September 2008 ECMWF analysis.
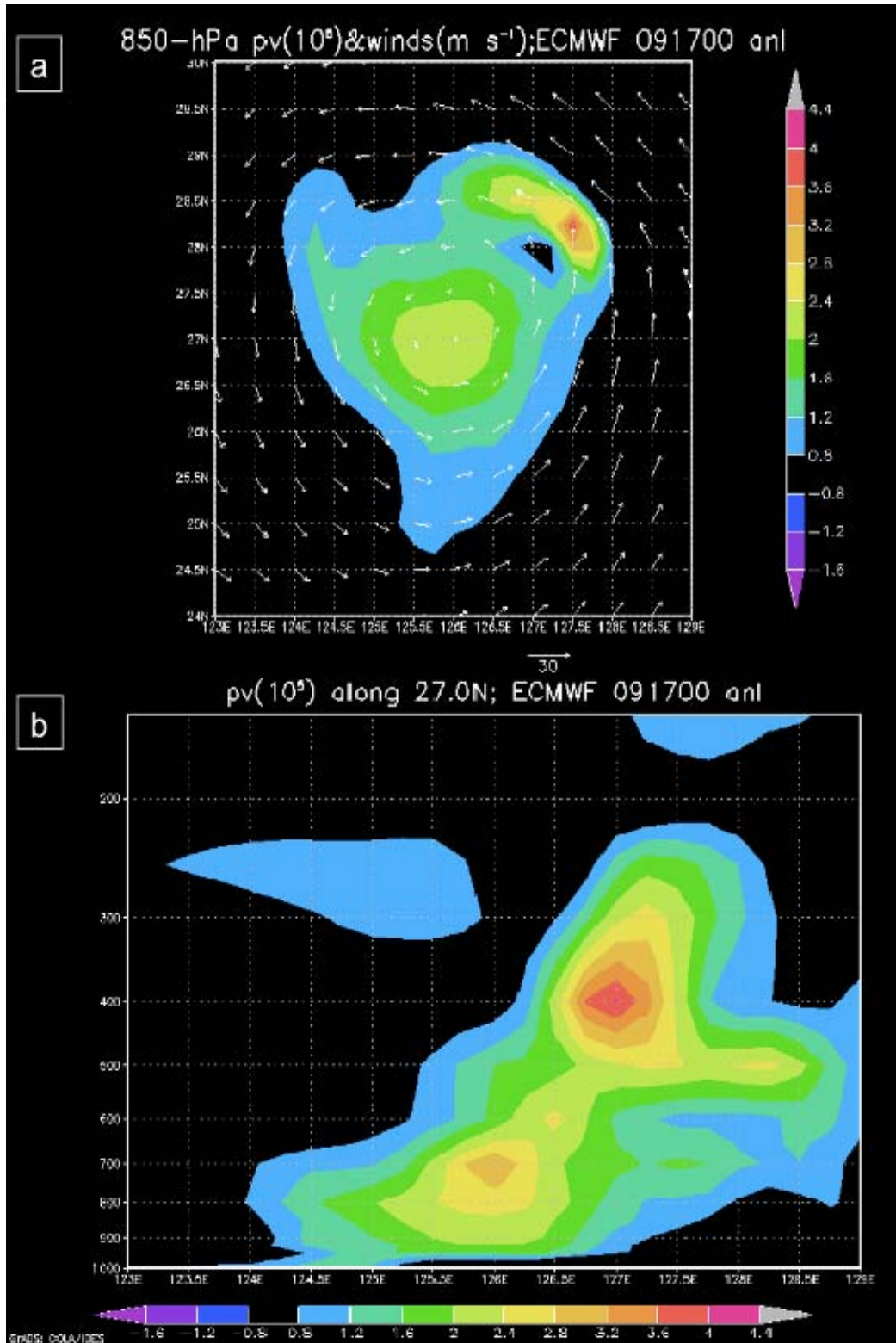
Figure 25. Potential vorticity from the ECMWF model analyses for 0000 UTC 17 September 2008 analogous to the relative vorticity analysis in Fig. 23.

pv(10⁶) along 127.5; ECMWF 091700 analysis

pv(10⁶) 24N123E—30N129E; ECMWF 091700 anl

Fig. 25, continued.

78
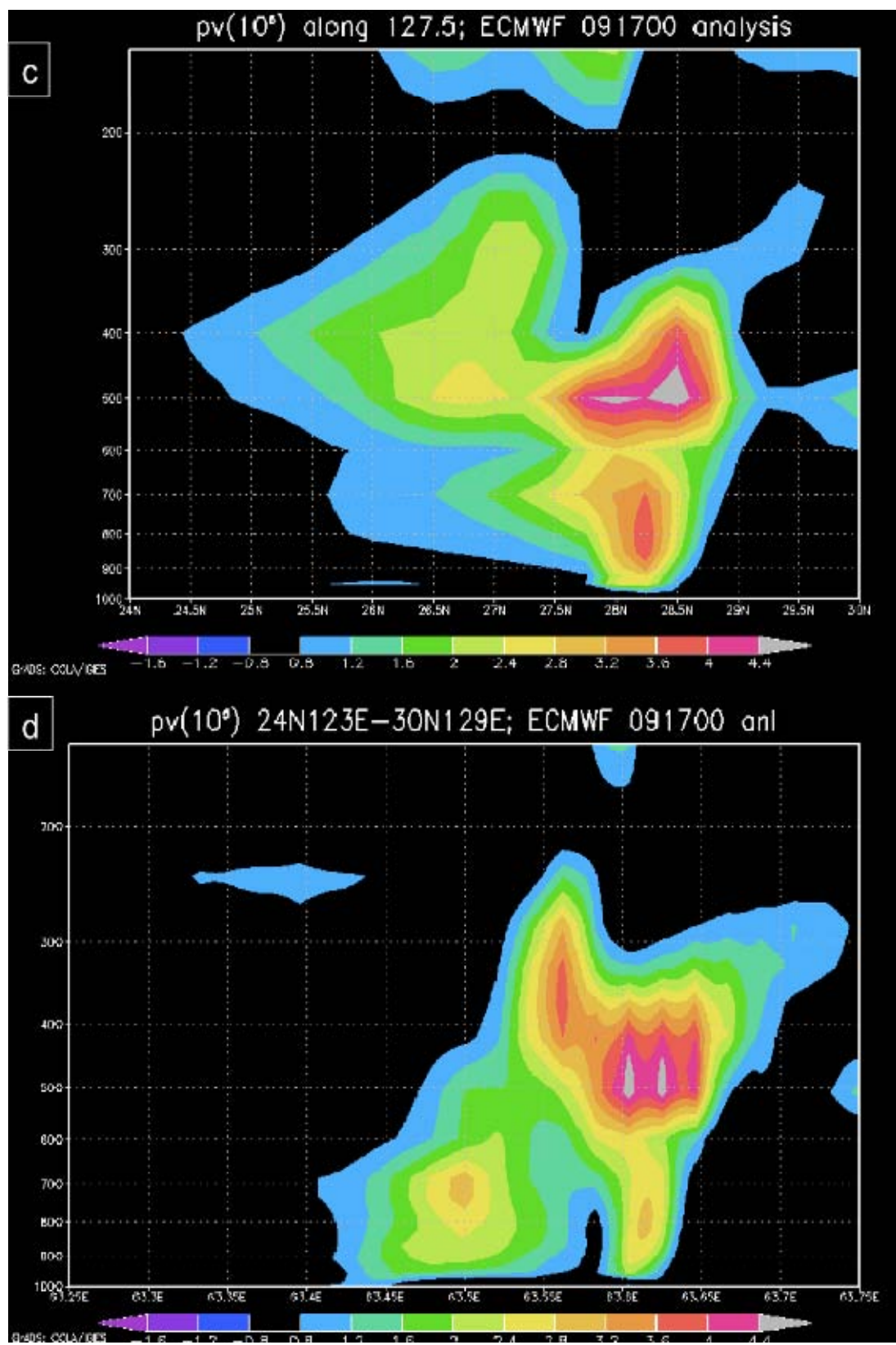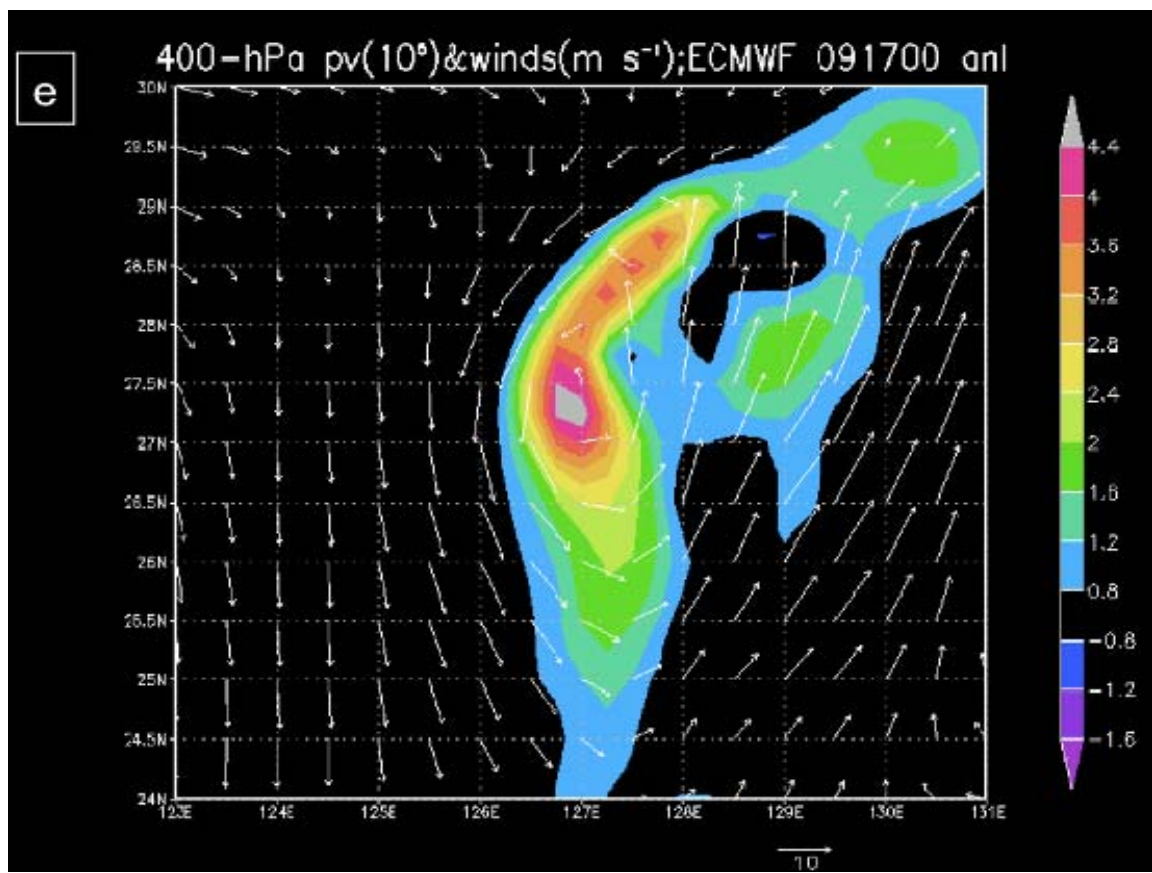
Fig. 25, continued.
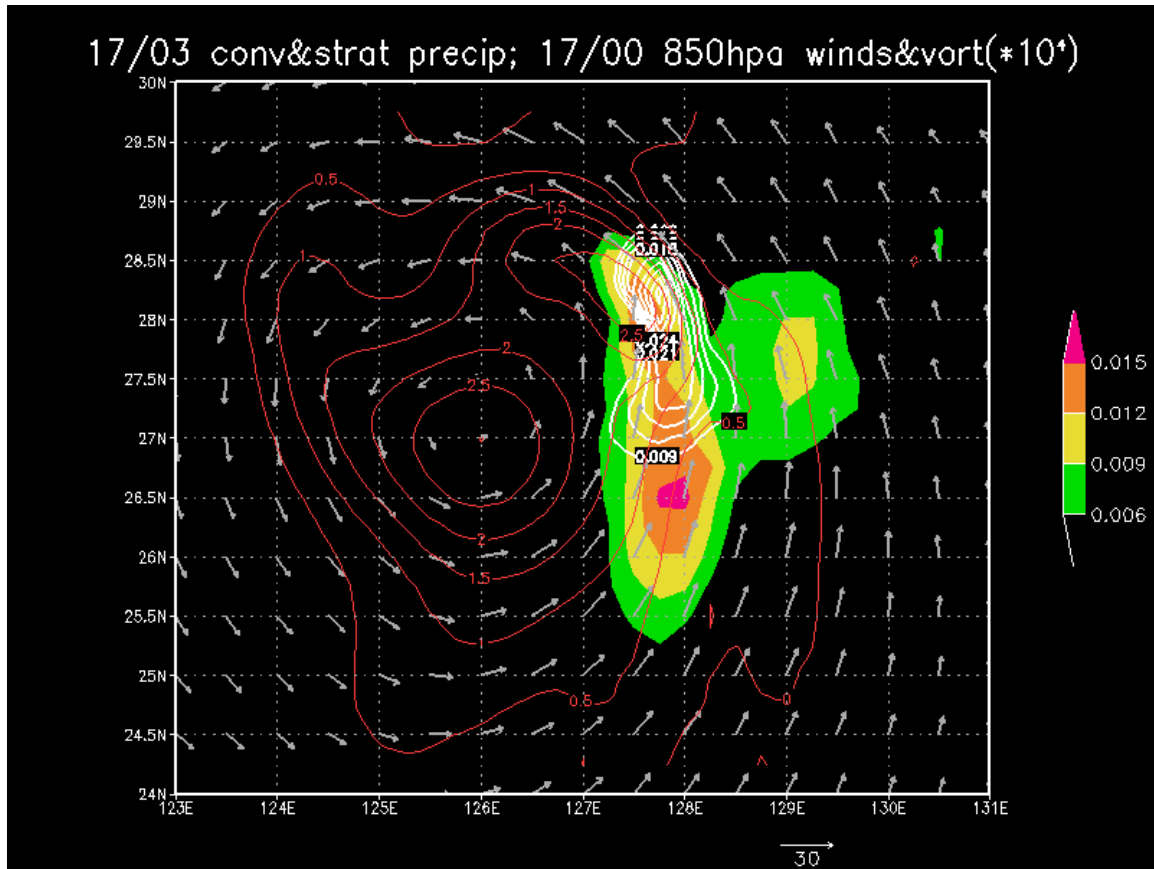
Figure 26. Convective (shaded) and stratiform (white contours) forecast precipitation accumulation (m) over the three hours between 0000-0300 UTC 17 September 2008. Red contours are the 850-hPa relative vorticity (10^4 s^{-1}) maxima, and light gray arrows indicate the 850-hPa wind speed (m s^{-1}, reference vector below panel) and direction at 0000 UTC 17 September 2008 in the ECMWF analysis.

IV.   THE INTERACTION BETWEEN TYPHOON SINLAKU AND MULTIPLE MESOSCALE VORTICES

In Chapter III, the evolution of the convection east of TY Sinlaku was investigated in satellite imagery, and the effect of that convection on the circulations in the vicinity of TY Sinlaku was investigated using the ECMWF YOTC data. In this chapter, the analysis of the convection and the impact of the convection on the TC structure(s) will be examined in further detail, and the contribution of the various features to the redevelopment of Sinlaku will be assessed. In Chapter V, the evolution of the precipitation structures from the third and subsequent convective episodes will be analyzed as Sinlaku re-develops to typhoon intensity.

In this chapter, the aircraft observations from the TCS-08/T-PARC 16-17 September 2008 flights are examined to investigate in more detail the convective and mesoscale structures and precipitation characteristics in the vicinity of TY Sinlaku. Dropwindsonde and flight-level observations enable vertical and horizontal analyses of the environment along the flight tracks. The foci in these analyses are the vortex structure, including the orientation with height, and circulations both near the TC vortex and in the environment beyond the inner TC circulation. The ELDORA data from the P-3 flight track segment adjacent to the TC center and deep convective burst that defines the third episode are examined to assess the three-dimensional structure of the convective and mesoscale features in the vicinity of Sinlaku.

A.   OBJECTIVES

The recurvature of TY Sinlaku and subsequent track toward the midlatitudes offered the first opportunity during the TCS-08/T-PARC field program to observe a tropical cyclone (TC) as it began the extratropical transition (ET) portion of its lifecycle. The primary objective of the research flights conducted by the WC-130J and P-3 on 16-17 September 2008 was to observe and record the structural evolution of TY Sinlaku through the transformation stage of ET. Additional objectives for the flights included the validation of satellite observations of intensity and the collection of observations in the

environment of Sinlaku to provide improved initial conditions for operational numerical forecast models. A separate logistical objective of the first flights was to re-position the WC-130J and P-3 aircraft forward to Yokota Air Base in Japan to minimize transit time and maximize on-station time during the subsequent Sinlaku ET flights. The German Aerospace Center (DLR) Falcon aircraft, already stationed in Japan, also conducted an ET mission on 17 September 2008 with the objective of measuring the outflow from Sinlaku and assessing the relationship between the evolving TC and the midlatitude jet.

B.   OBSERVING STRATEGY

As described in Chapter III, several episodes of deep convection had been occurring over a region of high ocean heat content and atmospheric moisture oriented southwest-to-northeast in a region east of Sinlaku. Therefore, the flight plans for the WC-130J and P-3 were designed to survey the eastern side of the TY Sinlaku circulation. The WC-130J would over-fly the bulk of the convection on the eastern side of Sinlaku and release dropwindsondes while collecting flight-level data. The P-3 would also release dropwindsondes and collect flight-level data, but would do so while flying at 500 hPa and surveying with the ELDORA the convective structures on the eastern side of the TC.

Both aircraft departed Andersen Air Force Base in Guam near 2045 UTC 16 September 2008 and flew northwest toward the southeast quadrant of Sinlaku. Shortly into the flight, the track for the P-3 was adjusted to transit south of Okinawa instead of north to enable the P-3 to maximize the aerial extent of its survey of the convection east of the Sinlaku center. Approximately three hours into the flights (at 2330 UTC 16 September 2008), a convective burst erupted east of the TC center and in the direct path of both aircraft. This convection defined the start of the third convective burst episode examined in Chapter III. At 0025 UTC 17 September 2008, while still nearly an hour southeast of the developing convective tower, the P-3 maneuvered left to a west-northwestward heading while maintaining a flight level near 500 hPa. This track

(Fig. 27a) placed the P-3 and ELDORA along the outer periphery of the convection to capture real-time observations of reflectivity and Doppler velocities while maximizing the safety of the aircraft.

Because of the asymmetric nature of the convection to the east of an exposed low-level circulation, the WC-130J continued to approach the intensifying convective tower to survey the upper-level winds and thermal structure. While passing through the region of deepest convection at 0100 UTC 17 September 2008, the WC-130J turned to the north and climbed to 275 hPa to avoid potential icing issues. Well to the south, the P-3 continued a clockwise path around the region of the current convective burst. At 0105 UTC 17 September 2008, the aircraft turned right to head north-northwestward, and then turned toward the northeast around 0130 UTC 17 September 2008. Ten minutes later, the P-3, in clear air at flight level, passed directly between low-level clouds that appeared to be the LLCC of Sinlaku (Fig. 28a) to the left (west) of the aircraft and the massive convective burst (Fig. 28c) to the right (east) of the aircraft. Reflectivity from the forward radar (Fig. 28b) at 0140 UTC 17 September 2008 illustrates the near absence of reflectivity at low levels and an extensive region of moderate reflectivity at upper levels to the left of the aircraft, which corresponds to Fig. 28a. To the right of the aircraft, extensive areas of high reflectivity are observed with multiple towers exceeding 50 dBZ. Although a dropwindsonde was released from the P-3 at 0141 UTC 17 September 2008, the parachute did not properly deploy to slow the sensor's descent. As a result, this dropwindsonde became classified as a "fast fall" dropwindsonde, and therefore the wind observations did not pass the post-mission quality control check (Young 2009b). After passing the developing tower, permission was requested from Japanese Air Traffic Control to fly a reciprocal course to make a second pass close to the developing convection and LLCC. Unfortunately, this request was denied. Both aircraft then proceeded to Yokota Air Base, and landed at 0426 UTC (WC-130J) and 0515 UTC (P-3) 17 September 2008.

To the north, the Falcon's ET mission (Fig. 27b) was an out-and-back path from Naval Air Facility (NAF) Atsugi to Marine Corps Air Station Iwakuni, and then back to NAF Atsugi. The first leg of that mission (Atsugi to Iwakuni) overlapped in time with

the WC-130J and P-3 flights to Yokota. The Falcon left Atsugi at 0320 UTC 17 September 2008, proceeded southwest along the eastern seaboard of Japan then turned northwest, passing between Korea and Japan. The Falcon then turned east and landed in Iwakuni at 0625 UTC 17 September 2008.

C.   STRUCTURAL CHARACTERISTICS OF TY SINLAKU

1.   Aircraft Observations

Dynamic and thermodynamic dropwindsonde and flight-level observations provided by the TCS-08/T-PARC aircraft are utilized in this section to locate the TC center, to define the extent of the outer TC circulation, and to identify other synoptic-scale features in the vicinity of the TC. The high-resolution ELDORA observations are then used to identify characteristics of the various mesoscale and convective-scale features in the vicinity of the TC vortex. All aircraft observations are also compared to the ECMWF operational analyses.

a.   *Dropwindsonde Winds*

Nearly all of the WC-130J and P-3 dropwindsondes (blue and green wind barbs in Fig. 29) released during the 16-17 September 2008 ET missions in the vicinity of TY Sinlaku are within the 2100-0300 UTC observation window for the ECMWF data assimilation supporting the 0000 UTC operational analysis. The exceptions were the last two drops from each aircraft. These last two drops were released at 0303 UTC 17 September 2008 (from the WC-130J) and at 0312 UTC 17 September 2008 (from the P-3). Although the dropwindsondes were obtained within the data cut-off time period for the ECMWF model, it is not known for sure whether the assimilation system accepted the data (T. Hewson, C. Cardinalli, 2009, personal communication). In contrast, the Falcon dropwindsondes (purple wind barbs in Fig. 30) were released between 0346-0559 UTC 17 September 2008 so these dropwindsondes were outside of the ECMWF observation window. Since the soundings within the observation window would be assimilated without adjustment to position, and all of the WC-130J and P-3 dropwindsondes were

84

either in or within a few minutes of the observation window, these soundings are plotted at their exact locations on each level. Because the Falcon dropwindsondes were also not adjusted in time and space, those soundings were not closely evaluated in this analysis.

Winds from the WC-130J dropwindsonde released at 0109 UTC 17 September 2008 near 27.97°N, 126.53°E and the P-3 dropwindsonde released at 0136 UTC 17 September 2008 near 27.26°N, 126.31°E bound the center of the TC circulation on the northern and southern sides between 975-650 hPa, respectively (Figs. 29 a-c, see box 1 in Fig. 29 a). The variation in wind directions with height (Fig. 30) is depicted in the skew-t diagrams for these two dropwindsondes in Figs. 30a,c. A third dropwindsonde (Fig. 30b) was released by the P-3 at 0141 UTC 17 September 2008 near 27.51°N 126.54°E (Fig. 30b), this dropwindsonde experienced a "fast fall" and only quality-controlled thermodynamic data were available. The thermodynamic data for each dropwindsonde in Fig. 30 will be analyzed further in the thermodynamic section. The WC-130J dropwindsonde winds (Fig. 30a) backed with height from southeasterly at 950 hPa, to easterly at 700 hPa, and north-northeasterly at and above 550 hPa. These winds define a TC center location that is southwest of the dropwindsonde at 950 hPa, south of the dropwindsonde at 700 hPa, and east-southeast of the dropwindsonde at and above 550 hPa. Therefore, a generally eastward tilt of the TC center with height existed from the surface through 550 hPa, which was somewhat similar to the northeast tilt in the ECMWF analysis discussed in the previous chapter.

On the opposite side of the vortex (Fig. 30c), the P-3 dropwindsonde was released from a lower flight level near 500 hPa, and as a result winds for the 0136 UTC dropwindsonde are measured from 550 hPa to the surface. These winds veered with height rather gradually from west-northwesterly at 950 hPa, to northwesterly 650 hPa, and then became northerly at 600 hPa and above. These winds reveal that the TC center was north-northeast of the dropwindsonde at 975 hPa, northeast of the dropwindsonde between 650 hPa, and east of the dropwindsonde at and above 600 hPa. As with the WC-130J dropwindsonde (Fig. 30a), the P-3 wind progression in the vertical also indicates a progressively eastward displacement of the TC center with height.

It is possible to consider the winds from both dropwindsondes simultaneously (Fig. 31) even though the WC-130J dropwindsonde (A in Fig. 31) was released 27 minutes before the counterpart P-3 dropwindsonde (B in Fig. 31). Since the speed and direction of the TC between 0000-0600 UTC 17 September 2008 was 7.73 kt toward the northeast (Figs. 2a, 6), to account for the 27-minute difference between drops the positions of the C-130 winds at each level would need to be moved 3.5 n mi, or 6.44 km northeastward. For this discussion, that distance is considered negligible, and the dropwindsonde winds are plotted at their true locations. Circulation center positions in Fig. 31 are estimated for several levels based on geostrophic reasoning given the dropwindsonde wind directions at those levels. The LLCC position at 950 hPa (gray TC symbol in Fig. 30c) is estimated to be near 27.65^{o}N, 126.38^{o}E. The winds at higher levels define a southeastward tilt in the TC from 950 hPa (gray TC symbol in Fig. 30c) through 600 hPa (green TC symbol in Fig. 30c). Recall that in the ECMWF analyses at 1200 UTC 16 September 2008 and 0000 UTC 17 September 2008, the lower tropospheric vortex tilted a full degree northeastward with height between 900 hPa – 400 hPa. The dropsonde winds and model observations both have an eastward component to the tilt and the offset in both cases is on the order of one degree.

Beyond the two dropwindsondes adjacent to the TC center, the broader TC circulation was identified by two groups of additional dropwindsonde winds from the WC-130J and P-3 flights (boxes 2 and 3 in Fig. 29a). Nearly 3° lat. south and 2° long. east of the TC center estimated above from the P-3/WC-130J dropwindsonde center pair, winds from two dropwindsondes along the P-3 flight track at 25°N (box 2 in Fig. 29a) define southerly and southwesterly winds throughout the lower-middle troposphere. These two dropwindsondes are in the southeast quadrant of the TC, south of the deep convection (Figs. 29a-d) and within the region of strong south-southwesterly flow identified in the model analyses (Fig. 21a). The second group of dropwindsondes within the TC region is located north of the TC center (box 3 in Fig. 29a), between 28.2^{o}-29.4^{o}N and 125°-128.8^{o}E. Winds from multiple WC-130J and P-3 dropwindsondes in this region identify the cyclonic flow about the TC center from the surface through 350 hPa (375 hPa in Fig. 29g).

Beyond the TC circulation, dropwindsondes released by the Falcon west of Japan (box 4 in Fig. 29a) defined southwesterly winds of 15-20 m s^{-1} at 300 hPa and 20-30 m s^{-1} at 275 hPa that support a broad pattern of anticyclonic outflow from the TC. South of Japan (box 5 in Fig. 29a) between 28.0^o-31.5^{o}N, 128.8^o-134.5^{o}E, southeasterly flow is observed below 850 hPa that is consistent with the cyclonic flow around the Sinlaku center (Figs. 29a-b). However, by 700 hPa the flow in the region had become southerly (Fig. 29c), and by 550 hPa winds in the eastern half of the region continued to veer and had become southwesterly (Fig. 29d). Nearly all the winds east of 131°E had a westerly component by 500 hPa, and flow along the southeastern coast of Japan was southwesterly Japan (Fig. 29e). Between 425-350 hPa, the flow along 30°N backed to easterly (Fig. 29f). East of Japan (box 6 in Fig. 29a), dropwindsonde winds released by all three aircraft (WC-130J, P-3, and Falcon) were east-northeasterly from the surface to 775 hPa, and then became southwesterly above 650 hPa, which defined the boundary of the eastern portion of Sinlaku and the western side of the subtropical anticyclone.

Although the ECMWF analysis is only used to provide a general background view of the environmental characteristics during the flight period, there are three principle findings from a comparison of dropwindsonde data and ECMWF model analyses. First, the TC vortex at low levels (975-850 hPa) in the model was nearly 0.5^o lat. southwest of the location determined by the dropwindsondes (Figs. 29-30). The 1.5-hour separation in time between the analyzed TC center position and the dropwindsonde release times could account for a northeastward shift of 11.6 n mi, or 21.47 km, in the TC center position, but this difference of less than 0.2^o lat. would account for less than half of the offset. Therefore, the TC was likely moving faster than estimated from best-track positions and/or the model analysis position was slightly southwest of the actual LLCC. Second, in contrast to the lower levels, the mid-level (675-400 hPa) (Figs. 29d-e) circulations defined by the model and the dropwindsondes were aligned more closely. This agreement could be due to the assimilation of conventional satellite data.

A third finding is that the broader TC circulation in the gridded fields did not always match the aircraft observations. This mismatch was particularly the case in

the orientation of the Sinlaku circulation center at middle and upper levels. Northeast of the LLCC, wind directions from dropwindsondes launched between 28-29°N, 127-129°E (eastern half of box 3 in Fig. 29a) were consistently 45-90° to the right of the wind direction in the analyses between 675-550 hPa (Fig. 29d). This direction difference indicated that the TC circulation was not only shifted east of the model position, but was more circular than the meridionally-oriented elliptical flow about the vortex in the analyses (Figs. 29d-e). Thus, the vortex in the model was being influenced by the midlatitude flow at a level lower than defined by the aircraft observations. A similar structural difference was defined by the comparison of model analyses and dropwindsonde winds at 375 hPa (Fig. 29f). Also, the vortex opened to a wave at 325 hPa in the ECMWF analyses (Fig. 29g), while the dropwindsonde winds at that level remained easterly, which indicates that the vortex is still closed at this level. The single dropwindsonde at 300 hPa (Fig. 29h) was westerly, which would confirm the vortex was an open wave at this level. However, the position of the wave in the model may be offset to the southwest of the position supported by the dropwindsonde.

b.   *Dropwindsonde Thermodynamics*

The dropwindsonde released by the WC-130J at 0011 UTC 17 September 2008 (Fig. 32a) was located well southeast of the TY Sinlaku LLCC and at the southeastern edge of the banded convection remaining from the first convective episode (Figs. 9-11). Similar to the four P-3 dropwindsondes released to the northwest (not shown), the 0011 UTC 17 September 2008 dropwindsonde data (Fig. 32c) defined generally moist flow at low-to-mid levels. Unlike the P-3 dropwindsondes that were released from 500 hPa, the WC-130J dropwindsonde was released from a flight level near 300 hPa, which enabled an estimate of Convective Available Potential Energy (CAPE). The WC-130J dropwindsonde data from 350 hPa to the surface defined a CAPE value of 1341 J kg^{-1}, which is similar to the CAPE values of between 1200-1500 J kg^{-1} at the drop location in the ECMWF analysis (Fig. 22, repeated in Fig. 32b).

Dropwindsondes released from the P-3 and WC-130J along the next leg of the P-3 flight track (Fig. 33a) reveal elevated values of Θ_e in the region of the Sinlaku

LLCC and deep convective burst (Fig. 33b). In particular, the P3 dropwindsonde released at 0141 UTC 17 September 2008 near 27.51^{o}N, 126.54^{o}E (dropwindsonde B in Fig. 33b) as the aircraft passed between the Sinlaku LLCC and the deep convective tower (Fig. 28) had the lowest surface pressure in the cross-section and was near the midpoint in the wind shift defined by the two dropwindsondes in Figs. 30a-b and 31. Dropwindsondes B and C (Fig. 33b) define a moist lower troposphere that is represented by high-Θ_e air that extendeds upward at the position of dropwindsonde B to 700 hPa and tilts slightly southwestward (left in the cross-section) to nearly 650 hPa (Fig. 33b) at the position of dropwindsonde C. The release location of dropwindsonde B (Fig. 31) was slightly south of the 700 hPa estimated TC center location (yellow TC symbol in Fig. 30c), which suggests the P-3 flew directly over the mid-level center of TY Sinlaku. Northeast of the TC center (right side in Fig. 33b), high-Θ_e values were confined to considerably lower levels than at the center.

Skew-t diagrams (Fig. 30b-c) from the first three dropwindsondes (labeled D, C, and B) along the path in Fig. 33a define the thermodynamic environment on the western edge of the third convective epidsode. (The skew-t for the southwestern-most dropsonde "D" is not shown). These three dropwindsondes define a rather dry mid level over a moist low level, which is the structure expected beneath the anvil region associated with the deep convection to the east.

c. Flight-Level Winds

The P-3 flight level winds (Fig. 29e) describe the flow in the region of the mid-level circulation center, as inferred from the P-3 and WC-130J center pair of dropwindsondes in Fig. 31. With a range spanning more than 400 km in diameter (24-28°N), the TC center is difficult to determine with precision; however, a simple connection of winds from the four cardinal directions places the center at approximately 27.7^{o}N, 128.3^{o}E, which is nearly half a degree both east and north of the 600 hPa center position (Fig. 31) estimated from the dropwindsonde data. This is consistent with the northeast tilt in the large-scale ECMWF analyses (Fig. 29), but less consistent with the trend of east-southeast tilt with heights observed in the dropwindsonde data (Fig. 31).

The circulation evident in the P-3 flight-level winds is elongated slightly in a northeast-to-southwest orientation. By contrast, the ECMWF 500-hPa analysis (Fig. 29e) has a circulation orientation around the TC was much more elliptical and was oriented almost meridionally. The direction differences between the ECMWF analysis and flight-level winds northeast of the TC center are very similar to the offset between the ECMWF analysis and winds from the group of dropwindsondes northeast of the TC center (box 3 in Fig. 29a). That is, the aircraft winds were consistently 45°-90° to the right of the wind direction in the analyses between 675-550 hPa (Fig. 29d). Just as in the dropwindsonde winds, a more circular orientation of the circulation is implied by the P-3 flight-level winds at 500 hPa.

The WC-130J provided the highest altitude aircraft flight-level observations (Figs. 29h, 34) in the vicinity of the TC vortex during the 16-17 September 2008 mission. At the WC-130J flight level of 300 hPa, the eastern (convective) side of the TC had southerly winds (Fig. 29h) and the winds became southwesterly as the aircraft approached the region of the third convective episode. In the vicinity of the deep convection, the flight-level winds became quite variable (Fig. 34). These wind observations suggest smaller-scale circulations were present that were not accepted in the ECMWF analysis. The turning of the wind observations near 27°N, 127.2^{o}E suggests a cyclonic circulation is immediately east of the aircraft flight path. Farther north, the flight-level wind observations indicate a cyclonic circulation was centered near 27.5^{o}N, 126.9^{o}E. Finally, turning of the winds north of 27.7^{o}N indicate a third cyclonic circulation to the northeast of the flight path. The combination of the wind observations north of 27.5^{o}N and the southerly wind observations along 29°N suggests that the trough in the ECMWF analysis should be shifted to the north-northeast. At the location of the trough in the analysis, two smaller-scale cyclonic circulations were defined by the aircraft flight-level data.

d.   *Flight-Level Thermodynamics*

As the WC-130J approached the area of deep convection (Fig. 35a), the temperature increased at the flight level of 300 hPa. The flight-level temperature was

-27°C between 0009-0041 UTC 17 September 2008. The temperature then increased to -26°C between 0041:30-0052:30 UTC 17 September 2008. Between 0053:00-0059:30 UTC 17 September 2008, the temperature increased again to -25°C, and then to -24°C between 0100:00-0101:30 UTC 17 September 2008. This 3°C increase over the initial flight-level temperature occurred in the immediate vicinity of the convective tower and before the aircraft commenced the climb to 275 hPa (10.3 km). Beyond the tower (on the northwest side), a cooling trend was evident at the higher altitude. Temperatures at 275 hPa were at -31°C for 7 minutes (0108:30-0115:30 UTC 17 September 2008), and then decreased to -32°C for 10 minutes (0116-0126 UTC 17 September 2008). On the approach to the tower as well as during the ascent around the tower, the WC-130J flight-level dew-point temperatures were occasionally coded as missing. As indicated above, this often indicated periods of supersaturation, and the flight-level temperatures at this time may be suspect (Zipser et al. 1981; Eastin 2002a,b). However, the unaffected data (Fig. 35b) substantiate the 3°C increase in the temperature at 300 hPa in the vicinity of the deep convective tower.

Two dropwindsondes were released from the WC-130J as the aircraft exited the convective region (between the "0100" and "0120" times marked along the WC-130J flight path in Fig. 35a). Since the aircraft was at a higher flight level along this segment, these dropwindsondes provided temperature observations near 300 hPa. The 0109 UTC 17 September 2008 dropwindsonde (Fig. 30a) indicated -26.54^{o}C near 300 hPa (see the blue asterisk along the right vertical dashed line in Fig. 35b). This temperature was a 2.5^{o}C decrease from the flight-level temperature observed near the center of the deep convection. Shortly thereafter, another dropwindsonde was deployed farther along the WC-130J flight path to the northwest. This 0122 UTC 17 September 2008 dropwindsonde (see the blue asterisk along the left vertical dashed line in Fig. 35b) measured an even lower temperature of -28.55^{o}C near 300 hPa. These dropsondes confirm that the highest temperatures at flight level were centered over the convective tower.

e. Summary of Large-Scale Aircraft Observations

Dropwindsonde and flight-level data enabled analysis of the TC circulation center as well as the outer TC circulation. From dropwindsondes on opposite sides of the TC center, the LLCC was estimated to be near 27.65°N, 126.38°E at 950 hPa, and the circulation center was tilted progressively southeastward with height through 600 hPa. A dropwindsonde with only thermodynamic data that was released at 27.51°N, 126.54°E, which is 22 km to the southeast of the estimated 950-hPa center, generally corroborated this estimation, with elevated Θ_e values and lower geopotential heights that extended to the mid-troposphere. At 500 hPa, the TC circulation was still generally circular and extended horizontally more than 400 km. By 300 hPa, the TC circulation had opened into a trough, and broad anticyclonic outflow extended northward from the TC. Also at 300 hPa, the WC-130J measured a 3°C increase in flight-level temperatures approaching the deep convective tower.

The dropwindsonde and flight-level data also identified other synoptic-scale features beyond the TC circulation. An extensive region of moist, southwesterly flow at lower levels was southeast of the TC along the southern edges of the banded convection remaining from the first convective episode and the remnant convection from the second episode. Anticyclonic flow at upper levels was also observed at the boundary between the TC circulation and the subtropical ridge northeast of the TC center and southeast of Japan. Perhaps the most revealing aspect of the WC-130J flight-level data was the identification of separate smaller-scale cyclonic circulations (Fig. 34b) to the east of the flight path and in the region of convection associated with the third convective episode.

2. ELDORA Observations

While dropwindsondes and flight-level data provide insight into the TC and broader environmental circulation characteristics, the ELDORA provides high-resolution observations that clarify the smaller mesoscale and convective structures in the immediate vicinity of the sheared and tilted TC vortex. The ELDORA observations between 0135-0205 UTC 17 September 2008 in the area between 27.0°N, 126.2°E and

29.0°N, 128.5°E (see flight path in Fig. 27a) reveal multiple vortices at varying levels and depths within various types of convection. At the southern end of this region, the Sinlaku circulation center tilts eastward (downshear) with height until it becomes centered over a linear band of deep convection (the third convective burst) with multiple towers reaching heights near 17 km. To the northeast in a region of older convection associated with the second convective burst, a large mid-level vortex is connected with a smaller mid-to-upper-level vortex that broadens with height and shifts southward to become centered over the northern edge of the deep towers that define the third convective burst.

The ELDORA observations are first mapped relative to the MTSAT brightness temperatures for comparison with the convective episodes described in Chapter III. Then, the dynamic properties associated with the various circulations will be analyzed to better understand the meso- and convective-scale structures, their relationships, and relative contributions to the re-development of Sinlaku. Thermal characteristics will then be deduced from the three-dimensional wind field and an environmental sounding, which produces virtual-cloud temperature perturbations that document the nature and extent of warm core associated with the Sinlaku vortex, the deep convective towers, and the two mid-level vortices to the northeast.

a.   *Comparisons with Satellite Data*

The third convective burst is identified by the low brightness temperatures in the 0145 UTC 17 September 2008 digitized MTSAT IR data between 27°-28.4°N, 126°-127.5°E (Fig. 36a). The minimum brightness temperature of 192 K is located near 27.5°N, 126.8°E in a line of deep convection that is oriented from west-southwest to east-northeast. To the northeast, the highest cloud tops associated with the second convective burst are oriented meridionally east of 127.7°E (Fig. 36a). In this region of older convection, minimum brightness temperatures are near 201°K, which is nearly 10 K higher than in the principle tower in the third convective region. The second and third convective bursts are separated by a meridionally-oriented band of higher brightness temperatures along 127.7°E.

93

The locations of the ELDORA reflectivity maxima near 40 dBZ match the locations of the minimum cloud-top brightness temperatures very well in the region of the third convective burst. At an elevation of 11.5 km (Fig. 36b), which is near 200 hPa, the maximum radar reflectivity (center of the third burst) is near 27.4^{o}N, 126.7^{o}E, which is within 15 km of the minimum brightness temperatures from the MTSAT digital data. The horizontal extent of this reflectivity pattern matches the distribution of higher brightness temperature and clearly defines the extent of upper-level anvil spreading almost radially from the convective center, as well as the break between the second and third convective bursts.

In the region of the second convective episode, the minimum brightness temperature near 28.0^{o}N, 128.0^{o}E was beyond the range of the ELDORA observations. However, the reflectivities that could be observed in the region of the older convection were much lower than those in the active convection to the south, and generally matched the pattern of brightness temperatures from the second convective episode.

At an elevation of 3 km (Fig. 36c), which is near 700 hPa, the two regions of high ELDORA reflectivity are closer together, but are still easily distinguishable. The core of the third convective episode was clearly defined by the linear band of high reflectivity over 45 dBZ between 27.4^{o}-27.5^{o}N (Fig. 36c). An area of reduced reflectivity along 27.6^{o}N corresponds to a break in convection between the third convective burst and the remnants of the second convective burst that extend from 27.6^{o}-28.6^{o}N to the northeast of the dBZ maximum. Over this region, the combination of higher brightness temperatures in the MTSAT data, low reflectivity values at upper levels (Fig. 36b), and relatively higher reflectivities at lower levels in the ELDORA data (Fig. 36c) suggest the change from convective to stratiform cloud structure (Houze 2004).

Houze et al. (2009) examined ELDORA reflectivity in a region of convection and stratiform cloud during the pre-Ophelia formation period. Vorticity stretching associated with a deep convective region, plus a broad region of mid-level vorticity within the extensive stratiform region, were observed within the pre-Ophelia environment. The pattern and magnitude of reflectivity in the region of the third convective burst are similar to those defined by Houze et al. (2009). Furthermore, the

lower reflectivity and higher brightness temperatures to the northeast of the third convective burst are indicative of stratiform precipitation (Yuter and Houze 1997, Houze 1997, 2004). Therefore, the reflectivity values in the second and third convective bursts suggest an equally rich and complex precipitation structure as defined by Houze et al. (2009) in the pre-Ophelia disturbance.

b. Dynamic Characteristics

(1) Winds and reflectivity. The location of the TC center identified by the WC-130J / P-3 dropwindsonde pair (Figs. 29-31) was further clarified by the ELDORA winds and reflectivity (Fig. 37). At an elevation of 1.5 km (Fig. 37a), which is near 850 hPa, the cyclonic circulation with an apparent center near 27.4^oN, 126.4^oE is the eastern half of the Sinlaku LLCC. East of the center, high reflectivity (>35 dBZ) associated with the third convective burst extended over 40 km along 27.45^oN and nearly 20 km southeastward along 126.6^oE. Directly northeast of the Sinlaku LLCC, the flow was uniformly southeasterly in a region of low reflectivity. A broad region of convection with reflectivities consistently between 30-35 dBZ and isolated regions exceeding 40 dBZ were found farther northeast of the LLCC. The winds in this region were also from the southeast.

The center of the Sinlaku LLCC was displaced progressively east-southeastward with increasing altitude. At an elevation of 3 km (Fig. 37b), which is near 700 hPa, the center was near 27.4^oN, 126.5^oE, which is just west of the deep convection. The circulation center was elliptical in shape with a principal axis to the east. Northeast of the deep convection along 27.45^oN (Fig. 37b), cyclonic turning indicates an axis of a trough near 28.0^oN, 127.3^oE, which is in the region of the second convective episode. Northeasterly winds on the west side of the trough axis represent a large shift from the southeasterly winds at 1.5 km (Fig. 37a). These northeasterlies extended southwestward to the linear band of deep convection where they converged with southerlies on the eastern side of the Sinlaku circulation center.

At an elevation of 5.5 km (Fig. 37c), which is near 500 hPa, the Sinlaku circulation center was displaced farther east-southeastward and was directly

associated with the deep convection at 27.38^{o}N, 126.70^{o}E. Although the ELDORA winds are only available in regions of elevated reflectivities, the TC circulation extends beyond the horizontal extent in these ELDORA observations. The cyclonic circulation was evident on three sides of the vortex – to the west, south, and east. Broad easterlies were absent north of the vortex, where northerlies extended southward from the west side of two mid-level vortices northeast of the TC center. These northerly winds also converged with the southerlies on the eastern side of the Sinlaku circulation in the region of deep convection along 27.4^{o}N between 126.8^o-127.0^{o}E. Notice the two mid-level vortices northeast of the TC center. The circulation about the mid-level vortex centered near 27.7^{o}N, 127.15^{o}E will be referred to as the central vortex. This central vortex at 5.5 km is above southeasterlies at 1.5 km (Fig. 37a) and a trough was 3 km (Fig. 37c).

Circulation about the northern mid-level vortex (the "northern vortex" hereafter) was centered near 27.9^{o}N, 127.3^{o}E. At 5.5 km this northern vortex is immediately adjacent to the central vortex. However, the radius of the cyclonic circulation about the northern vortex is near 30 km as opposed to near 15 km around the central vortex. Whereas the northern vortex was also in a region of high reflectivity associated with an isolated region of convection within the predominantly stratiform second episode, the central vortex circulation was in a region of much lower reflectivity.

At an elevation of 7.5 km (Fig. 37d), which is near 375 hPa, the reduced cyclonic flow around the Sinlaku center was now present only on the western and southwestern sides of the deep convection associated with the third convective episode. Strong northerlies were prevalent on the north and west sides of the convection. Southwest of the convection the winds did become northwesterly, but there was no longer a westerly wind south of the deep convection. Along the eastern side of the convection, southerlies were much stronger than at 5.5 km. As a result, convergence of these southerlies with northerly and northwesterly winds about the central vortex resulted in stronger westerly flow along 27.6^{o}N south of the central vortex, which had two effects. First, increased eastward turning of the strong southerlies defined an anticyclonic turning at the eastern end of the deep convection. Next, the increase in westerly winds enhanced the cyclonic flow about the central vortex, northeast of the deep convection. Farther to

the northeast (Fig. 37d), circulation around the northern vortex had disappeared as flow was southeasterly over that region (north of 27.8^{o}N) in conjunction with the cyclonic circulation around the central vortex that was much more broad at 7.5 km than at 5.5 km. Thus, the northern vortex was a shallow, mid-tropospheric mesoscale vortex that had an associated ELDORA reflectivity pattern at 5.5 km (Fig. 37c) but had diminished by 7.5 km.

Since 7.5 km is above the freezing level, a general decrease in the reflectivity associated with the convective towers along 27.4^{o}N has occurred. In particular, fewer areas on the western side of the convection exceeded 45 dBZ than there had existed at 5.5 km. Over the eastern half of the linear band, only two very small regions southeast of the primary convective line exceeded 35 dBZ. However, the near-meridional band of convection along 127.0^{o}E between 27.3^o-27.4^{o}N did have higher reflectivity than at 5.5 km, which may have been related to a stronger convective cell beyond the region of ELDORA coverage.

At an elevation of 9.5 km (Fig. 37e), which is a little below the plotted 300 hPa flight-level observations, the prominent cyclonic circulation present was about the central vortex, centered near 27.68^{o}N, 127.01^{o}E. Anticyclonic turning at the eastern end of the deep convection near 27.45^{o}N, 127.05^{o}E is consistent with the WC-130J flight-level winds about 40 minutes prior to the ELDORA observation of that region. The WC-130J flight-level winds were southerly between 27.45-27.5^{o}N, then turned southwesterly at 27.55^{o}N, then westerly at 27.58^{o}N, all of which were coincident with the anticyclonic flow at the eastern edge of the deep convection. As the aircraft continued north of 27.6^{o}N, the flight-level winds became northerly, which is generally consistent with the cyclonic circulation about the central vortex. Further weakening of the deep convection continued with only two small regions of reflectivities exceededing 40 dBZ. A second anticyclonic turning of the winds southwest of the high reflectivity region appears to be associated with the beginning of outflow from this deep tower associated with the third convective burst.

At an elevation of 10.5 km (Fig. 37f), the central vortex was displaced southwestward from 27.68^{o}N, 127.04^{o}E in conjunction with the flow on the

north side of the convective band along 27.5°N. While it is difficult to track the exact center of the central vortex above 10 km, the shift in the vortex center is evident in the westward and southern progression of the southerly and easterly winds to the east and north of the central vortex. On the broader scale, southerlies were evident east of 127.0°E, easterlies were still evident north of 27.67°N, and westerly winds were dominant in the southwest region of ELDORA coverage. By 11.5 km elevation (Fig. 37g), southerlies were prevalent east of 126.9°E and easterlies were evident north of 27.60°N, which indicated the central vortex had moved southwestward between 10.5-11.5 km. At 11.5 km, the vortex was centered at 27.56°N, 126.87°E, on the northern side of the deep convection and was surrounded by nearly symmetric cyclonic flow. The central vortex remained as a closed circulation over the region of deep convection through 12 km (not shown).

A dramatic transition to strong outflow in all quadrants at an elevation of 15 km (Fig. 37h) is documented by the ELDORA winds. Since this elevation corresponds to a pressure of 125 hPa, the re-intensifying Sinlaku circulation has an outflow layer that is characteristic of western North Pacific tropical cyclones. While the outflow to the southwest through northeast semi-circle will turn toward the midlatitudes and interact with the jet, the outflow in the opposite semi-circle will likely turn equatorward and serve as a second outflow channel. Such a dual outflow channel is generally considered to be favorable for intensification, and this highly divergent flow aloft is expected to lead to low-level convergence and spin-up of the vortex.

(2) Structure inferred from ELDORA observations. Based on the ELDORA winds and reflectivity, three cyclonic vortices were evident below 5.5 km in the region bounded by 27-28.2°N, 126.2-127.8°E. The southern vortex was the Sinlaku LLCC that tilted east-southeastward with height from 1 km to 5.5 km. At 5.5 km, the center of the Sinlaku circulation became connected with the circulation center associated with the deep convection of the third episode. This Sinlaku vortex circulation narrowed and became less symmetric with height. To the northeast, the central and northern vortices appeared to be connected within the low-to-mid level predominantly stratiform region of the second convective episode, but both remained separate from the southern

98

vortex at low levels. The northern vortex was above an open trough at low levels that became a closed circulation at 27.9°N, 127.3°E by 5.5 km. This vortex was limited in the vertical, as southeasterly flow existed over the northern vortex region by 7.5 km. The central vortex was initially defined by the cyclonic shear in the inverted trough, but by 4 km a separate closed circulation was discernable, and by 5 km the distinction between the northern and central vortices was very clear. However, the reflectivity in the region of the central vortex was smaller than that associated with the northern vortex. The central vortex circulation expanded with height and was coherent vertically through 9.5 km, before shifting southwestward and becoming centered over the northern side of the deep convection associated with the third convective episode at 11.5 km.

The eastward tilt with height of the convection associated with the Sinlaku lower tropospheric circulation and the deep convective tower is evident in a vertical cross-section of reflectivity along 27.4°N (Fig. 38a). The region of reflectivity exceeding 30 dBZ tilts eastward with height from 1 km through 5.5 km before extending upward to 16 km. Within that slanted-then-upright region of reflectivity greater than 30 dBZ, four regions of reflectivity exceeding 40 dBZ are found. The westernmost 40-dBZ tower reaches 3 km in height, while the eastern three extend to over 8 km.

The towers of reflectivity evident in the meridional cross-section along 126.9°E (Fig. 38b) are predominantly upright in the vertical. The deepest tower of high reflectivity is near 27.5°N, which is just north of the zonal cross-section at 27.4°N in Fig. 38a. Within that deep tower, the maximum reflectivity of greater than 50 dBZ is at 2 km. The portion of the tower exceeding 40 dBZ does exhibit a very slight tilt to the south. To the north, the region of higher reflectivity near 27.6°N associated with the northern vortex is evident from 27.75°-28.0°N between 2-4 km in height. A region of moderate (25-35 dBZ) reflectivity exists between the deep tower to the south and the shallow regions of higher reflectivity to the north appeared in the 3-km plan view (near 27.63°N, 126.9°E in Fig. 37b) at the very northern edge of the third convective burst. Reflectivity at low levels is reduced over 27.7°N, which is the latitude of the central vortex. There is also an overall absence of reflectivity at mid-levels on the northern side of the cross-section that corresponds with the cloud-free flight levels observed at 0140

UTC 17 September 2008 (Fig. 28). When the P-3 passed 28.0°N, 126.9°E at 0149 UTC 17 September 2008, it was in the cloud-free region beneath the anvil spreading from the third episode of deep convection (defined by the low reflectivity above 6 km) and above the stratiform region associated with the second convective episode.

The vertical cross-section of reflectivity oriented southwest-to-northeast in Fig. 38c from the eastern side of the tilted Sinlaku vortex passes through the central and northern vortices to the northeast (see the dashed lines in Fig. 37). The deep convective towers that define the third convective burst are evident as multiple cores of high reflectivity with values consistently in excess of 35 dBZ through 12 km at 126.7°E and 126.8°E. A maximum reflectivity in excess of 50 dBZ exists at 4 km near 126.75°E. The break between the third and second episodes of deep convection that was evident in the satellite data at 27.6°N (Fig. 36c) is evident in this cross-section near 126.93°E. To the northeast (right side, Fig. 38c), the general region of stratiform cloud has a region of high reflectivity that extends to 6 km between 127°E and 127.24°E. The convective core near 127.43°E extends to 8 km. A more stratiform region of weaker reflectivity to 6 km exists to the northeast.

The structural characteristics of these features, as well as the relationships among them, will be examined in terms of vorticity, vertical motion and divergence. In the subsequent section, the thermodynamic characteristics related to these circulations will be evaluated.

(3) Relative vorticity. The relative vorticity in the ELDORA winds is calculated from an analysis with a horizontal grid size of 500 m. At low levels (Fig. 39a), the only region with significant positive relative vorticity was near the Sinlaku LLCC, where values were generally between $1\text{-}3*10^{-3}\text{s}^{-1}$. Within that broad region, much smaller regions with much greater vorticity (e.g., near 27.45°N, 126.6°E) were co-located with the embedded deep convective towers (indicated by higher reflectivity in Fig. 37a). Very small values of positive or negative relative vorticity were present in the nearly uniform southeasterly flow northeast of the Sinlaku LLCC. This is a region beneath the central and northern vortices (Figs. 37a-c) and within the predominantly stratiform region of the second convective episode (Fig. 38c).

By 3 km (Fig. 39b), the maximum positive relative vorticity extended eastward in association with the deep convection along 27.45^{o}N. Isolated regions of negative vorticity were interspersed among the centers of high positive vorticity. To the northeast, a broad region of lower values of positive relative vorticity was associated with the trough that was below the mid-level central and northern vortices. The maximum positive vorticity in this region was located at the poleward end of the trough and in the vicinity of the northern vortex near 27.9^{o}N, 127.3^{o}E.

This pattern of larger positive vorticity values over a smaller region of deep convection in the southern vortex and smaller positive vorticity values over a larger region of the adjoining central and northern vortices continued through 5.5 km (Fig. 39c). In the region of the southern vortex and deepest convection near 27.35^{o}N, 126.7^{o}E, relative vorticity values exceeded $4*10^{-3}$ s^{-1}. The positive relative vorticity values were also larger over the region of the central and northern vortices.

At 7.5 km (Fig. 39d), relative vorticity in the vicinity of the northern vortex is greatly diminished as the winds over the region where the northern vortex had been became southeasterly. An increase in the magnitude of positive relative vorticity is analyzed 27.7^{o}N, 127.05^{o}E, which is near the central vortex center. To the southwest, couplets of highly positive and highly negative relative vorticity are analyzed in the area of the third convective burst. Notice the couplet of positive and negative relative vorticity near 27.5^{o}N, 127.0^{o}E, which is at the eastern end of the line of convection. On the eastern side of the couplet, the negative relative vorticity is associated with the anticyclonic turning of the southerlies on the eastern side of the deep convection as they converge with the northerlies originating west of the central and northern vortices and result in westerlies south of the central vortex. On the western side of the couplet, the positive vorticity is associated with a region of high reflectivity (Fig. 37d).

At 9.5 km (Fig. 39e), couplets of strongly positive and negative vorticity remained prevalent in the region of the deep convection. In addition to the large couplet at the eastern end of the convection near 27.5^{o}N, 127.0^{o}E, a region of negative vorticity is also found at 9.5 km at the southwestern edge of the deep convection between

27.4^{o}N, 126.6^{o}E and 27.26^{o}N, 126.75^{o}E, which corresponds to the southward turning of the northwesterly winds on the southwest side of the deep convection.

To the northeast beyond the deep convection, the positive vorticity in the region of the central vortex near 27.7^{o}N, 127.0^{o}E is reduced in magnitude and slightly in horizontal extent compared to the relative vorticity associated with that vortex at 7.5 km (Fig. 39e). A region of positive relative vorticity is present between 27.5-27.6^{o}N, 127.0-127.1^{o}E close to the negative half of the vorticity couplet at the eastern end of the deep convection associated with the third convective episode. Farther to the northeast, little positive vorticity remains in the region of the northern vortex.

At 10.5 km (Fig. 39f), the positive vorticity associated with the central vortex is displaced southwest of the position at 9.5 km (Fig. 39e), and is adjacent to the couplet of strongly positive and negative vorticity at the eastern end of the deep convection associated with the third convective burst. This shift parallels the southwestward progression of the central vortex circulation at that level (Fig. 39f). Southwest of the deep convection, the large region of negative relative vorticity extending northwest to southeast at the edge of the deep convection is of greater magnitude and horizontal extent than at 9.5 km (Fig. 39e), which may be attributed to the westward turning of the northerly winds near 27.15^{o}N between 126.6-126.75^{o}E in Fig. 37f.

The dominant relative vorticity at 11.5 km (Fig. 39g) is in the region of the third convective burst. Irregular couplets of strongly positive and negative relative vorticity are again prevalent. The strong negative vorticity to the southwest is associated with the southern outflow that sharply turns anticyclonically to become poleward flow along the western edge of the domain (Fig. 37g). On the northeast side of the deep convection, strong positive vorticity is dominant, which coincides with the location of closed circulation of the central vortex that is over the northern side of the deep convection. Even though the extreme outflow at 15 km in Fig. 37h appears to be dominated by divergent wind components, embedded within the region of the convective burst are cores of large positive vorticity (Fig. 39h). Some streamers of alternating

positive and negative vorticity seem to extend outward in the northwest quadrant, while the outflow to the south has more consistently negative (anticyclonic) vorticity.

In a vertical cross-section of relative vorticity along the TC latitude of 27.4^{o}N (Fig. 40a), the weaker positive relative vorticity noted in the vicinity of the TC vortex at low levels (Figs. 39a-b) is evident between 1-5 km from 126.5^o-126.6^{o}E. Furthermore, the eastward tilt with height is similar to the tilt in the reflectivity (Fig. 38a). This region of tilted positive relative vorticity merges at 6 km with the more vertically oriented positive vorticity center associated with the deep convection over 126.65^{o}E. A single tower of positive relative vorticity then extends to above 14 km. Just to the east, a second tower near 126.75^{o}E extends from near 4 km to above 14 km. Two other regions of vertically upright vorticity maxima begin near 8 km and also extend to above 14 km. Isolated coherent towers regions of negative relative vorticity of varying depths exist among these towers of positive vorticity. It is noteworthy that these coherent towers of relative vorticity begin at elevations that are progressively higher to the east along the cross-section, which was also a feature in the reflectivity maxima in Fig. 38a.

The slightly southward tilt with height that was evident in the higher reflectivity associated with the third convective burst (Fig. 38b) is also evident in the large tower of positive vorticity near 27.48^{o}N (Fig. 40b) in the meridional vertical cross-section of relative vorticity along 126.9^{o}E. This deep tower of positive relative vorticity extends from 2-13 km in height, and to the north there is a second tower of much weaker positive vorticity. In this second tower, positive maxima occur near 2 km, 6 km, and 10 km, and this feature connects with an upper level vorticity maximum to the north that extends from 7-15 km.

At lower levels to the north (Fig. 40b), a region of strongly positive relative vorticity near 27.9^{o}N extends in the vertical between 1.5-4 km. As in the horizontal display at 27.9^{o}N, 126.9^{o}E in Figs. 39a-b, this positive vorticity region is also only a few km in diameter and is among scattered regions of positive and negative vorticity within the southeasterly flow at 1.5 km and northeasterly flow on the west side of the trough at 3 km, which is below and to the west of the northern vortex. While prominent in this vertical cross-section and associated with elevated reflectivity at lower

levels, circulation near this couplet appears to be influenced more by the northern and central vortices than by the couplet (or coincident reflectivity). The apparent absence of relative vorticity between 4-6 km at the northern end of the meridional vertical cross-section (Fig. 40b) coincides with the absence of reflectivity (Fig. 38b) in the region, and therefore is indicative of missing data, rather than near zero relative vorticity.

In the southwest-to-northeast vertical cross-section of relative vorticity that extends from the eastern side of the tilted TC vortex through the central and northern vortices (Fig. 40c), coherent towers of positive vorticity in excess of $4.0*10^{-3}$ s^{-1} throughout the column are associated with the deep convective towers in the third convective burst. Between these regions of strongly positive relative vorticity are regions of strongly negative relative vorticity that are also oriented nearly vertically and at varying levels. In the region of the second convective episode to the northeast, the positive relative vorticity associated with the central vortex near 127.05^{o}E has maximum values in excess of $0.5*10^{-3}$ s^{-1} that begin near 3 km in height, which is consistent with the plan view at 3 km in Fig. 39b, and extend through 8 km. This structure is consistent with a mid-tropospheric mesoscale vortex that decays upward and downward. Above 8 km, the maximum begins to extend southwestward through 11.5 km, which is also consistent with the plan views between 5.5-11.5 km in Figs. 39c-g. Farther to the northeast (Fig. 40c), the positive relative vorticity maximum associated with the northern vortex is between 3-5.5 km near 127.4^{o}E, which is consistent with the depiction of that feature in the plan views (Figs. 39b-c). A region of negative relative vorticity is above the northern vortex circulation between 8-10 km in height.

In summary, four vorticity features (Sinlaku lower tropospheric circulation, mesoscale circulations associated with the deep convection, central vortex, and northern vortex) can be identified from the ELDORA winds. Comparisons of these features with the corresponding reflectivity indicates which of these features are coincident with the "new" and "old" convective regions at low levels and how they are connected at upper levels. Specifically, the vorticity features associated with the Sinlaku circulation and the deep convection comprised one region, while the central and adjoining northern vortices comprised a separate region to the northeast. The relative

vorticity in Sinlaku and the convective towers had a broad region of small positive relative vorticity from near the surface to 5 km that decreased in areal extent with elevation, but increased in magnitude. The embedded regions of consistently high positive relative vorticity associated with deep convective towers extended 16.5 km into the atmosphere. These narrow regions of positive vorticity were interspersed with regions of large negative relative vorticity through most of the column. By contrast, the second region to the northeast had smaller values of positive relative vorticity in the regions of the central and northern vortices from 3-5.5 km (near 700-500 hPa) without interspersed regions of negative vorticity. Above 5.5 km, the positive vorticity signal over the weakening northern vortex decayed. However, over the central vortex, relative vorticity continued to increase through 9.5 km (near 300 hPa). Above 9.5 km, the vorticity of the central vortex extended southwestward and was over the northern side of the deep convection by 11.5 km.

(4) Vertical motion. In the processing of the ELDORA data, an ascent/descent couplet was noted in the winds above the flight level along the flight track that amplified with increasing height. Even after additional quality control measures were applied to adjust for possible aircraft errors (Bosart 2002), low confidence remained in the ELDORA winds in the vicinity of the flight track, and thus these winds were removed at all levels for both the divergence and vertical motion calculations. Fortunately, nearly all of the eastern Sinlaku circulation, the deep convection, and the central and northern vortices were east of the affected regions.

Vertical motion calculations at 1.5 km and 3 km (not shown) revealed the presence of downward vertical motion on the southern side of the Sinlaku low-tropospheric circulation (along 27.3^{o}N) beneath regions of high reflectivity (i.e., precipitation). However, ascent was present at 5.5 km associated with the deep convection in this third convective burst (Fig. 41a). On the west side of the deep convection, strong upward motion is present between 27.3-27.45^{o}N and 126.6-126.8^{o}E, which coincides with the elevated reflectivity in that region (Fig. 37c). Strong ascent is also present at the east end of the deep convection along 127.0^{o}E that is associated with the high reflectivity in that region (Fig. 41c). To the northeast, only a small, isolated

upward motion near 27.95^oN, 127.40^oE is found with the region of high values of reflectivity on the northeast side of the northern vortex. An extended region of descent with magnitude of 2-3 m s^{-1} is calculated along the northwestern edge of the domain.

At 7.5 km (Fig. 41b) and 9.5 km (Fig. 41c), the distribution of vertical motion is very similar to that at 5.5 km (Fig. 41a). Widespread ascent with increasing magnitudes exists in the deep convection to the south. As indicated previously, this convective region tilts eastward between 5.5 and 9.5 km. At 11.5 km (not shown) and 13 km (Fig. 41d), the magnitude of the ascent in the deep convection to the south continues to increase. Furthermore, ascent increases in the region between the central vortex and the southern convective region. At 15 km (not shown), there is still ascent over the deep convection of the third burst, but the magnitude is reduced. The beginning of the outflow toward the south from this region of strong ascent is evident at 13 km.

The distribution of vertical motion in the zonally-oriented vertical cross-section along the TC latitude of 27.4^oN (Fig. 42a) reveals a slight eastward tilt with height between 4-9 km in the westernmost tower and an increase in upward vertical motion with height in each of the deep towers of the third convective episode. At the base of the deep towers, regions of downward vertical motion are present presumably due to evaporation of deep convection. The largest vertical motion exceeds 30 m s^{-1} between 9-12 km in the region of ascent near 126.7^oE within the ascent region that extends from 3-16.5 km. Just west of this deep region of ascent there is an equally deep region of descent that may result from evaporation of precipitation air adjacent to the deep convection. To the east, a broad layer of mid-level ascent is present over the eastern end of the deep convection that coincides with the elevated reflectivity (Fig. 38a) as well as the divergence (Fig. 44a) in that region. As identified in the cross-section of relative vorticity (Fig. 40a), the initiation elevation of each primary updraft increases to the east, which reflects the tilted TC structure identified by the aircraft and ELDORA winds.

The meridional vertical cross-section of vertical motion along 126.9^oE (Fig. 42b) also has a region of maximum ascent near 10 km in the deep convective towers near 27.5^oE. To the north, alternating regions of downward and

upward vertical motion occur, which may coincide with regions of banded convection with subsidence adjacent to the towers. Little ascent or descent is noted in the region of the central vortex (near 27.7°N) or in the region of the northern vortex (27.9°N).

Even though a region of ascent between 2.5 km and 9.5 km exists near 127.4°E in Fig. 42c, the southwest-to-northeast vertical cross-section of vertical motion (Fig. 42c) again has alternating regions of deep ascent and descent over the region of deep convection, with the maximum ascent in upper levels as in Fig. 42a. Regions of descent are interspersed with the updrafts and in the deepest cases the magnitude of the descent increases toward the surface. Also of note, small values of descent are evident at low levels in the area of the central vortex (127.1°E), which may have resulted from precipitation beneath the stratiform cloud.

The magnitude of vertical motion in the regions of the central and northern vortices is notably less than that over the deep convection to the southwest. To better diagnose vertical motion in the vicinity of the northern and central vortices, the northeastern two-thirds of the southwest-to-northeast vertical cross-section is re-plotted with a smaller range of values (Fig. 42d). Deep regions of upward vertical motion associated with the northeastern edge of the convective towers are evident near 126.9-127.0°E. The central vortex, which is located between 127.0-127.1°E in this cross-section, has two regions of descending air with maximum values near 5 km. Above 7.5 km, where the central vortex circulation broadens (Fig. 37d), there is a region of weak ascent that extends southwestward with height through 10 km. At 10 km, the upward vertical motion over the central vortex connects with a region of stronger ascent to the southwest that is associated with the deep convection of the third convective episode. The region of ascent then arcs slightly northeastward. The northern vortex extends between 127.3°-127.5°E in this cross-section has a region of ascent (noted also in Fig. 42c) with a maximum between the levels of 3-7.5 km, which generally coincides with the depth of that circulation.

(5) Divergence. Little convergence or divergence is evident at the lower levels (not shown), although convergent/divergent couplets are present, particularly on the northeastern side of the Sinlaku LLCC along 27.5°N. At 3 km (not shown),

increased convergence is present in the region of deep convection between 27.4^o-5°N, 126.6^o-8°E, which is the arc where the wind shifts from the southwesterlies to northeasterlies across the trough. These winds on the western side of the trough axis converged with the southeasterlies on the northeast side of the Sinlaku lower tropospheric circulation near 27.5^{o}N, 126.8^{o}E, and then the flow became easterly along 27.5^{o}N. The flow to the north also resulted in convergence east of the wave axis under the northern vortex near 28.0^{o}N, 127.4^{o}E, and divergence west of the wave axis near 28.1^{o}N, 127.2^{o}E.

At 5.5 km (Fig. 43a), mesoscale convergence into the deep convection associated with the third convective burst is consistent with the increasing magnitude of the updrafts above this level. At the eastern end of the line of convection along 27.5^{o}N between 126.9-127.0^{o}E, the convergence was smaller than at 3 km, where the southerlies around the Sinlaku LLCC had converged with the northeasterlies around the central vortex. In addition to the convergence along the northern side of the northern vortex, northerly flow west of the northern vortex converged with the northeasterly flow on the northwest side of the central vortex and resulted in a broad area of convergence.

The largest change in the distribution of divergence at 7.5 km (Fig. 43b) was at the eastern end of the deep convection where a convergent/divergent couplet existed in the region of the cyclonic/anticyclonic couplet in Fig. 39d. Divergence on the eastern side of the couplet appears to result from the diffluence of southerlies and southwesterlies near 27.4^{o}N, 127.0^{o}E. The convergence to the west side is likely the result of these southwesterlies interacting with northwesterlies near 27.5^{o}N, 126.95^{o}E. Convergence at 27.6^{o}N, 127.15^{o}E south of the central vortex is analyzed between the southerlies at the eastern end of the deep convection and the northwesterlies southwest of the central vortex. Convergence was also analyzed on the west side of the central vortex between the northerly flow west of the circulation center and strong northwesterly winds to the northwest. Some small divergence is analyzed between 28.0^o-28.1^{o}N along 127.4^{o}E over the region associated with the northern vortex.

Strong divergence at 13 km (Fig. 43c) is evident in the southern outflow from the deep convective towers associated with the third convective episode. Highly divergent outflow is also analyzed near 27.5^{o}N, 126.9^{o}E. An isolated region of

strong divergence near 27.9^{o}N, 127.45^{o}E is associated with the outflow above the convection in the region of the northern vortex, which dissipates almost completely by 15 km (Fig. 43d). The divergence in the region of the deep convection, however, continues to increase at 15 km, where there is a vast expanse of divergence with values averaging near $5*10^3$ s^{-1} and narrow columns exceeding $15*10^3$ s^{-1}. Maximum values of divergence extend along 27.4^{o}N between 126.65^o-126.9^{o}E and are associated with outflow toward the southwest. The northern side of the dual outflow channel is associated with a second region of maximum divergence located along 27.5^{o}N between 126.8^o-127°E.

In the zonal vertical cross-section along 27.4^{o}N (Fig. 44a), multiple tilted regions of alternating strong divergence and convergence regions are analyzed in the area of deep convection, which is the same region of tilted reflectivity (Fig. 38a), relative vorticity (Fig. 40a), and vertical motion (Fig. 42a) values. Although convergence is a maximum in the lower troposphere, the frictionally-induced convergence is not evident in these ELDORA observations. However, the large divergence aloft was revealed, particularly above 12.5 km. The region of strong divergence near 127°E is the divergent portion of the convergent/divergent couplet at the eastern end of the line of deep convection associated with the third convective episode (Fig. 37). Absence of a corresponding convergence area below may be due to missing observations or a tilted updraft that is not in the plane of this cross-section. The strongly divergent outflow at upper levels is also evident in the meridional cross-section along 126.9^{o}E (Fig. 44b) between 10-14 km over 27.5^{o}N, where there were also multiple convergent/divergent couplets of varying sizes.

Alternating towers of strong divergence and convergence are analyzed in the southwest-to-northeast cross-section (Fig. 44c). As in the zonal cross-section, convergence is prevalent at the lowest levels and divergence is strongest at upper levels. At the northeastern end, there is a broad region of mid-level divergence over the region of the northern vortex, with weak convergence at low levels, which may result from developing convection. As was the case with the vertical motion field, the magnitude of divergence is much greater in the region of the deep convection (left side in

Fig. 44c) than in the regions of the central and northern vortices (right side in Fig. 44c). Therefore, an expanded view with a smaller range of divergence values is given in Fig. 44d. In the region of the central vortex near 127.05E in Fig. 44d, divergence is analyzed at low levels beneath the central vortex circulation. Although a weak convergence maximum near 7 km seems to be connected to the southwest and to the northeast at upper levels, divergence becomes prevalent above 10 km.

In the region of the northern vortex, convergence exists at low levels below 4 km, but an extensive region of divergence occurs above 5 km. This vertical profile of convergence and divergence is consistent with the maximum in vertical motion around 5 km (Fig. 42d) and vorticity (Fig. 40c). The increased depth in reflectivity (Fig. 38c) suggests that some localized convection existed in this region that may have contributed to the maintenance of the northern vortex.

c.   *Thermodynamic Characteristics*

Reflectivity is the only indicator of thermodynamic activity that is directly measured by the ELDORA. However, utilizing the dynamic parameters measured directly (Doppler winds), other thermodynamic data may be derived (Roux and Ju 1990; Roux et al. 1993; Reasor et al. 2009). Here, the virtual-cloud temperature perturbation, a virtual temperature that includes contributions from the cloud water content and water vapor perturbation, is calculated to reveal the relative temperature distribution among the features analyzed from the dynamic data (the Sinlaku lower tropospheric circulation, deep convection, and the northern and central vortices). The mass transport field will then be analyzed as it has been shown to be an effective proxy for latent heat release (Ooyama 1982, Davis et al. 2008).

(1) Temperature perturbations. Calculation of the virtual-cloud temperature perturbations relies on an accurate assessment of the vertical motion. Since the vertical motion was determined to be of low confidence in the vicinity of the flight track, the temperature perturbations are not calculated in that region. The temperature perturbations are also assessed relative to a composite environmental sounding. An upper air sounding was selected downstream from the region of the convective episodes

(Minami Daito Jima (ROMD) at 0000 UTC 17 September 2008), and was merged as in Houze et al. (2009) with profiles from two aircraft dropwindsondes in the vicinity of the TC (dropwindsonde B and the WC-130J dropwindsonde released at 0122 UTC 17 September 2008 near 28.93^{o}N, 126.04^{o}E).

At 1.5 km (Fig. 45a), a large positive temperature perturbation is calculated in the region of the Sinlaku LLCC, which indicates that the circulation is substantially warmer than the surrounding environment. To the northeast, alternating regions of small positive and negative temperature perturbations are calculated within the southeasterly flow beneath the northern and central vortices.

At 3 km (Fig. 45b), the Sinlaku lower tropospheric circulation continues to be warmer than the surrounding environment. To the northeast, a broad region of slightly warmer temperatures is associated with the trough. The maximum temperature in that region is near the apex of the trough, which is close to the center of the northern vortex at 5.5 km (27.9^{o}N, 127.3^{o}E).

The distribution of temperature perturbations at 5.5 km (Fig. 45c) is similar to that of the relative vorticity (Fig. 39c), in that there are much higher values localized over a small region in the vicinity of the TC and deep convection, and less-positive values over a broader region to the northeast in the vicinity of the northern and central vortices. Small regions that are much warmer than the surrounding environment are associated with the convective towers and Sinlaku vortex. A broad warm region is evident to the northeast that is associated with the central vortex.

At 7.5 km (Fig. 45d), isolated regions of maximum temperatures are prevalent in the deep convection, particularly near 27.4^{o}N, 126.67^{o}E, which is within a region of elevated reflectivity (Fig. 37d), relative vorticity (Fig. 39d), and ascent (Fig. 41d). Two other regions within the third convective burst are also warmer than the surrounding environment. These warm anomalies near 27.4^{o}N, 127.5^{o}E and near 27.4^{o}N, 126.95^{o}E also coincide with regions of elevated reflectivity, vorticity, and upward motion. These three regions of much warmer temperatures are even more evident at 9.5 km (enclosed by the white 2°C temperature perturbation contours in Fig. 45e)

111

between 27.4°-27.5°N, 126.7°-127.0°E. For comparison, the WC-130J flight-level temperatures (Fig. 35b) increased 3°C as the aircraft approached and passed the deep convection. Similar warm anomalies detected at the WC-130J flight level 40 minutes prior to the ELDORA observations are also calculated in the virtual-cloud temperature perturbations derived from the 3-D wind field. A significant cold anomaly first appears at 9.5 km (Fig. 45e) along 27.4°N near 126.65°E. This warm/cold couplet is in the same vicinity as the vorticity and divergence couplets. Another cold anomaly over a larer horizontal area is calculated to the southwest of the deep convective area. To the northeast, the regions of the northern and central vortices continue to be warm, but are less so than at 7.5 km (Fig. 45d).

At both 10.5 km (Fig. 45f) and 11.5 km (Fig. 45g), the warm anomalies in the vicinity of the northern and central vortices are further reduced. However, lower perturbation temperatures prevail on the southwest side of the deep convection that are coincident with the anticyclonic circulation. Within the deep convective region, three temperature perturbation relative maxima are again in regions of increased reflectivity, vorticity, and upward motion.

By 15 km (Fig. 45h), nearly the entire region of the third convective episode is cooler than the temperatures at the same level in the environmental sounding, which may be related to the tropopause height. Assuming the deep convection may have resulted in a higher tropopause height due to possible overshooting tops in the region, this would have resulted in comparatively lower temperature perturbations relative to the environmental sounding at upper levels above the deep convective region.

In the zonal vertical cross-section of temperature perturbations along the TC latitude of 27.4°N (Fig. 46a), the shading scale has been doubled to more effectively illustrate the features within the cross-section. As in the zonal vertical cross-sections of reflectivity, vorticity, vertical motion, and divergence, the temperature perturbations also are tilted eastward with height along 27.4°N. Broad warming is prevalent beneath 6 km, and two towers with positive temperature perturbations extend to 12 km and 11 km in the atmosphere. These vertically tilted warm regions coincide with similar structures in relative vorticity (Fig. 40a), upward motion (Fig. 42a), and

convergence (Fig. 44a). The broad region of warming beneath 6 km is consistent with the presence of the inner Sinlaku circulation through that level, although the maximum temperature perturbation at 4 km near 126.8^{o}E may be questionable due to its proximity to the border. Away from the borders, the maxima in the western tower are near 8.5 km and 12 km and have contrasting minima at proximal levels to the west.

In the meridional cross-section along 126.9^{o}E (Fig. 46b), the contour scale is again the standard as in previous plots. Again, a broad region of higher temperature perturbations is associated with the Sinlaku circulation through 6 km. Above that, a tower that is warmer than its surroundings exhibits a slight tilt to the south through 11.5 km, then tilts northward through 12 km. To the north, a broad region of mid-level warming is calculated with, and a maximum at 5 km at the latitude of the central vortex (27.7^{o}N). This maximum is also on a boundary and thus may be suspect.

In the southwest-to-northeast cross-section through the east end of the Sinlaku circulation, the deep convection, and the central and northern vortices (Fig. 46c), the large gradients at the upper and lower boundaries and the two small minima along the surface near 126.85^{o}E and 127.50^{o}E are artifacts of the plotting technique. The very warm region to the southwest in the vicinity of the deep convection is associated with the Sinalku circulation through 6 km. Above the broad region, towers warmer than the surrounding environment extend to over 12 km. Adjacent to these towers at upper levels are regions of cooler air. To the northeast, in the vicinity of the central vortex (127.1^{o}E), the warm anomalies are at mid-levels. Farther to the north, larger warming at 4 km in the region of the northern vortex near 127.4^{o}E at the corresponding levels of that circulation (between 3-5.5 km) (Figs. 37b-c). Farther to the northeast, colder air is prevalent between 3-5.5 km.

From these temperature perturbations, it is evident that the region of the organized inner Sinlaku circulation is warmer than the surrounding environment. Above 5.5 km, where the Sinlaku inner circulation is far less well-defined, the convective towers are in the regions of warm anomalies, with maximum positive temperature

113

anomalies near 8.5 km and 12 km. Broad regions of warm anomalies are prevalent in the regions of the central and northern vortices, with maxima in those regions between 4-6 km.

(2) Mass Transport. As a proxy for latent heat release, the vertical gradient of mass transport may be used to roughly identify regions where PV is being concentrated or diluted (Ooyama 1982, Houze et al. 2009). Mass transport (ρw) is determined using the environmental density, which is calculated by fitting an exponential curve to the density profile determined by the environmental sounding. As in the vertical motion fields, the mass transports are not calculated in the vicinity of the flight track.

Since the mass transport is just the vertical motion multiplied by the density, the plan-view pattern of mass transport is the same as the vertical motion pattern (Fig. 41) and thus these plan views are not shown. Similarly, the pattern of mass transport in the zonal vertical cross-section along 27.4^{o}N (Fig. 47a) will be the same (e.g., the regions of positive mass transport are tilted eastward with height just as in the vertial motion cross-section in Fig. 42a. The multiplication by density shifts the maximum upward mass transport downward to between 8-11 km within the westernmost tower of elevated reflectivity (Fig. 38a) and upward vertical motion (Fig. 42a). Similar downward shifts in the maximum upward mass transport occur for the adjacent tower to the east that extends between 2-13 km and the region of upward vertical motion that is coincident with the eastern band of elevated reflectivity (Fig. 38a) along 127.0^{o}E. Multiplying with the density makes the low-level descent regions relatively larger (e.g., the downward mass transport on the west side of the deep convection in Fig. 47a). Similar changes of shifting downward the maxima of upward and downward mass transport compared to the levels of maximum ascent and descent in Fig. 42b and c are found in the meridional vertical cross-section along 126.9^{o}E (Fig. 47b) and in the southwest-to-northeast vertical cross-section of mass transport (Fig. 47c).

In each cross-section in Fig. 47, it is clear that PV is being produced at levels below the maximum in upward mass transport in the deep convective area. However, the destruction of PV in the adjacent downward mass transport is more

emphasized than might be inferred from the vertical motion field. To a lesser extent, PV is being produced at mid-levels over the central vortex and at low levels over the northern vortex.

d.   Circulation Structure Based on ELDORA Observations

At each level above 1.5 km, the Sinlaku circulation was affected in various ways by circulations associated with convection at various stages from the second and third convective episodes. The eastern half of the TY Sinlaku lower tropospheric circulation was the prominent feature in the lowest levels of the ELDORA analysis, while to the northeast there was uniform southeasterly flow. At 3 km, the low-level trough to the northeast had southeasterlies reversing to become northeasterlies across the trough axis that converged with southerlies on the east side of Sinlaku and contributed to stronger easterlies north of the vortex. At 5.5 km, the Sinlaku center (which was tilted progressively east-southeastward with height) became embedded in the deep convection of the third convective episode. Strong northerly flow on the west side of two mesoscale vortices to the northeast resulted in strong northerly flow over the north side of the Sinlaku vortex. At 7.5 km, cyclonic flow about the Sinlaku vortex was only evident in the southwestern and southeastern quadrants in the ELDORA coverage. To the northeast, southeasterlies prevailed where the northern vortex had been at 5.5 km, so this vortex was a relatively shallow circulation. However, the central vortex continued to be well defined, in part due to convergence of northwesterlies southwest of the central vortex with southeasterlies at the northeastern end of the deep convection that resulted in enhanced westerly flow south of the central vortex. Thus, the central vortex was the primary circulation feature at 7.5 km. By 9.5 km, circulation around the central vortex was reduced and there was anticyclonic turning of the northwesterlies southwest of the deep convection (in what had been the southwestern quadrant of Sinlaku). At 10.5 km, the central vortex circulation was displaced southwestward closer to the region of the deep convection. Southwest of the deep convection, anticyclonic flow developed in response to the southern outflow from the deep convection. By 11.5 km, the dominant circulations were the anticyclone at the southwestern end, and the cyclonic central vortex

which was now located over the northeastern end of the deep convection. At 15 km, the ELDORA winds documented a dramatic radial outflow from the region of the deep convection with an indication of outflow channels both poleward toward the midlatitude jet and equatorward.

e. *Comparison with Other Aircraft Observations and ECMWF Analysis*

Comparison of the ELDORA analyses with the other aircraft data and ECMWF operational analyses described in Chapter III demonstrates the increasing complexity of dynamic and diabatic features with decreasing scale in the vicinity of the TY Sinlaku vortex. On the dynamic side, the multiple cyclonic and anticyclonic circulations of various sizes and at varying levels and in the immediate vicinity of the TC center from the ELDORA observations provide more detail than was possible from the flight-level winds of the WC-130J. While two cyclonic circulations were detected in the flight-level winds at 300 hPa in the deep towers of the third convective episode (a third cyclonic circulation was detected at 27^oN south of the ELDORA analysis region), three principle cyclonic features and two anticyclonic circulations were defined at various levels in the ELDORA observations. The principle cyclonic circulation centers detected in the ELDORA data include TY Sinlaku, which became centered over the deep convection at high elevations, and the northern and central vortices. The anticyclonic features were associated with the outflow region on the southwestern side of the deep convection, and the eastward turning of southerly flow that converged with northwesterlies at the eastern end of the deep convection. Both the ELDORA and WC-130J flight-level winds defined circulations that were different from the ECMWF analysis, which defined the Sinlaku circulation as the single circulation center in the region. Given the differences in resolution, this is somewhat expected. The mesoscale circulations detected by the ELDORA were often 30 km or less in diameter, which of course could not be resolved in the 0.25^o lat./long. ECMWF analysis.

A region of larger cyclonic relative vorticity was analyzed northeast of the ECMWF-defined TC center. The independence of these features at low levels and

subsequent connection at 400 hPa (Fig. 23) was incredibly similar to the southwestward progression of the central vortex to the southwest above 9.5 km in the ELDORA observations.

From a diabatic perspective, the ECMWF did not accurately resolve the spatial distribution of all three convective episodes in the +3-h precipitation accumulation fields from the ECMWF 0000 UTC 17 September 2008 operational analysis. The features associated with the first and second episodes were well-defined but the third episode of deep convection, which erupted essentially at the valid time of the analysis, was not distinct from the second convective episode. The maximum in convective precipitation accumulation in the ECMWF analysis was east-southeast of the Sinlaku LLCC, which correlates well with the location of the deep convective towers of the third convective episode. The maximum in stratiform precipitation accumulation was northeast of the TC in the ECMWF data, which coincides with the stratiform precipitation in the regions of the central and northern vortices on the north side of the second convective episode in the ELDORA and MTSAT IR data. Lesser values of convective precipitation accumulation were also found to the northeast in the ECMWF data, and this correlates well with the isolated regions of convection that were interspersed throughout the second convective episode region in the ELDORA data. The co-location of a near-vertical column of positive relative vorticity that then tilts southwestward with height with the stratiform precipitation accumulation region was also very similar between the YOTC ECMWF analysis and the central vortex in the ELDORA data.

The primary deficiency in the ECMWF analysis is in the separation of these features. In the model, the convective maximum is 200 km east-southeast of the TC center, and the stratiform precipitation / vorticity maximum is 200 km northeast of the TC center. In the ELDORA observations, the deep convection associated with the third convective episode is 25 km east and east-southeast of the Sinlaku LLCC, and the tower of mid- and upper-level vorticity associated with the central vortex is only about 75 km to the northeast of the Sinlaku mid-level pressure minima.

D. SYNTHESIS

The first TCS-08/T-PARC ET flight through the region of the re-intensifying Sinlaku and the deep convection associated with the third convective episode provided detailed observations of three inter-related cyclonic circulations associated with the convection. Deep convective towers associated with the third convective episode were adjacent to the Sinlaku center, and two regions of mid-level vorticity to the northeast were in the region of the predominantly stratiform convection remaining from the second convective episode. Various dynamic and diabatic parameters were evaluated in the region of the TY Sinlaku vortex and third convective episode at multiple levels in the horizontal and in several vertical cross-sections. In this section, each feature will be examined independently to more fully assess each structure.

Analyses in vertical cross-sections at the latitude of the Sinlaku center (27.4^oN) revealed an eastward tilt with height in reflectivity, vorticity, convergence, warm anomaly, and mass flux. Additionally, all these parameters were organized into distinct features and the initial level of each feature increased to the east, or with the vertical tilt. To examine the relationships among these parameters and more fully characterize the structure of Sinlaku and the third convective burst, wind vectors and relative vorticity contours are plotted over reflectivity values in a vertical cross-section (Figs. 48a). The most striking feature is the western-most area of high reflectivity that is associated with the western tower of deep convection. An updraft exceeding 40 m s^{-1} is analyzed within a region of $2*10^{-3}$ s^{-1} positive relative vorticity and reflectivity values greater than 35 dBZ. At the base of this tower, the region of positive relative vorticity (Figs. 40a and 48a) associated with the Sinlaku circulation center near 3.5 km along 126.57E tilts eastward with height and connects near 5 km with the $2*10^{-3}$ s^{-1} contour of positive relative vorticity that extends slightly westward with height from above the 45-50 dBZ region of reflectivity at 3 km along 126.67^{o}E. Recall that the height where the tilted Sinlaku circulation becomes centered in the deep convection is 5.5 km. The joining of these two relative vorticity maxima is coincident with convergence in the winds at 5 km. Convergence (Fig. 44a) is evident close to the eastern and western boundaries of the

$2*10^{-3}$ s^{-1} positive relative vorticity contour and is prevalent throughout the column in the vertical through nearly 12 km, and then divergence becomes dominant above this level.

This pattern is repeated in the eastern tower of elevated mid-level reflectivity (Fig. 48a) along 126.8^{o}E, but is somewhat weaker in magnitude. Positive relative vorticity exceeding $2*10^{-3}$ s^{-1} generally follows the 35 dBZ contour (although less closely), and upward vertical motion is prevalent throughout the column. Convergence values are smaller (Fig. 44a), but prevail through this column until 11 km and then divergence becomes dominant at higher levels.

At 126.72^{o}E, the center of the three towers of reflectivity in excess of 35 dBZ that extend to 12 km exhibits slightly different characteristics. Negative vorticity exists at mid-levels as opposed to positive vorticity throughout the region of elevated reflectivity. In this center region, the maximum upward motion occurs above 10 km. Below this level, divergence (Fig. 44a) exists as air is entrained into the two primary updrafts to the west and east.

Patterns described above in the eastward-tilted regions are also evident in a cross-section extending from the southwest to northeast (Fig. 48b) from 27.25^{o}N, 126.5^{o}E to 27.65^{o}N, 127.0^{o}E. This enlarged view of the deep convective towers is from the same transect as previous southwest-to-northeast cross-sections (along the dashed red lines in Fig. 37). In these cross-sections, deep towers of positive relative vorticity generally follow the maxima in reflectivity. The southwestern-most tower near 126.67^{o}E is the same tower as the western-most tower in the zonal vertical cross-section (Fig. 48a). In this view, the reflectivity maximum exceeds 45 dBZ at 4 km. Positive relative vorticity exceeding $2*10^{-3}$ s^{-1} extends upward from this reflectivity maximum and connects with another region of elevated positive vorticity from the southwest near 5 km that extends vertically through 16 km. Strong vertical motion exists in the tower due to convergence (Fig. 44c) throughout the layer to 13 km, and then divergence becomes prominent at higher levels. Regions of negative vorticity border the mid- and upper-levels of this tower of positive relative vorticity. The adjacent tower of negative vorticity to the northeast is between two regions of very deep convection and large positive relative

vorticity. As the reflectivity begins to decrease to the northeast, the positive and negative vorticity become weaker and are discontinuous through the column.

Farther to the northeast (Fig. 48c), the central vortex (near 127.05°E) is a predominantly a mid-level feature. As previously described, this vortex first appears as an independent feature at 5 km, which is near the top of the 30-dBZ region of reflectivity. The maximum positive relative vorticity associated with the central vortex is at 7.5 km along 127.05°E (Fig. 40c). Below the level of maximum relative vorticity in the central vortex near 127.05°E, flow is directed from right to left in the plane of the cross-section, which represents the trough and flow about the Sinlaku circulation. As indicated in Fig. 48c, descending motion is occurring under the central vortex. Above 6 km, the flow is left to right in the plane of the cross-section, which represents the midlevel flow that has exited the deep convective region to the southwest. Ascent is occurring in this flow, so a vertical stretching of the column may explain he existence of this mid-tropospheric central vortex.

The vertical reversal of the winds may also be interpreted as representing rear-to-front and front-to-rear flow patterns through an MCS. If the southwestern portion of the central vortex is taken to be the front, then the flow around Sinlaku enters under the mid-level vortex and descends. The mid-level flow from the convective region to the southwest rises over the low-level flow at the level of maximum vorticity that defines the central vortex at 6-8 km.

Although an isolated tower of elevated reflectivity exists at upper levels above the northern vortex (Fig. 48c), the northern vortex (located between 127.3-127.4°E in this cross-section) is predominantly a low-level feature. Analyzed previously to be a trough at 3 km and a broad, nearly closed circulation at 5.5 km with southeasterlies above and below the circulation, the northern vortex is in a localized region of high reflectivity values associated with the second convective episode. Unlike the central vortex, for which the vorticity maximum (7.5 km) is above the 25 dBZ reflectivity (6 km), the region of maximum vorticity in the northern vortex is coincident with the higher values of reflectivity (at 4 km along 127.3°E and near 127.4°E), which is expected with a deep convective region. Upward vertical motion exists in both columns (Fig. 42d), although it

is much larger in the northeastern of the two positive vorticity regions and extends to 10 km above the elevated reflectivity and positive vorticity regions. Upper-level divergence compensates for this upward vertical motion.

Although Sinlaku had been weakened by the vertical wind shear, the sequence of three convective episodes contributed to a rich structure of precipitation processes, circulations, and thermodynamic characteristics that were identified with a combination of aircraft, dropwindsonde, and ELDORA data. In the region of deep convection that defined the third convective episode, the most significant characteristic is a series of three updrafts that exceed 30 m s^{-1} and extend to at least 13 km. Although some numerical simulations have produced updrafts of these magnitudes (Montgomery and Enagonio 1998; Montgomery et al. 2006; Hendricks et al. 2004), direct observations of these types of features have been rare. An equally significant feature is the distribution of vorticity through the region of the third convective burst. At nearly all levels, positive vorticity is concentrated in areas of strong updrafts that are somewhat aligned along 27.4^{o}N with a slight shift to the northeast (Figs. 48 a,b). The concentration of positive vorticity in these regions is due to the stretching by the vigorous updrafts (not shown). Regions of anticyclonic vorticity are not as coherent as those of positive vorticity, but appear to be generated by divergence associated with air being entrained into updrafts and by tilting due to vertical wind shear and the strong horizontal gradients of vertical motion associated with the vigorous updrafts.

The western-most updraft begins between 3-4 km and is tilted toward the east in the vertical near 126.66^{o}E (Fig. 48a). Between 4-6 km, positive vorticity is co-located with the updraft to the west and anticyclonic vorticity is co-located with the area to the east (Figs. 48a, 40c,d). The anticyclonic vorticity to the east is between the western-most updraft along 126.66^{o}E and the eastern-most updraft at 126.77^{o}E. The anticyclonic vorticity is due to the spreading of air (Figs. 44a, 48a) that is being entrained into the two primary updrafts that surround the region. Above 10 km along 126.66^{o}E (Fig. 48), the vorticity in the region of the primary updraft changes to one of negative relative vorticity to the west and positive to the east. The reversal in sign of vorticity in the region of the updraft at low versus upper levels is consistent with tilting of vorticity associated with the

121

core of the strong updraft. At 4 km, strong vertical wind shear exists in the Sinlaku circulation, and this shear would lead to a horizontal vorticity vector that is generally toward the east below 7 km (Figs. 49a,b). The tilting of that horizontal vorticity by the updraft would contribute to positive vorticity to the west and negative vorticity to the northeast of the updraft (Montgomery et al. 2006). While the tilting of positive vorticity is evident to the west of the primary updraft along 27.4^{o}N, the horizontal vorticity vector is aligned such that the tilting of negative vorticity east of the updraft is very small (a,b). In the column next to the updraft, another possible explanation is that negative relative vorticity generation results from diabatic (i.e., evaporation of precipitation) processes. These regions do project somewhat into the zonal cross-section along 27.4^{o}N as the extension of positive (negative) vorticity westward (eastward) of 126.65^{o}E between 4-6 km (Fig. 48a), and project more directly onto the cross-section from the southwest to northeast (Fig. 48b). At upper levels (Fig. 49c), the vertical wind shear changes sign due to the strong outflow. This results in a horizontal vorticity vector that points in a direction opposite to the low level.   Therefore, the pattern of positive and negative vertical vorticity due to tilting at upper levels along 27.4^{o}N is reversed from what it was at lower levels. At the center of the vigorous updraft near 27.4^{o}N, 126.67^{o}E, the horizontal vorticity is near zero as vertical vorticity due to stretching in the updrafts is maximized. The production of vorticity due to tilting is computed to be at most of order 10^{-5} s^{-2}, which is one order of magnitude less than the production due to stretching.

A very different environment exists in the region of the central vortex (Fig. 48c). The vorticity characteristic is such that positive vorticity at mid-levels (6-8 km) is produced by stretching associated with convergence near 127.05^{o}E (Figs. 44d, 48c). The factors discussed above in relation to the production and placement of negative vorticity are not prevalent in this region of stratiform precipitation processes.

Yet another type of environment exists in the region of the northern vortex where shallow convection has contributed to stronger updrafts and vorticity production between 4-6 km (Fig. 48c). Again, the processes defined in the region of deep convection do not appear to be as dominant in the region of shallow convection and the northern vortex.

The lack of evaporative-driven downdrafts may result from the presence of stratiform rain associated with the second convective burst that has moistened the lower troposphere over large areas.

In the previous chapter, the post-recurvature evolution of TY Sinlaku and the three convective episodes east of Sinlaku were evaluated from a synoptic-scale perspective on 16 September 2008. The first TCS-08/T-PARC ET flights by the WC-130J and P-3 occurred at the place and time of the intersection of these features. In this chapter, observations from these flights have been examined to reveal the effects of the convective episodes on the structure and circulation of the re-intensifying Sinlaku, particularly the effects of two mid-level vortices associated with the second convective episode and the deep convective towers associated with the third convective episode. Analysis of the three cyclonic circulations reveals very different environmental factors contributed to the structural characteristics of each circulation.

The final issue is then what role each vortex played in the re-intensification of Sinlaku. Unfortunately, a 24-h time gap exists until the next set of flights and detailed observations. Thus, it is not possible to provide a detailed description of the period between the observations of these structures and the emergence of a typhoon 24 h later. Because the tropical cyclone did intensify, it must be assumed that the overall impact of each vortex was to contribute to the increase in total cyclonic circulation and thus the contribution by production and regions of cyclonic vorticity overwhelmed those of anticyclonic vorticity in the region of the intensifying inner circulation. This would be consistent with results from high-resolution models (Montgomery et al. 2006, Hendricks et al. 2004) that documented the movement of cyclonic vorticity inward toward the center of the background circulation and anticyclonic vorticity outward away from the circulation center. The character of the increase in cyclonic circulation is investigated in the next chapter using satellite imagery to identify regions of deep convection and their evolution during the 24-h period between the first and second flights.
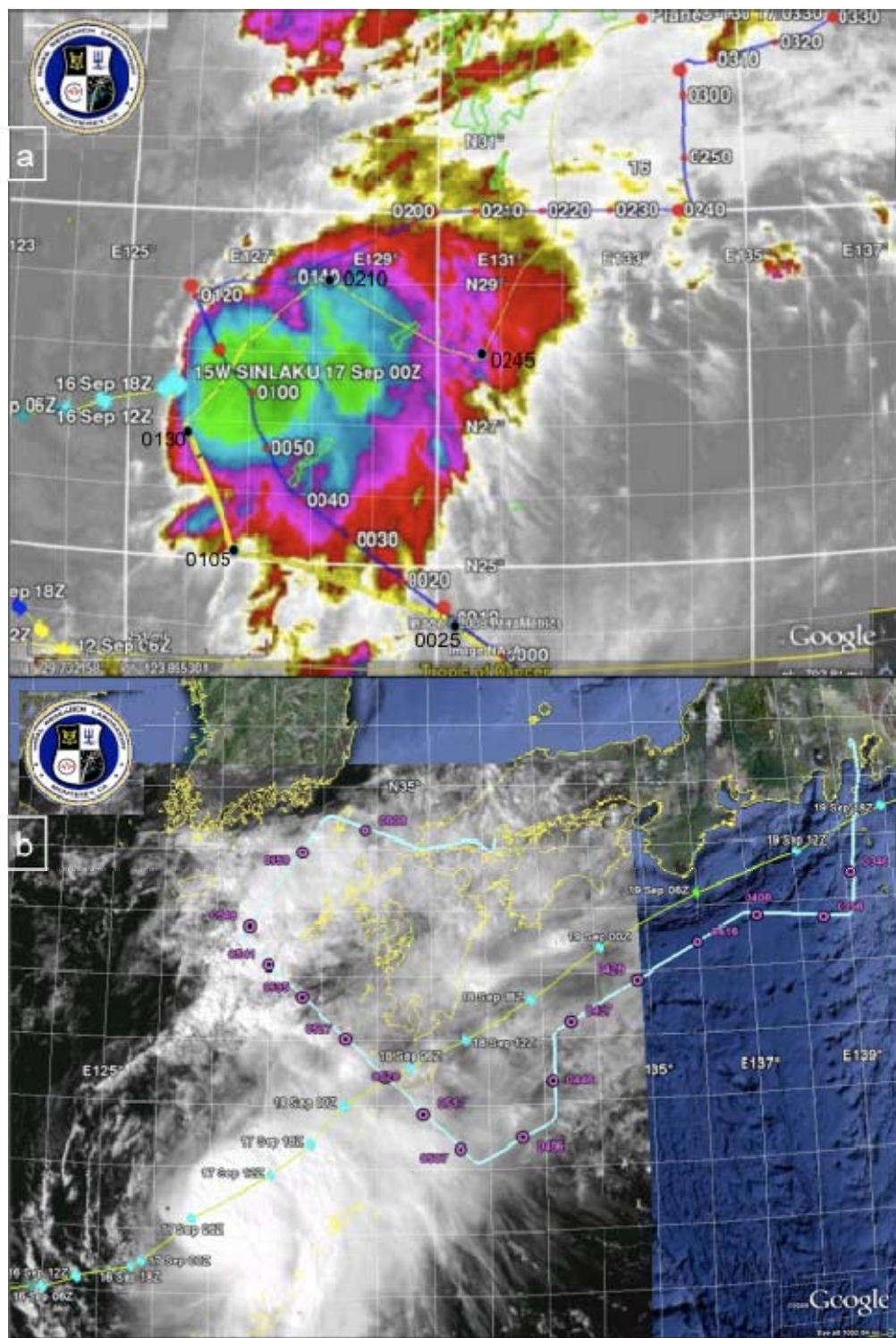
Figure 27.   Flight tracks of the (a) P-3 (yellow line) and WC-130J (royal blue line) 16-17 September 2008 over enhanced IR MTSAT imagery from 0257 UTC 17 September 2008, and the (b) DLR Falcon (light blue line) aircraft track during 17 September 2008 over MTSAT visible satellite imagery from 0530 UTC 17 September 2008. Waypoint times are marked along each flight track.
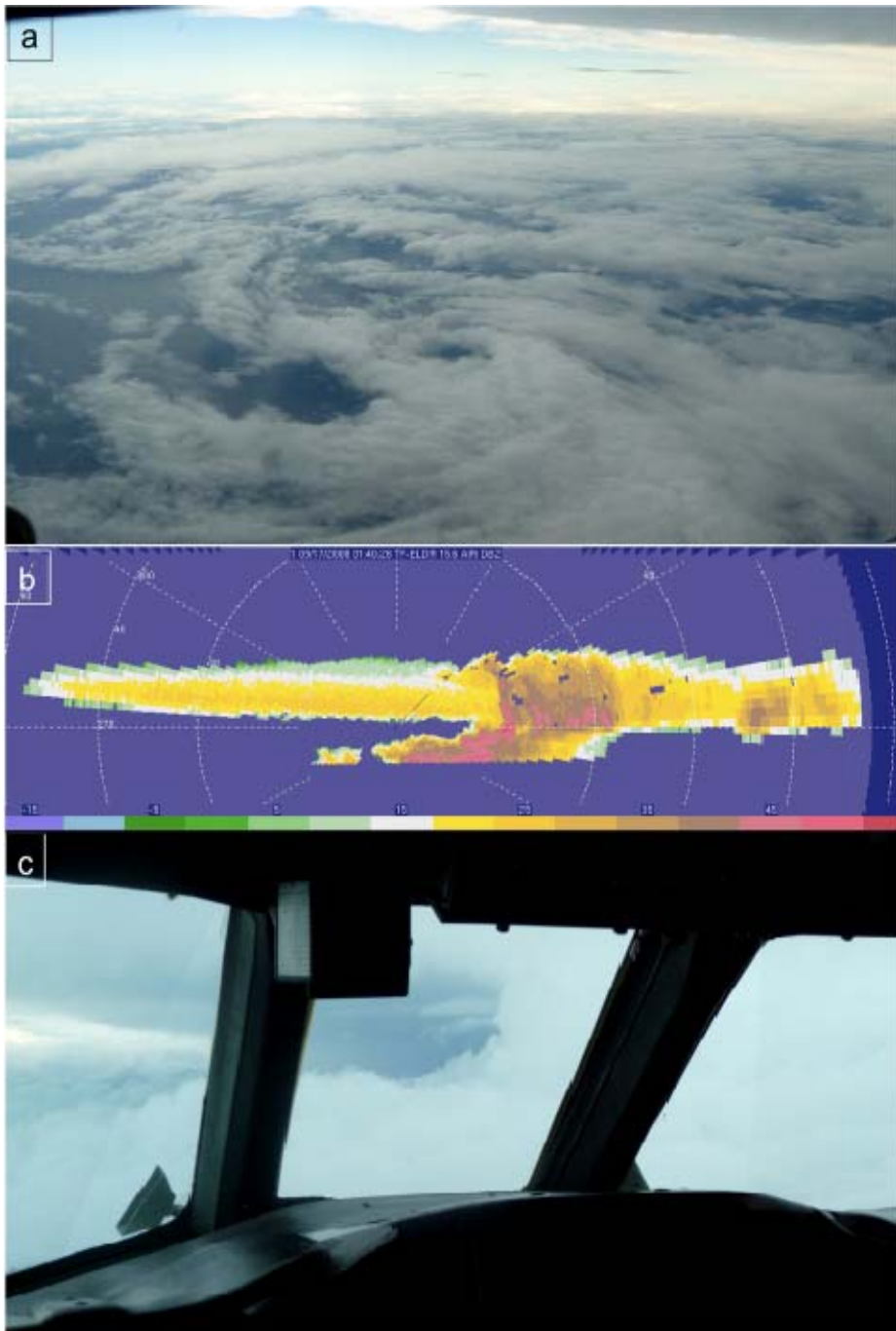
Figure 28.   Photographs taken by the author from the NRL P-3 cockpit at 0140 UTC 17 September 2008 to the (a) left and (c) right of the aircraft.   In panel (b), reflectivity from the forward radar in the ELDORA at 0140 UTC 17 September 2008 defines low reflectivity to the left of the aircraft that represents the Sinlaku surface circulation and upper-level cirrus shield, and high reflectivity to the right of the aircraft that defines the deep convective tower. The absence of reflectivity in the center indicates the aircraft was flying in cloud-free air beneath the cirrus shield.

Figure 29.   Dropwindsonde winds released during the 16-17 September 2008 TCS-08/T-PARC research flights over ECMWF streamlines for the 0000 UTC 17 September 2008 analysis at (a) 975 hPa, (b) 850 hPa, (c) 700 hPa, (d) 550 hPa, (e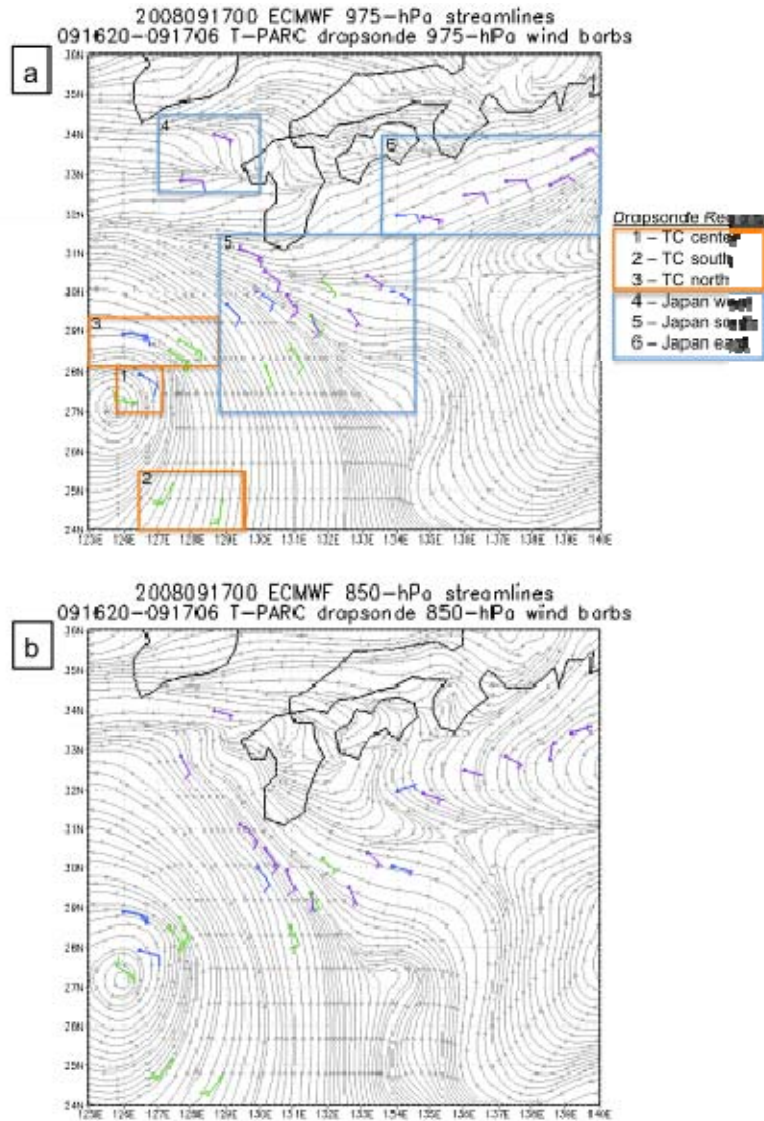) 500 hPa, (f) 375 hPa, (g) 325 hPa, and (h) 300 hPa. Green wind barbs (long barb is 10 m s^{-1}) identify P-3 dropwindsondes; blue identify WC-130J dropwindsondes, and purple identify Falcon dropwindsondes. Flight-level winds (long barb is 10 m s^{-1}) thinned to 5-minute intervals for the (e) P-3 (500-hPa, green wind barbs) and (g) C-130 (300 hPa in winds in dark blue, 275 hPa in light blue). In panel (a), boxed regions represent areas of the Sinlaku circulation as annotated in the legend at the right. In panel (e), flight-level observations between 24.5-25.0^{o}N were removed during the quality control process, and data northeast of 28.2^{o}N, 131°E were collected following a temperature sensor malfunction and are inconsistent with data collected prior to the malfunction, so these data are not included. In panel (g), the maroon box outlines the region portrayed in Fig. 34.

126

2008091700 ECMWF 700-hPa streamlines
091620–091706 T-PARC dropsonde 700-hPa wind barbs
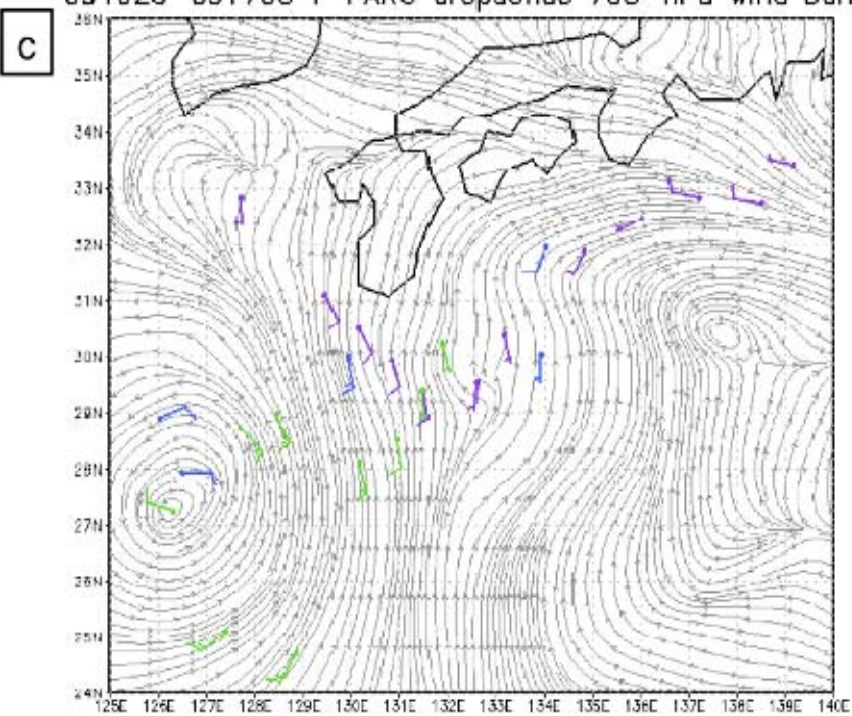
2008091700 ECMWF 550-hPa streamlines
091620–091706 T-PARC dropsonde 550-hPa wind barbs

Fig. 29, continued.

2008091700 ECMWF 500-hPa streamlines
091620–091706 T-PARC sonde&flvl 500-hPa wind barbs

2008091700 ECMWF 375-hPa streamlines
091620–091706 T-PARC dropsonde 375-hPa wind barbs

Fig. 29, continued.

128

2008091700 ECMWF 325-hPa streamlines
091620-091706 T-PARC dropsonde 325-hPa wind barbs
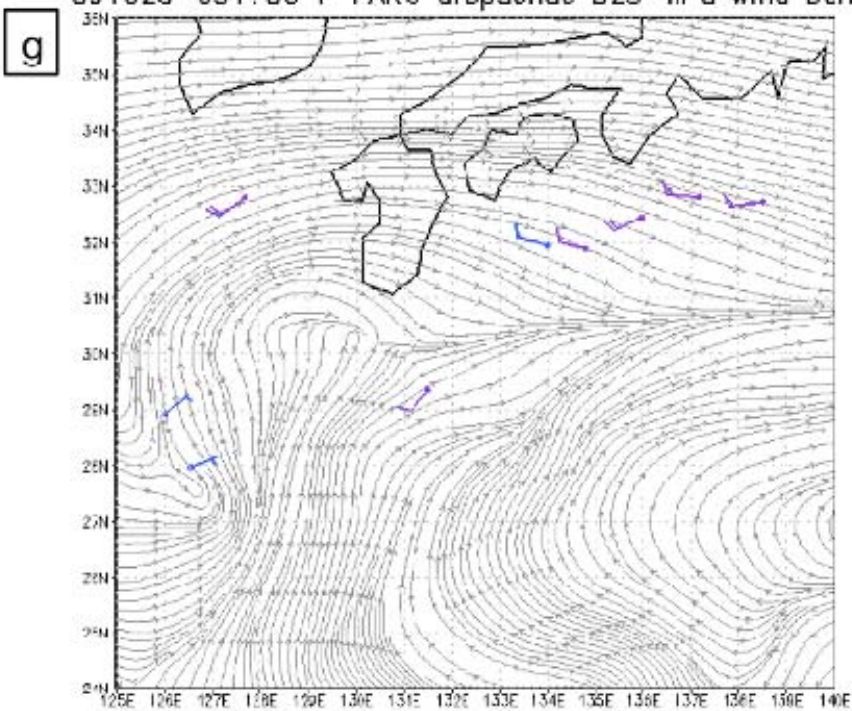
2008091700 ECMWF 300-hPa streamlines
091620-091706 T-PARC sonde&flvl 300-hPa wind barbs
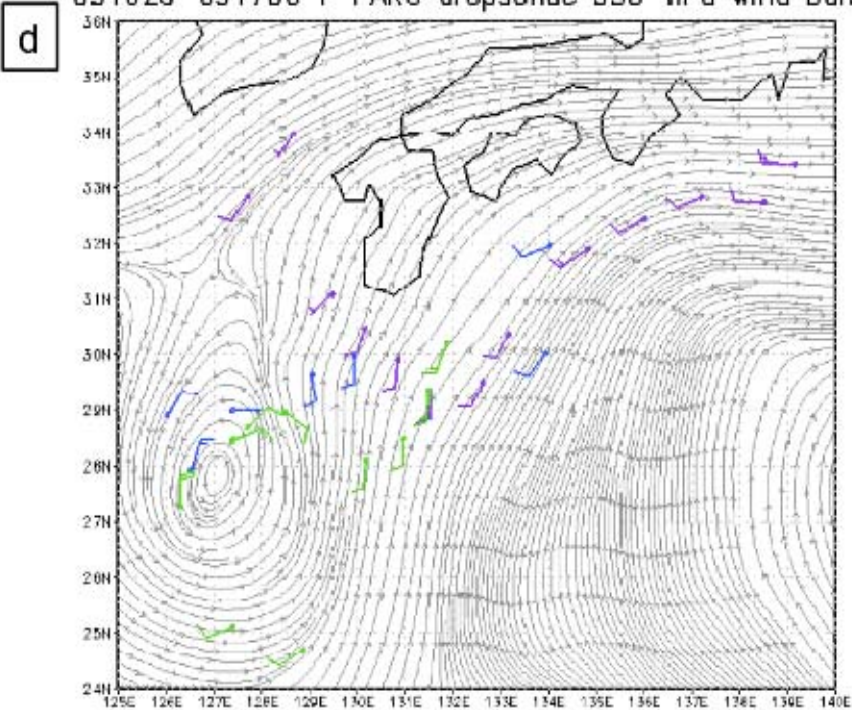
Fig. 29, continued.

129
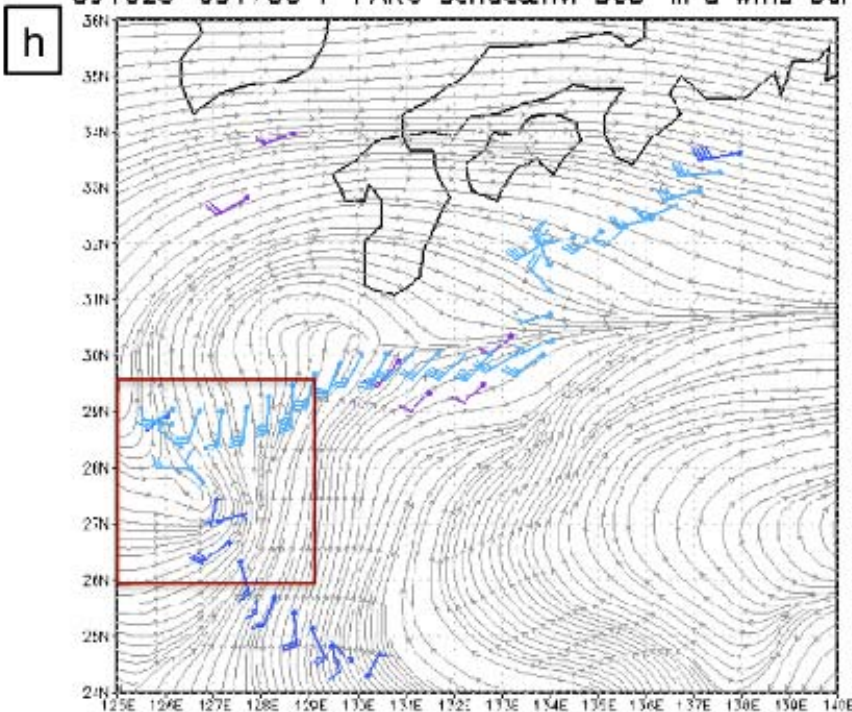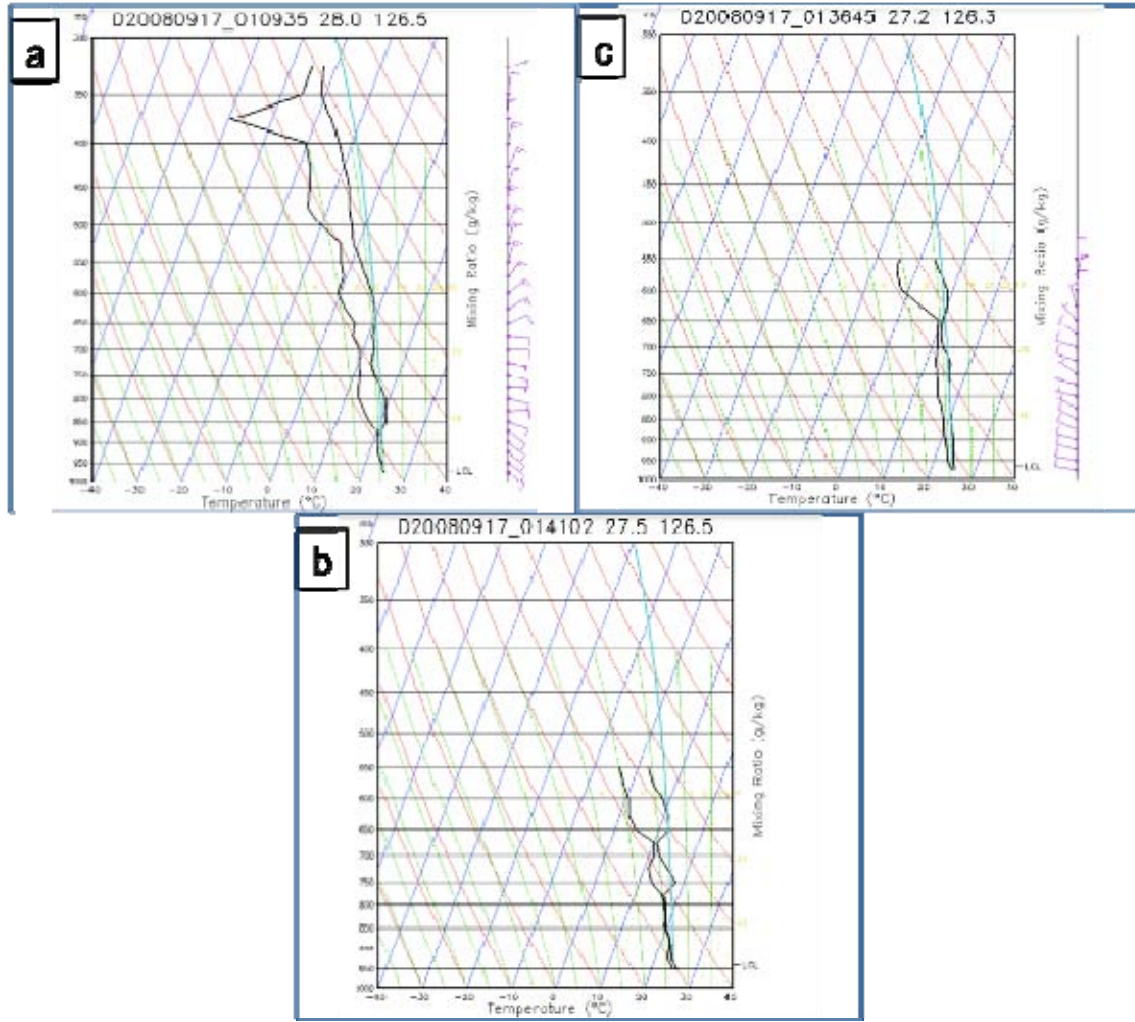
Figure 30.   Dropwindsonde winds (long barb is 10 m s^{-1}) near the center of TY Sinlaku during the first TCS-08/T-PARC ET flight on 17 September 2008. The (a) WC-130J dropwindsonde was released at 0109 UTC 17 September 2008 and the (b-c) P-3 dropwindsondes were released at (b) 0141 UTC and (b) 0136 UTC 17 September 2008.   In each panel, the left vertical black line defines the environmental dew point (^{o}C), and the right vertical black line defines the environmental temperature (^{o}C). The light blue vertical line defines the path a surface parcel would follow if lifted from the surface.

130
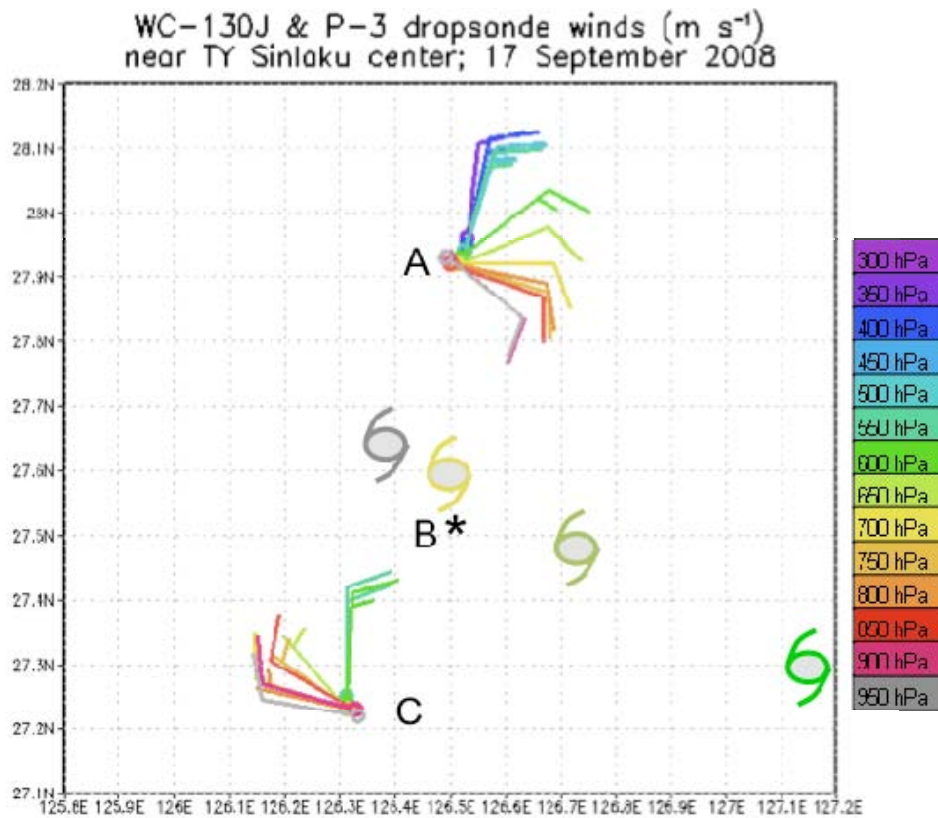
Figure 31.   Dropwindsonde winds (long barb is 10 m s^{-1}) near the center of TY Sinlaku defined by the (A) WC-130J dropwindsonde released at 0109 UTC 17 September 2008 and (C) P-3 dropwindsonde released at 0136 UTC 17 September 2008 during the first TCS-08/T-PARC ET flights. The wind barbs and TC symbols are color coded by height per the color bar at the right. The TC symbols identify an estimated center position at the indicated levels based on geostrophic reasoning from the wind directions at those levels from both dropwindsondes. The black asterisk (B) identifies the location of the 0141 UTC 17 September 2008 P-3 dropwindsonde release point.
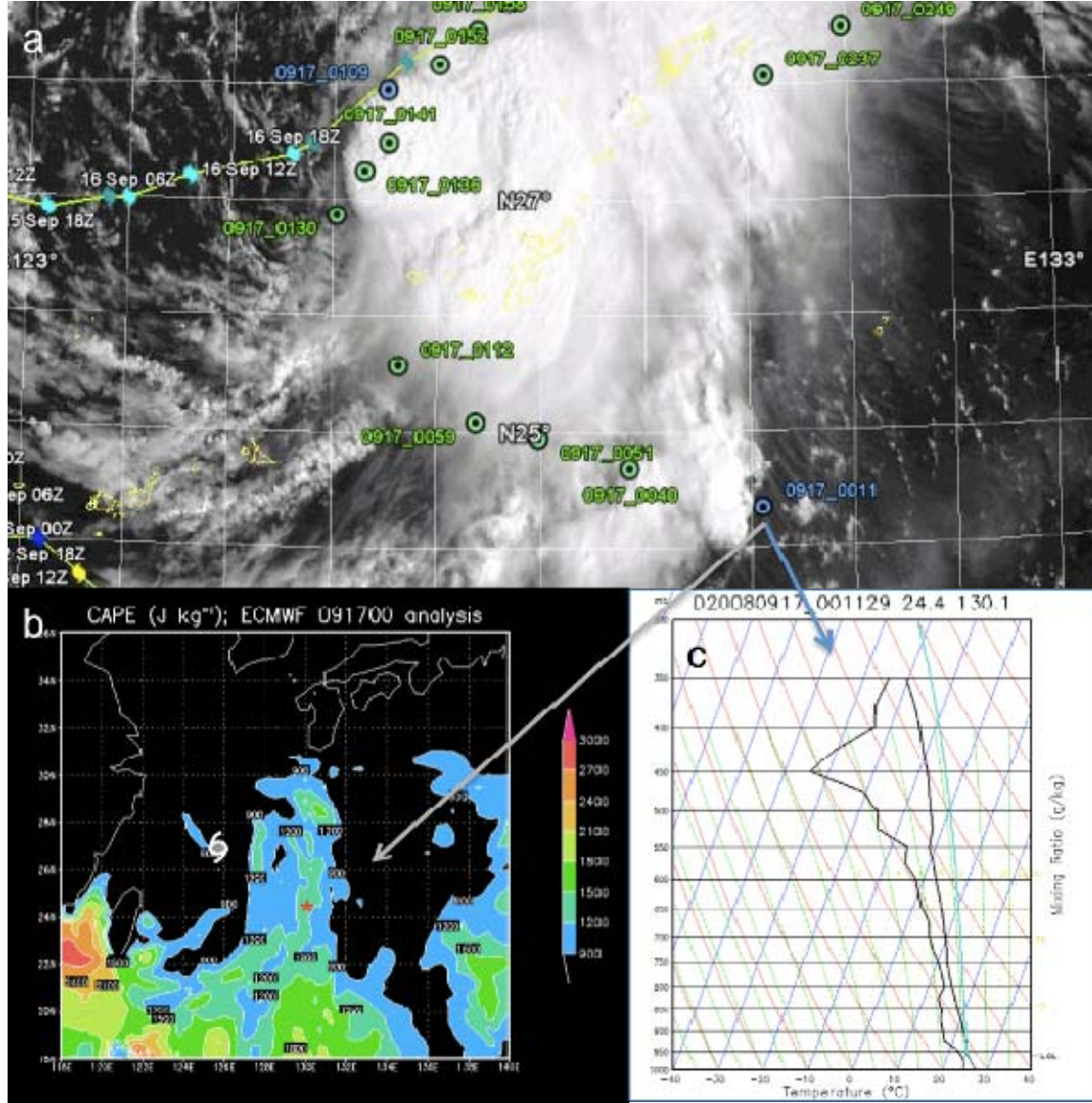
Figure 32. (a) Dropwindsonde release points and times over MTSAT visible imagery from 0030 UTC 17 September 2008. (b) Values of CAPE (J kg^{-1}) for the region of TY Sinlaku in the ECMWF model analysis for 0000 UTC 17 September 2008. (c) Skew-T diagram as in Fig. 30 from the WC-130J dropwindsonde released southeast of of TY Sinlaku at 0011 UTC 17 September 2008. In panel (a) WC-130J release points and times are annotated in blue, and P-3 release points and times are annotated in green. The red asterisk in panel (b) defines the location of the dropwindsonde released by the WC-130 at 0011 UTC 17 September 2008.

132
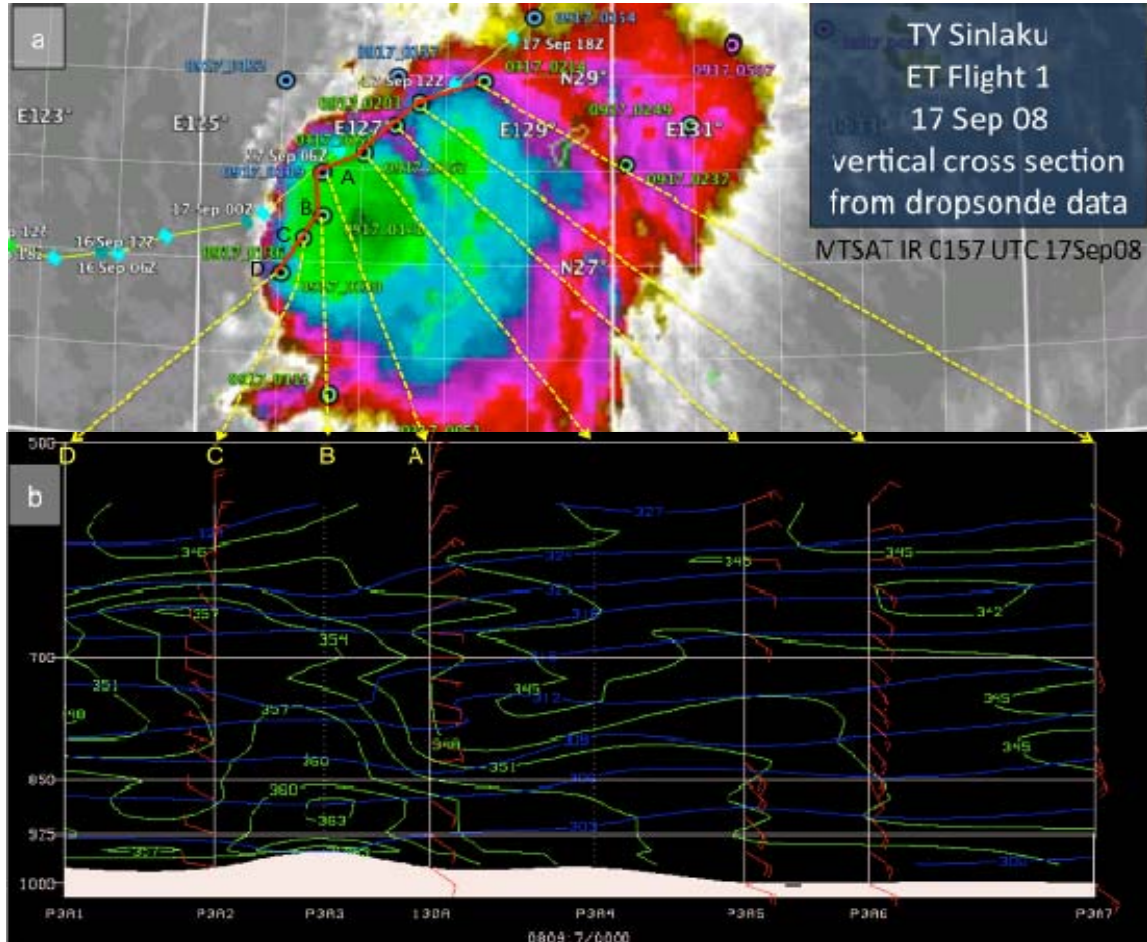
Figure 33.   Dropwindsonde (a) release points and times as in Fig. 32a, except over MTSAT IR imagery from 0157 UTC 17 September 2008, and (b) vertical cross-section oriented nearly southwest-to-northeast, predominantly along the P-3 flight track. In panel (b), available winds (long barb is 10 m s^{-1}) are plotted at 25-hPa intervals. Surface pressure is indicated by the top of the area in white (read on the scale on the left side). Blue lines are isentropes and green lines are contours of constant Θ_e. Dropwindsondes released near the Sinlaku LLCC and described in Figs. 30-31 include the WC-103J dropwindsonde released at 0011 UTC 17 September 2008 (labeled "A") and the P-3 dropwindsondes released at 0141 UTC (labeled "B") and 0136 UTC (labeled "C") 17 September 2008.
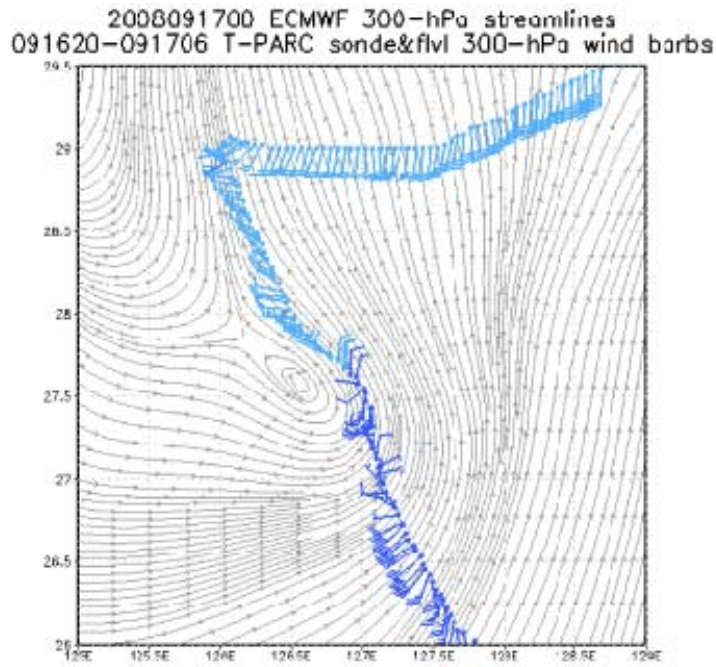
Figure 34. WC-130J flight level winds (m s^{-1}) at 300 hPa (dark blue wind barbs) and at 275 hPa (light blue wind barbs) with dropwindsonde winds (m s^{-1}) over the ECMWF analysis at 300 hPa as in Fig. 29.
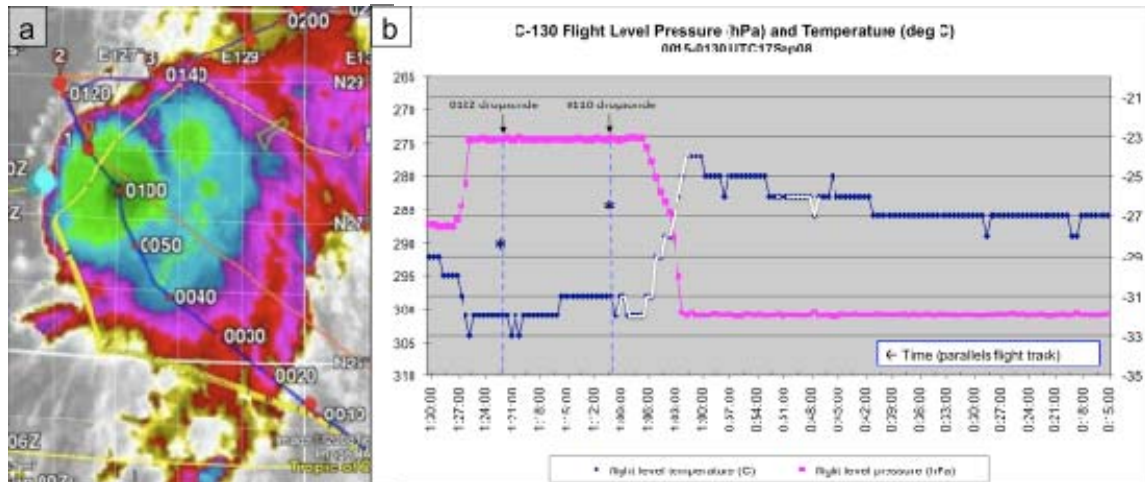
Figure 35. The WC-130J (a) flight track (blue line with times marked) over MTSAT enhanced IR satellite imagery from 0157 UTC 17 September 2008, and (b) flight-level pressure (purple line) and temperature (dark blue solid line). Dashed light blue vertical lines indicate times of WC-130J dropwindsonde releases. Blue asterisks define dropwindsonde temperatures at 300 hPa (the average WC-130J flight level prior to ascent). White lines define temperatures that were recorded when dew-point temperatures were coded as missing and may indicate suspect measurements.
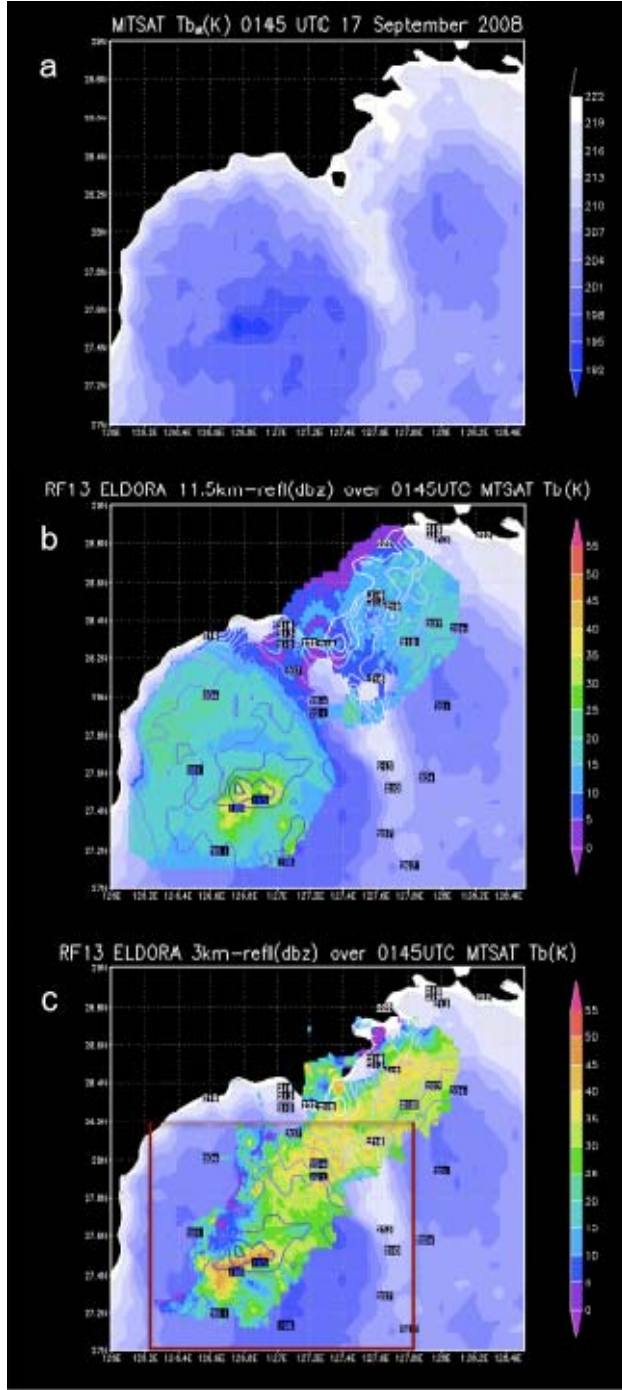
Figure 36.   (a) Brightness temperatures (K) less than 222 K from the geostationary infrared channel 1 (10.3-11.3 μm) MTSAT data at 0145 UTC 17 September 2008. (b) Reflectivity (dBZ) at 11.5 km from ELDORA overlaid on the brightness temperatures in panel (a).   Contours over the ELDORA display also define the brightness temperatures as defined in panel (a).   (c) As in panel (b), except for ELDORA reflectivity at 3 km. The boxed region in panel (c) defines the region in Fig. 37.
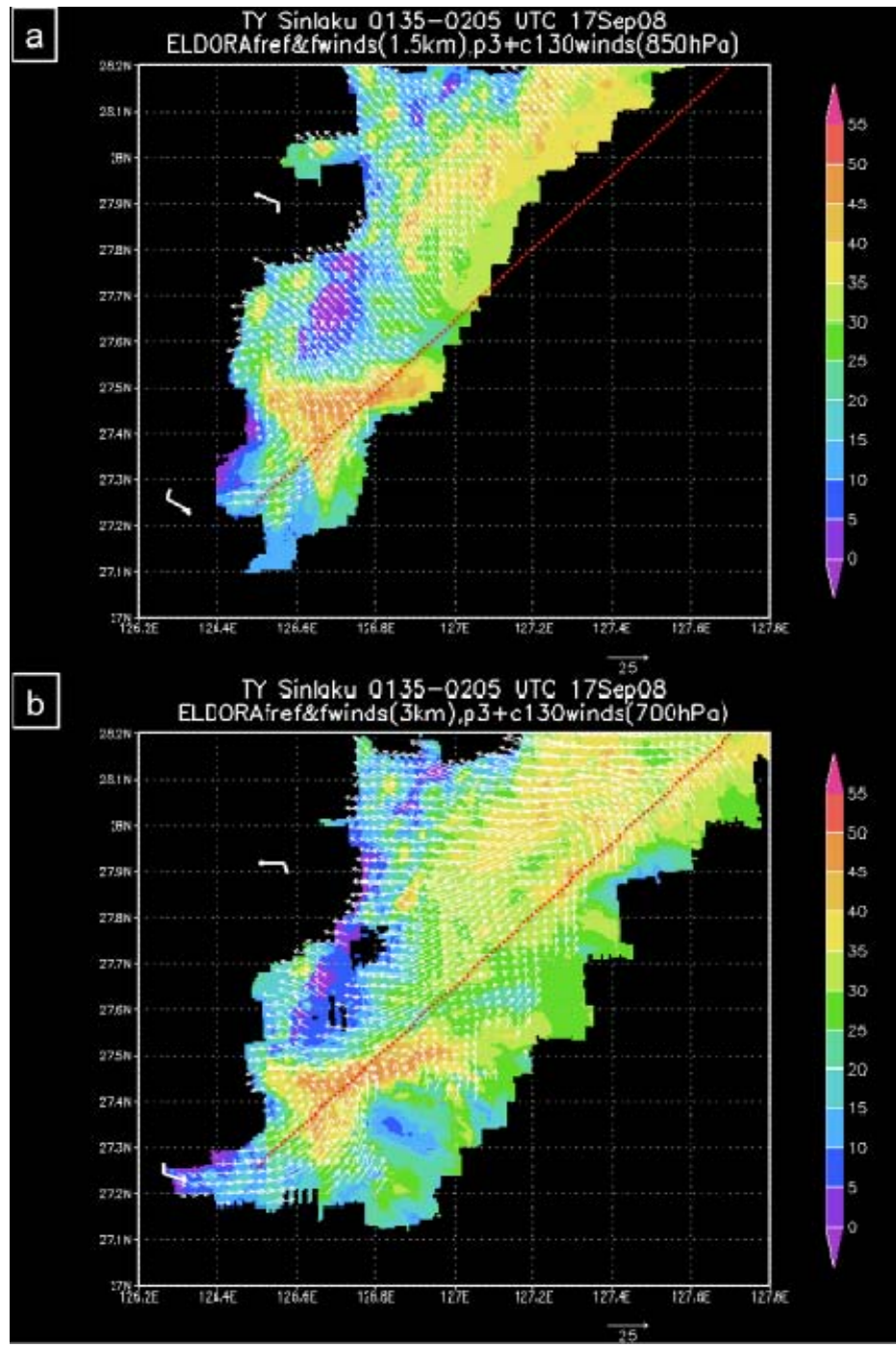
Figure 37. Reflectivity (dBZ, shaded) and winds (m s^{-1}, reference vector below each panel) at (a) 1.5 km, (b) 3 km, (c) 5.5 km, (d) 7.5 km, (e) 9.5 km, (f) 10.5 km, (g) 11.5 km, and (h) 15 km from the ELDORA between 0135-0205 UTC 17 September 2008. Wind barbs are as in Fig. 29, except all drops are plotted in white. The dotted red line indicates the location of the vertical cross-section in Fig. 38.

Fig. 37, continued.

TY Sinlaku 0135-0205 UTC 17Sep08
ELDORAfref&fwinds(9.5km),c130winds(300hPa)

TY Sinlaku 0135-0205 UTC 17Sep08
ELDORAfref&fwinds(10.5km),c130winds(250hPa)

Fig. 37, continued .

138
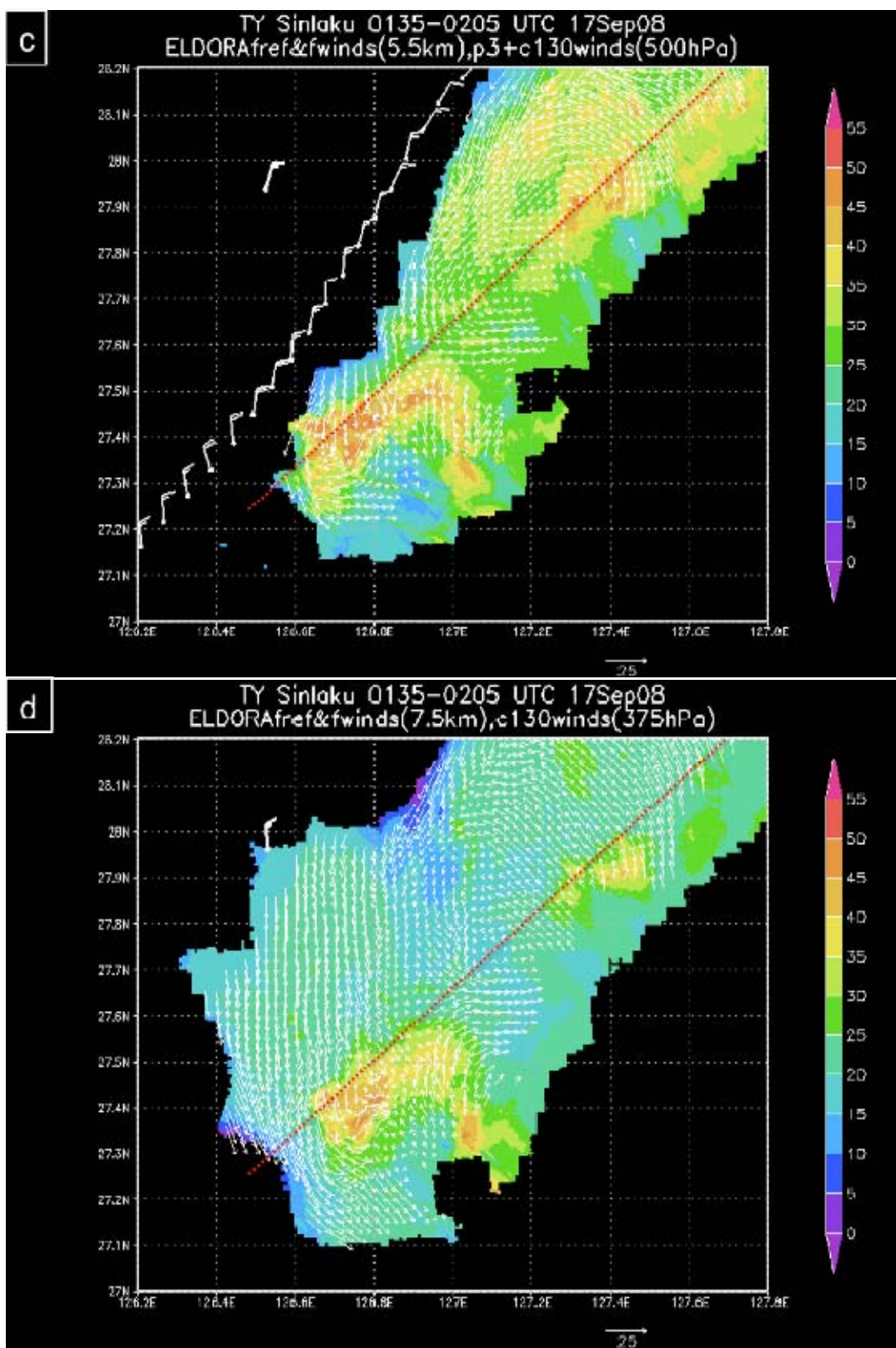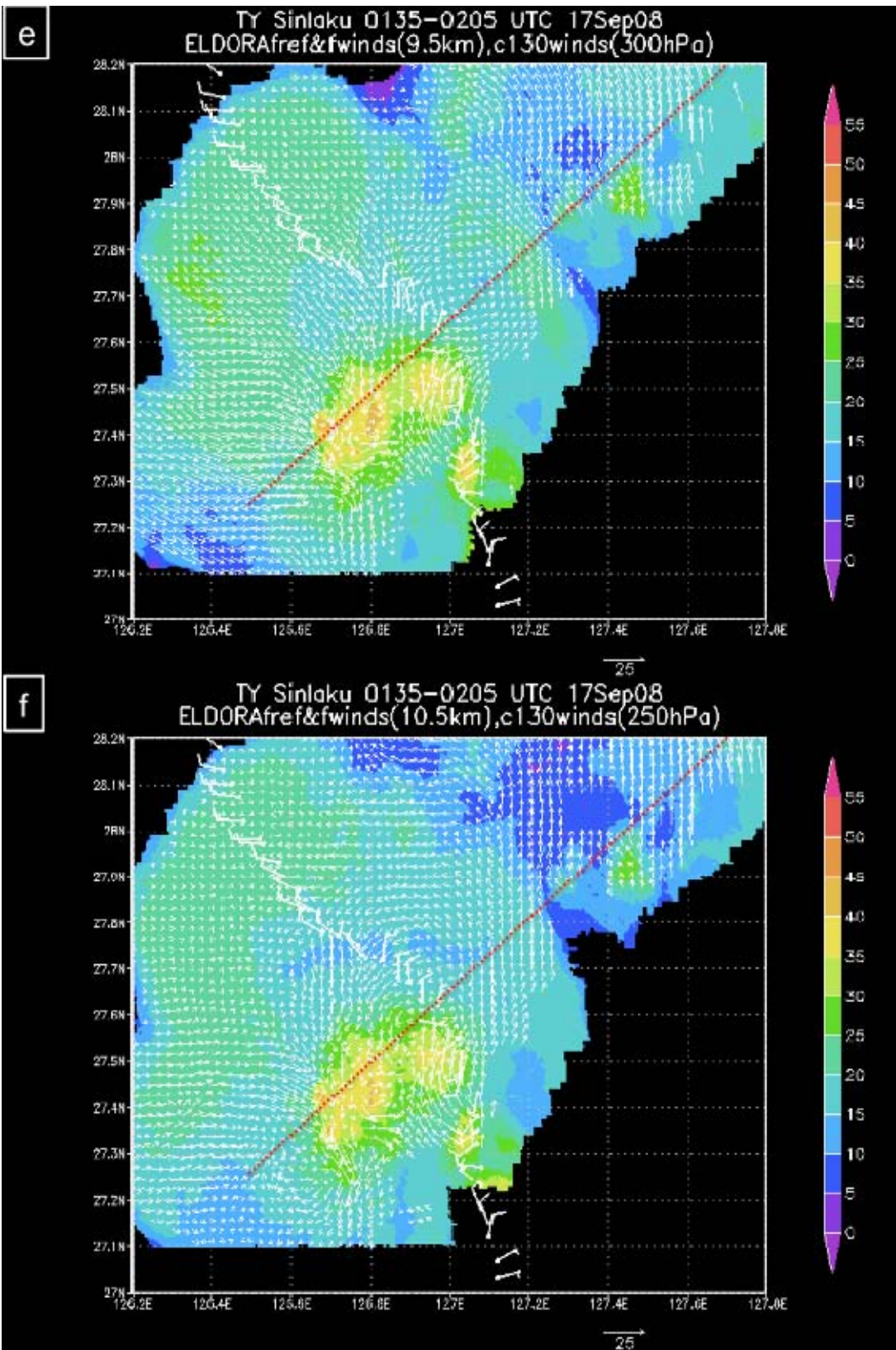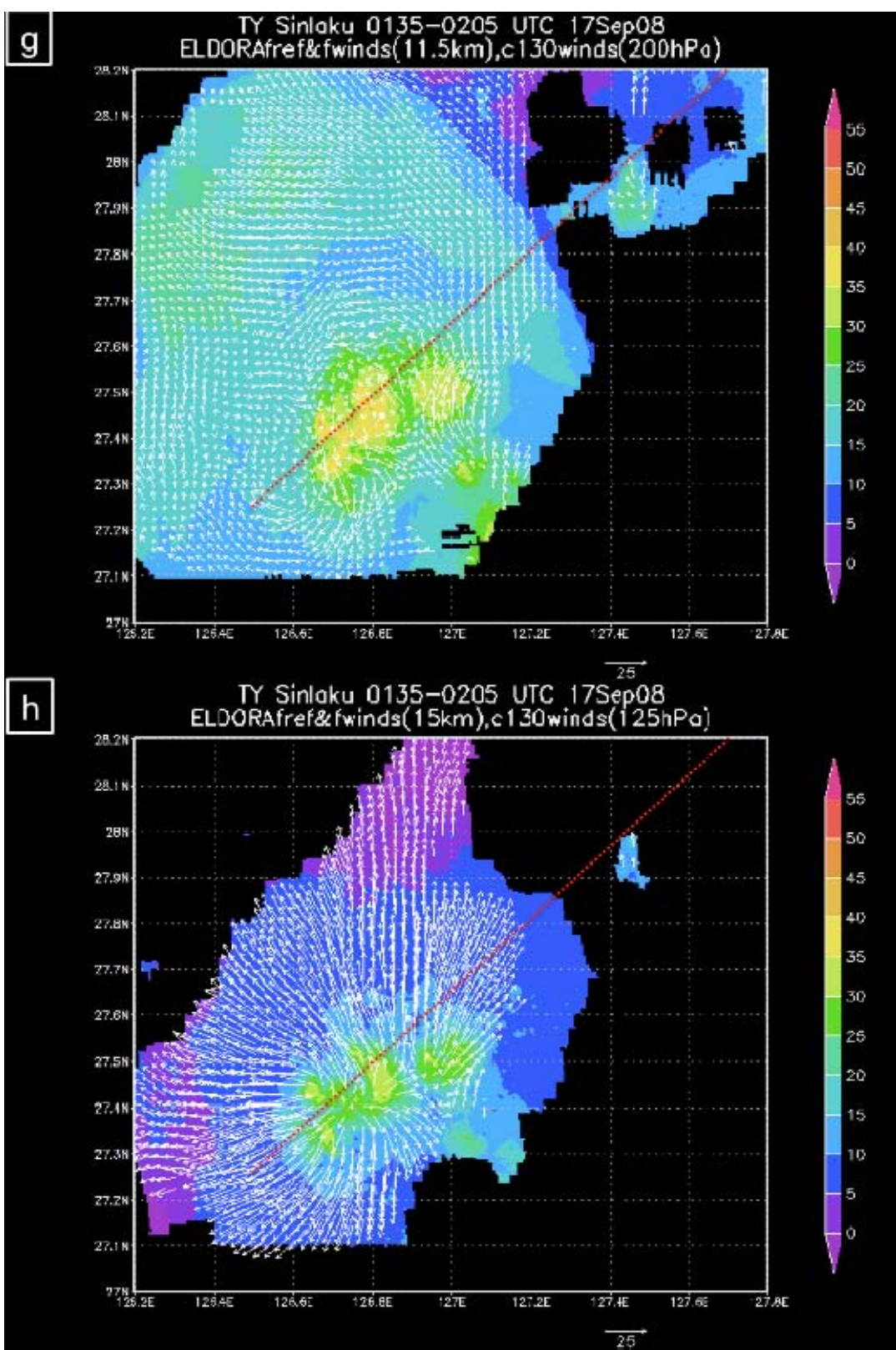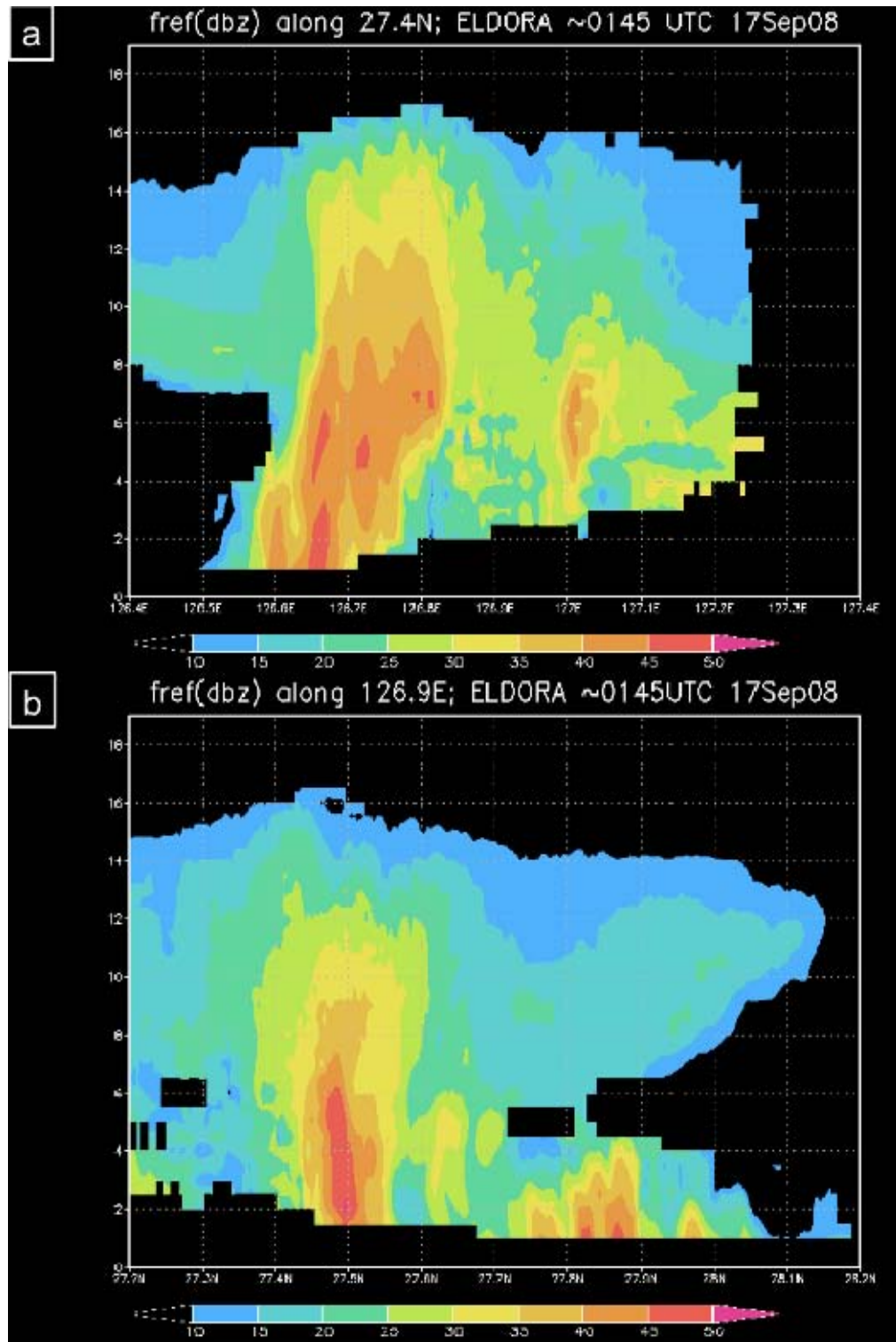
Fig. 37, continued .

Figure 38.   Vertical cross-sections of ELDORA reflectivity (dBZ) (a) along 27.4°N from 126.4°-127.4°E, (b) along 126.9°E from 27.2°-28.2°N, and (c) southwest to northeast, from 27.25°N, 126.6°E through 28.2°N, 127.7°E, between 0135-0205 UTC 17 September 2008.

Fig. 38, continued.

141
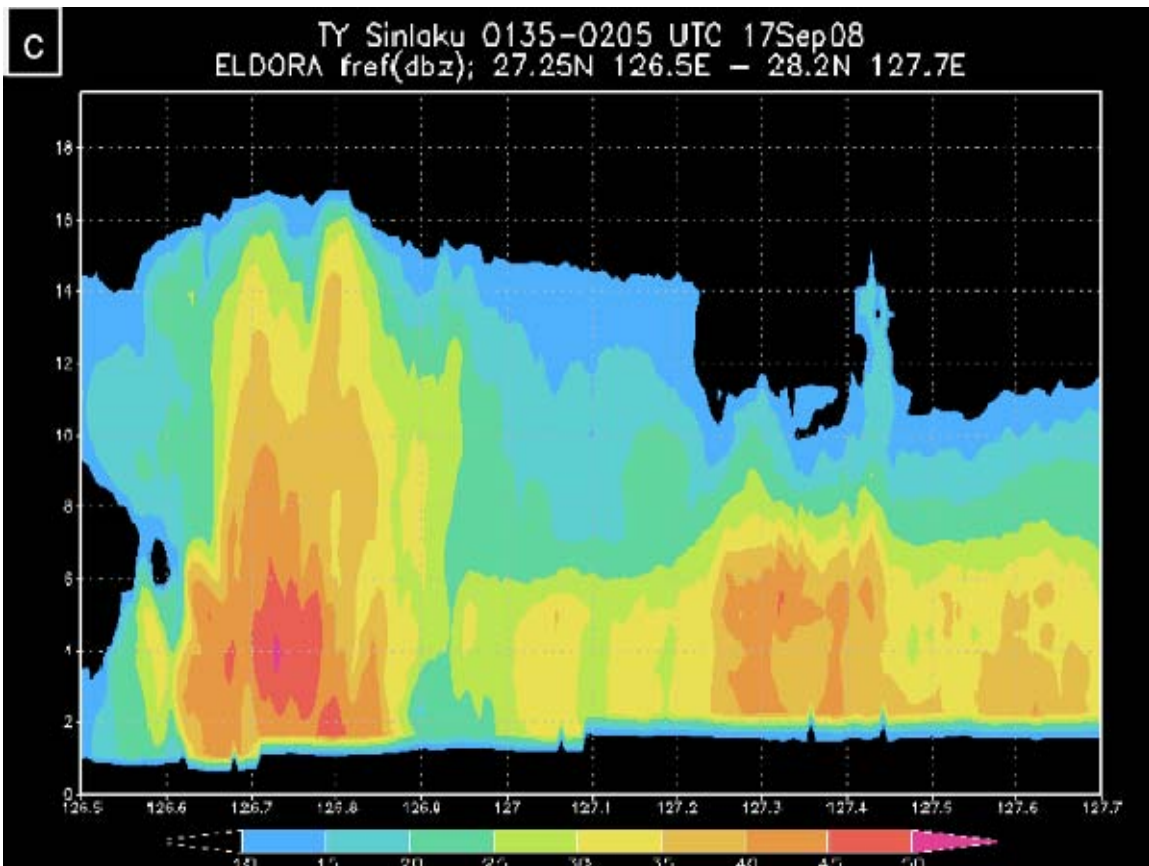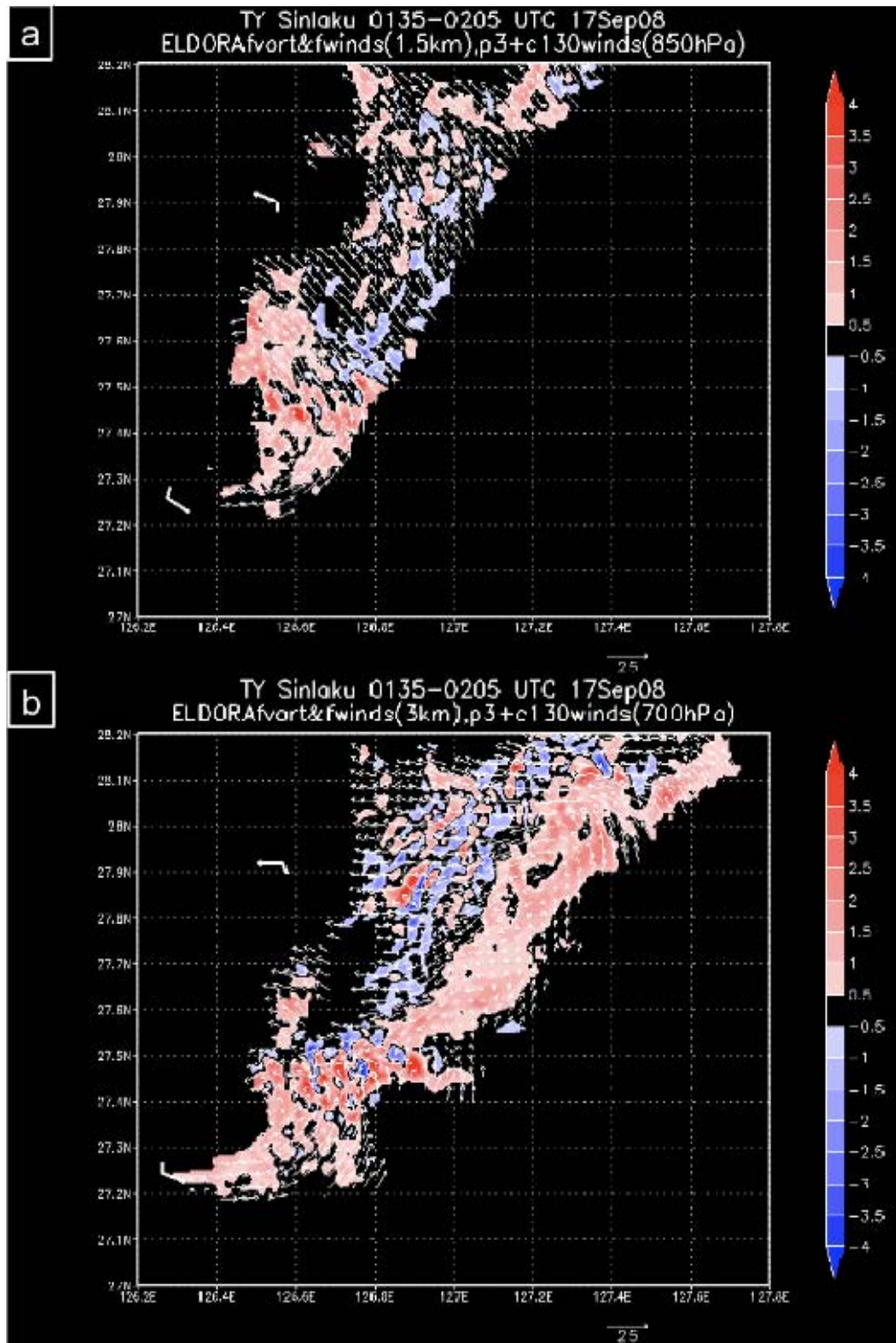
Figure 39.   Relative vorticity (10^{-3} s^{-1}, shaded, scale on right side) and winds (m s^{-1}, vectors, reference vector below each panel) at (a) 1.5 km, (b) 3 km, (c) 5.5 km, (d) 7.5 km, (e) 9.5 km, (f) 10.5 km, (g) 11.5 km, and (h) 15 km from the ELDORA between 0135-0205 UTC 17 September 2008.
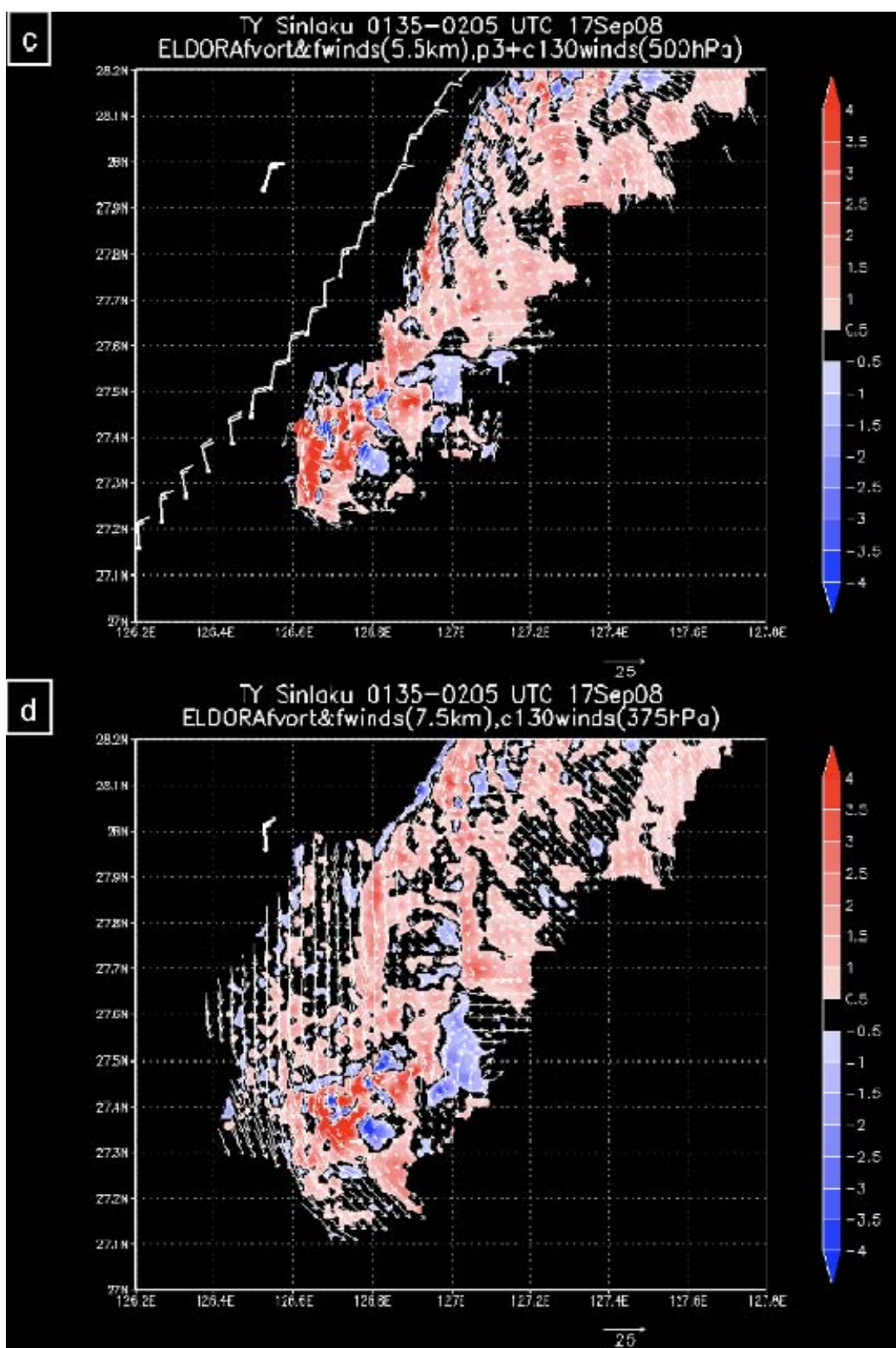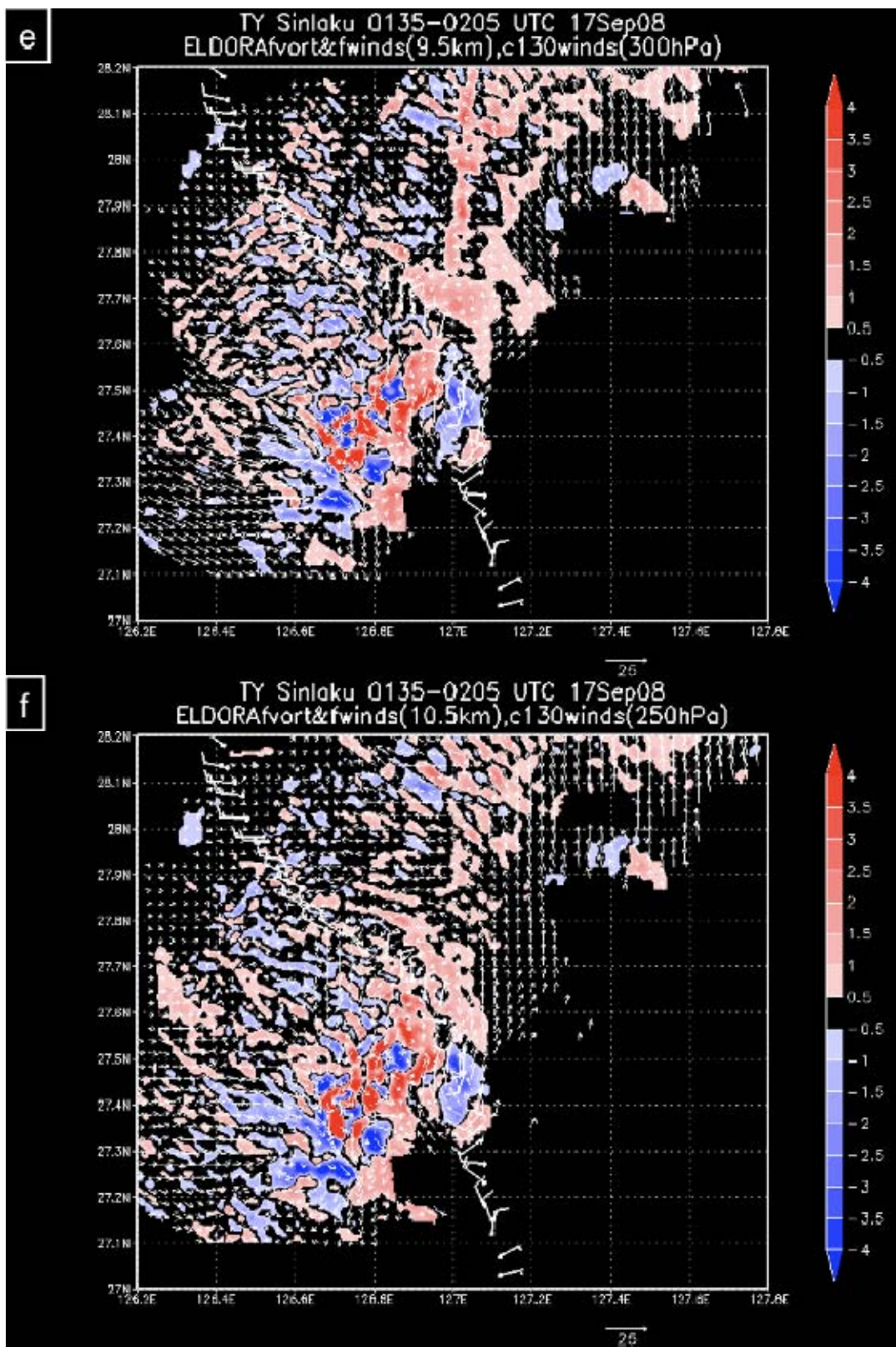
Fig. 39, continued.

Fig. 39, continued.

144
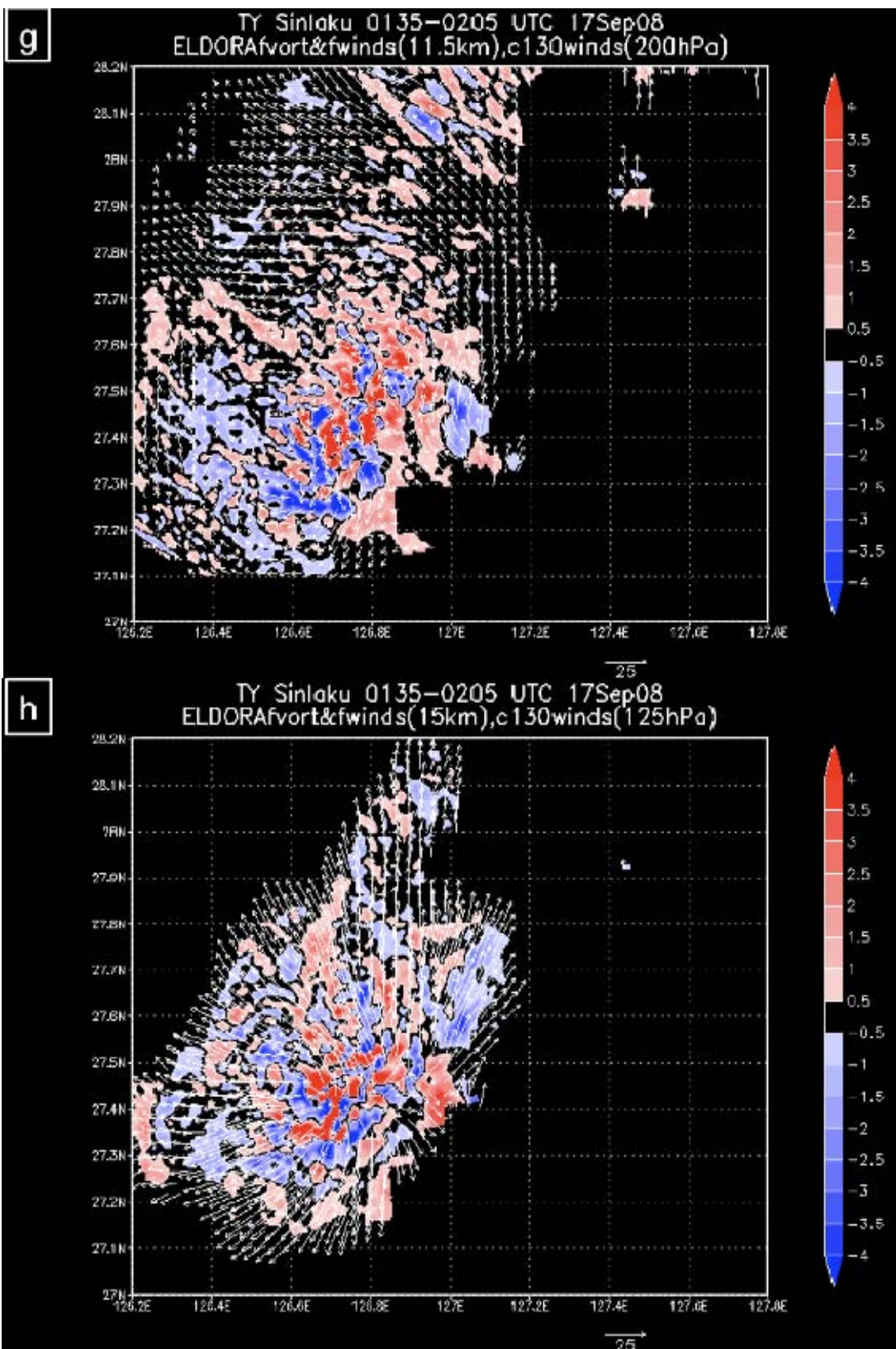
Fig. 39, continued.
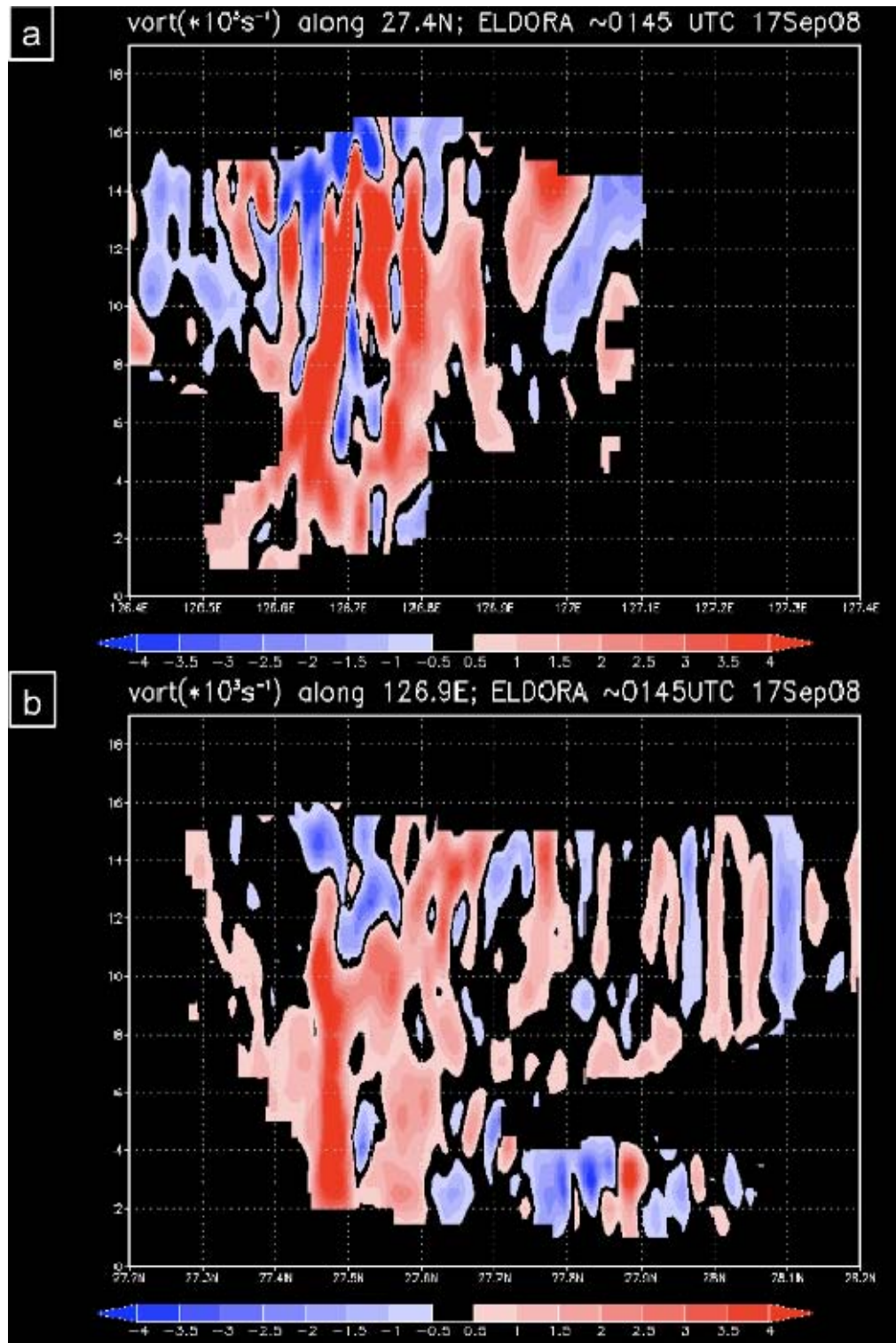
Figure 40.   Vertical cross-sections of relative vorticity (10^{-3} s^{-1}) (a) along 27.4°N from 126.4°-127.4°E, (b) along 126.9°E from 27.2°-28.2°N, and (c) southwest to northeast from 27.25°N, 126.5°E through 28.2°N, 127.7°E, calculated from the ELDORA observations between 0135-0205 UTC 17 September 2008.

146

Fig. 40, continued.

147
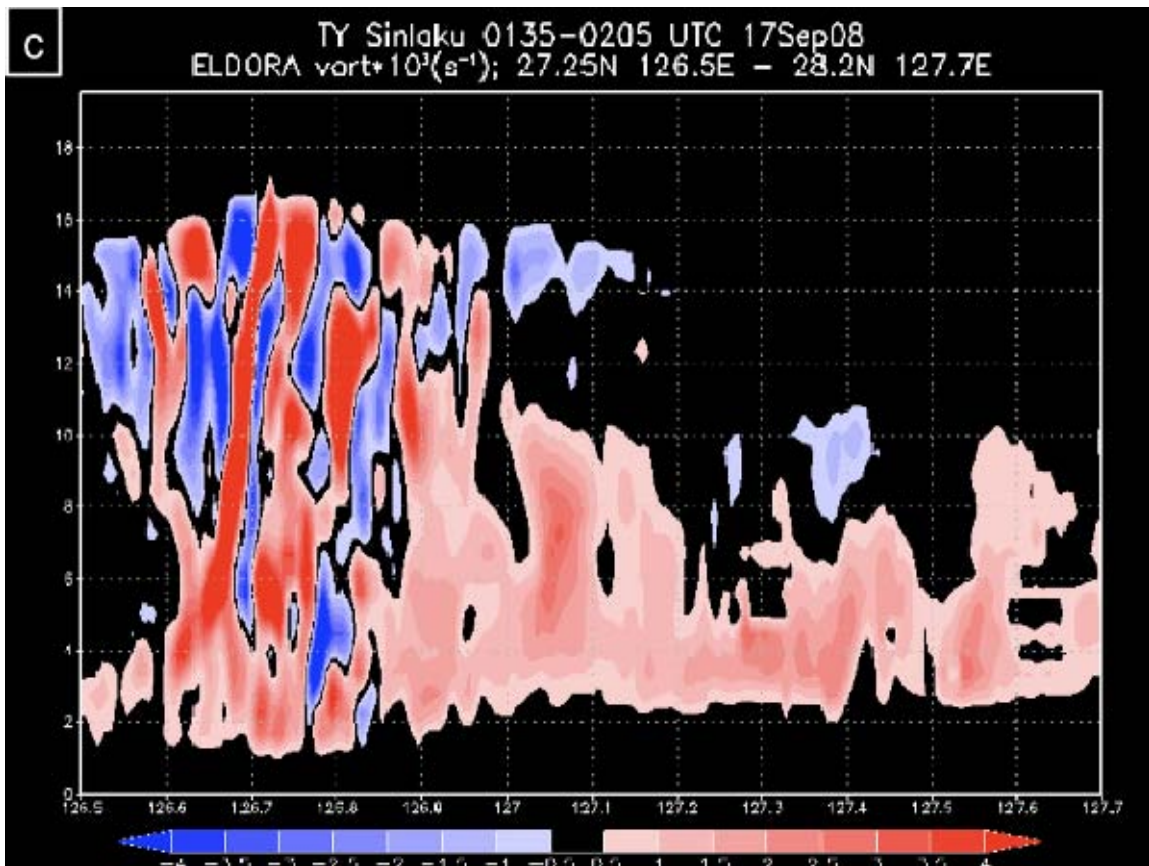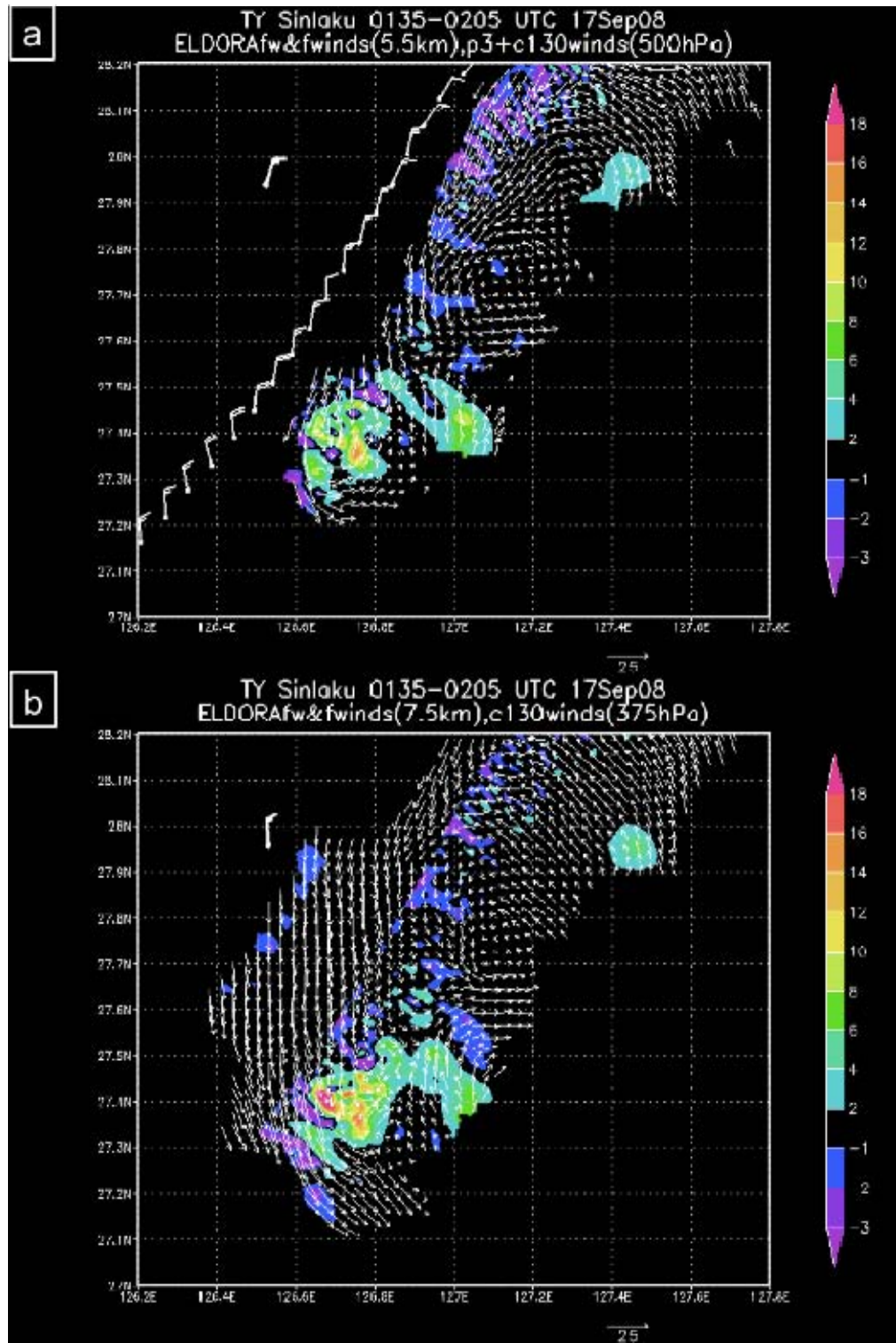
Figure 41. Vertical motion (m s^{-1}, shaded, scale on right) and winds (m s^{-1}, vectors, reference vector below each panel) at (a) 5.5 km, (b) 7.5 km, (c) 9.5 km, and (h) 13 km from the ELDORA observations between 0135-0205 UTC 17 September 2008.

148
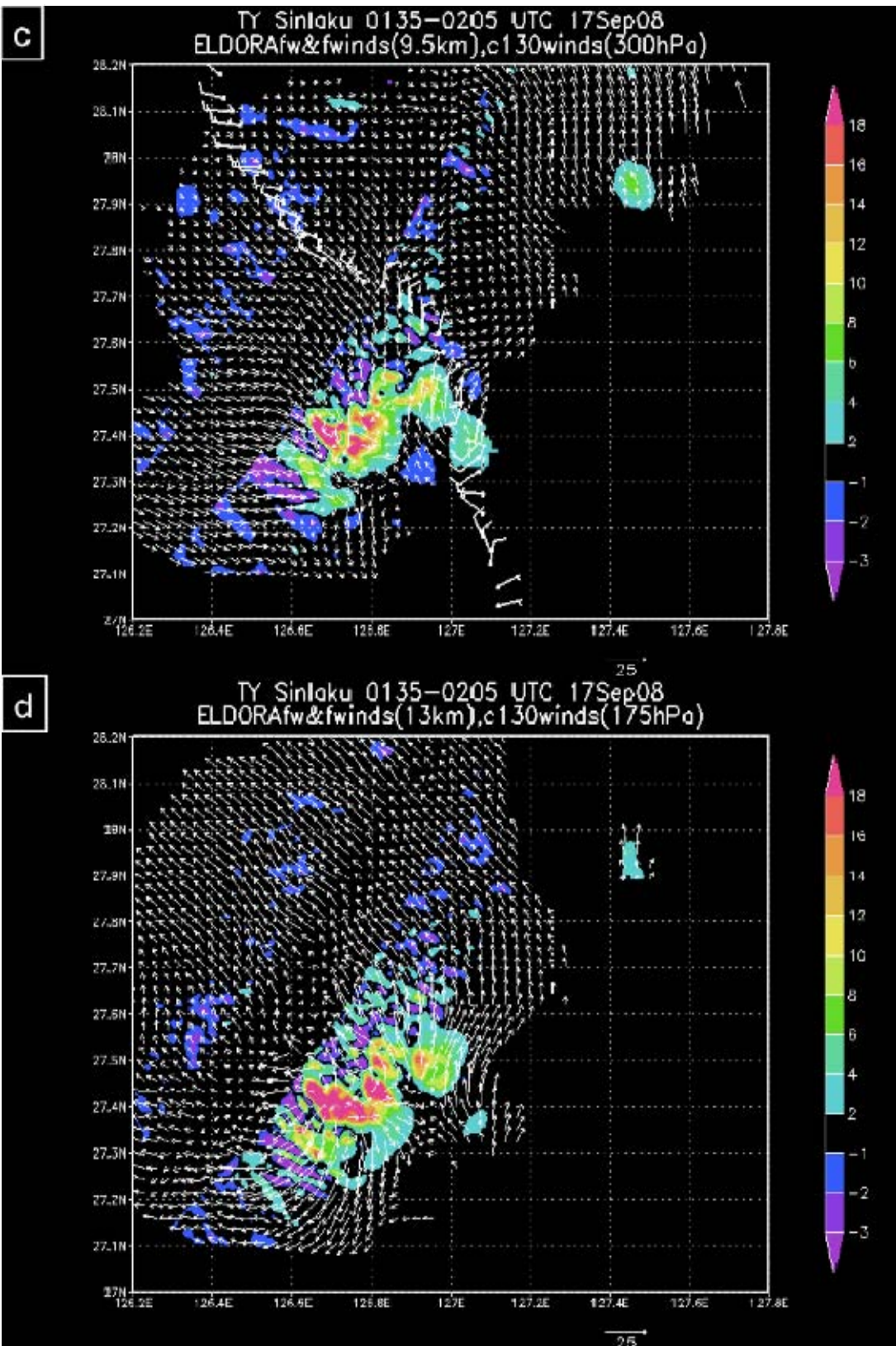
Fig. 41, continued.
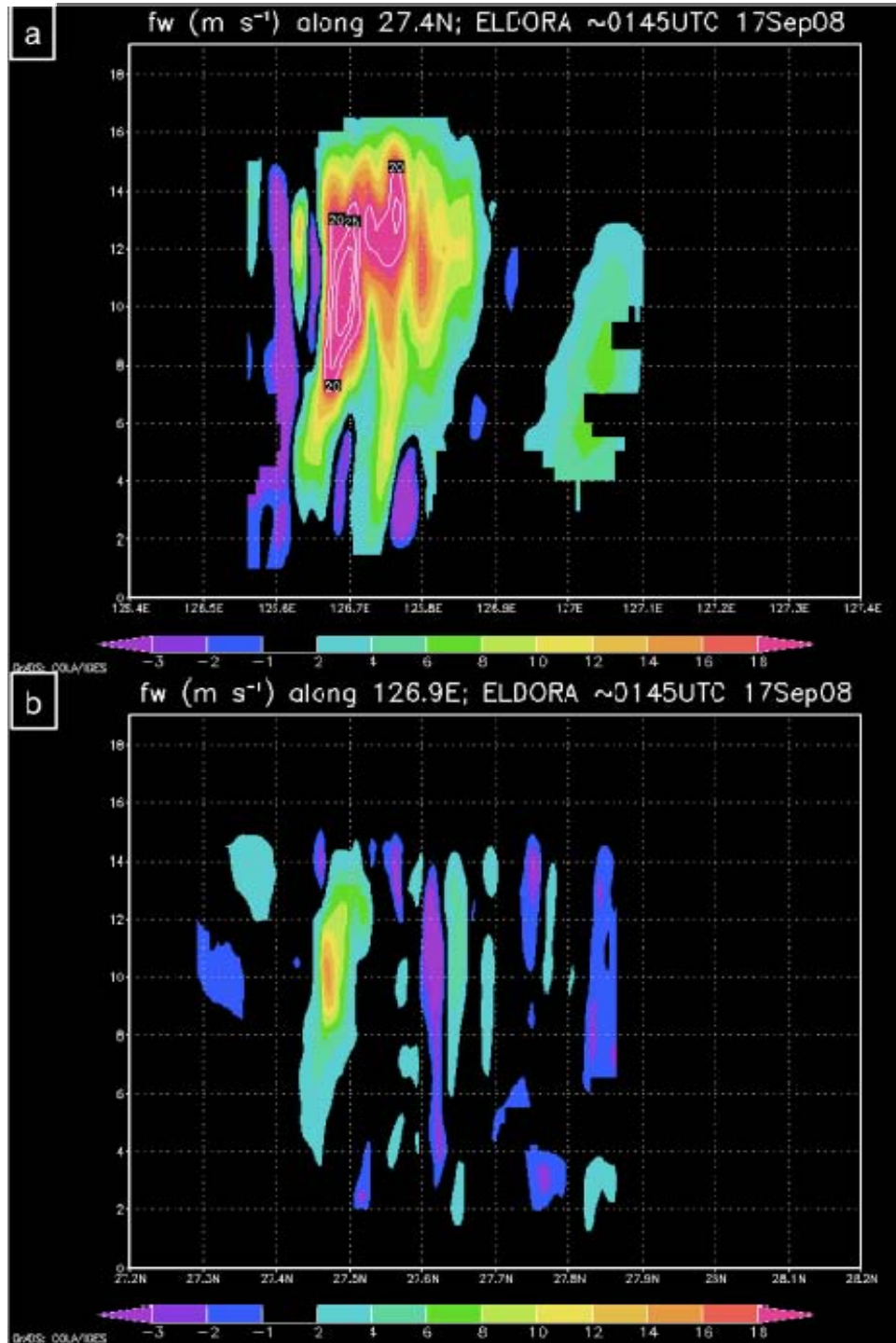
Figure 42.   Vertical cross-sections of vertical motion (m s^{-1}, shaded, scale at base) (a) along 27.4°N from 126.4°-127.4°E, (b) along 126.9°E from 27.2°-28.2°N, and southwest to northeast from (c) 27.25°N, 126.5°E to 28.2°N, 127.7°E, and (d) 27.59°N, 126.9°E to 28.2°N, 127.7°E from the ELDORA observations between 0135-0205 UTC 17 September 2008. Contours of updrafts exceeding 20 m s^{-1} are indicated in panel a at 5 m s^{-1} intervals.

150

Fig. 42, continued.

151
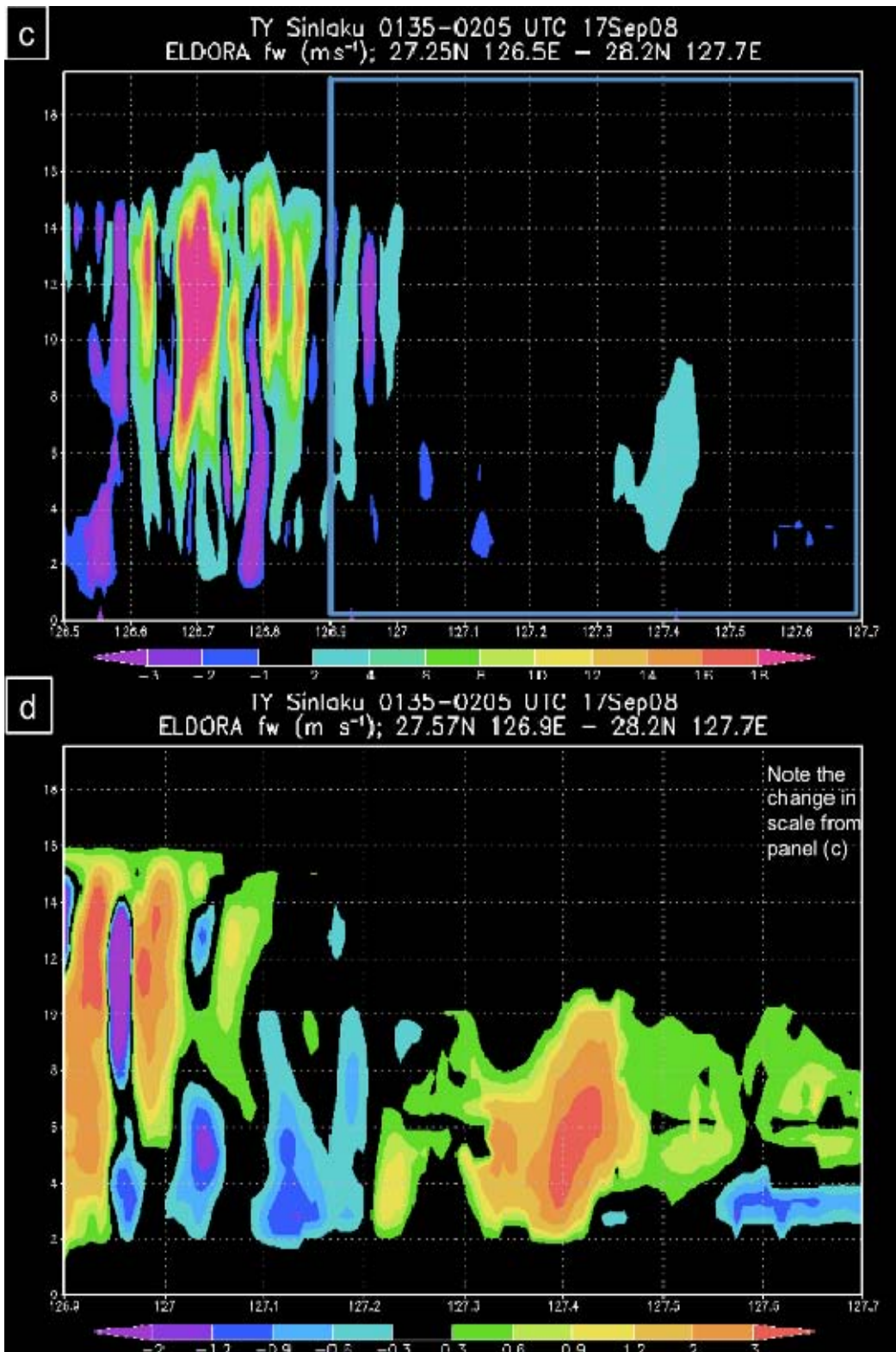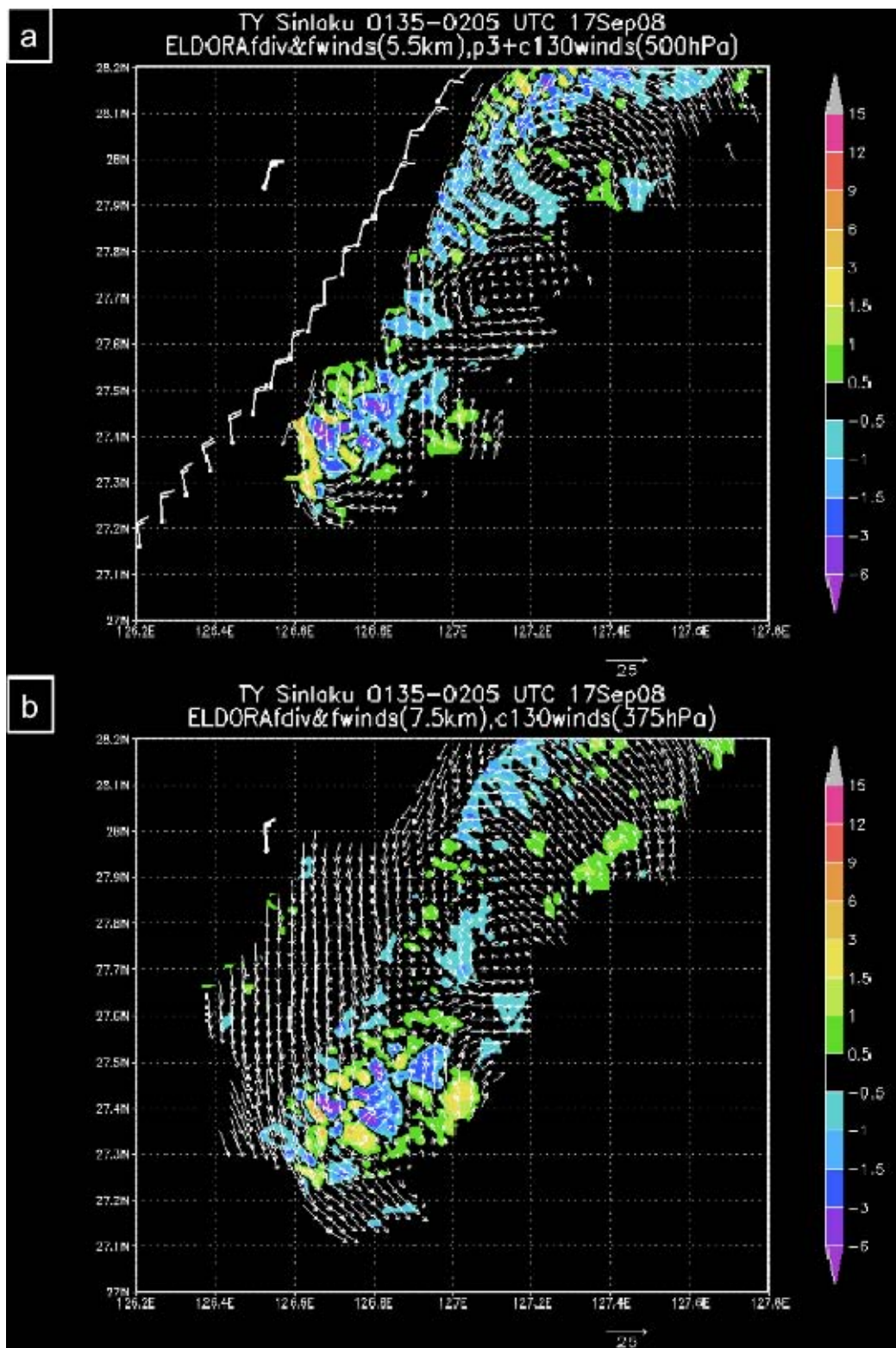
Figure 43.   Divergence (10^{-3} s^{-1}, shaded, scale on right) and winds (m s^{-1}, reference vector below each panel) at (a) 5.5 km, (b) 7.5 km, (c) 9.5 km, and (h) 13 km from the ELDORA observations between 0135-0205 UTC 17 September 2008.

Fig. 43, continued.

153
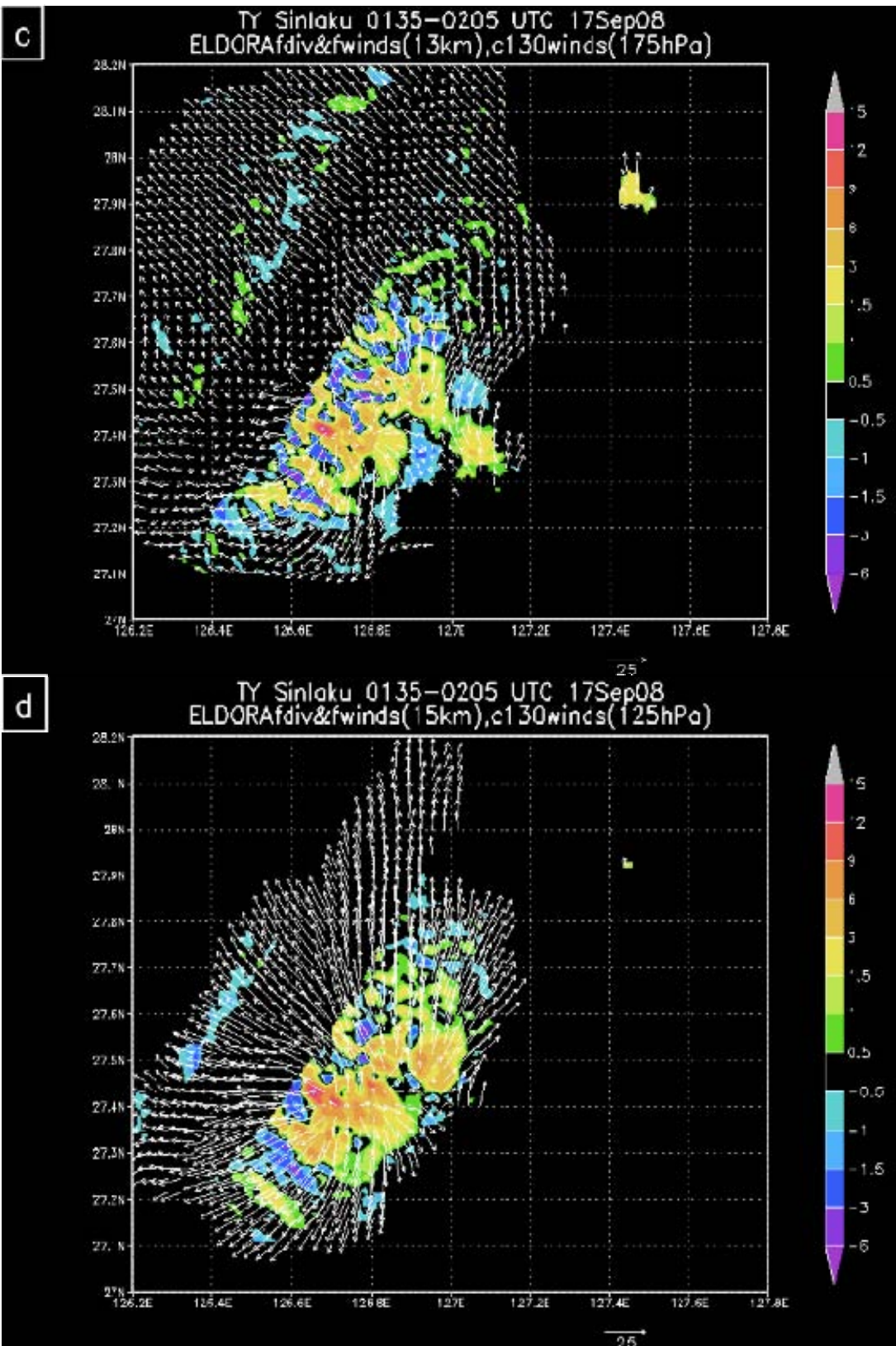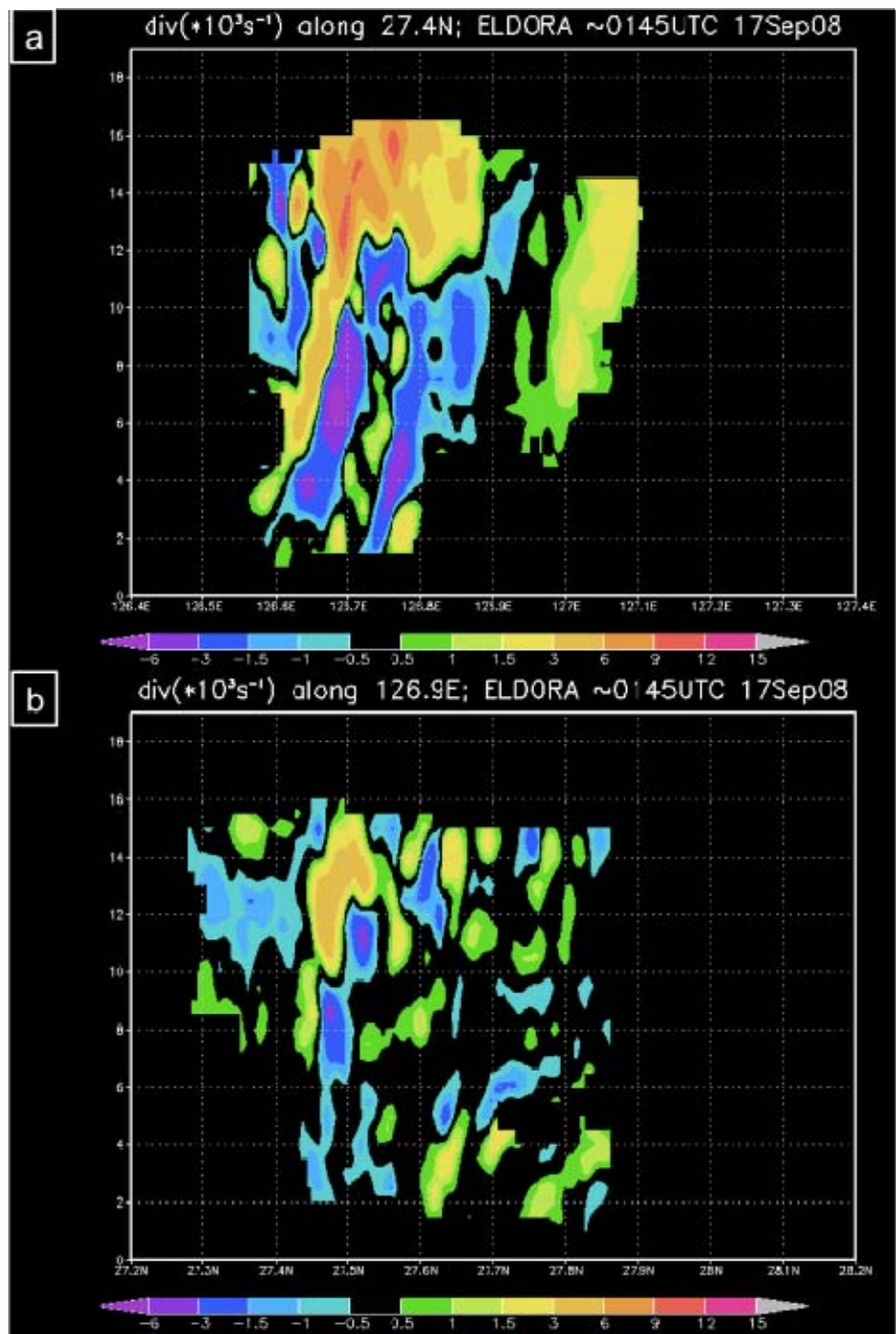
Figure 44.   Vertical cross-sections of divergence (10^{-3} s^{-1}, shaded, scale at base) (a) along 27.4^{o}N from 126.4-127.4^{o}E, (b) along 126.9^{o}E from 27.2^{o}-28.2^{o}N, and southwest to northeast from (c) 27.25^{o}N, 126.5^{o}E to 28.2^{o}N, 127.7^{o}E, and (d) 27.59^{o}N, 126.9^{o}E to 28.2^{o}N, 127.7^{o}E from the ELDORA observations between 0135-0205 UTC 17 September 2008.

154

c

TY Sinlaku 0135-0205 UTC 17Sep08
ELDORA divergence(s⁻¹); 27.25N 126.5E − 28.2N 127.7E

d

TY Sinlaku 0135-0205 UTC 17Sep08
ELDORA divergence(s⁻¹); 27.57N 126.9E − 28.2N 127.7E

Note the change in scale from panel (c)

Fig. 44, continued.

155

Figure 45.   Temperature perturbations (K, shaded, scale on right) and winds (m s^{-1}, vectors, reference vector below each panel) at (a) 1.5 km, (b) 3 km, (c) 5.5 km, (d) 7.5 km, (e) 9.5 km, (f) 10.5 km, (g) 11.5 km, and (h) 15 km from the ELDORA observations between 0135-0205 UTC 17 September 2008. In panel (e), WC-130J flight-level winds are defined by pink (287.5-312.5 hPa) and purple (267.5-287.5 hPa) wind barbs, and winds from the ELDORA are not plotted.

156

Fig. 45, continued.

ELDORA temp pert (K) & winds (m s⁻¹) at 9.5 km
c130 flt-lvl winds (300-275hPa); 0135-0205 UTC 17Sep08

ELDORA temp pert(K) & winds(m/s) at 10.5 km; 17Sep08/~02z

Fig. 45, continued.

158
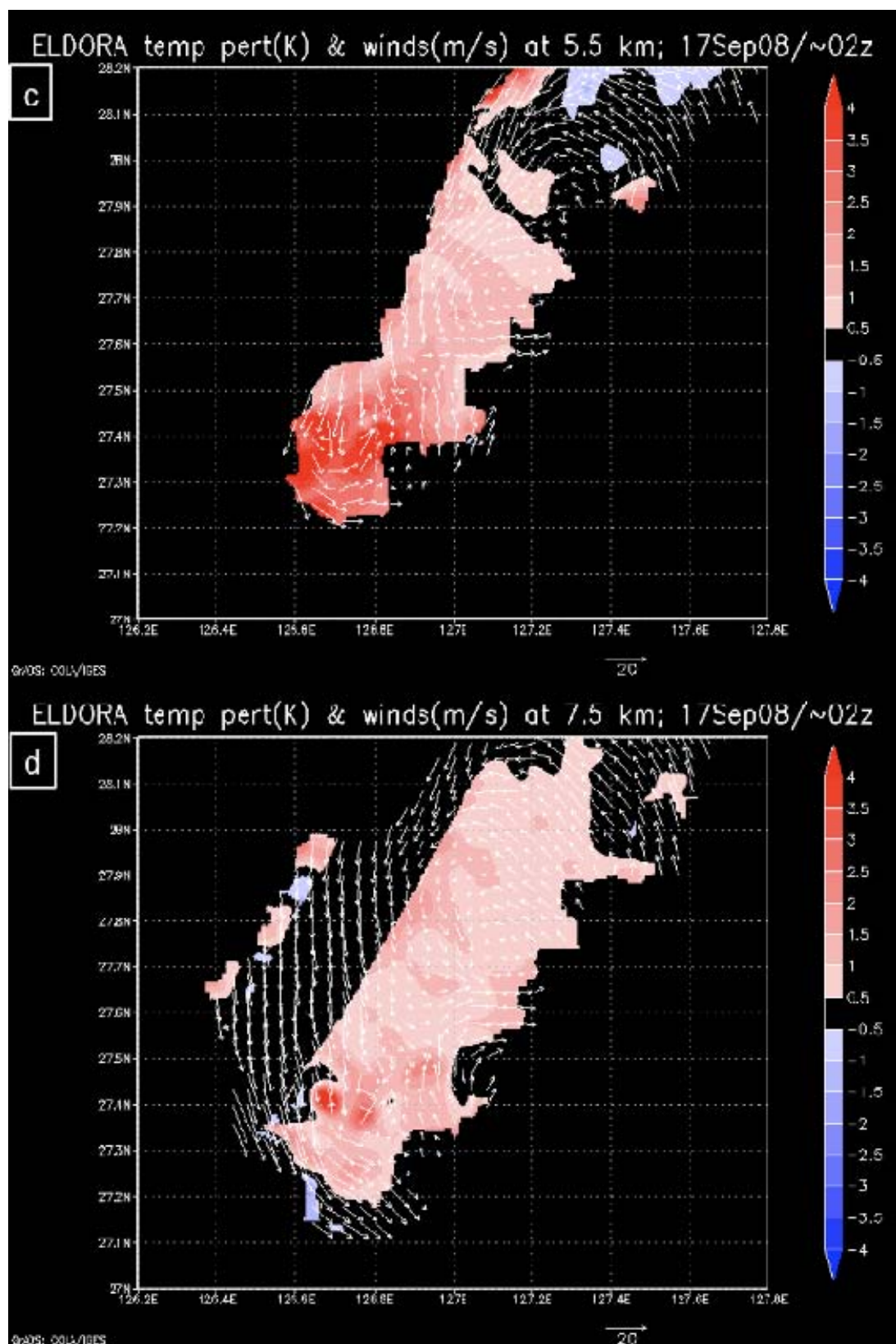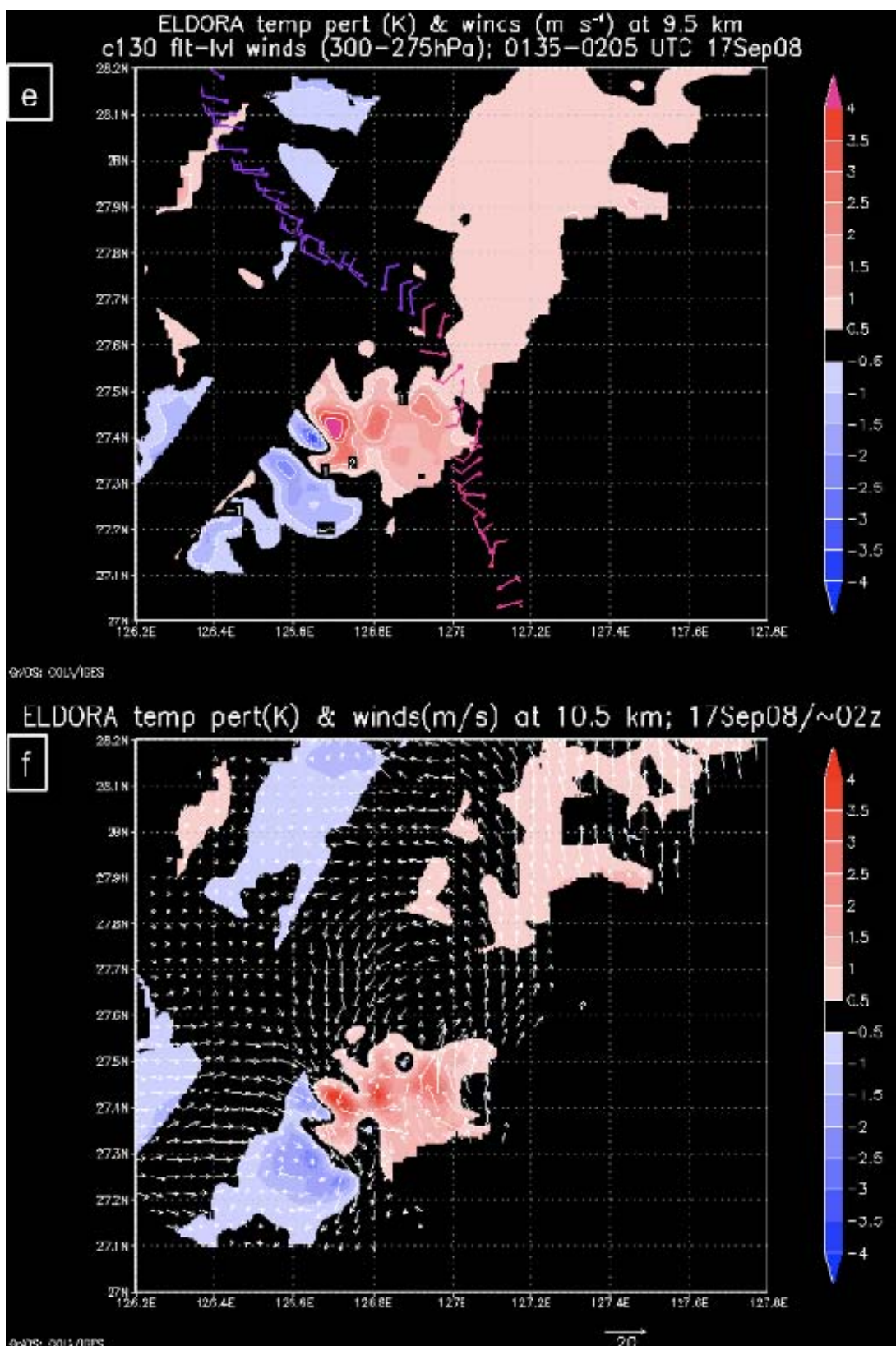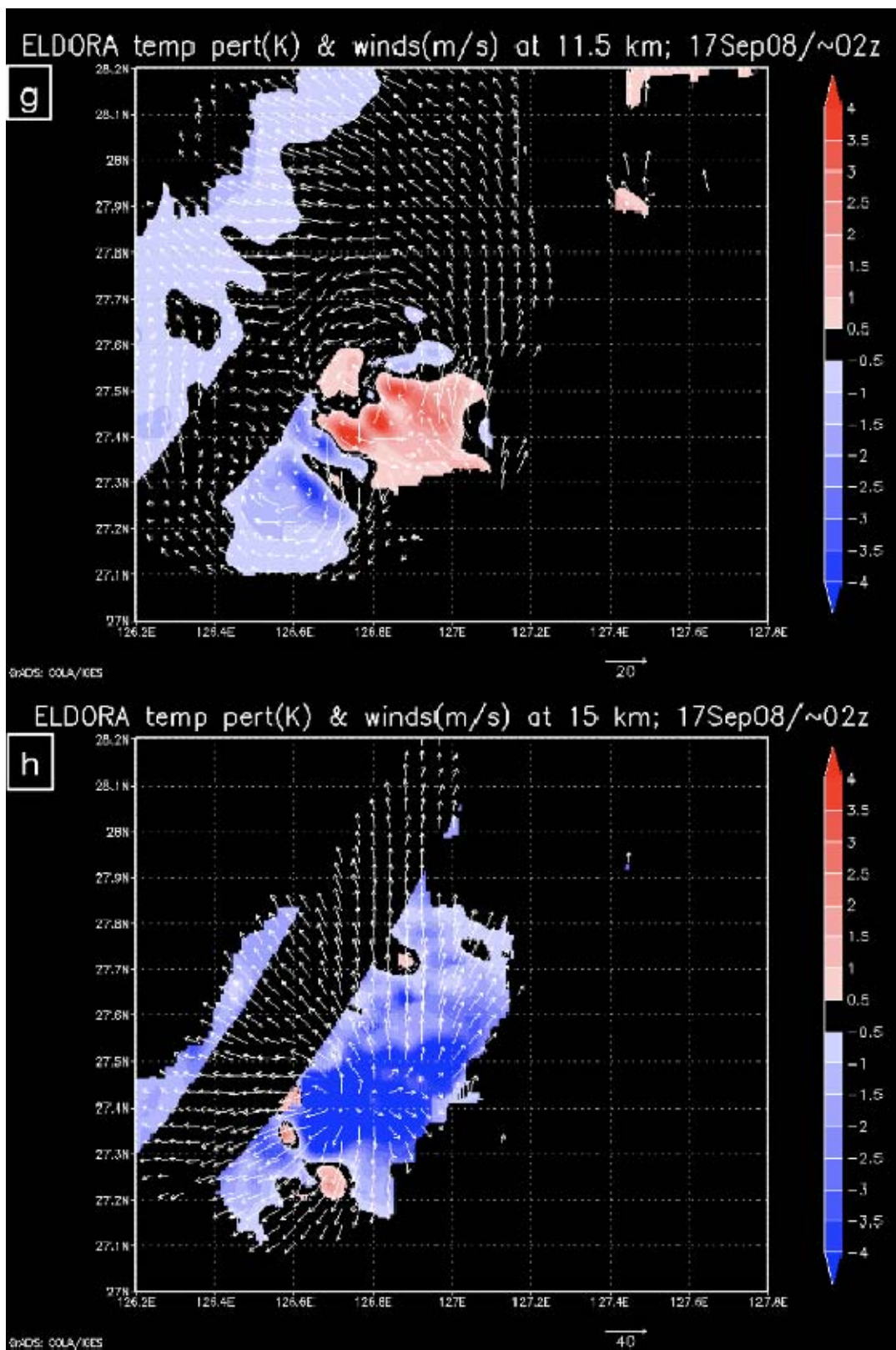
Fig. 45, continued.
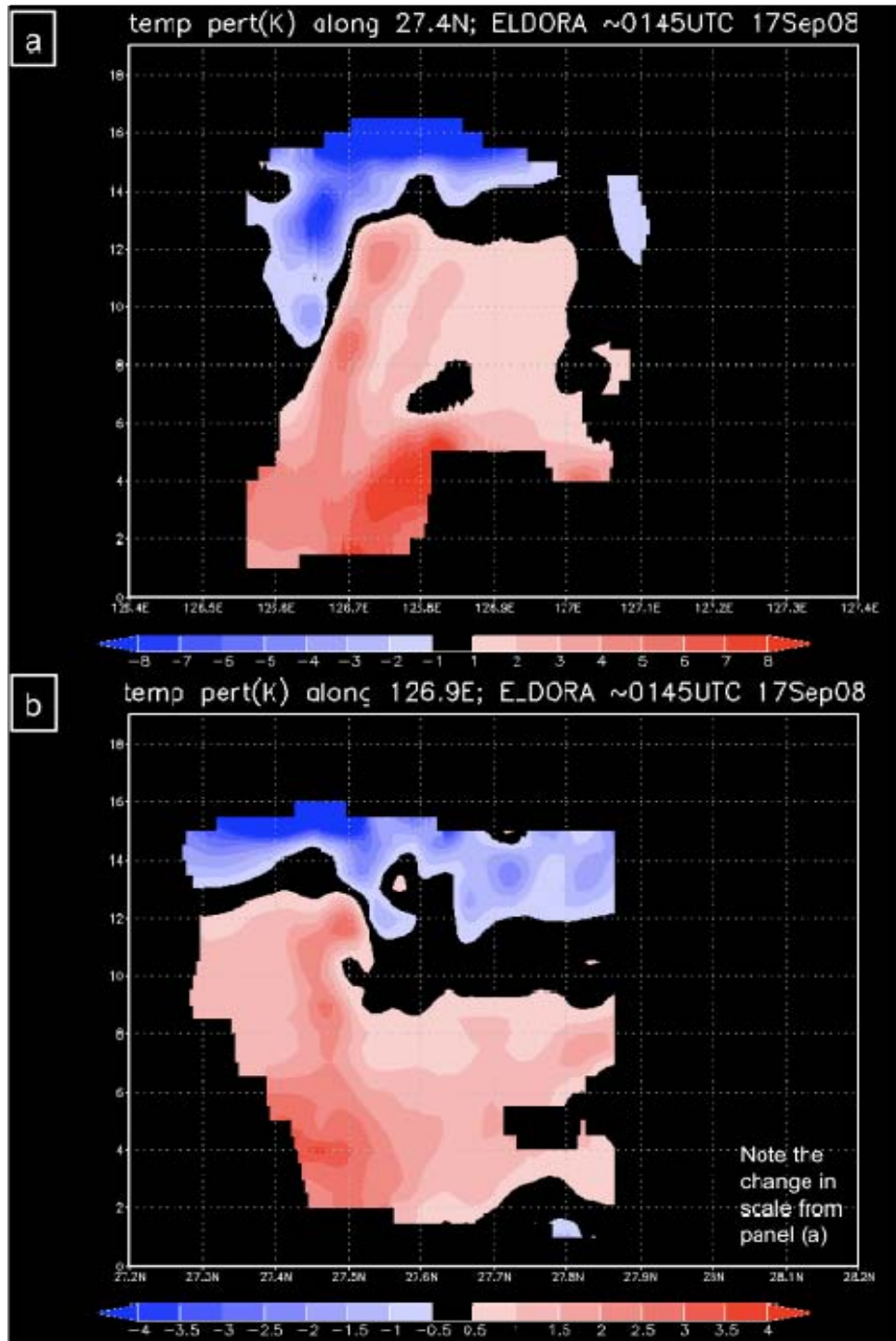
Figure 46.   Vertical cross-sections of virtual-cloud temperature perturbations (K, shaded, scale at base) (a) along 27.4^{o}N from 126.2^o-127.2^{o}E, (b) along 126.9^{o}E from 27.2^o-28.2^{o}N, and (c) southwest to northeast, from 27.25^{o}N, 126.5^{o}E through 28.2^{o}N, 127.7^{o}E from the ELDORA between 0135-0205 UTC 17 September 2008. In panel (c), the minima at the surface along 126.85^{o}E and 127.5^{o}E are artifacts of the plotting program.
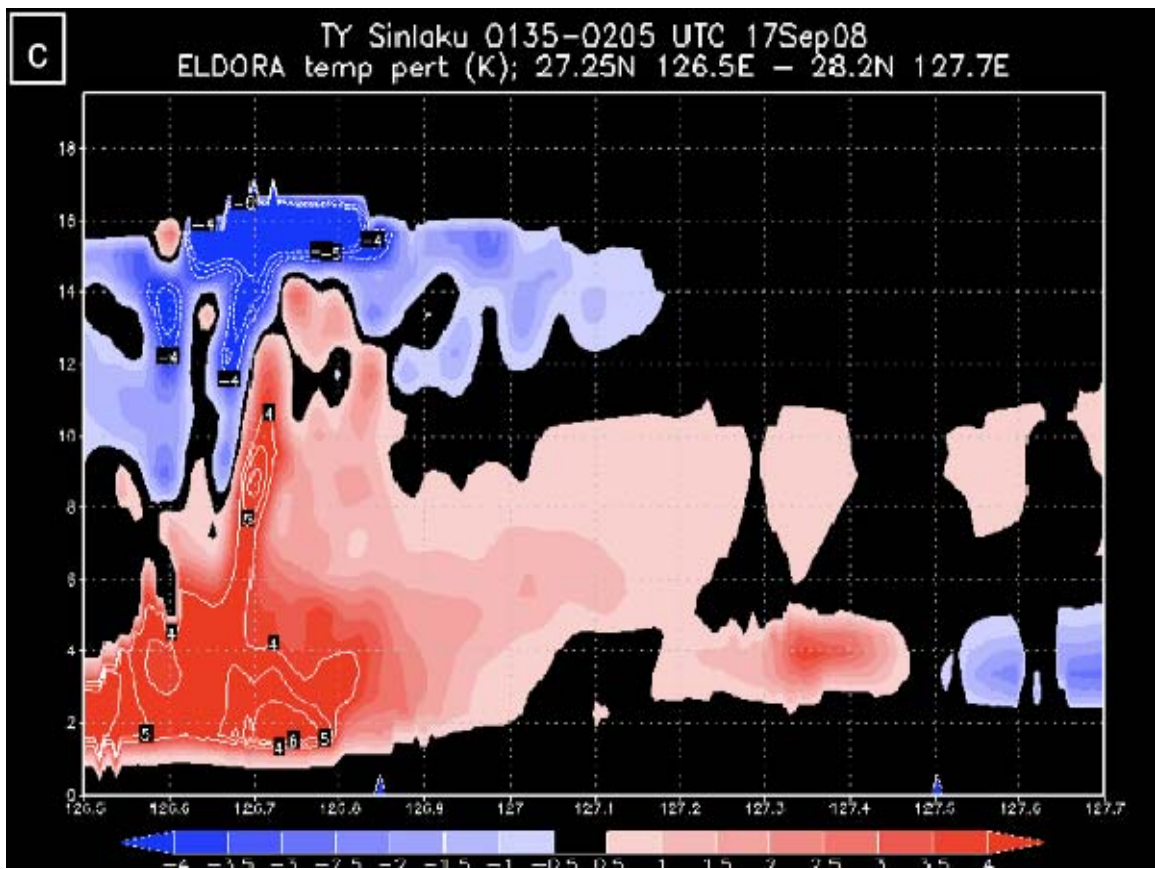
Fig. 46, continued.
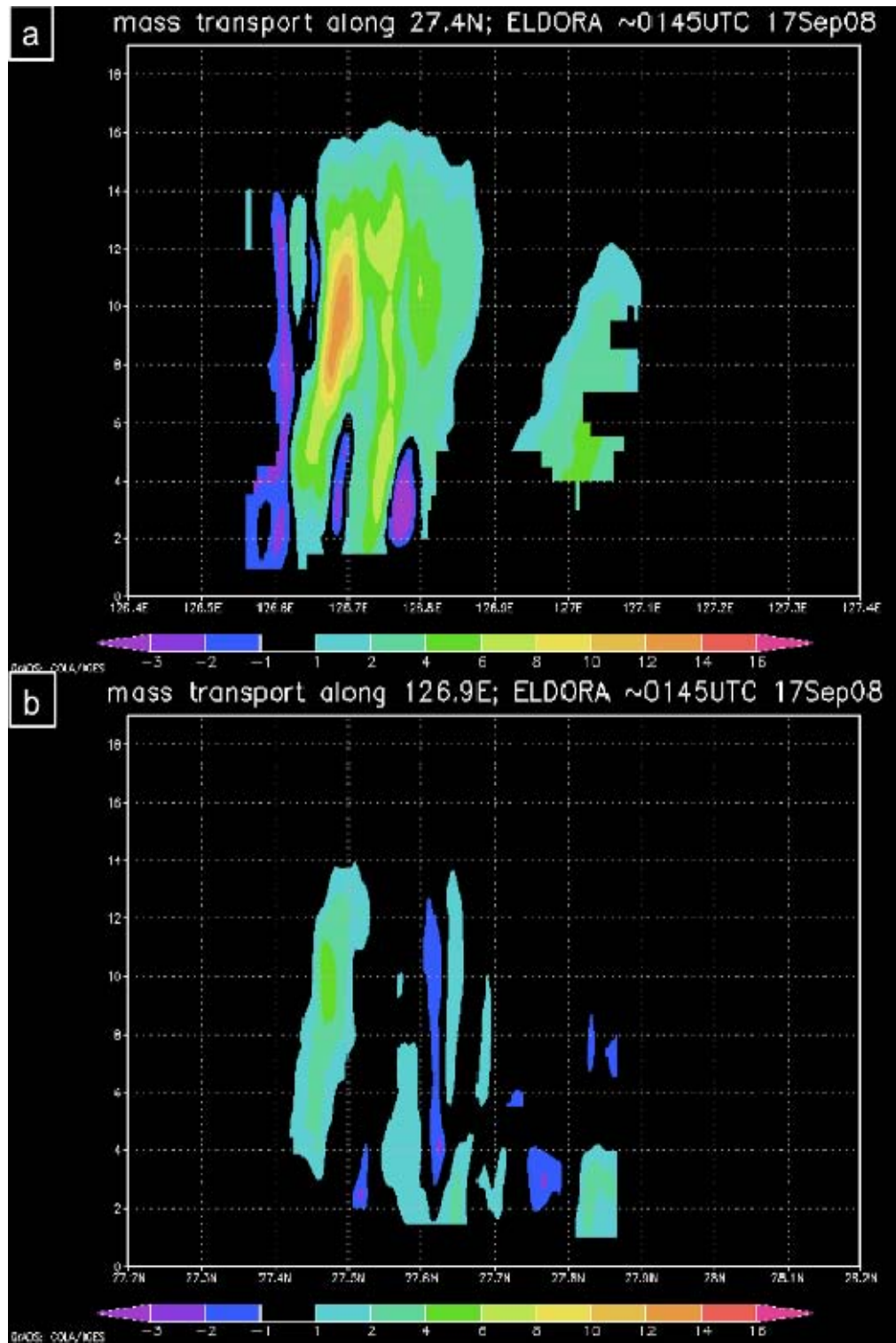
Figure 47.   Vertical cross-sections of mass transport (kg m^{-2} s^{-2}, shaded, scale at base) (a) along 27.4°N from 126.4°-127.4°E, (b) along 126.9°E from 27.2°-28.2°N, and (c) southwest to northeast, from 27.25°N, 126.5°E through 28.2°N, 127.7°E, from the ELDORA observations between 0135-0205 UTC 17 September 2008.
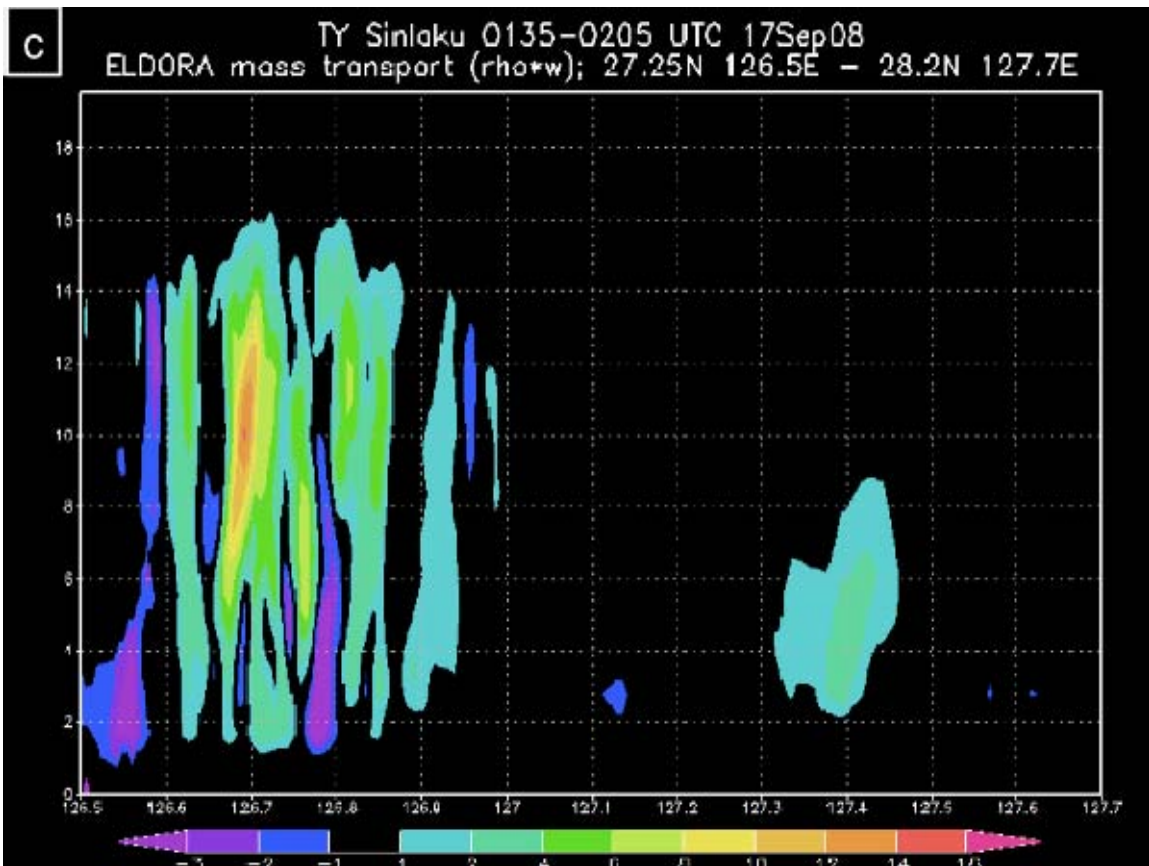
Fig. 47, continued.
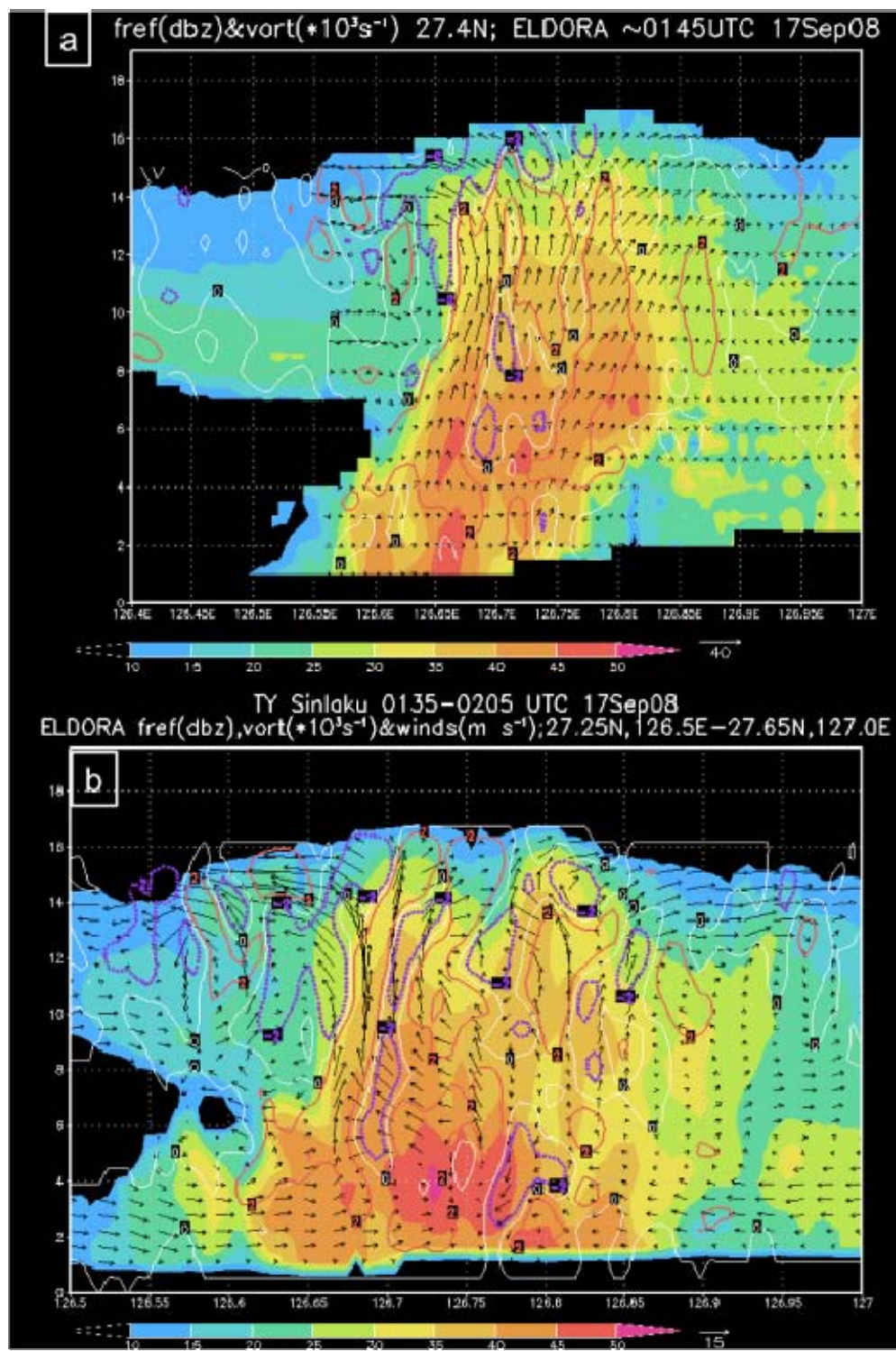
Figure 48.   Reflectivity (dBZ, shaded), vorticity (10^{-3} s^{-1}, positive contours in red, 0 contour in white, and negative contours in dashed purple), and wind (m s^{-1}, reference vectors below each panel) (a) along 27.4^{o}N between 126.4^o-127.0^{o}E, and between (b) 27.25^{o}N, 126.5^{o}E and 27.65^{o}N, 127.0^{o}E, and (c) 27.57^{o}N, 126.9^{o}E and 28.20^{o}N, 127.70^{o}E.
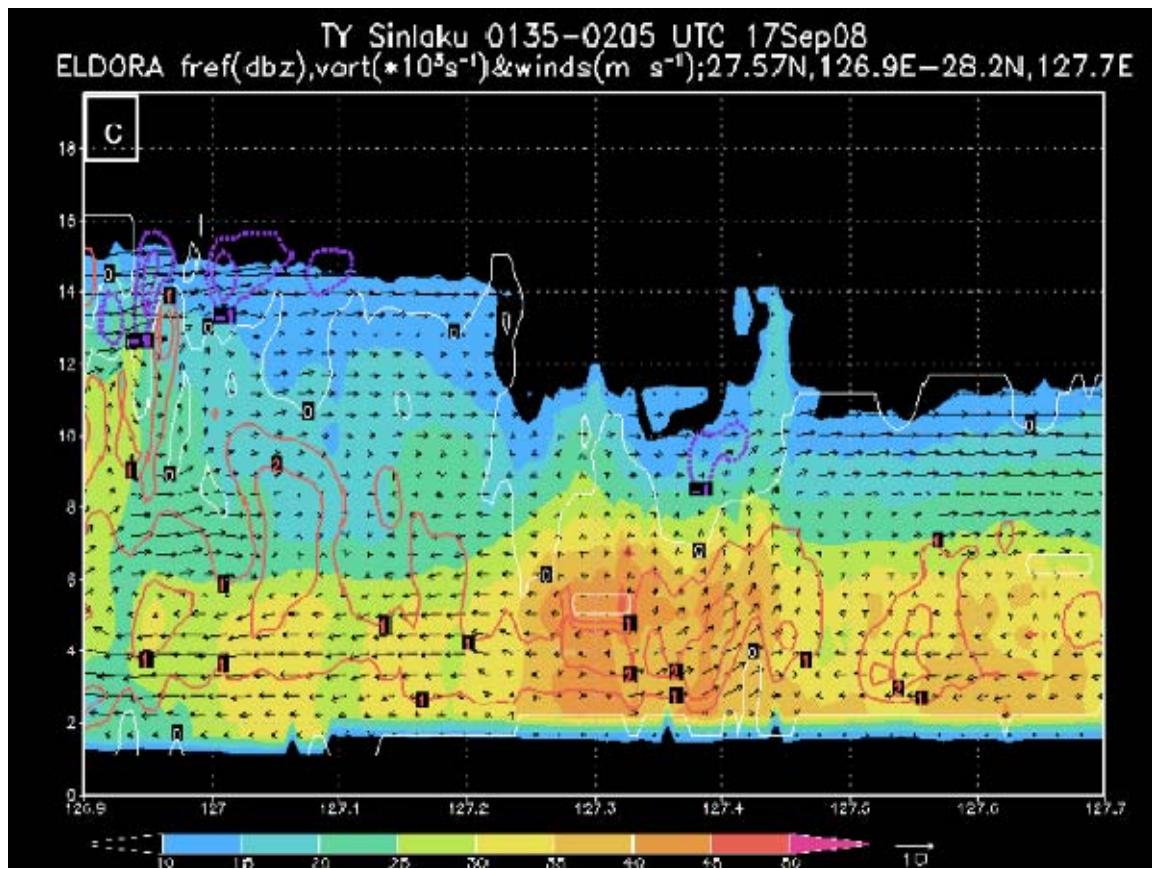
Fig. 48, continued.
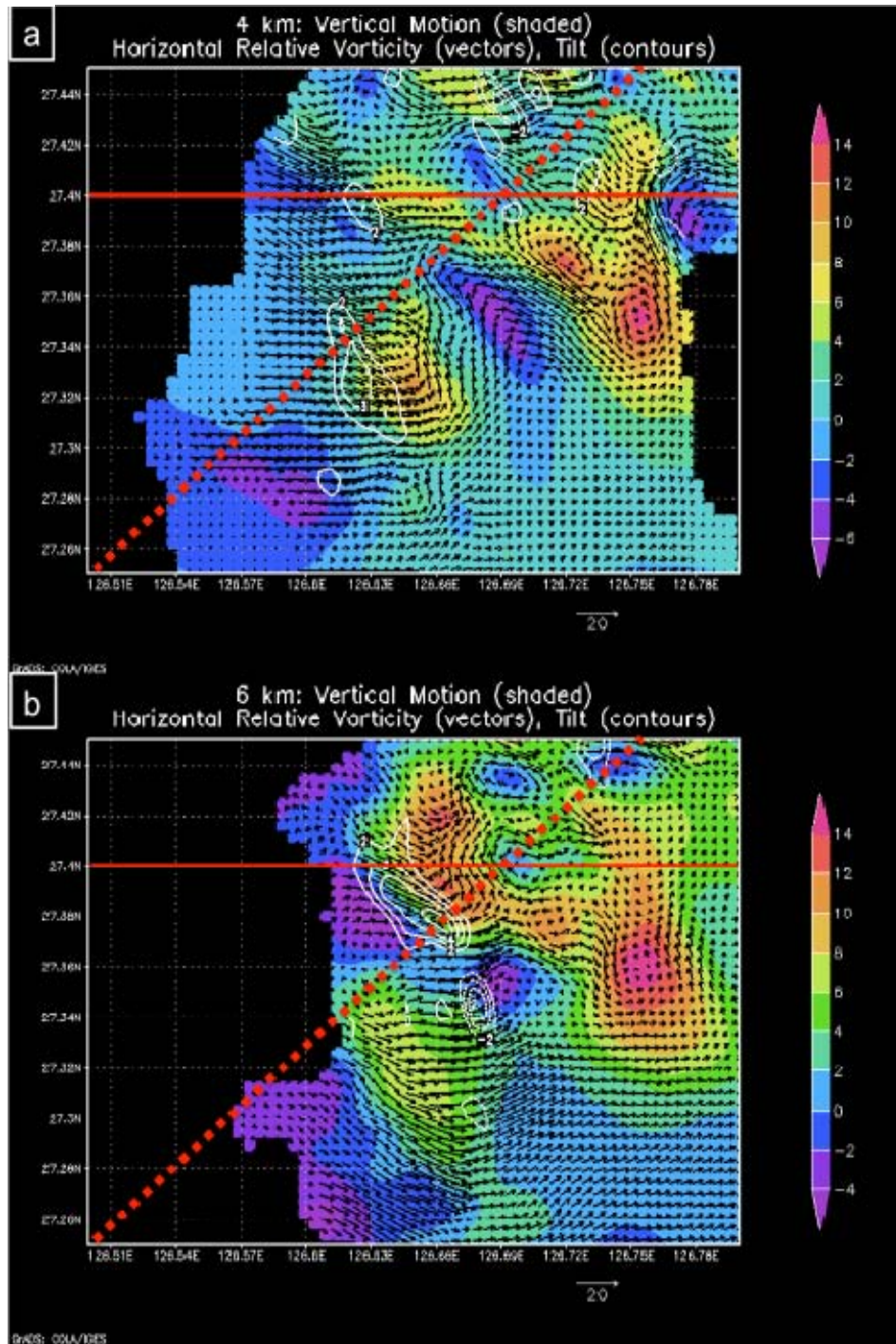
Figure 49.   Vertical motion (m s^{-1}, shaded, scale on right), horizontal relative vorticity (10^{-3} s^{-1}, reference vector below each panel), and tilt component of the vertical relative vorticity (10^{-5} s^{-1}, white contours; positive values are solid, negative values are dashed) at (a) 4 km, (b) 6 km, and (c) 12 km.   The solid red line identifies the TC latitude and location of the cross-section in Fig. 40a.   The dashed red line is a subsection of the southwest-to-northeast vertical cross-section in Fig. 40 c.

166
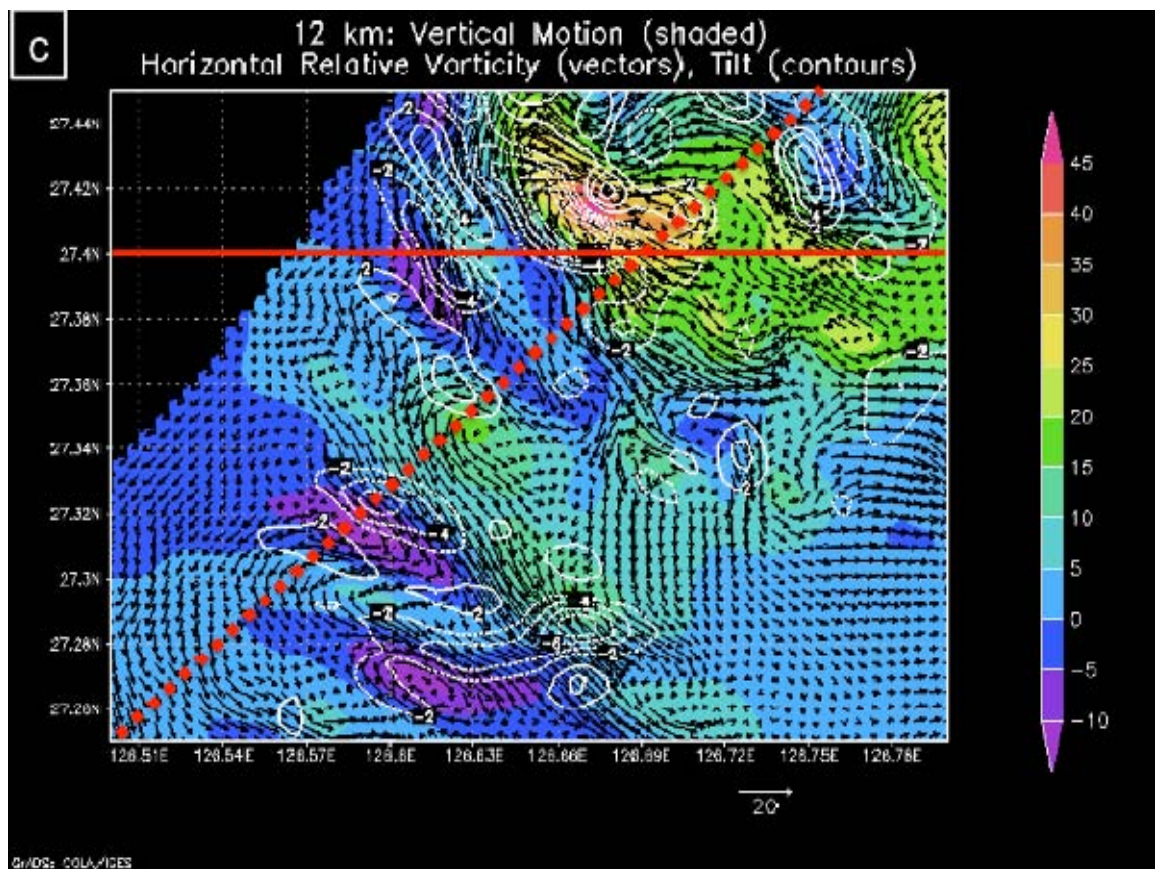
Fig. 49, continued.

THIS PAGE INTENTIONALLY LEFT BLANK

V. RE-INTENSIFICATION

Following observation of the interaction of the Sinlaku inner circulation and the convective-scale vortices by the WC-130J and P-3, deep convection continued to develop in close proximity to the TC center. The third convective episode from 16 September 2008 continued well into the next 24-h period and was followed by subsequent convective bursts. During this time, no TCS-08/T-PARC flights were conducted. Therefore, the evolution of the deep convection will be assessed through detailed analysis of satellite data. As was the case on 16 September 2008, multiple convective episodes occurred throughout the remainder of 17 September 2008. However, following the TC-multivortex interaction, a new pattern was clearly evident in the paths of current and subsequent convection, as these regions rotated cyclonically and inward, which contrasts with older convection from previous episodes that does not exhibit this type of rotation. Instead, a portion of an older convective region translates radially outward and dissipates while another portion moves slightly outward and develops into a principal band east of the TC vortex. In this section, the evolution of the convection on 17 September 2008 following the TC-multivortex interaction between 0135-0205 UTC 17 September 2008 is analyzed, the structure of the re-intensified TC is examined, and a possible mechanism for intensification is presented.

A. EVOLUTION OF DEEP CONVECTION

The third convective burst of 16 September 2008 that was analyzed in Chapter IV was the first of three convective episodes that formed near the TC center and rotated cyclonically about and inward toward the center on 17 September 2008. In the 0230 UTC 17 September 2008 enhanced IR imagery (Fig. 50a), the deep convection, noted as region "A", was near 27.5^{o}N 127.0^{o}E east-southeast of the TC center, which was near 27.7^{o}N, 126.4^{o}E. As detailed in the previous chapter, the second episode of deep convection from 16 September 2008 is defined as the crescent region of lower brightness temperatures between 128-129°E to the east and northeast of the third convective burst. Farther to the northeast, the remnants of the first convective episode dissipated.

Two hours later (Fig. 50b), the center of the deepest convection in region A had rotated cyclonically about the TC center and was located due east of the TC near 27.9^{o}N, 126.7^{o}E. The second convective episode east of the third burst shifted eastward and was located between 128.5-130°E. Within the region of the second convective episode, new convection had developed near 128.5^{o}E between 26.5-27.5^{o}N, which was east of Okinawa and southeast of the TC center.

By 0630 UTC 17 September 2008 (Fig. 50c), the minimum brightness temperatures associated with region A were located near 28.5^{o}N, 127.7^{o}E, which was northeast of the TC center position at 28.2 ^{o}N, 127.1^{o}E. The majority of the second convective episode had moved northeastward and weakened along 130°E. However, the convection east of Okinawa persisted between 26.5-27.5^{o}N.

Three hours later (Fig. 50d), the region of minimum brightness temperatures associated with region A elongated from northwest (28.5^{o}N, 127.2^{o}E) to the northeast (29°N, 129°E) of the TC center as over half of the coldest cloud tops were immediately northwest of the TC center. The northern half of the second convective episode had further weakened and nearly dissipated, but was still evident as the banded feature oriented from southeast to northwest on the northeastern periphery of the TC convection between 29°N, 132°E and 31°N, 129°E. However, the remnant southern half of the second convective episode had deepened dramatically and extended northward from near 27.5^{o}N to near 29°N along 129.5^{o}E. This region of convection was now beginning to organize into a principal band structure.

By 1257 UTC 17 September 2008 (Fig. 51a), brightness temperatures associated with region A were no longer evident in the enhanced IR imagery. However, a new burst of deep convection, defined as "region B" and defined by circular spreading of minimum brightness temperatures, erupted near 29.0^{o}N, 128.5^{o}E northeast of the TC center. To the east, the southern remnant of the second convective episode continued to evolve into a linear band of deep convection defined by minimum brightness temperatures along 130.5^{o}E.

Over the next hour (Fig. 51b), the deep convection in region B had rotated cyclonically northwestward to 29.7°N, 128.6°E while the TC moved northeastward to 29.1°N, 128.2°E. This relative motion altered the relative position of the convection to north-northeast of the TC center.

By 1457 UTC 17 September 2008 (Fig. 51c), the lowest brightness temperatures in region B rotated west-southwestward to near 29.5°N, 128.1°E, which coupled with the northeastward TC motion had shifted the deep convection northwest of the TC center.

By 1557 UTC 17 September 2008 (Fig. 51d), brightness temperatures associated with region B began to increase, which indicated that the initial dissipation stage of the convection had begun. The center of the lowest brightness temperatures became stretched cyclonically and was located directly over the TC center near 29.3°N, 128.4°E.

The third convective burst to rotate cyclonically into the center of TY Sinlaku on 17 September 2008 is defined as "region C" and began near 1857 UTC 17 September 2008 (Fig. 52a) north-northwest of the Sinlaku center. An hour later (Fig. 52b), the minimum brightness temperatures associated with region C increased slightly but expanded in areal extent as the region moved slowly westward. The TC continued to move northeastward as the deep convection remained northwest of the center. To the east, a new region of deep convection developed just west of the southern half of the second convective episode along 130.5°E. By 2057 UTC 17 September 2008 (Fig. 52c), region C was west-northwest of the TC center position while convection to the east-northeast of the TC center had increased in areal extent.

An hour later (Fig. 52d), region C had moved much closer to the TC center near 29.8°N, 129.2°E. The region of deep convection to the northeast of the TC center intensified rapidly. However, the most significant change at this time was the organization of curved bands that extended cyclonically from the west to the east of the TC center.

The second set of ET flights through the environment of TY Sinlaku by the WC-130J and P-3 began near 2230 UTC 17 September 2008. As the two aircraft approached the TC vortex from the northeast, the low brightness temperatures associated with deep

convection (Figs. 53a-b) persisted to the northwest of the TC center. The deep convection to the northeast also continued to develop and linear bands of precipitation arced anticyclonically to the south. The P-3 flight track (not shown) crossed the northern extent of this principal band in the region of deep convection near 30°N, 131°E and the aircraft had to alter course southward enroute to the TC vortex to pass safely through the band near 29.6°N, 131.5°E at around 0120 UTC 18 September 2008.

The cyclonic rotation regions A, B, and C around the TC center is summarized in a Hovmoller diagram (Fig. 54a) of IR brightness temperatures less than 210 K. The digitized satellite data are placed into a cylindrical grid centered on the interpolated JTWC best-track position. Azimuthal distribution of relevant parameters were defined from specific radius intervals. The rotations of the 2330 UTC 16 September 2008 (region A), 1257 UTC 17 September 2008 (region B), and 1857 UTC 17 September 2008 (region C) convective bursts between 55-165 km from the TC center are evident in the cyclonic (left-to-right) progression of the minimum IR brightness temperatures beginning at the onset of each convective burst.

While the lowest IR brightness temperatures define the coldest cloud tops, the WV and IR brightness temperatures difference (Fig. 54b) was also examined to further clarify the cloud-top height and associated depth of the convection. Differences greater than 2K define regions of overshooting tops in which clouds associated with very deep convection penetrate the tropopause (Fritz and Laszlo 1993; Ackerman 1996; Olander and Velden 2009). The three episodes of cyclonic rotation are also evident in the WV-IR brightness temperature differences that indicate the persistence of very deep convection through these periods. Consequently, continued production of low-level cyclonic potential vorticity that results from mid-level latent heat release may therefore be assumed based on the findings of Chen and Yau (2001).

B.   STRUCTURE OF THE RE-INTENSIFIED TY SINLAKU

The best-track intensity for Sinlaku at 0000 UTC 18 September 2008, which was immediately prior to the observation of the TC by the WC-130J and P-3, was assessed by the JTWC as 60 kt. This 25-kt increase in the 24 h since the preceding flight is consistent

with the structures observed in the satellite, aircraft, and radar data during the second ET flight. The TC vortex has a defined eye and eyewall structures (Fig. 55), and there is a significant increase in the symmetry and height of the TC over the past 24 h.

Minimum brightness temperatures near 30.3°N, 129.6°E in the 0145 UTC MTSAT IR imagery (Fig. 55a) are consistent with those associated with the deep convection northwest of the TC center in the 0130 UTC 18 September 2008 MTSAT enhanced IR imagery (Fig. 53b). The location of the eye in the region of higher brightness temperatures to the south near 29.95°N, 129.70°E compares favorably as well. Northeast of the center, minimum brightness temperatures along 131.5°E (Fig. 55a) are consistent with the location of the principle band that developed from the second consecutive episode of deep convection on 16 September 2008 (Fig. 53b).

As was the case during the previous flight, elevated ELDORA reflectivities at upper levels (11.5 km in Fig. 55b) match the locations of the IR brightness temperature minima reasonably well. Here, the offset is principally attributed to the timing of the pass. The environment of Sinlaku was in the northern portion of the MTSAT disk scan that was completed at 0145 UTC 18 September 2008. The eye location in the brightness temperatures coincided almost exactly with the shift in the WC-130J flight-level winds observed during the 0114 UTC 18 September 2008 center penetration (not shown). It is assessed that the offset between the IR brightness temperatures and ELDORA data results from digital data being given a time stamp later than the time at which the region was actually sampled. Despite the offset in time, the data are in generally good agreement.

Beneath the colder cloud tops, the distribution of lower-level reflectivities differed from that at upper levels (Fig. 55c), as had been the case during the previous ET flight. The characteristics of the ELDORA reflectivities and winds at 3 km (Fig. 55c) were very different than those observed 24 h prior. In an expanded display (Fig. 56a), the TC center, which is near 30.05°N, 129.8°E, was surrounded by multiple nearly symmetric bands of elevated reflectivity. An inner circle of high reflectivities spanned nearly 40 km in diameter, and an outer circle was nearly 110 km in diameter. The dimensions of the inner circle of increased reflectivities were consistent with the 25-n mi (near 46-km)

173

closed eyewall reported from the WC-130J during the first center penetration by that aircraft at 0114 UTC 18 September 2008 (WC-130J AF306 1033W Sinlaku mission scientist report, 17-18 September 2008).

The circulation about the vortex at 3 km during the second ET flight was both stronger and broader than during the first ET flight. Surface winds were measured at 63 kt (32.41 m s^{-1}) by the 0118 UTC 18 September 2008 WC-130J dropwindsonde released near 29.8^{o}N, 129.5^{o}E in the southwest eyewall, while the near-surface winds from the P-3 0136 UTC 17 September 2008 dropwindsonde southwest of the TC center had been near 10 m s^{-1}. Within the observed reflectivities on 18 September 2008 (Fig. 56a), the circulation was nearly symmetric, and cyclonic winds extended at least 55 km from the TC center. These structure characteristics were consistent with flight-level wind observations from the P-3 (Fig. 56a) and contrasted with the elliptical vortex and irregular cyclonic circulation at 3 km the day before.

At 9.5 km (Fig. 56b), the region of elevated brightness temperatures northwest of the TC center coincided with the region of deep convection previously noted (Fig. 53b). However, the 9.5-km maximum of near 30 dBZ was much less than the 45 dBZ that was associated with the deep convective towers at 9.5 km the day before. Based on the ELDORA reflectivity, the cyclonic circulation extended to 12 km, which was more than twice the height of the TC vortex 24 h prior.

The vertical extent of the eyewall convection (Fig. 57) was significantly less than that associated with the third convective burst 24 h prior (Fig. 38a). Two bands of elevated reflectivities on either side of the TC are evident in a vertical cross-section along the TC latitude of 30.05^{o}N (Fig. 57). The decrease in vertical extent from the convective towers 24 h prior (Fig. 38a) is noted, as reflectivities greater than 35 dBZ extend to more than 7 km in only one location. While the vertical extent of these structures is less than that of the third convective burst during the first ET flight, the consolidation of the reflectivities and winds about the vortex during that period is significant. Whereas an isolated region of deep convection had been situated over the eastern half of the Sinlaku

circulation 24 h previously, a nearly symmetric distribution of organized convection now comprised the Sinlaku eyewall and inner spiral bands to define the convection signature of a mature typhoon.

The increase in symmetry was also evident in the relative vorticity structure of the re-intensified Sinlaku. The relative vorticity at 3 km (Fig. 58a) near the Sinlaku vortex on 18 September 2008 is predominantly positive, with the maximum located in a ring-like feature near the center. Outside the vortex, isolated regions of negative relative vorticity are found, but these are of much smaller frequency and magnitude compared to the regions of positive relative vorticity.

At 9.5 km (Fig. 58b), the TC vortex is still surrounded by nearly uniform positive vorticity. However, the regions of alternating positive and negative relative vorticity are in much closer proximity to the TC center than at lower levels. The signature here contrasts significantly with the distribution of relative vorticity at 9.5 km 24 h prior (Fig. 39e), in which there had been no evidence of a ring of positive vorticity associated with the TC vortex at 9.5 km (because the TC vortex was less than 6 km in height).

In a vertical cross-section of relative vorticity (Fig. 59) along the TC latitude of 30.05^{o}N on 18 September 2008, the regions of positive relative vorticity that surround the vortex are evident. As in the vertical cross-section along the TC latitude from the first ET flight (Fig. 40a), there are columns of large positive vorticity with some negative vorticity interspersed among the regions of positive vorticity. Contrary to the distribution of vorticity during the previous flight, the columns of positive vorticity are not tilted. Additionally, the eastward increase in the base height of the reflectivity maxima and vorticity maxima that had been present on 17 September 2008 was no longer present. The increase in elevation of these features on 17 September 2008 was likely the result of the interaction between the TC flow and the synoptic-scale monsoon flow. In the 24 h between 0145 UTC 17-18 September 2008, the Sinlaku vortex had re-intensified, become vertically upright, and developed a much more symmetric distribution of eyewall convection.

The relationships among reflectivity, relative vorticity, and vertical motion were complex based on the vertical cross-section along the TC latitude (Fig. 60). The inner ring of positive relative vorticity was more closely aligned with the vortex than with the towers of reflectivity in the eyewall. The positive relative vorticity was larger on the east side of the eye. To the west of the eye, the positive relative vorticity was a maximum at upper levels and coincided with strong upward motion. Negative vorticity and downward motion existed between the two regions of high reflectivity to the west of the eye. General ascent extended above each strong reflectivity tower as well, and noteworthy descent between the towers on the west side of the vortex.

Virtual-cloud temperature perturbations (Fig. 61) calculated from the 0137-0207 UTC 18 September 2008 ELDORA observations reveal drastic changes in the 24 h following the TC-multivortex interaction. The reference sounding was kept constant to provide a basis of comparison between observations from the two flights. In the 24 h between flights, temperature anomalies at low levels had become much cooler, and temperature anomalies at upper levels had become much warmer. At an elevation of 3 km (Fig. 61a), the only positive temperatures anomalies present were in the region of the eyewall. Outside the eyewall, widespread cold anomalies prevailed. These regions of cold anomalies may have been due to precipitation falling from the deeper convective clouds that comprise the banded structure of the now mature TC. This contrasts sharply with the high positive temperature anomalies 24 h earlier (Fig. 45b) near the TC center and in the deep convective towers. Sea-surface temperatures and ocean heat content were very similar between the two days, so extreme differences in the surface heat fluxes are unlikely.

At upper levels (Fig. 61b), the situation was reversed. Widespread warm anomalies extended from the eyewall to outer radii. The region was warmer on average than at the same level the day before, when aside from the three localized maxima in the region of the third convective burst (Fig. 45e), most of the 9.5 km temperature anomalies the previous day had been ≤ 1 K.

The vertical cross-section of temperature anomalies (Fig. 62a) from the second flight is similar to the temperature profile in a mature typhoon (Houze 2010). On both

sides of the eyewall, a low-level maximum is near 5 km elevation (reducing the likelihood of an error at the boundaries), and there are multiple maxima aloft. The dual-maxima structure is loosely corroborated by brightness temperature anomalies from the 2104 UTC AMSU-A (the red-boxed region in Fig. 62b). While the AMSU-A grid scale (48 km at nadir) is nearly 100 times the ELDORA grid scale, in each case a comparatively small warm anomaly exists at low levels, and a broad and much warmer anomaly is present at upper levels. In both the ELDORA and AMSU-A temperature retrievals, cold anomalies exist at outer radii in association with precipitation falling from the convective bands of the outer TC circulation.

Flight-level observations by the WC-130J in multiple passes through the TC vortex on 18 September 2008 (Fig. 63) also revealed the warm core of Sinlaku at 700 hPa. The first pass through the center at 0114 UTC 18 September 2008 most closely coincided with the 0137-0207 UTC 18 September 2008 passage of the P-3 through the environment of the Sinlaku vortex and the ELDORA data from that period. In that WC-130J center penetration, flight-level temperatures increased from 5°C northeast of the center to 12°C in the center and then decreased to 7°C on the southwest side of the center. Several flight-level temperatures may have again been affected by sensor wetting, as multiple dew-point temperatures were coded as missing as the WC-130J transited through the eyewall (white lines in Fig. 63). Even with the suspect temperatures, the TC center was warmer than the surrounding environment at 700 hPa. Therefore, Sinlaku had re-intensified into a warm-core, upright TC near typhoon intensity.

C. SYNTHESIS

The cyclonic rotation of regions of deep convection (labeled A, B, and C in Figs. 50-52) about and toward the TC center and the development of a principal band that occurred during the re-intensification of TY Sinlaku on 17 September 2008 fit a conceptual framework of TC intensification by axisymmetrization. As in Carr and Williams (1989), the asymmetric nature of the third convective burst on the eastern side of the TC evolves into a symmetric circulation about the TC center 24 h later, as asymmetries appear to be dampened by shear in the tangential wind. The eruption of

these convective bursts in close proximity to the TC center was similar to the "single cluster" numerical experiments of Montgomery and Enagonio (1998) and Enagonio and Montgomery (2001) in which a single convective-like PV asymmetry was introduced east of a mean vortex in a quasigeostrophic (Montgomery and Enagonio 1998) and shallow water primitive equation (Enagonio and Montgomery 2001) framework. In these experiments, interaction between the PV anomaly and the mean vortex resulted in intensification of the parent (mean) vortex.

While the PV anomaly introduced in Montgomery and Enagonio (1998) was designed to mimic the behavior of cumulus convection, simulations by Chen and Yau (2001) further defined the coupled nature of PV and cloud bands. Following these theories, it is suggested here that the deep convection defined by >2K differences in the WV-IR brightness temperatures resulted in mid-level latent-heat release that generated a low-level PV anomaly. The persistence of this deep convection resulted in the growth of these low-level PV anomalies, and the cyclonic rotation of the convection into the TC center enhanced the PV (and relative vorticity) associated with the TC center, deepening the system.

Each of the three convective bursts that rotated about the Sinlaku center on 17 September 2008 became elongated as they began to weaken. This tendency is particularly evident between 0630-0930 UTC 17 September 2008 (Figs. 50c-d) for region A, 1457-1557 UTC 17 September 2008 (Figs. 51c-d) for region B, and 1857-2157 UTC 17 September 2008 (Fig. 52) for region C. This filamentation of deep convection occurs in the axisymmetrization process as positive vorticity is stripped from the low-level PV centers and transported into the central vortex.

The development of the principal band east of the Sinlaku vortex from the southern half of the second convective episode from 16 September 2008 may also fit the axisymmetrization paradigm. In this instance, the convection did not rotate inward, but propagated slightly outward before anchoring 2.5^o lat. east of the TC center. This defines an outward propagation of positive relative vorticity to a stagnation point, and subsequent development into a principal band. Although the primary mechanism for this has been shown previously to be vortex Rossby waves, here it is thought to also result from the

178

initial orientation of the second and third convective episodes with respect to the TC vortex. In the Montgomery and Kallenbach (1997) formulation for the radial group velocity of vortex Rossby wave packets (based on the Wenzel-Kramers-Brillouin analysis) in cases of downshear tilt, the sign of the radial group velocity was shown to be dependent on the relative vorticity gradient. A positive radial gradient of relative vorticity would result in a negative radial group speed and propagation of the wave packets radially inward. A negative radial gradient, however, would result in a positive radial group speed and propagation of wave packets radially outward. In the previous chapters, it was shown that the relative vorticity associated with the third convective burst was far greater than that associated with the TC to the west and with the remnants of the second convective burst to the northeast. As a result, the radial gradient of relative vorticity would increase from the TC center to the region of the third convective burst, but would then decrease between the third convective burst and second convective episode. The increase in the radial gradient of relative vorticity between the TC center and the third convective burst would then account for the inward motion of the deep convection associated with the third convective episode, as well as with the 1257 UTC (region B) and 1857 UTC (region C) 17 September 2008 bursts. The decrease in the radial gradient between the third and second convective episodes would then account for the outward movement of the older second convective episode. In numerical experiments, outward propagating waves reach stagnation points and develop into spiral bands. While it is unknown whether the second episode of deep convection reached a stagnation point, the southern half of that episode did evolve into the principal spiral band nearly 2.5^o long. east of the TC center with intense convection that necessitated the adjustment of the P-3 flight track.

The development of deep convection in close proximity to the TC center, subsequent rotation of that convection into the TC center, and filamentation of the decaying convection near the TC vortex defined the 24-h period following the first ET flight through the environment near TY Sinlaku on 17 September 2008. These observations fit the framework of intensification by axisymmetrization. The impact of these convective and mesoscale processes on the vortex scale was evident in the structure

179

of the re-intensified TY Sinlaku during the second TCS-08/T-PARC ET flights by the WC-130J and P-3. The warm core, upright TC near typhoon intensity on 18 September 2008 bore little resemblance to the disorganized minimal tropical storm Sinlaku had been 24 hours before.

In Chapter III, the decay of TY Sinlaku following recurvature and development of three episodes of deep convection east of the TC were investigated. In Chapter IV, the interaction between the TC and the three mesoscale vortices associated with the third convective episode were shown to arrest the decay of the TC. Here, a mechanism for the sustained re-intensification on 17 September 2008 has been elucidated and the structure of the re-intensified TC has been defined. In the next chapter, this sequence of events will be examined in the context of scale analysis.
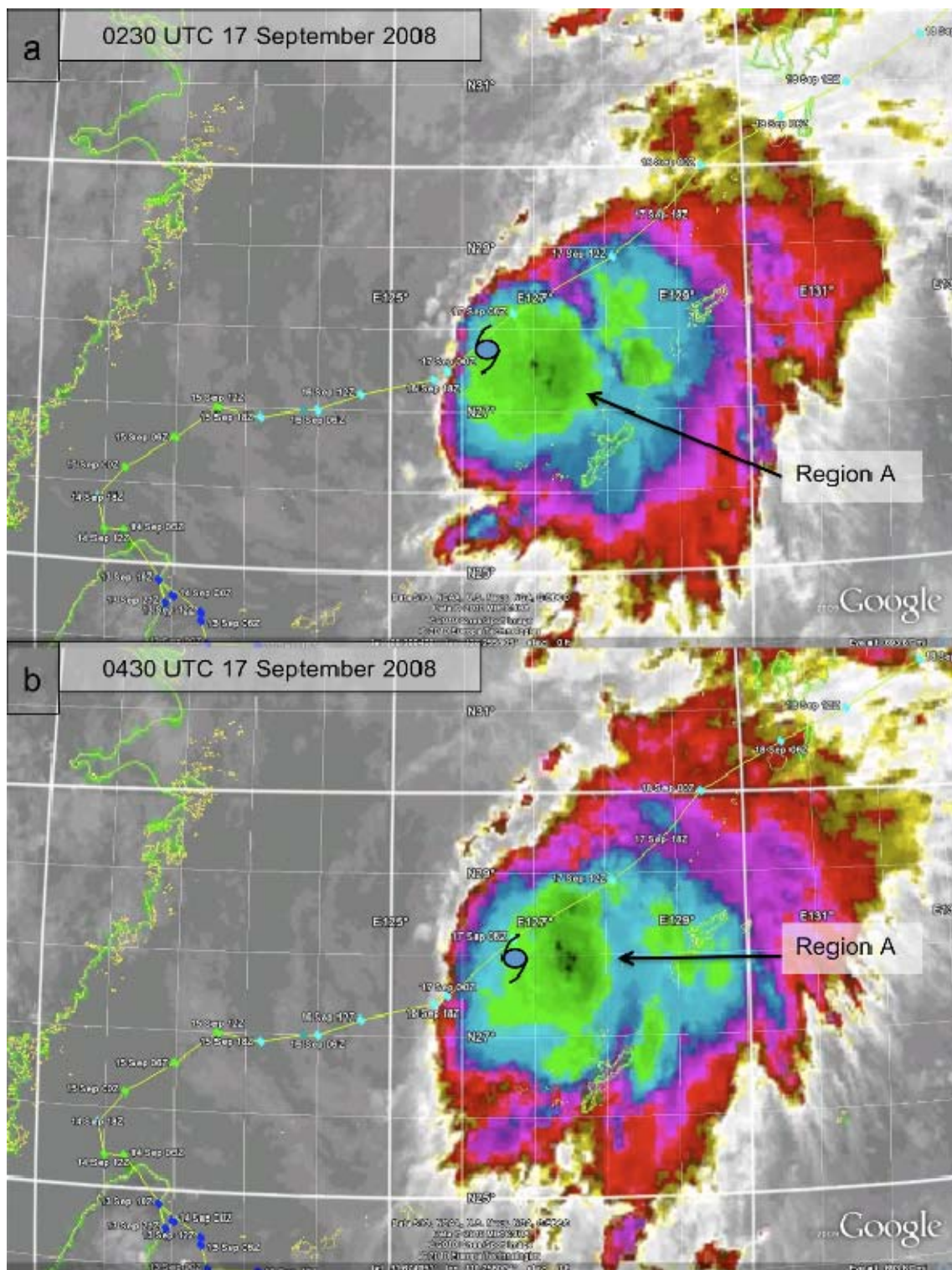
Figure 50.   Enhanced MTSAT IR imagery of TY Sinlaku at (a) 0230, (b) 0430, (c) 0630, and (d) 0930 UTC 17 September 2008. The typhoon symbol is located at the center of the TY Sinlaku circulation at the time of each image based on the JTWC best-track positions in Fig. 2b.

181
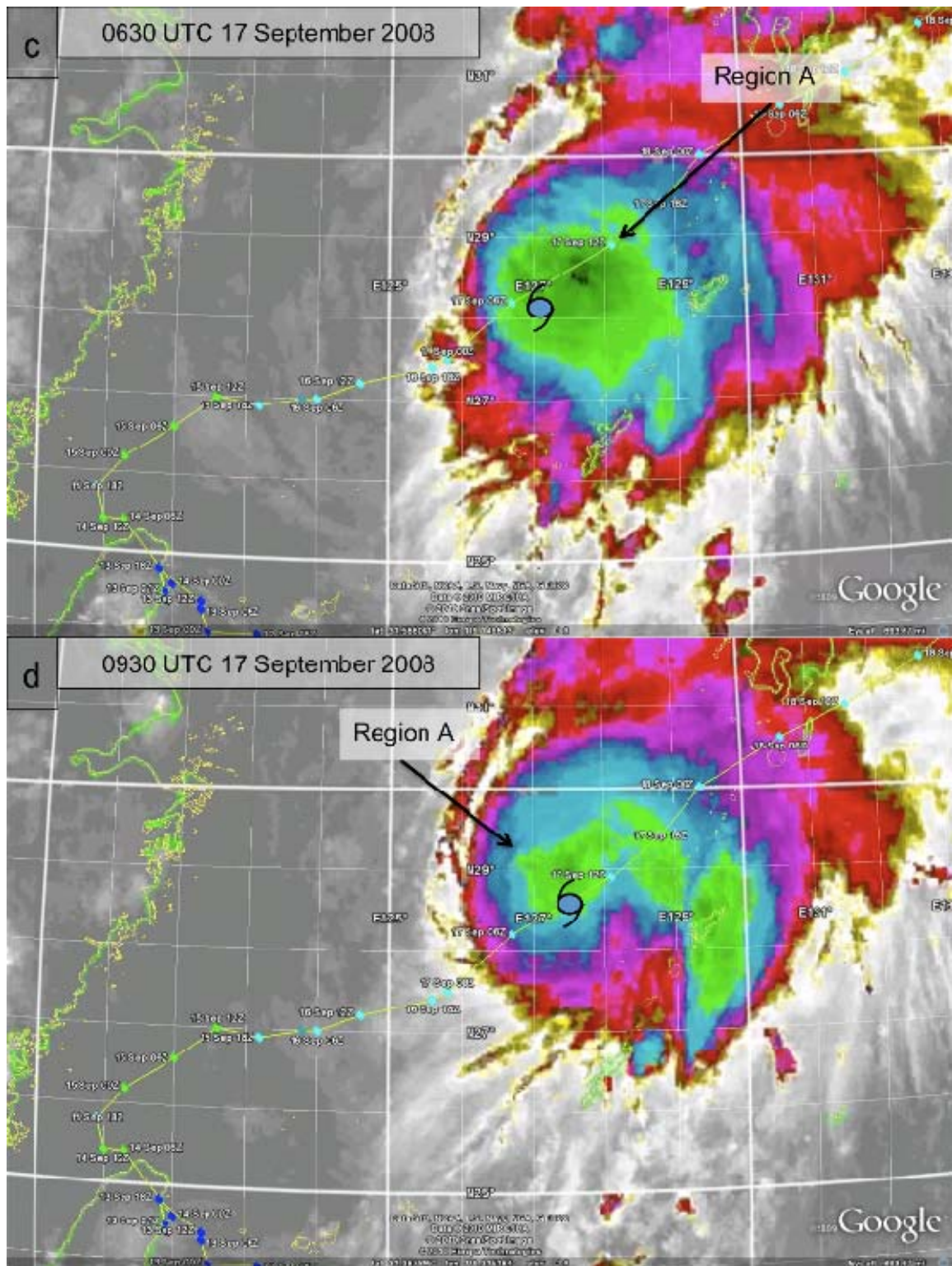
Fig. 50, continued.
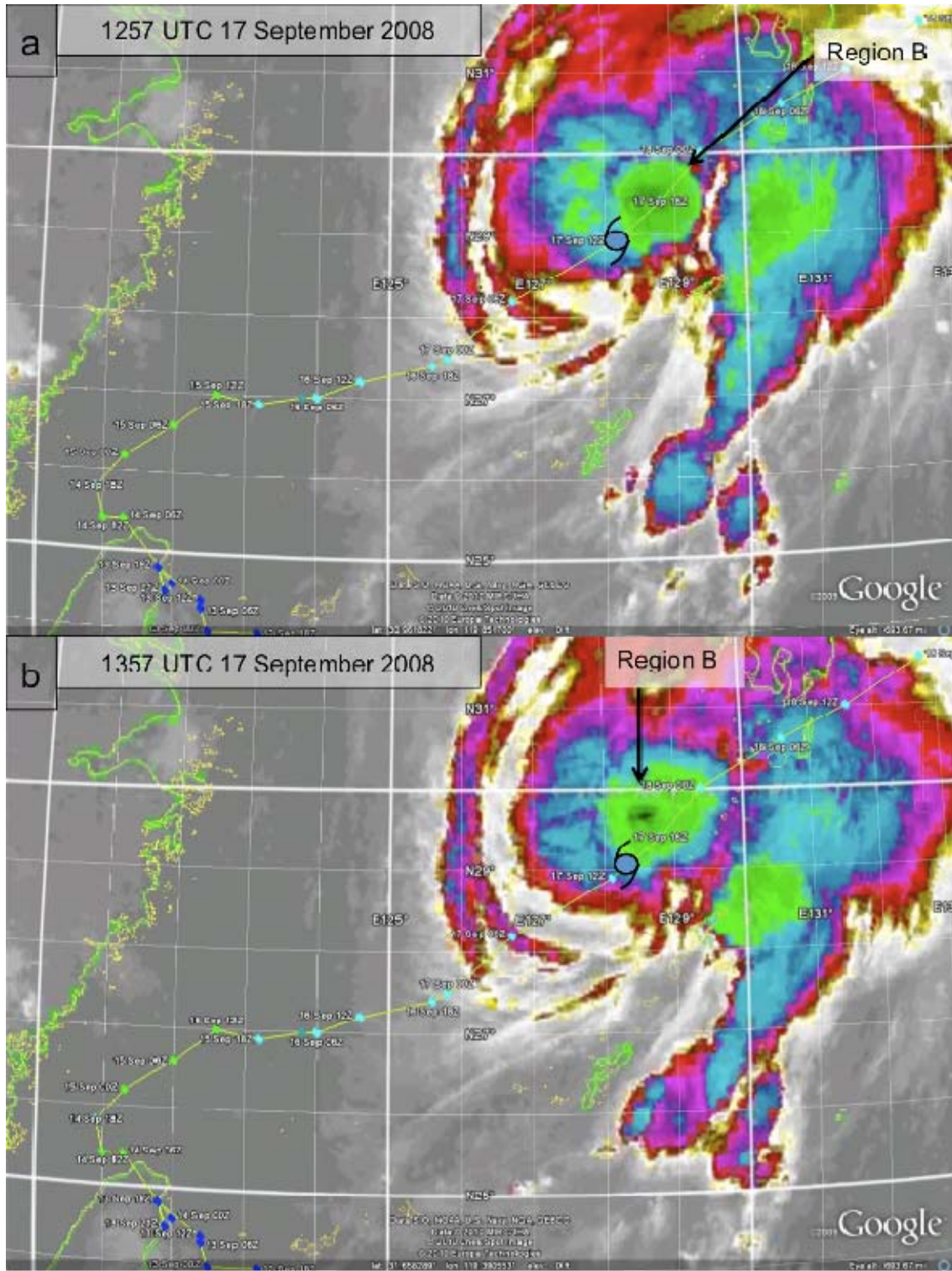
Figure 51.   Enhanced MTSAT IR imagery of TY Sinlaku at (a) 1257, (b) 1357, (c) 1457, and (d) 1557 UTC 17 September 2008. The typhoon symbol is located at the center of the TY Sinlaku circulation at the time of each image based on the JTWC best-track positions in Fig. 2b.
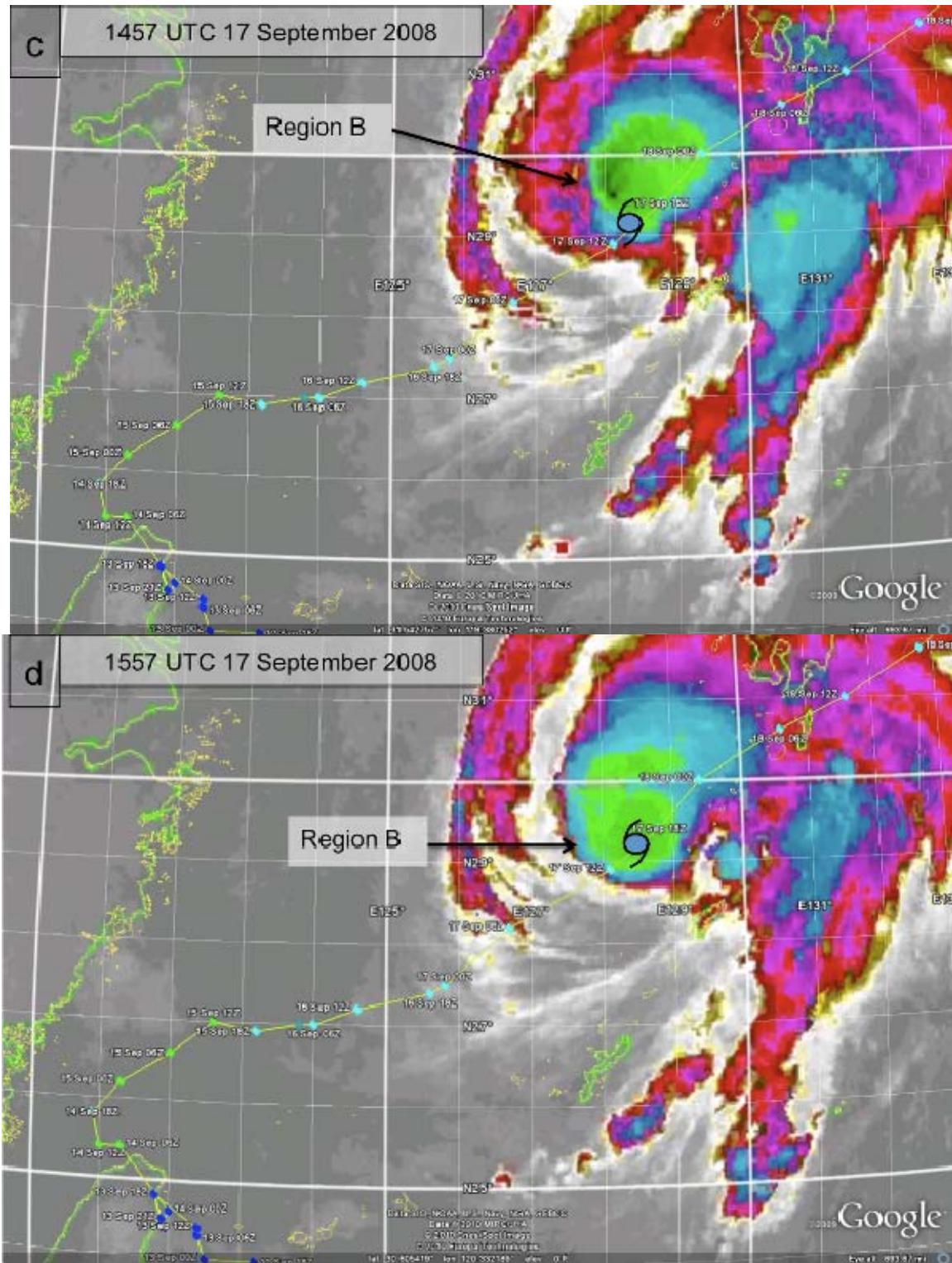
Fig. 51, continued.
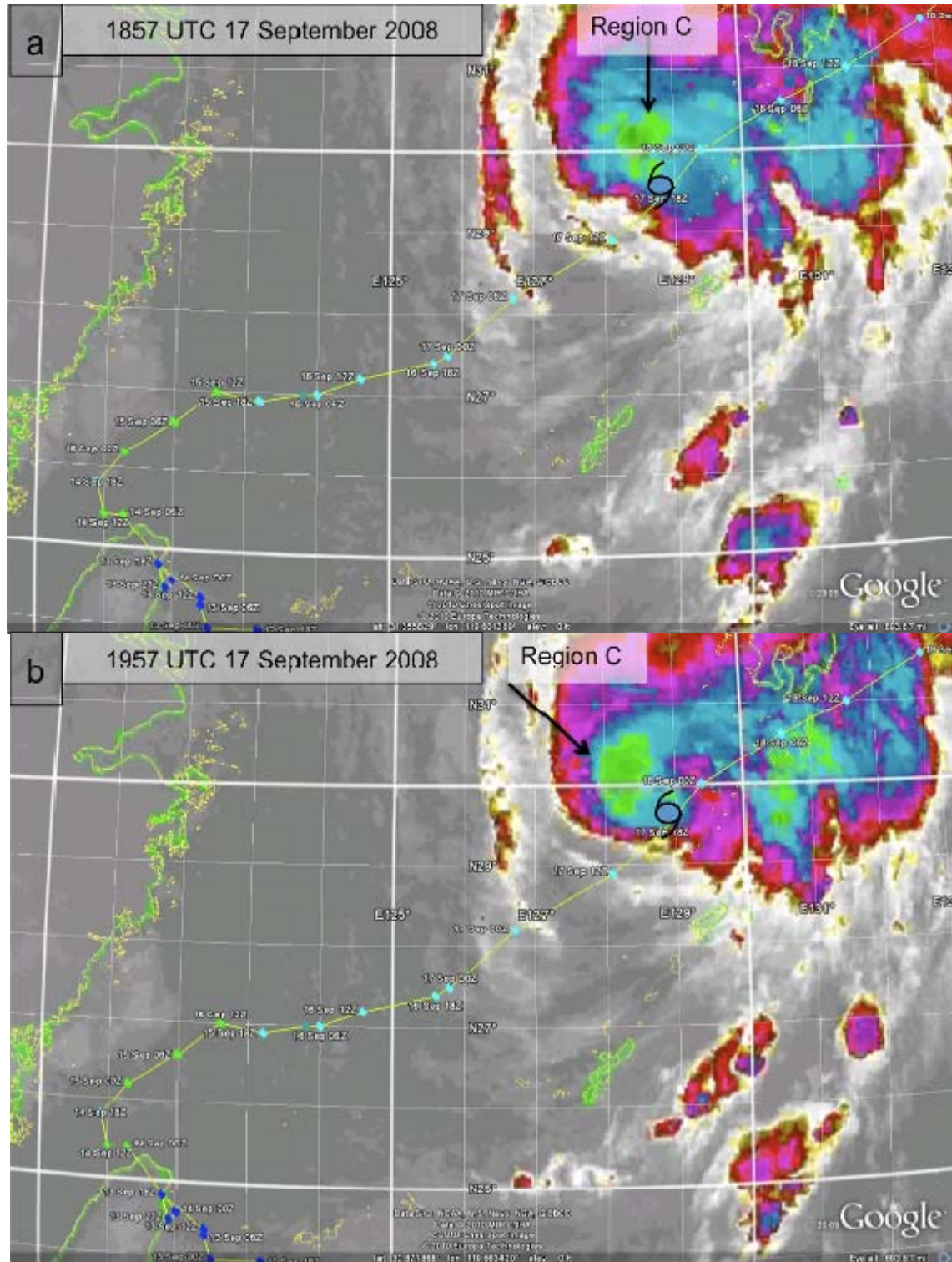
Figure 52.   Enhanced MTSAT IR imagery of TY Sinlaku at (a) 1857, (b) 1957, (c) 2057, and (d) 2157 UTC 18 September 2008. The typhoon symbol is located at the center of the TY Sinlaku circulation at the time of each image based on the JTWC best-track positions in Fig. 2b.

185
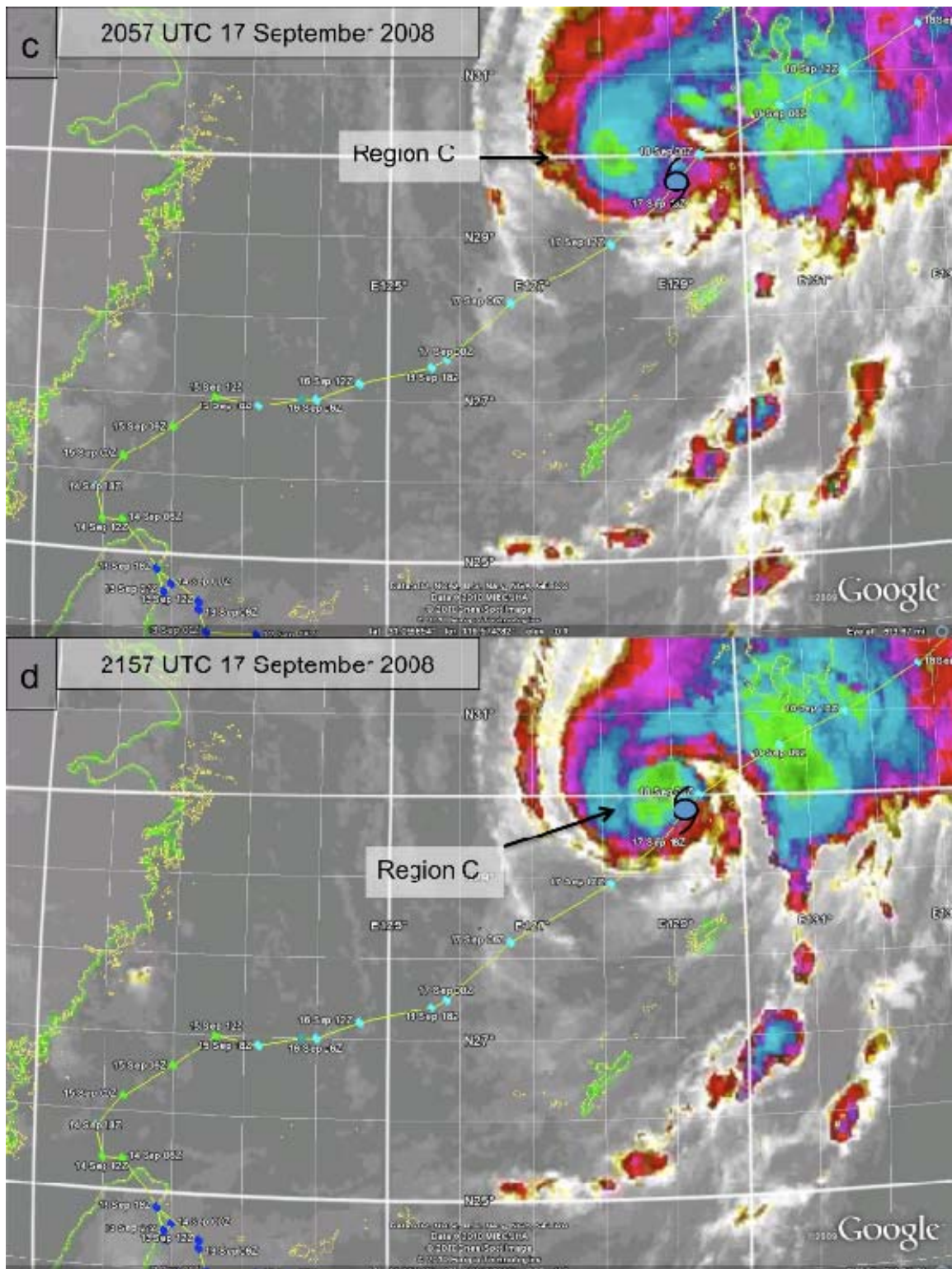
Fig. 52, continued.
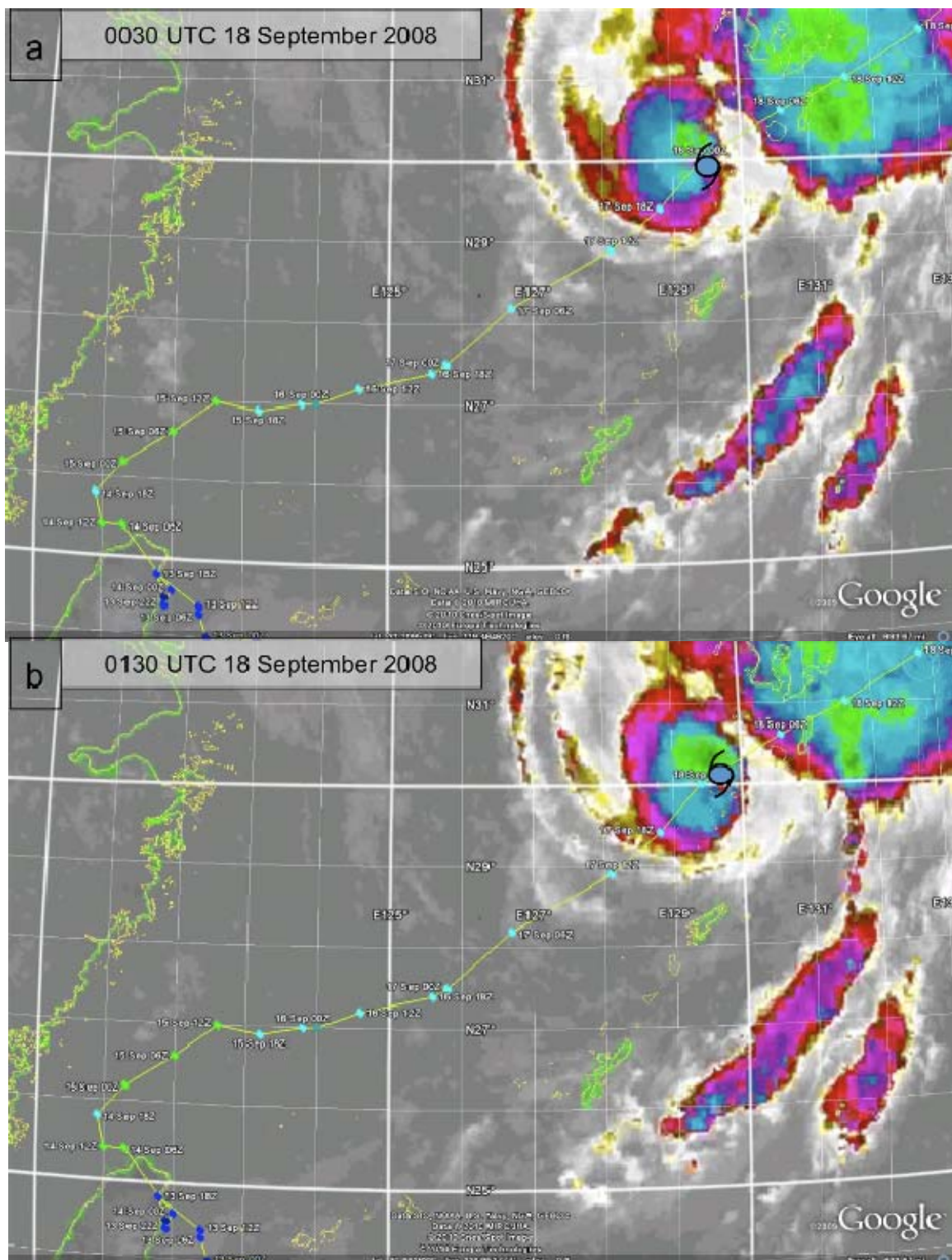
Figure 53.   Enhanced MTSAT IR imagery of TY Sinlaku at (a) 0030 and (b) 0130 UTC
18 September 2008. The typhoon symbol is located at the center of the TY
Sinlaku circulation at the time of each image based on the JTWC best-track
positions in Fig. 2b.
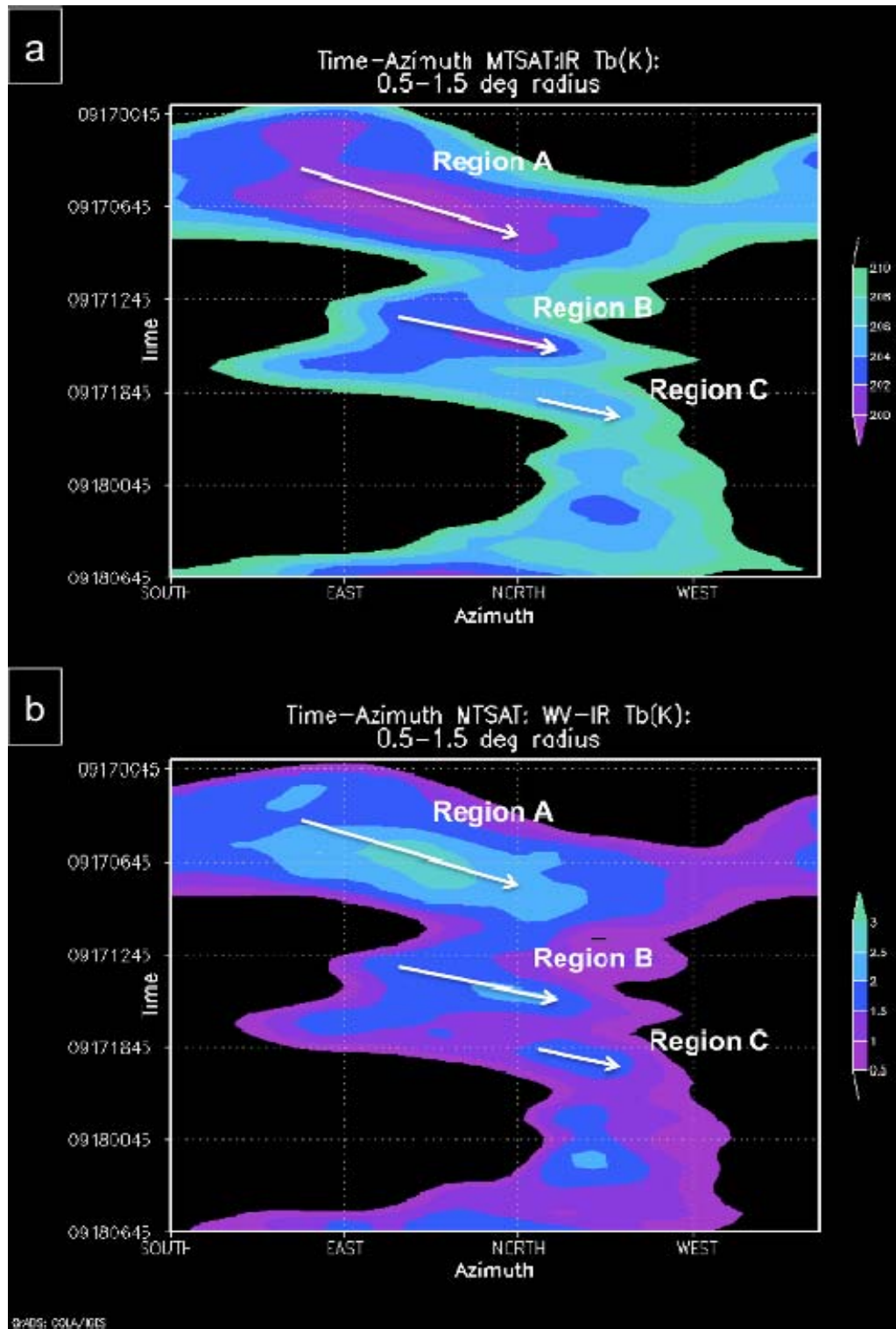
Figure 54.   Radial-averaged satellite brightness temperatures from MTSAT-1R (a) IR (b) IR-WV difference between 0045 UTC 17 September 2008 and 0645 UTC 18 September 2008. Shaded regions are in a radial band about 55-165 km from the TC center.
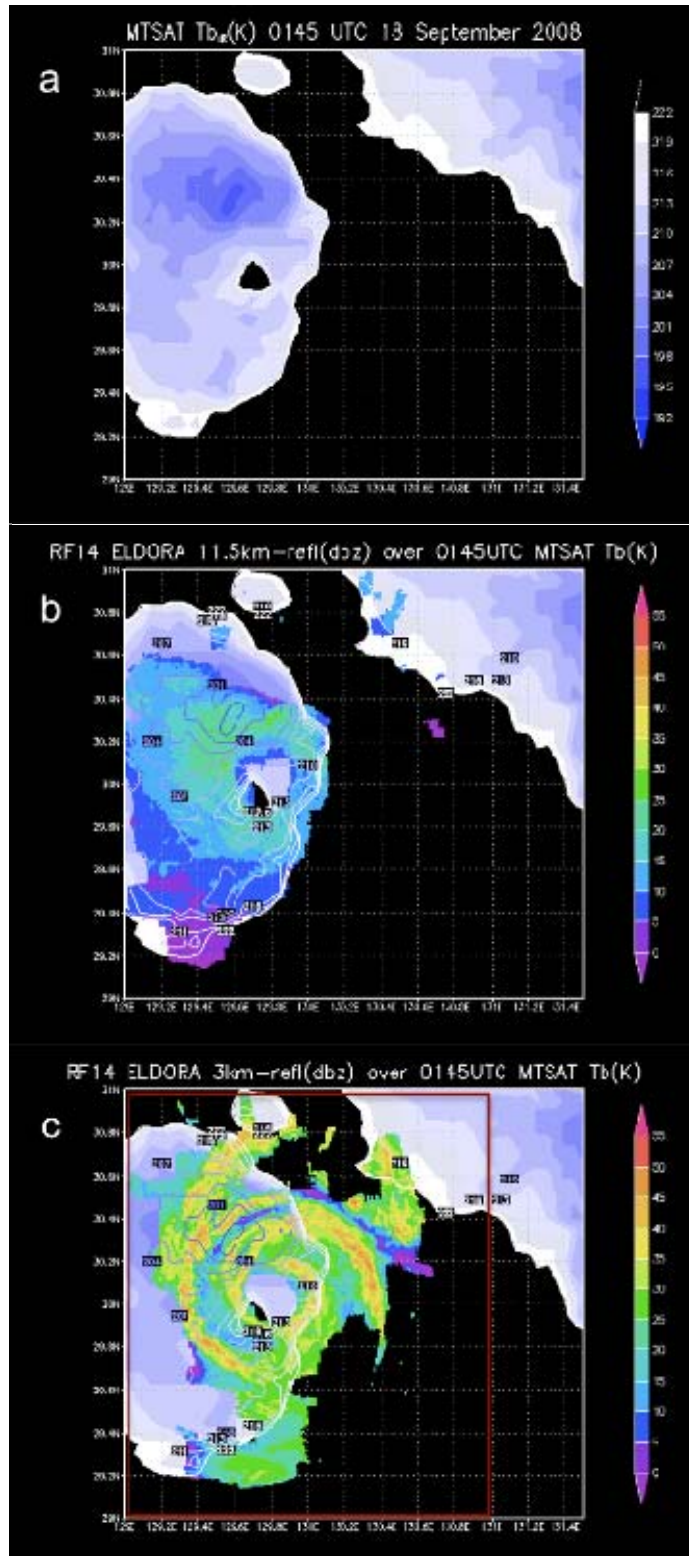
Figure 55.   As in Fig. 36, except for 0145 UTC 18 September 2008 and between 29°-31°N, 129°-131.5°E. The boxed region in (c) defines the region in Fig. 56.

189
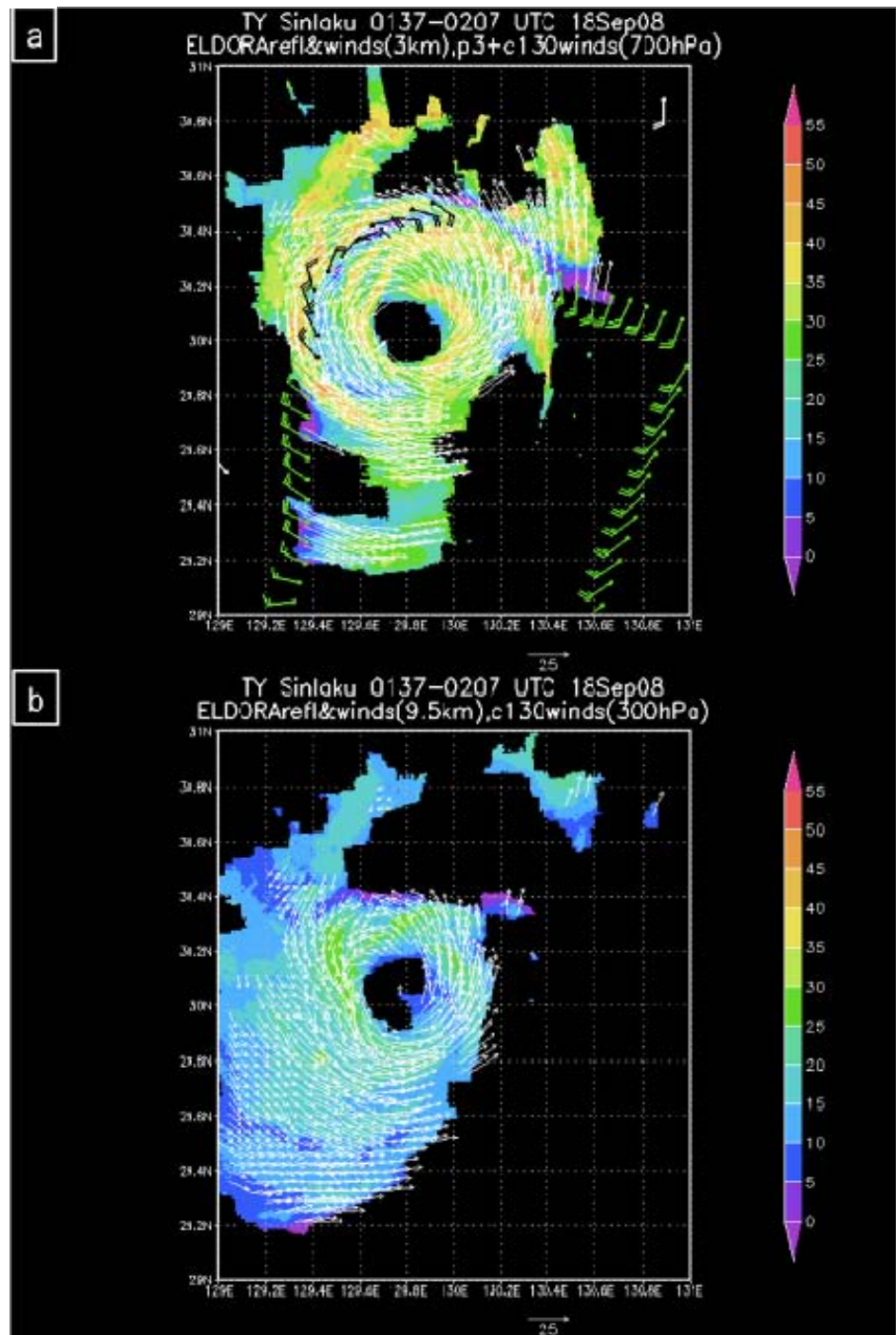
Figure 56.   Reflectivity (dBZ, shaded, scale at right) and winds (m s^{-1}, reference vector below each panel) at (a) 3 km and (b) 9.5 km from the ELDORA between 0137-0207 UTC 18 September 2008. Wind barbs (m s^{-1}, long barb is 10 m s^{-1}) are from the WC-130J dropwindsondes between 0000 UTC – 0200 UTC 18 September 2008 (in white) and P-3 flight-level (in green near 700 hPa and black near 650 hPa).

190
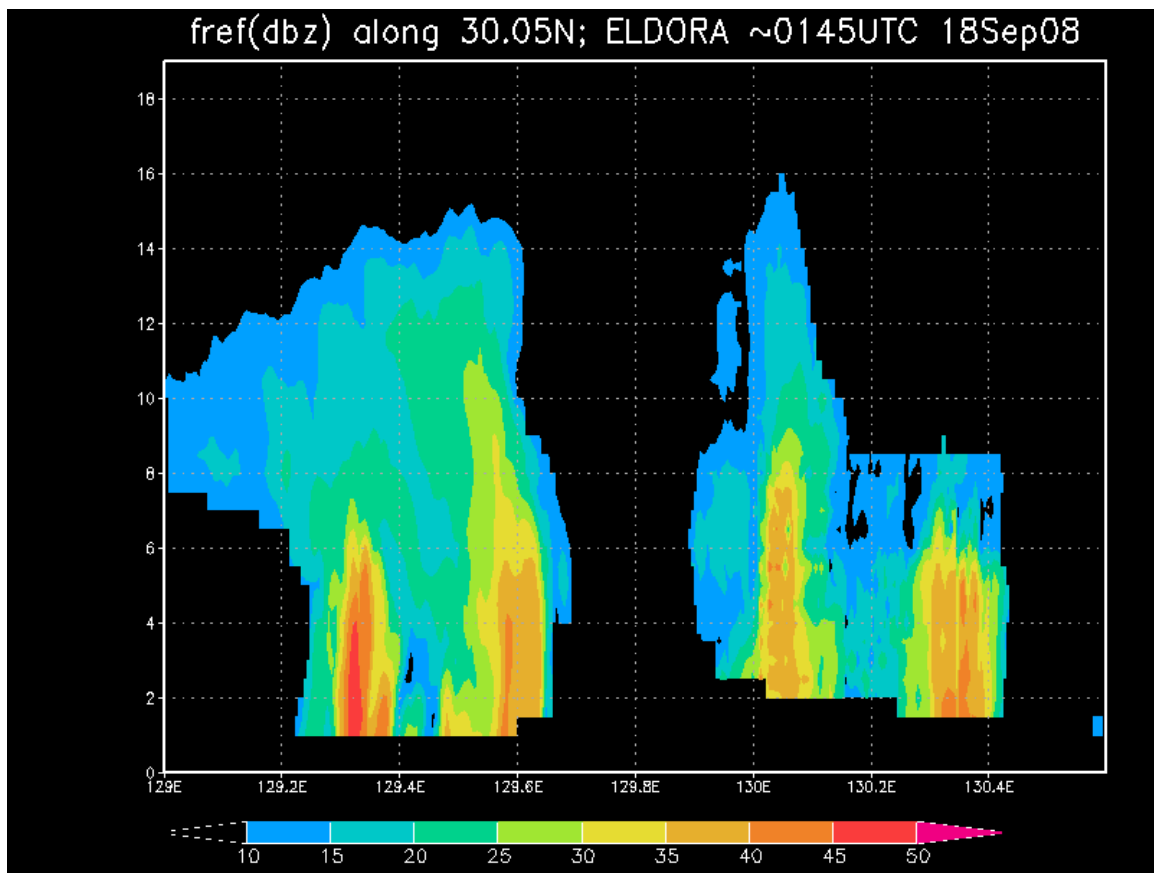
Figure 57.   Vertical cross-section of ELDORA reflectivity (dBZ, shaded, scale at base) along 30.05°N between 129.0°-130.6°E between 0137-0207 UTC 18 September 2008.
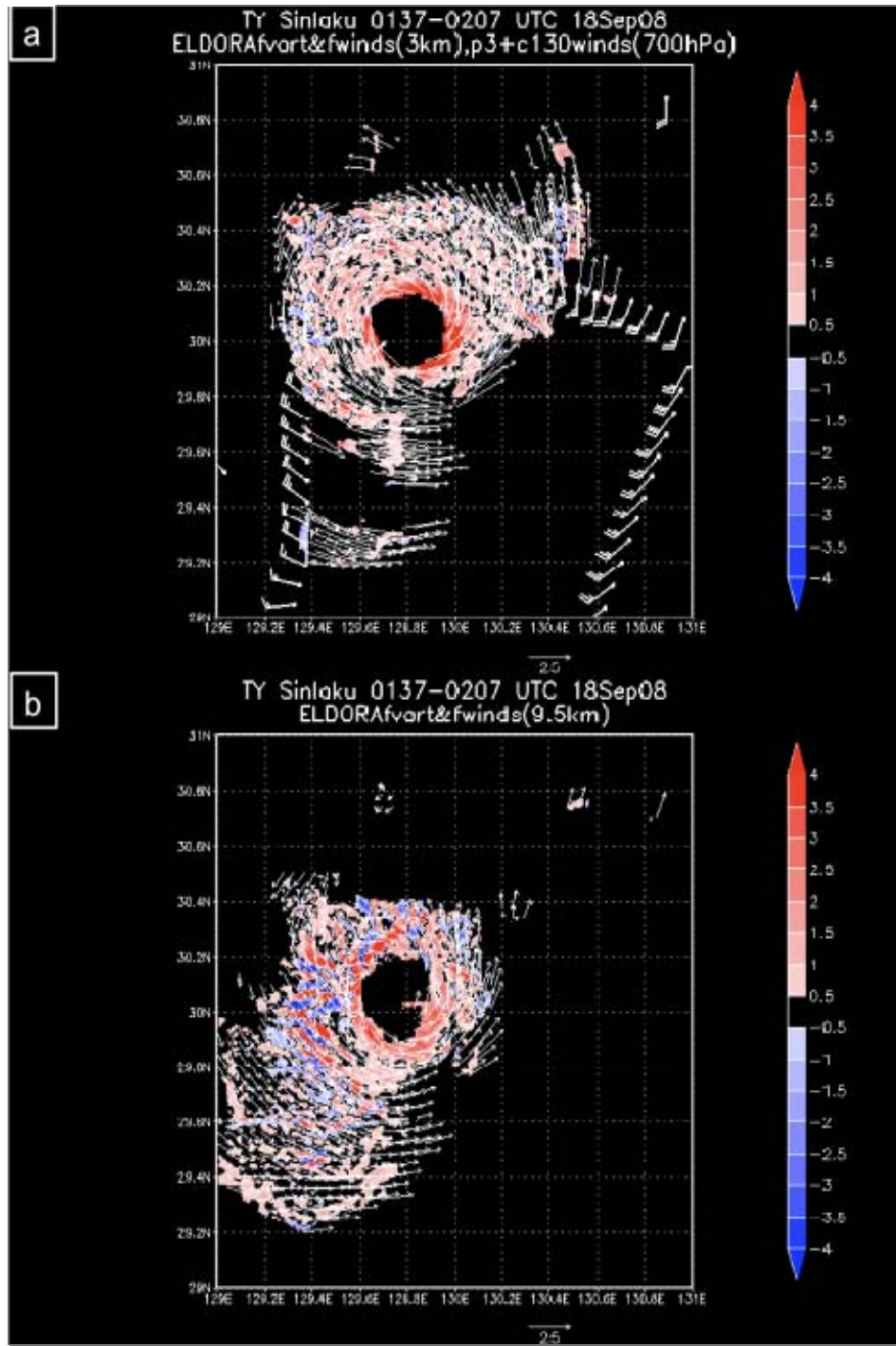
Figure 58.   Relative vorticity (10^{-3} s^{-1}, shaded, scale at right) and winds (m s^{-1}, vectors, reference vector below each panel) at (a) 3 km and (b) 9.5 km from the ELDORA between 0137-0207 UTC 18 September 2008. Wind barbs (long barb is 10 m s^{-1}) are from the WC-130J dropwindsondes between 0000 UTC – 0200 UTC 18 September 2008 and P-3 flight-level.
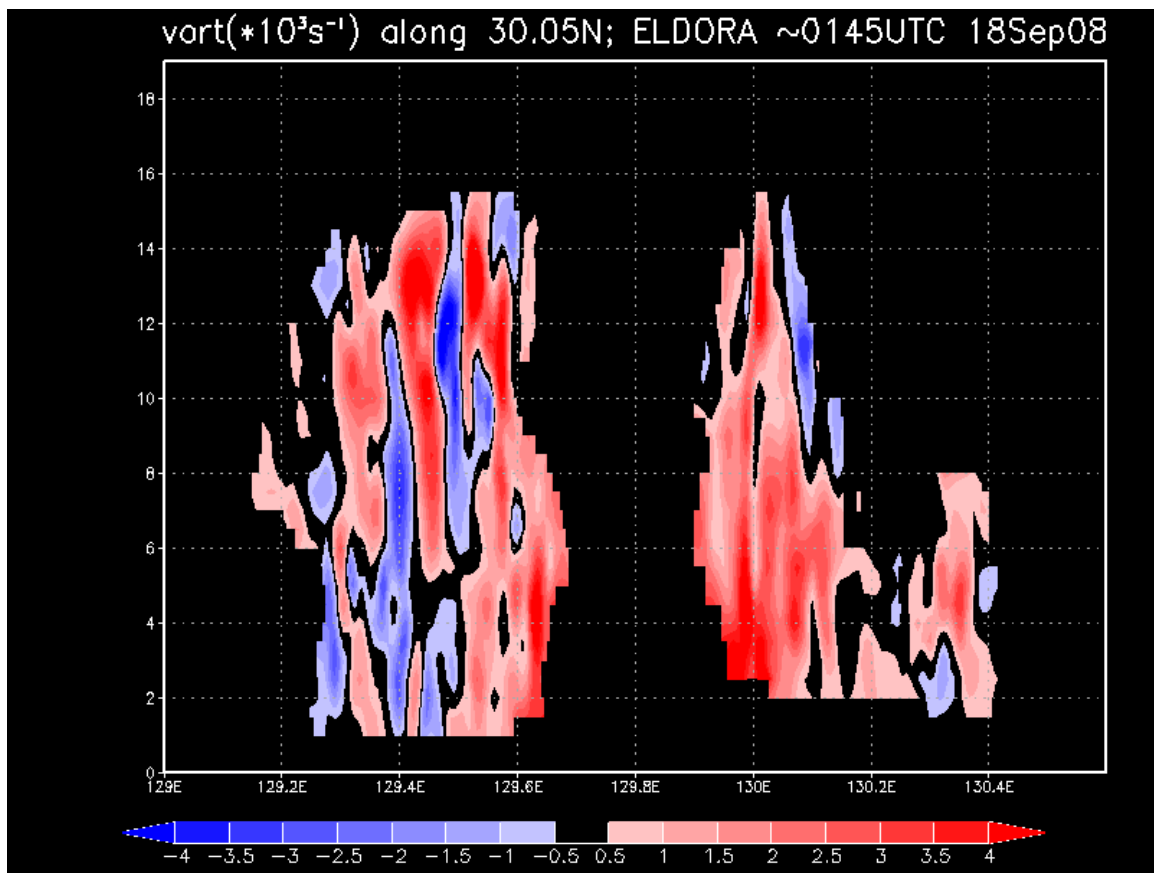
Figure 59.   Vertical cross-section of ELDORA relative vorticity (10^{-3} s^{-1}, shaded, scale at base) along 30.05°N between 129.0°-130.6°E between 0137-0207 UTC 18 September 2008.
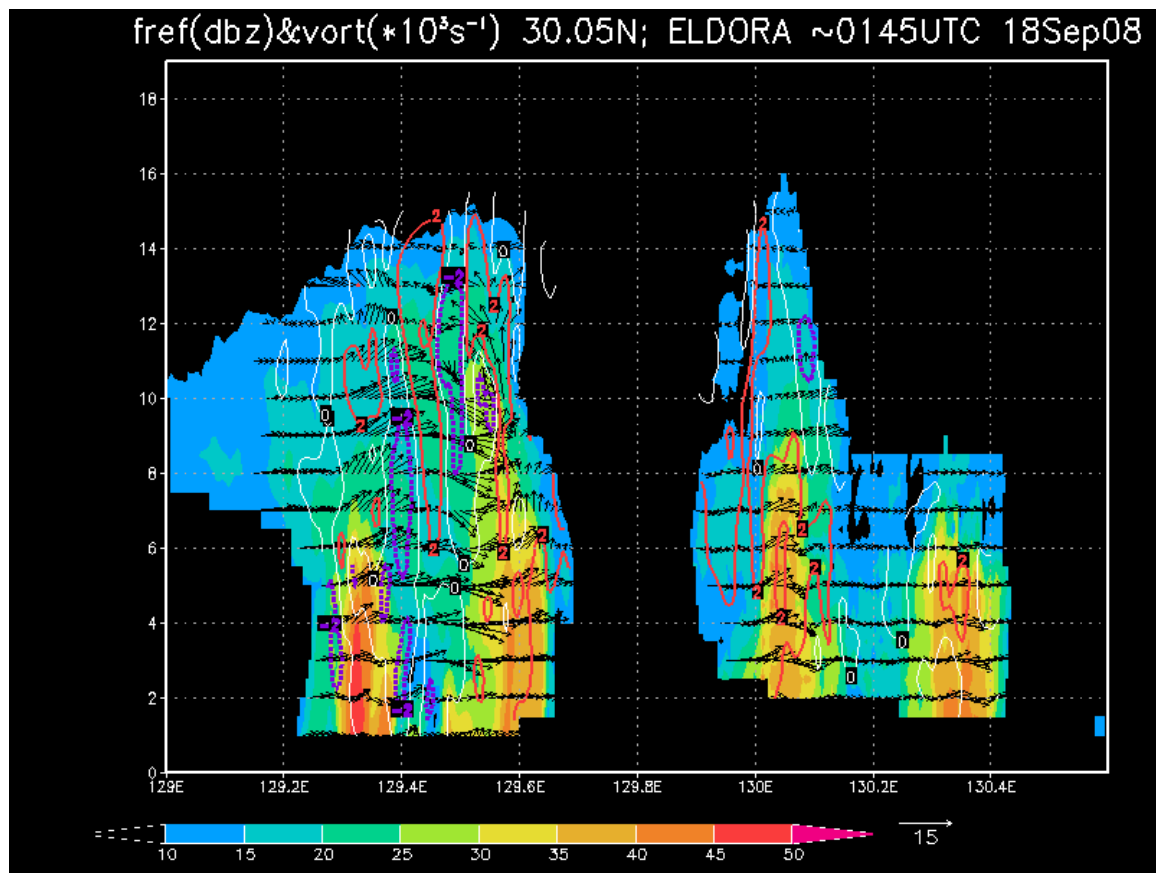
Figure 60.   Reflectivity (dBZ, shaded, scale at base), vorticity (10^{-3} s^{-1}, positive contours in red, 0 contour in white, and negative contours in dashed purple), and wind (m s^{-1}, reference vectors below each panel) along 30.05^{o}N between 129.0^o-130.6^{o}E.
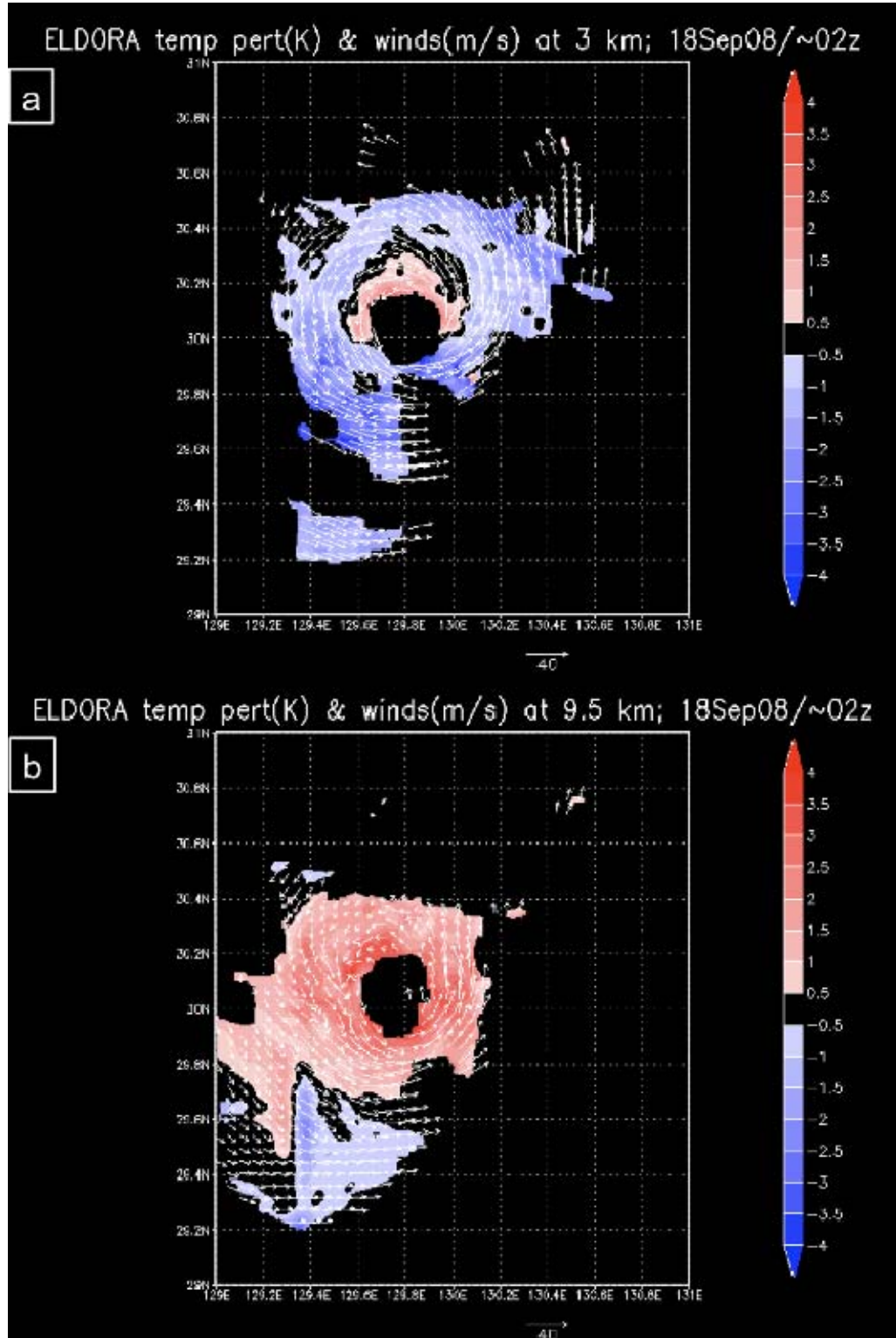
Figure 61.   Temperature perturbations (K, shaded, scale on right) and winds (m s^{-1}, reference vector below each panel) at (a) 3 km and (b) 9.5 km from the ELDORA observations between 0137-0207 UTC 18 September 2008.
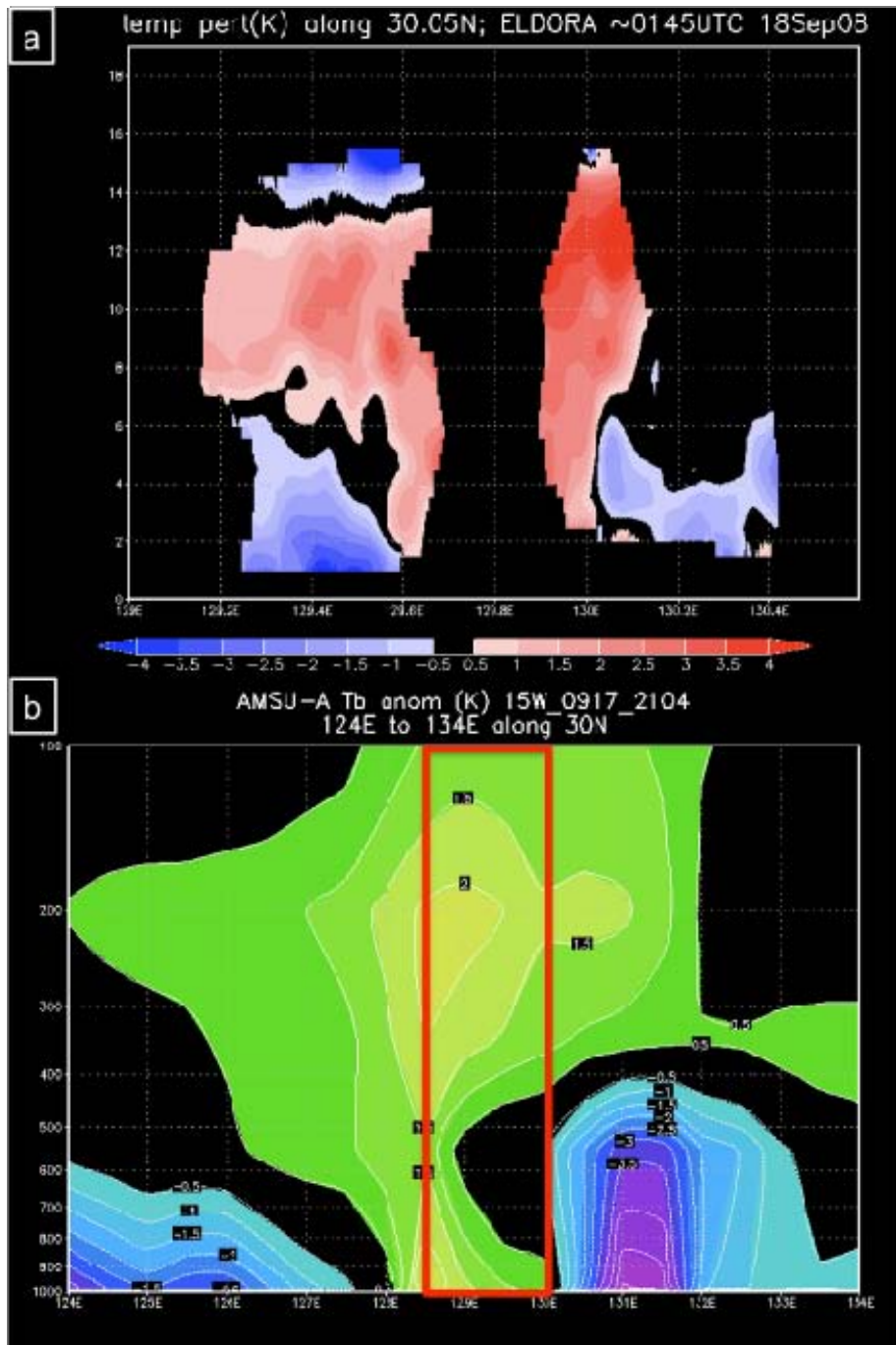
Figure 62.   Vertical cross-section of (a) virtual-cloud temperature perturbations (K, shaded, scale at base) along 30.05°N from 129.0°-130.6°E from the ELDORA observations between 0137-0207 UTC 18 September 2008 and (b) AMSU-A brightness temperature anomalies (K, shaded and contoured. Warm colors outlined by solid lines are positive anomalies and cool colors outlined by dashed lines are negative anomalies) along 30.0°N between 124°-134°E from 2104 UTC 17 September 2008.   The red box outlines the time-adjusted location of the vertical cross-section in panel a.
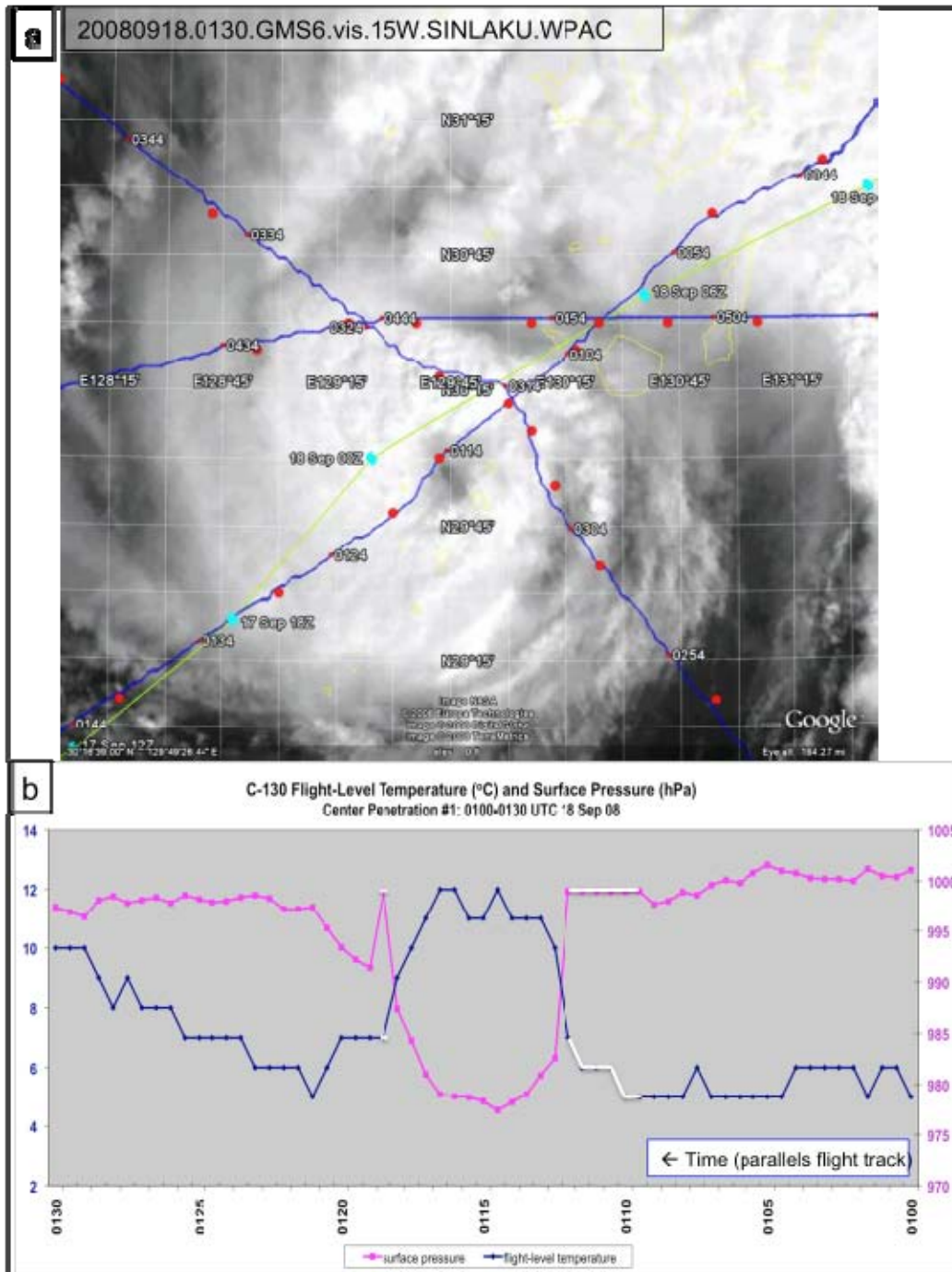
Figure 63. The WC-130J (a) flight track (blue line with times marked) at a flight level of 640 hPa (near 3.75 km) over MTSAT visual satellite imagery from 0130 UTC 18 September 2008 and (b) flight-level temperature (^{o}C, blue line) and extrapolated surface pressure (hPa, purple line). White lines define times when surface pressures and dew-point temperatures are coded as missing. During these times, extrapolated surface pressures (purple line) of 999 hPa are invalid, and flight-level temperatures (blue line) are considered suspect.

197

THIS PAGE INTENTIONALLY LEFT BLANK

VI. DISCUSSION AND CONCLUSIONS

A. DISCUSSION

The redevelopment of TY Sinlaku following recurvature began shortly after 0000 UTC 17 September 2008 when the tilted TC vortex interacted with the second convective episode that was weakening and the third convective episode that was intensifying. Synoptic-scale processes in two regions were primarily responsible for facilitating this interaction. Following the interaction, a combination of mesoscale and vortex-scale processes were responsible for altering the distribution of vorticity and convection in the Sinlaku vortex, which reversed the weakening trend. Mesoscale and vortex-scale processes continued to influence multiple episodes of deep convection that rotated cyclonically toward the TC center and increased the relative vorticity of the inner TC circulation.

1. Synoptic-Scale Contributions

a. *Land Interaction, Vertical Wind Shear and TC Decay*

The intensity of Sinlaku was 100 kt as the outer TC circulation made landfall over Taiwan at 0000 UTC 13 September 2008. During sustained interaction with the island of Taiwan, precipitation structures in the eyewall of Sinlaku were significantly degraded. At the point of recurvature at 1800 UTC 14 September 2008, the intensity was reduced to 65 kt, and Sinlaku entered a region of moderate vertical wind shear that was 10 m s^{-1} from the northwest. Although the shear magnitude was not excessive, the combination of land interaction and shear prevented redevelopment of deep eyewall convection. The low-level center was exposed in microwave imagery and deep convection was limited to the downshear (i.e., east) side of the TC. At the time when the decaying TC interacted with the convective episodes between 0135-0205 UTC 17 September 2008, the TC intensity was 35 kt, which was the weakest intensity following recurvature (Fig. 1).

199

b.   *Preconditioning and the Development of Deep Convection*

Persistent southwest monsoon flow from the South China Sea brought warm, moist air toward the northeast and over the region west of Okinawa. This region of the East China Sea was characterized by high ocean heat content and above-normal sea-surface temperatures. The combination of monsoon flow and ocean conditions resulted in elevated surface-based values of CAPE that preconditioned the region to be favorable for episodes of convection that erupted in the region on 16 September 2008.

The combination of the storm-scale cyclonic flow and synoptic-scale monsoon flow with large CAPE contributed to enhancement of the conditions that defined the three convective bursts. In this sense, the monsoon flow is thought to precondition the region into which the decaying TC was moving, such that convection rapidly developed as the TC approached from the west. The preconditioned region was on the downshear side of the TC, which suggests that vortex-scale dynamics probably contributed to the interaction with the monsoon flow. Therefore, while the synoptic-scale vertical wind shear contributed to the decay of the TC, the resulting tilt in the TC vortex may have intensified the deep convection that developed on 16 September 2008. Over larger scales, convergence between the southwest monsoon flow and outer TC circulation contributed to the lifting that initiated the three episodes of deep convection on 16 September 2008.

2.   Meso- and Vortex-Scale Processes

a.   *TC-Multivortex Interaction and TC Re-intensification*

While synoptic-scale processes contributed to the initiation of the three convective episodes, mesoscale processes embedded within the deep convection contributed to the three mesoscale vortices that occurred during the re-intensification of the TC on 17 September 2008. At the time of investigation by the aircraft, the three mesoscale vortices had very different vertical and horizontal characteristics. Furthermore, the structure of each vortex was closely linked to the character of the convection associated with the weakening second episode and intensifying third

convective episode. As defined in the vorticity analysis, the tilted Sinlaku vortex merged with the westernmost tower of deep convection that extended from low levels to near 14 km between 0135-0205 UTC 17 September 2008. The deep convective updraft was also a region of very large positive vorticity. Therefore, this interaction augmented the vorticity associated with the TC vortex and contributed to a redistribution of relative vorticity throughout the troposphere. Additional deep towers of convection and positive relative vorticity existed farther east and also contributed to the distribution of vorticity in the TC. Regions of negative relative vorticity on both sides of the westernmost tower were likely formed due to tilting and divergence of air between updrafts that was entrained into surrounding vigorous updrafts. This increased convergence at levels between 8-10 km enhanced the updraft. The relevant pattern of convergence straddling the western and eastern updrafts and divergence in the central updraft is clear in Fig. 43a. The relative coverage and contribution to vortex spin-up by positive relative vorticity was much greater than that due to limited regions of negative relative vorticity.

Comparison of vertical towers of relative vorticity and vertical motion that define the third convective episode indicate that the maximum positive vorticity is associated with the maximum in vertical motion. However, the distribution of temperature (Fig. 45a) indicates that the warmest air is offset to be below the maximum upward motion, which suggests that buoyancy from below was more of a contribution to the updraft rather than latent heat of fusion in the updraft itself.

The northern and central vortices also impacted the redevelopment of Sinlaku. These vortices were respectively located 55 km and 85 km from the TC 5.5-km circulation center. The positive relative vorticity generated by the northern vortex between 2-8 km and by the central vortex between 2.5-11 km likely enhanced the overall positive vorticity of the region associated with the total TC circulation.

The northern and central vortices also affected the circulation around the Sinlaku vortex. At 3 km, convergence between the northeasterlies on the west side of the trough axis converged with the southerlies and southeasterlies northeast of the TC center. This convergence resulted in enhanced easterly flow on the north side of the TC center, but disrupted the symmetric flow about the vortex. Degradation of the cyclonic flow

around the TC vortex continued at 5.5 km, where northerlies on the west side of the northern and central vortices eradicated easterly flow on the north side of the TC. It is concluded that the degradation of symmetry resulting from the circulation about the mesovortices within the older convection was overcome by the enhancement of the TC circulation that resulted from the addition of positive relative vorticity to the TC vortex and inner TC circulation and resulted in the continued intensification of the TC.

b. TC Intensification

At the times of the second and third episodes of deep convection, Sinlaku was at its weakest intensity. The contribution of positive relative vorticity associated with interaction with these vortices increased circulation of the TC and Sinlaku began to reintensify. Over the next 24 hours, mesoscale and convective-scale processes continued to reintensify Sinlaku. At least three episodes of deep convection wrapped cyclonically into the TC center.

The latent heat release in deep convection also generates low-level potential vorticity. Through the radial shear in the tangential velocity that accompanied cyclonic low-level circulation, positive vorticity is transported into the TC center as negative relative vorticity is exported outward. As the episodes of deep convection wrapped into the TC center, positive relative vorticity was added nearly continuously to the inner TC circulation on 17 September 2008 and the TC continued to deepen. Although no in situ observations exist during this period of re-intensification, infrared satellite imagery indicates a distribution and motion of deep convection that is consistent with the process of axisymmetrization.

3. Characteristics of the Re-intensified TC

The combination of synoptic scale, mesoscale, and convective-scale interactions resulted in a warm-core upright TC near typhoon intensity. During the second ET flights by the WC-130J and P-3, Sinlaku was defined by the P-3 as a vortex with an inner circulation near 16 km in diameter and cyclonic winds that reached nearly 12 km in height. The WC-130J crew documented the eye diameter as 25 n mi (near 46 km) on the

first center penetration at 0114 UTC 18 September 2008, which was followed by a contraction of the eye to 16 n mi (near 30 km) during the third center penetration two hours later (WC-130J AF306 1033W Sinlaku mission scientist report, 17-18 September 2008). The maximum wind speed detected by the WC-130J SFMR was 75 kt and the minimum sea-level pressure was 979 hPa (WC-130J mission report 18 September 2008). The JTWC best-track intensity defined the intensity of the system as 60 kt at 0000 UTC 18 September 2008 and weakened it to 55 kt by 0600 UTC 18 September 2008, even though dropwindsondes released in multiple passes through the TC center by the WC-130J detected winds in excess of 70 kt in the eyewall. Irregardless, Sinlaku had redeveloped in less than 24 hours from a TC of barely tropical storm intensity to a TC near typhoon intensity through a myriad of processes over varying space and time scales.

B.   CONCLUSIONS

The interaction between the TC and multiple mesoscale vortices is concluded to be the critical process in the redevelopment of Sinlaku. Vigorously growing deep convective towers contributed to the direct infusion and redistribution of positive relative vorticity into the TC vortex. Broad regions of mid-level positive vorticity from multiple mesoscale vortices at larger radii also contributed positive relative vorticity. The combination of these processes arrested the decay of Sinlaku and began the re-intensification process. An accurate assessment of the relative importance between the mesoscale vortices is difficult to make from the single observation data set. However, remotely-sensed data imply an evolution consistent with the hypothesized contributions to the re-intensification of Sinlaku. Without additional observations, assessment of the relative importance of the mesoscale vortices is left to future numerical experiments and simulations.

In the 24 h following the TC-multivortex interaction, the process of re-intensification continued to result from convective and mesoscale mechanisms. It is hypothesized that the continued generation of low-level potential vorticity beneath deep convection and the rotation of that deep convection and associated potential vorticity into the TC center resulted in the intensification of the TC. The concurrent down-gradient

203

movement of the second region of deep convection and subsequent evolution into a principal band also indicates axisymmetrization was the likely mechanism for re-intensification.

While mesoscale features and processes were critical to the re-intensification, synoptic-scale mechanisms are considered equally vital. Deep southwest monsoon flow over a region of high SSTs and high ocean heat content facilitated the development of the deep convective episodes in the path of the oncoming TC. In addition to preconditioning, the synoptic scale converged with the vortex-scale outer TC circulation to provide the lifting mechanism that initiated the convection. Finally, the synoptic scale land interaction and vertical wind shear were responsible for weakening Sinlaku. The slow eastward movement of the sheared TC toward the preconditioned region facilitated generation of multiple convective episodes of deep convection and subsequent TC-multivortex interaction that was critical to the redevelopment of Sinlaku.

The detailed observations from the ELDORA observations on 17 September 2008 allow a unique look at the characteristics of the tilted Sinlaku vortex, three mesoscale circulations, and the reintensified TC. The merger of the tilted Sinlaku vortex vorticity maximum with a deep tower of strongly positive relative vorticity, reflectivity, and upward motion may lend credence to intensification theories based on vortex mergers. The tilt in the convective towers, alignment of reflectivity, vorticity, and vertical motion maxima within and positive temperature perturbation beneath the deepest convective columns provide quantitative detailed observational data from which to baseline future numerical experiments and simulations.

While the ECMWF operational model analyses accurately depicted precipitation and vorticity structures that were consistent in placement and relative orientation with the key features in the aircraft observations during the TC-multivortex interaction, the distances between the features of interest were much greater in the model than they were in the observational data. This may have contributed to the errors in the forecast based on the 0000 UTC 17 September 2008 ECMWF operational analysis, in which the extratropical transition of Sinlaku and subsequent downstream development were not accurately depicted.

C.   FUTURE WORK

Observations of the re-intensification of Sinlaku from the TCS-08 / T-PARC field programs comprise a unique data set that has enabled detailed analysis of the synoptic, mesoscale, and convective-scale processes that were critical to the rapid re-intensification of Sinlaku from a weak tropical storm to a TC near typhoon intensity in a 24-h period. The future work recommended here is intended to seize relevant and interesting threads in research areas that will build upon the results of this work. Following the conclusion that the synoptic-scale forcing facilitated the development of deep convection and subsequent TC-multivortex interaction, a modeling study is recommended to determine if the synoptic-scale forcing was a necessary ingredient to the redevelopment.

Additional research is also recommended to further clarify the roles of the three mesoscale vortices defined in the vicinity of Typhoon Sinlaku on the initiation of the re-intensification.   Because of the temporal gaps in aircraft observations, a numerical modeling study is required to provide continuity in time such that the contribution of the convective features to vortex spin-up could be captured. The merger between the relative vorticity maximum associated with the tilted Sinlaku vortex and the westernmost convective tower is of significant interest and may lend credence to theories that describe intensification through vortex mergers (Montgomery et al. 2006).   The presence of several convective towers in close proximity is also considered noteworthy. Simulations of TC spinup following vortex mergers of this type where vorticity is contributed directly to the TC core with and without the contribution of additional positive vorticity to the inner TC circulation by mid-level vortices would further define the relative roles of these mesovortices. The contribution of positive vorticity across a broad region at mid-levels as occurred in the northern and central vorticities is also considered interesting, and it is suggested that research focus on the likely distribution of such vortices across the second convective episode and quantifying the contribution of such a distribution to the increase in positive vorticity within the inner TC circulation. Finally, continued research is recommended to quantify the link between this redevelopment and errors in forecast intensity of the TC during ET and of the subsequent downstream development by the ECMWF and other global numerical models.

Identification and detailed characterization of the scales and mechanisms responsible for the re-intensification of TY Sinlaku meets several science objectives in both the T-PARC and TCS-08 research programs and is a critical step toward improving the forecast accuracy of the structure, structure change, and intensity of tropical cyclones in the western North Pacific. Extending the results of this work to a more general case through numerical experiments and simulations will be the next step toward improving our understanding of tropical cyclone structure and intensity, and increasing our predictive capabilities.

LIST OF REFERENCES

Ackerman, S. A., 1996: Global satellite observations of negative brightness temperature differences between 11 and 6.7 μm. *J. Atmos. Sci*., **53**, 2803–2812.

ATCR, 2008: *Annual Tropical Cyclone Report*. U.S. Naval Maritime Forecasting Center/Joint Typhoon Warning Center, 117 pp. [Available online http://www.usno.navy.mil/NOOC/nmfc-ph/RSS/jtwc/atcr/2008atcr/2008atcr.pdf]

Bartels, D. L., and R. A. Maddox, 1991: Midlevel cylonic vortices generated by mesoscale convective systems. *Mon. Wea. Rev.,* **119**, 104–118.

Bedka, K., J. Brunner, R. Dworak, W. Feltz, J. Otkin, and T. Greenwald, 2010: Objective satellite-based detection of overshooting tops using infrared window channel brightness temperature gradients. *J. Appl. Meteor. Climatol*., **49**, 181–202.

Bell, M. M., and M. T. Montgomery, 2010: Sheared deep vortical convection in pre-depression Hagupit during TCS08, *Geophys. Res. Lett.*, **37**, L06802, doi:10.1029/2009GL042313.

Bister, M, and K. A. Emanuel, 1997: The genesis of Hurricane Guillermo: TEXMEX analysis and a modeling study. *Mon. Wea. Rev.,* **125**, 2662–2682.

Bosart, B. L., W. C. Lee, and R. M. Wakimoto, 2002: Procedures to improve the accuracy of airborne Doppler radar data. *J. Atmos. Oceanic Technol.,* **19**, 322–339.

Carr, L. E., III, and R. T. Williams, 1989: Barotropic stability to perturbations from axisymmetry. *J. Atmos. Sci*., **46**, 3177–3191.

Chen, Y., and M. K. Yau, 2001: Spiral bands in a simulated hurricane. Part I: Vortex Rossby wave verification. *J. Atmos. Sci*., **58**, 2128–2145.

Corbosiero, K. L., and J. Molinari, 2003: The relationship between storm motion, vertical wind shear, and convective asymmetries in tropical cyclones. *J. Atmos. Sci.,* **60**, 366–376.

Cressman, G. P., 1959: An operational objective analysis system. *Mon. Wea. Rev*., **87**, 367–374.

Davis, C. A., S. C. Jones, and M. Riemer, 2008: Hurricane vortex dynamics during Atlantic extratropical transition. *J. Atmos. Sci*., **65**, 714–736.

Eastin, M.D., P. G. Black, and W. M. Gray, 2002a: Flight-level instrument wetting errors in hurricanes. Part I: Observations. *Mon. Wea. Rev.,* **130**, 825–841.

——, ——, and ——, 2002b: Flight-level instrument wetting errors in hurricanes. Part II: Implications. *Mon. Wea. Rev.,* **130**, 842–851.

Enagonio, J., and M. T. Montgomery, 2001: Tropical cyclogenesis via convectively forced vortex Rossby waves in a shallow water primitive equation model. *J. Atmos. Sci*., **58**, 685–706.

Evans, J. L., and R. E. Hart, 2003: Objective indicators of the onset and completion of ET for Atlantic tropical cyclones. *Mon. Wea. Rev.,* **131**, 909–925.

Fox, D. N., W. J. Teague, C. N. Barron, M.R. Carnes, and C.M. Lee, 2002: The Modular Ocean Data Assimilation System (MODAS). *J. Atmos. Oceanic Technol.,* **19**, 240–252.

Fritz, S., and I. Laszlo, 1993: Detection of water vapor in the stratosphere over very high clouds in the tropics. *J. Geophys. Res*., **98** (D12), 22,959–22,967.

Gray, W. M., 1968: Global view of the origin of tropical disturbances and storms. *Mon. Wea. Rev.,* **96**, 669-700.

Guinn, T. A., and W. H. Schubert, 1993: Hurricane spiral bands. *J. Atmos. Sci*., 50, 3380–3403.

Harr, P.A., and R. L. Elsberry, 2000: Extratropical transition of tropical cyclones over the western North Pacific. Part I: Evolution of structural characteristics during the transition process. *Mon. Wea. Rev.,* **128**, 2613–2633.

Hart, R. E., 2003: A cyclone phase space derived from thermal wind and thermal wind asymmetry. *Mon. Wea. Rev.,* **131**, 585–616.

Hendricks, E. A., M. T. Montgomery, and C. A. Davis, 2004: On the role of "vortical" hot towers in the formation of Tropical Cyclone Diana (1984). *J. Atmos. Sci*., **61**, 1209–1232.

Hildebrand, P. H., W. C. Lee, C. A. Walther, C. Frush, M. Randall, E. Loew, R. Neitzel, R. Parsons, J. Testud, F. Baudin, and A. LeCornec, 1996. The ELDORA/ASTRAIA airborne doppler weather radar: High-resolution from TOGA COARE, *Bull. Amer. Meteor. Soc.,* **77,** 213–232.

Houze, R. A. Jr., 1997: Stratiform precipitation in regions of convection: A meteorological paradox? *Bull. Amer. Meteor. Soc.,* **78,** 2179–96.

——, 2004: Mesoscale convective systems. *Rev. Geophys.,* **42**, RG4003, doi:10.1029/2004RG000150.

——, 2010: Clouds in tropical cyclones. *Mon. Wea. Rev.,* **138**, 293–344.

——, W. C. Lee, and M. M. Bell, 2009: Convective contribution to the genesis of Hurricane Ophelia (2005). *Mon. Wea. Rev.,* **137**, 2778–2800.

——, S. A. Rutledge, M. I. Biggerstaff, and B. F. Smull, 1989: Interpretation of Doppler weather radar displays of midlatitude mesoscale convective systems, *Bull. Amer. Meteor. Soc.,* **70,** 608–619.

——, S. S. Chen, J. Moore, R. Dirks, and J. Meitin, 2005: *The Hurricane Rainband and Intensity Change Experiment (RAINEX) Operations Plan.* NCAR/Earth Observing Laboratory, 53 pp.

Jensen, J., 2009: Project managers quality report, Jorgen Jensen – T-PARC. NCAR/Earth Observing Laboratory, 15 pp.

Jones, S. C., 1995: The evolution of vortices in vertical shear. Part I: Initially barotropic vortices. *Quart. J. Roy. Meteor. Soc.,* **121**, 821–851.

——, P. A. Harr, J. Abraham, L. F. Bosart, P. J. Bowyer, J. L. Evans, D. E. Hanley, B. N. Hanstrum, R. E. Hart, F. Lalaurette, M. R. Sinclair, R. K. Smith, C. Thorncroft, 2003: The extratropical transition of tropical cyclones: forecast challenges, current understanding, and future directions. *Wea. Forecasting*, **18**, 1052-1092.

Klein, P. M., P. A. Harr, and R. L. Elsberry, 2000: Extratropical transition of western North Pacific tropical cyclones: An overview and conceptual model of the transformation stage. *Wea. Forecasting*, **15**, 373-396.

Lee, W.C., M. Bell, C. Wolff, E. Loew, and M. Donovan, 2009: *THORPEX Pacific Asian Regional Campaign (TPARC) and Tropical Cyclone Structure (TCS08) ELDORA data quality report*. NCAR/Earth Observing Laboratory, 9 pp.

Martin, P., C. N. Barron, L. F. Smedstad, A. J. Wallcraft, R. C. Rhodes, T. J. Campbell, and C. Rowley, 2008: *Software design description for the Navy Coastal Ocean Model (NCOM) Version 4.0.* NRL/MR/7320—08-9149, 149 pp.

Molinari, J., D. Vollaro, and K. L. Corbosiero, 2004: Tropical cyclone formation in a sheared environment: A case study. *J. Atmos. Sci*., **61**, 2493–2509.

——, P. Dodge, D. Vollaro, K. L. Corbosiero, and F. Marks, Jr., 2006: Mesoscale aspects of the downshear reformation of a tropical cyclone. *J. Atmos. Sci*., **63**, 341–354.

Montgomery, M. T., and R. J. Kallenbach, 1997: A theory for vortex Rossby-waves and its application to spiral bands and intensity changes. *Quart. J. Roy. Meteor. Soc.,* **123**, 435–465.

——, and J. Enagonio, 1998: Tropical cyclogenesis via convectively forced vortex Rossby waves in a three-dimensional quasi-geostrophic model. *J. Atmos. Sci.,* **55**, 3176–3207.

——, M. E. Nicholls, T. A. Cram, and A. B. Saunders, 2006: A vortical hot tower route to tropical cyclogenesis. *J. Atmos. Sci*., **63**, 355–386.

Olander, T. L., and C. S. Velden, 2009: Tropical cyclone convection and intensity analysis using differenced infrared and water vapor imagery. *Wea. Forecasting*, **24**, 1558–1572.

Orlanski, I., 1975: A rational subdivision of scales for atmospheric processes. *Bull. Amer. Meteor. Soc.,* **56,** 527–530.

Ooyama, K. V., 1982: Conceptual evolution of the theory and modeling of the tropical cyclone. *J. Meteor. Soc. Japan,* **60,** 369–380.

Reasor, P. D., and M. T. Montgomery, 2001: Three-dimensional alignment and corotation of weak, TC-like vortices via linear vortex Rossby waves. *J. Atmos. Sci*., **58**, 2306-2330.

——, Eastin, J. D. Gamache, 2009: Rapidly intensifying Hurricane Guillermo (1997). Part I: Low-wavenumber structure and evolution. *Mon. Wea. Rev.,* **137,** 603–631.

——, M. T. Montgomery, F. D. Marks, Jr., and J. D. Gamache, 2000: Low-wavenumber structure and evolution of the hurricane inner core observed by airborne dual-doppler radar. *Mon. Wea. Rev.,* **128**, 1653–1680.

Riedlinger, S., R. Preller, and P. Martin, 2006: *Validation Test Report for the 1/16° East Asian Seas Navy Coastal Ocean Model Nowcast/Forecast System.* NRL/MR/7320—06-8978, 143 pp.

Riehl, H., and J. S. Malkus, 1958: On the heat balance in the equatorial trough zone. *Geophysica,* **6,** 503–538.

Ritchie, E. A. and G. J. Holland, 1997: Scale interactions during the formation of Typhoon Irving. *Mon. Wea. Rev.,* **125**, 1377–1396.

Rogers, R., 2010: Convective-scale structure and evolution during a high-resolution simulation of tropical cyclone rapid intensification. *J. Atmos. Sci*., **67**, 44-70.

——, and J. M. Fritsch, 2001: Surface cyclogenesis from convectively driven amplification of midlevel convective vortices. *Mon. Wea. Rev.,* **129**, 605–637.

Roux, F. and S. Ju, 1990: Single-Doppler observations of a West African squall line on 27–28 May 1981 during COPT 81: Kinematics, thermodynamics, and water budget. *Mon. Wea. Rev.,* **118**, 1826–1854.

——, V. Marecal, and D. Hauser, 1993: The 12-13 January 1988 narrow cold-frontal rainband observed during MFDP/FRONTS 87. Part I: Kinematics and thermodynamics. *J. Atmos. Sci*., **50**, 951–974.

Shelton, K. L., and J. Molinari, 2009: Life of a six-hour hurricane. *Mon. Wea. Rev.,* **137**, 51–67.

Shimazu, Y., 1998: Classification of precipitation systems in mature and early weakening stages of typhoons around Japan. *J. Meteor. Soc. Japan*, **76**, 437–445.

Simpson, J., E. Ritchie, G. J. Holland, J. Halverson, S. Stewart, 1997: Mesoscale interactions in tropical cyclone genesis. *Mon. Wea. Rev.,* **125**, 2643–2661.

Vigh, J. L., and W. H. Schubert, 2009: Rapid development of the tropical cyclone warm core. *J. Atmos. Sci*., **66**, 3335–3350.

Wang, J., J. Bian, W. O. Brown, H. Cole, V. Grubisic, and K. Young, 2009: Vertical air motion from T-REX radiosonde and dropsonde data. *J. Atmos. Oceanic Technol.,* **26,** 928–942.

WC-130J AF306 1033W Sinlaku mission scientist report, 16–17 September 2008. http://catalog.eol.ucar.edu/cgi-bin/tparc_2008/htmlwrap?file_url=/tparc_2008/report/usaf_c130/20080917/report.usaf_c130.200809172224.mission_summary.html

Young, K., J. Wang, and D. Lauritsen, 2009a: *THORPEX Pacific Regional Campaign (TPARC) 2008 Quality Controlled Air Force C-130 Dropsonde Data Set.* NCAR/Earth Observing Laboratory, 9 pp.

——, ——, and ——, 2009b: *THORPEX Pacific Regional Campaign (TPARC) 2008 Quality Controlled NRL-P3 Dropsonde Data Set.* NCAR/Earth Observing Laboratory, 9 pp.

——, ——, and ——, 2009c: *THORPEX Pacific Regional Campaign (TPARC) 2008 Quality Controlled DLR Falcon Dropsonde Data Set.* NCAR/Earth Observing Laboratory, 7 pp.

Yuter, S. E., and R. A. Houze Jr., 1997: Measurements of raindrop size distributions over the Pacific warm pool and implications for Z-R relations, *J. Appl. Meteorol.* **36**, 847–867.

Zipser, E. J., R. J. Meitin, and M. A. LeMone, 1981: Mesoscale motion fields associated with a slowly moving GATE convective band. *J. Atmos. Sci.,* **38,** 1725–1750.

INITIAL DISTRIBUTION LIST

1.   Defense Technical Information Center
        Ft. Belvoir, Virginia

2.   Dudley Knox Library
        Naval Postgraduate School
        Monterey, California

3.   Professor Patrick A. Harr
        Naval Postgraduate School
        Monterey, California

4.   Professor Russell L. Elsberry
        Naval Postgraduate School
        Monterey, California

5.   Professor Michael T. Montgomery
        Naval Postgraduate School
        Monterey, California

6.   Professor Philip A. Durkee
        Naval Postgraduate School
        Monterey, California

7.   Professor Francis X. Giraldo
        Naval Postgraduate School
        Monterey, California

8.   Commander Elizabeth R. Sanabia
        Naval Postgraduate School
        Monterey, California

9.   Commander Daniel Eleuterio
        Office of Naval Research
        Arlington, Virginia

10.   Director, Joint Typhoon Warning Center
        Naval Pacific Meteorology and Oceanography Center
        Pearl Harbor, Hawaii